

ISSN 2074-272X

**науково-практичний
журнал**

2025/5



ЕІЕ **Електротехніка і Електромеханіка**

Electrical Engineering

& Electromechanics

**Електричні машини та апарати
Електротехнічні комплекси та системи
Промислова електроніка
Техніка сильних електричних та магнітних полів,
інженерна електрофізика
Електричні станції, мережі і системи**

**Журнал включено до найвищої категорії «А»
Переліку фахових видань України**

З 2019 р. журнал індексується у Scopus

**З 2015 р. журнал індексується
у Web of Science Core Collection:
Emerging Sources Citation Index**



Electrical Engineering & Electromechanics

Scientific Journal was founded in 2002

Co-founders: National Technical University «Kharkiv Polytechnic Institute» (Kharkiv, Ukraine);

Anatolii Pidhorneyi Institute of Power Machines and Systems of NAS of Ukraine (Kharkiv, Ukraine)

EDITORIAL BOARD

Sokol Ye.I.	Editor-in-Chief , Professor, Corresponding member of NAS of Ukraine, National Technical University «Kharkiv Polytechnic Institute» (NTU «KhPI»), Ukraine
Bolyukh V.F.	Deputy Editor , Professor, NTU «KhPI», Ukraine
Korytchenko K.V.	Deputy Editor , Professor, NTU «KhPI», Ukraine
Rozov V.Yu.	Deputy Editor , Professor, Corresponding member of NAS of Ukraine, Anatolii Pidhorneyi Institute of Power Machines and Systems of NAS of Ukraine (IEMS of NAS of Ukraine), Kharkiv, Ukraine
Abu-Siada A.	Professor, Curtin University, Perth, Australia
Babak V.P.	Professor, academician of NAS of Ukraine, General Energy Institute of NAS of Ukraine, Kyiv, Ukraine
Baltag O.	Professor, Grigore T. Popa University Medicine and Pharmacy, Romania
Baranov M.I.	Senior Researcher, NTU «KhPI», Ukraine
Batygin Yu.V.	Professor, Kharkiv National Automobile and Highway University, Ukraine
Bezprozvannykh G.V.	Professor, NTU «KhPI», Ukraine
Bíró O.	Professor, Institute for Fundamentals and Theory in Electrical Engineering, Graz, Austria
Boiko M.I.	Professor, NTU «KhPI», Ukraine
Bouktir T.	Professor, Ferhat Abbas University, Setif 1, Algeria
Buriakovskiy S.G.	Professor, NTU «KhPI», Ukraine
Butkevych O.F.	Professor, Institute of Electrodynamics of NAS of Ukraine, Kyiv, Ukraine
Colak I.	Professor, Nisantasi University, Istanbul, Turkey
Cruz S.	Professor, University of Coimbra, Portugal
Danylchenko D.O.	Associate Professor, NTU «KhPI», Ukraine
Doležel I.	Professor, University of West Bohemia, Pilsen, Czech Republic
Féliachi M.	Professor, Technological Institute of Saint-Nazaire, University of Nantes, France
Grinchenko V.S.	Chief Researcher, General Energy Institute of NAS of Ukraine, Kyiv, Ukraine
Guerrero J.M.	Professor, Aalborg University, Denmark
Hammarström T.	Professor, Chalmers University of Technology, Sweden
Ida N.	Professor, The University of Akron, Ohio, USA
Izykowski J.	Professor, Wrocław University of Science and Technology, Poland
Kildishev A.V.	Associate Research Professor, Purdue University, USA
Klepikov V.B.	Professor, NTU «KhPI», Ukraine
Korzeniewska E.	Professor, Lodz University of Technology, Poland
Kuznetsov B.I.	Professor, IEMS of NAS of Ukraine, Kharkiv, Ukraine
Kyrylenko O.V.	Professor, academician of NAS of Ukraine, Institute of Electrodynamics of NAS of Ukraine, Kyiv, Ukraine
Malik O.P.	Professor, University Of Calgary, Canada
Maslov V.I.	Professor, National Science Center «Kharkiv Institute of Physics and Technology», Ukraine
Mikhaylov V.M.	Professor, NTU «KhPI», Ukraine
Miljavec D.	Professor, University of Ljubljana, Slovenia
Milykh V.I.	Professor, NTU «KhPI», Ukraine
Nacke B.	Professor, Gottfried Wilhelm Leibniz Universität, Institute of Electrotechnology, Hannover, Germany
Oleschuk V.	Professor, Institute of Power Engineering of Technical University of Moldova, Republic of Moldova
Petrushin V.S.	Professor, Odessa National Polytechnic University, Ukraine
Podoltsev A.D.	Senior Researcher, Institute of Electrodynamics of NAS of Ukraine, Kyiv, Ukraine
Reutskiy S.Yu.	Senior Researcher, IEMS of NAS of Ukraine, Kharkiv, Ukraine
Rezinkina M.M.	Professor, NTU «KhPI», Ukraine
Rusanov A.V.	Professor, academician of NAS of Ukraine, IEMS of NAS of Ukraine, Kharkiv, Ukraine
Sikorski W.	Professor, Poznan University of Technology, Poland
Strzelecki R.	Professor, Gdansk University of Technology, Poland
Suemitsu W.	Professor, Universidade Federal Do Rio de Janeiro, Brazil
Trichet D.	Professor, Institut de Recherche en Energie Electrique de Nantes Atlantique, France
Vaskovskiy Yu.M.	Professor, National Technical University of Ukraine «Igor Sikorsky Kyiv Polytechnic Institute», Kyiv, Ukraine
Vazquez N.	Professor, Tecnológico Nacional de México en Celaya, Mexico
Vinnikov D.	Professor, Tallinn University of Technology, Estonia
Yagup V.G.	Professor, Kharkiv National Automobile and Highway University, Ukraine
Yamnenko Yu.S.	Professor, National Technical University of Ukraine «Igor Sikorsky Kyiv Polytechnic Institute», Kyiv, Ukraine
Yatchev I.	Professor, Technical University of Sofia, Bulgaria
Zagirnyak M.V.	Professor, academician of NAES of Ukraine, Kremenchuk M.Ostrohradskyi National University, Ukraine
Zgraja J.	Professor, Lodz University of Technology, Poland
Grechko O.M.	Executive Managing Editor , Associate Professor, NTU «KhPI», Ukraine

From no. 1 2019 Journal «Electrical Engineering & Electromechanics» is indexing in **Scopus**

and from no. 1 2005 Journal is indexing in **Web of Science Core Collection: Emerging Sources Citation Index (ESCI)**

Also included in DOAJ (Directory of Open Access Journals), in EBSCO's database, in ProQuest's databases – Advanced Technologies & Aerospace Database and Materials Science & Engineering Database, in Gale/Cengage Learning databases.

Editorial office address:

National Technical University «Kharkiv Polytechnic Institute», Kyrpychova Str., 2, Kharkiv, 61002, Ukraine

phone: +380 67 3594696, e-mail: a.m.grechko@gmail.com (**Grechko O.M.**)

ISSN (print) 2074-272X

© National Technical University «Kharkiv Polytechnic Institute», 2025

ISSN (online) 2309-3404

© Anatolii Pidhorneyi Institute of Power Machines and Systems of NAS of Ukraine, 2025

Approved for printing on 29 August 2025. Format 60 × 90 1/8. Paper – offset. Laser printing. Edition 50 copies.

Printed by Printing house «Madrid Ltd» (18, Gudanova Str., Kharkiv, 61024, Ukraine)



no. 5, 2025

Table of Contents

Electrical Machines and Apparatus

Iegorov O.B., Kundenko M.P., Iegorova O.Yu., Mardziavko V.A., Rudenko A.Yu. The influence of the design of the stator winding of a synchronous-reactive generator on increasing its energy efficiency..... 3

Electrotechnical Complexes and Systems

Hafaiedh H., Saudi Y., Benamor A., Chrifi-Alaoui L. Wind farms integration into power system with improved location and stability problem solving..... 10

Jeridi A., Moulahi M.H., Khaterchi H., Zaafouri A. Maximum power point tracking improving of photovoltaic systems based on hybrid triangulation topology aggregation optimizer and incremental conductance algorithm 17

Kuznetsov B.I., Nikitina T.B., Bovdii I.V., Chunikhin K.V., Kolomiets V.V., Kobylanskyi B.B. Optimization of combined active-passive electromagnetic shielding system for overhead power lines magnetic field normalization in residential building space 27

Mehedi F., Bouyakoub I., Yousfi A., Taleb R., Reguieg Z. Improve of the direct torque control strategy applied to a multi-phase interior permanent magnet synchronous motor using a super twisting sliding mode algorithm 38

Senani F., Rahab A., Benalla H. Performance evaluation and analysis by simulation for sliding mode control with speed regulation of permanent magnet synchronous motor drives in electric vehicles 43

Zdiri S., Moulahi M., Messaoudi F., Zaafouri A. Takagi-Sugeno fuzzy model identification using improved multiswarm particle swarm optimization in solar photovoltaics 49

Industrial Electronics

Romashko V.Y., Batrak L.M. Regulation characteristics of a step-down pulse regulator in continuous and discontinuous conduction mode..... 57

High Electric and Magnetic Fields Engineering, Engineering Electrophysics

Boiko M.I., Makogon A.V. Disinfectant treatment of liquids with high specific electrical conductivity by high-voltage nanosecond pulses with a subnanosecond front 62

Khrysto O.I. Analysis of energy characteristics of a transistor pulse generator in the process of electric spark dispersion of current-conductive granular media 70

Power Stations, Grids and Systems

Shevchenko S.Yu., Danylenko D.O., Hanus R.O., Dryvetskyi S.I., Berezka S.K., Grechko O.M. Features of designing high-voltage overhead power lines in an underground collector..... 80

O.B. Iegorov, M.P. Kundenko, O.Yu. Iegorova, V.A. Mardziavko, A.Yu. Rudenko

The influence of the design of the stator winding of a synchronous-reactive generator on increasing its energy efficiency

Introduction. Increasing the energy efficiency of electric generators is a pressing task for various areas of energy, in particular for autonomous systems and transport. Synchronous-reactive generators (SRGs) are becoming increasingly widespread due to their simple design, absence of magnets and mechanical contacts, and high reliability. The **task** of the proposed work is to study the influence of the design of the double winding of the stator of a SRG on its energy characteristics, determine the optimal parameters of the mutual arrangement of the windings, and develop recommendations for increasing the generator efficiency. **Goal.** Analysis of the influence of the design of the double winding of the stator of a SRG on the output energy characteristics and determine recommendations when designing this type of electrical machines. **Methodology.** The analysis was carried out using numerical modeling by the finite element method in the ANSYS Maxwell environment. Various options for the mutual arrangement of the main and excitation windings in the generator stator were considered. **Results.** The influence of the single-layer and double-layer winding design on the output characteristics of the generator was studied. It was found that a two-layer arrangement with a phase shift of 2 slots provides minimal torque ripple, improves the stability of the generator operation and helps to increase the efficiency to 92.5 %. **Scientific novelty.** For the first time, the effect of the phase shift of the windings on electromagnetic processes in the SRG has been studied in detail, which allows optimizing its design and improving operational performance. **Practical value.** The results can be used in the design of new generators with improved characteristics for use in wind power, diesel generator sets and autonomous electrical systems. References 19, table 1, figures 12.

Key words: synchronous-reactive generator, winding, rotor, speed, torque, energy efficiency.

Вступ. Підвищення енергоефективності електричних генераторів є актуальною задачею для різних сфер енергетики, зокрема для автономних систем та транспорту. Синхронно-реактивні генератори (СРГ) завдяки простій конструкції, відсутності магнітів та механічних контактів, а також високій надійності набувають все більшого поширення. **Задача** даної роботи полягає у дослідженні впливу конструкції подвійної обмотки статора СРГ на його енергетичні характеристики, визначенні оптимальних параметрів взаємного розташування обмоток та розробці рекомендацій для підвищення ефективності генератора. **Мета.** Аналіз впливу конструкції подвійної обмотки статора СРГ на вихідні енергетичні характеристики та визначення рекомендацій при проектуванні такого типу електричних машин. **Методологія.** Аналіз проводився за допомогою чисельного моделювання методом скінчених елементів у середовищі ANSYS Maxwell. Розглянуто різні варіанти взаємного розташування головної та збуджуючої обмоток у статорі генератора. **Результати.** Досліджено вплив одношарової та двошарової конструкції обмотки на вихідні характеристики генератора. Встановлено, що двошарове розташування з фазовим зміщенням на 2 пази забезпечує мінімальні пульсації крутного моменту, покращує стабільність роботи генератора та сприяє підвищенню ККД до 92,5 %. **Наукова новизна.** Вперше детально досліджено вплив фазового зміщення обмоток на електромагнітні процеси в СРГ, що дозволяє оптимізувати його конструкцію та покращити експлуатаційні показники. **Практична значимість.** Результати можуть бути використані при проектуванні нових генераторів з покращеними характеристиками для застосування у вітроенергетиці, дизельних генераторних установках та автономних електричних системах. Бібл. 19, табл. 1, рис. 12.

Ключові слова: синхронно-реактивний генератор, обмотка, ротор, частота обертання, обертовий момент, енергоефективність.

Introduction. Currently, there is a growing need to create energy-efficient AC electric generators. They are widely used in many energy devices and facilities, such as wind power plants, diesel generators, as sources of electricity in railway, aviation and road transport [1].

The most widespread generators are self-excited generators, namely synchronous generators with permanent magnets, induction generators with dual power supply and phase rotor, asynchronous generators with excitation capacitors, synchronous generators with excitation windings on the armature.

Permanent magnet synchronous generators have higher efficiency, higher power density, which does not require an additional power source to excite the magnetic field, and higher reliability due to the absence of mechanical components, such as carbon brushes and slip rings [2] and include rare-earth magnetic materials, namely neodymium-iron-boron (NdFeB). Recently, the

increased demand for electric vehicles has led to a sharp increase in the demand and cost of such magnets [3].

Induction generators with dual power supply and phase rotor have good energy characteristics, but the presence of a mechanical brush contact for supplying excitation to the rotor winding reduces their operational characteristics [4].

Generators with excitation capacitors have advantages over traditional AC generators, which consist in the absence of brush contact systems in their design, as well as in the simplicity of the design of the machine itself [5]. However, the operation of these generators is characterized by extreme instability, the dependence of the induced voltage on the value of the connected load and the frequency of rotation of the generator rotor.

Synchronous generators with excitation windings on the armature are the most studied electric machines today. They have good control and external characteristics.

However, the main disadvantage is the mechanical brush contact for supplying excitation windings.

A synchronous-reactive generator (SRG) with a double stator winding is a promising source of electricity, capable of operating effectively in many energy facilities and systems.

The goal of the work is to analyze the influence of the design of the double stator winding of the SRG on the output energy characteristics and to determine recommendations when designing this type of electrical machines.

Literature review. In recent years, the SRG has become a major competitor to synchronous generators with permanent magnets and induction generators due to its reliability, simple rotor design, no losses in the rotor winding, no magnets (thus eliminating the problem of demagnetization), and lower cost [6]. Numerous research works have been devoted to the study of SRG. In [7], the results of studies of SRG with a double stator winding with different variants of air barriers in the rotor are presented. It is shown that the use of SRG with a slotted rotor core allows inducing an open-circuit voltage 10 % higher than for SRG with a rotor of conventional air barriers. In [8], the operation of SRG with a series and shunt connection and its influence on transient processes in the generator are reported.

Works [9, 10] present the results of studies of the vibration characteristics of synchronous-reactive machines depending on the design of the rotor air barriers. In [11–13], a dynamic and performance analysis of a three-phase SRG was carried out to check the operation of the generator under various load conditions. The dependencies of the output voltage and power of the generator on the excitation current supplied to the winding located on the stator are presented. Work [14] presents the results of the finite element analysis to determine the generator performance depending on its design. Modeling the influence of the electromagnetic field on structural elements is also considered in [15].

The analysis of the literature indicates that the interest in SRG is significant, but questions remain regarding the influence of the design of the stator winding and the mutual influence of the working winding and the excitation winding on its energy characteristics. Therefore, this issue is devoted to the study, the results of which are presented in this work.

Presentation of the main material. Analytical and conditional-analytical dependencies used in the design and assessment of the operating properties of an electric machine based on its electrical parameters (resistance, inductance) and variables (voltages, currents) have sufficient convergence of the results of calculations and tests. Currently, in the design of SRGs, methods for determining the optimal design and energy parameters using the finite element method have also become widespread [12, 16]. In particular, research using multispheroidal models is presented in [17]. When modeling SRGs in a fixed coordinate system, difficulties arise in taking into account the change in parameters (inductance) of the stator phases during rotor rotation. To

obtain the most acceptable result, it is better to consider the equations of synchronous machines in the d - q coordinate system rotating with the rotor [18]. The d axis is the axis of the highest magnetic rotor conductivity (rotor magnetic axis), the q axis is the axis of the lowest rotor conductivity (Fig. 1).

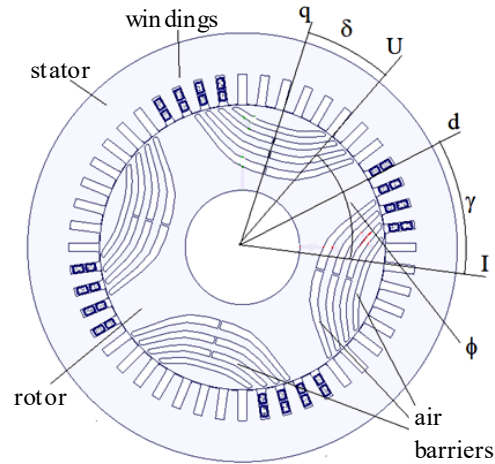


Fig. 1. Determining the relationship between angles ϕ , δ , γ

When writing the equations of the steady-state mode of the SRG, it is necessary to determine the electrical load factor, which should determine the external torque, for example, from a wind turbine or a diesel internal combustion engine. The angle δ or the angle γ is used as the load factor. The balance of the generator phase angles can be represented as:

$$\phi = \pi/2 - \delta + \gamma, \quad (1)$$

where ϕ is the phase angle between the current and voltage vectors; δ is the phase angle between the q axis and the voltage vector; γ is the phase angle between the d axis and the current vector.

The energy parameters of the SRG depend on the value of the angle γ . An increase in the electrical load connected to the generator stator winding leads to an increase in the value of this angle.

In [6], the influence of the phase angle between the magnetic axis of the rotor and the current vector of the stator winding on the characteristics of a synchronous-reactive motor was considered. Since a synchronous-reactive machine is a reversible machine, even when it operates in generator mode, we can talk about the dependence of the generator parameters on the angle γ . In the nominal mode of operation of the motor, the equations of longitudinal and transverse voltages have the form:

$$\dot{U}_d = (r + jx)i_d + jL_q\omega i_q; \quad (2)$$

$$\dot{U}_q = (r + jx)i_q + jL_d\omega i_d, \quad (3)$$

where L_d , L_q are the total stator inductances along the d and q axes; i_d , i_q are the stator winding currents along the d and q axes; r is the stator phase resistance; x is the stator phase leakage resistance; ω is the generator shaft angular frequency.

In the operating mode, the electrical equilibrium equation at synchronous frequency for one phase of the SRG stator can be written as:

$$\dot{U} = I(r + jx) + jI_d x_d + jI_q x_q. \quad (4)$$

The dependence of the longitudinal and transverse resistances on the inductances L_d and L_q can be expressed as follows:

$$x_d = 2\pi f L_d; \quad (5)$$

$$x_q = 2\pi f L_q. \quad (6)$$

The currents of the longitudinal and transverse components of the generator winding can be found as:

$$I_d = \frac{U_i}{x_d} \cos \delta; \quad (7)$$

$$I_q = \frac{U_i}{x_q} \sin \delta. \quad (8)$$

The expression for the stator current can be written [6] as:

$$\dot{I} = \frac{U_i}{r + j(x + x_d)} + \frac{U_i}{\frac{r_\gamma}{\tan \gamma} + jx_\gamma}. \quad (9)$$

Variable values of the angle γ can be simulated by rotating the rotor relative to the stator at a constant value of the load on the stator winding in a fixed coordinate system, which corresponds to a constant amplitude of the phase current. At the same time, in a stationary coordinate system, the direction and value of the stator MMF vector will remain unchanged, and the position of the d axis will change. This was the basis for research on the SRG with different design options and mutual arrangement of the working winding and the stator excitation winding.

The research was carried out when designing a SRG with a power of 160 kW with a rotor speed of 1500 rpm and linear voltage at the output of 380 V for a diesel generator set. The diesel engine, which is supposed to be used with the SRG, develops a torque of 1100 N·m, at a shaft speed of 1500 rpm. The mechanical output power from the diesel engine will be 172.8 kW. Therefore, the useful electric power of the generator, taking into account losses, will be ≈ 160 kW. The outer diameter of the stator is 450 mm, of the rotor is 299 mm, the length of the stator and rotor packages is 265 mm. The geometry of the rotor air barriers and the electrical symmetrical load on the phases of the main winding, which was purely active, remained unchanged. This allowed us to conduct a comparative assessment of the options and select, in the opinion of the authors, the most optimal generator in terms of efficiency and dynamic characteristics. Of course, the dimensions of the rotor air barriers, the geometry of the rotor and stator, the materials of the stator or rotor affect the characteristics of the SRG, but the goal of this study is to determine the influence of the stator windings and their location on the output characteristics. Therefore, SRGs with the same geometry of the stator, rotor and unchanged magnetic core materials were studied.

In the first case, the design of the SRG with an equal distribution of the main winding and the excitation winding in 48 stator slots was considered (Fig. 2).

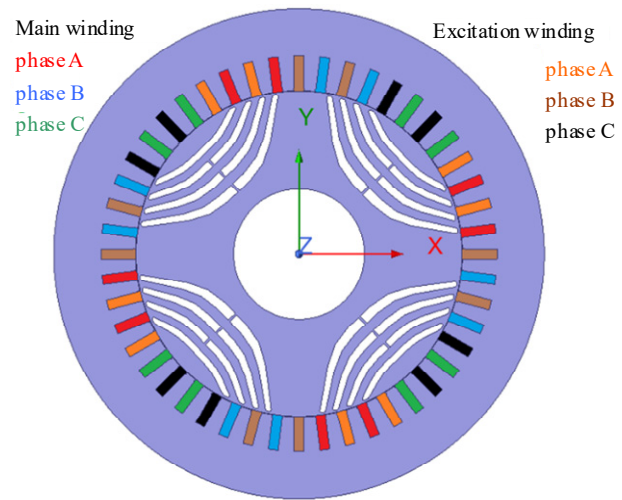


Fig. 2. Single-layer arrangement of the main and excitation windings of the SRG stator

Simulation and results. As mentioned above, by changing the angle γ , i.e., rotating the rotor relative to the stator, it is possible to simulate a change in the operating mode of the SRG at constant values of load and excitation. The results of this study are shown in Fig. 3.

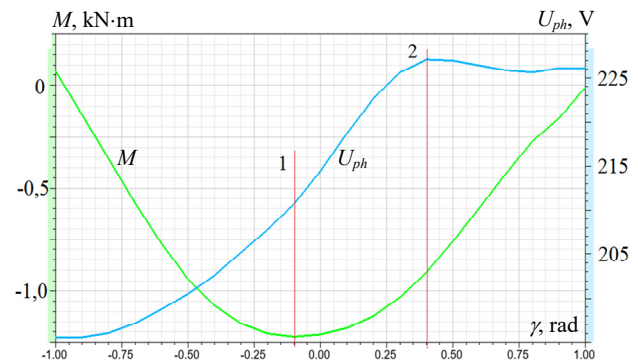


Fig. 3. Dependencies of external torque and output phase voltage on the angle γ

Lines 1 and 2 show the values of the angle γ for the maximum value of the torque (and, therefore, for the maximum input power of the generator) and for the maximum value of the output voltage. It can be seen that the values of these maxima do not coincide, which reduces the characteristics of the generator.

Figure 4 shows the distribution of magnetic flux density in the magnetic core with a single-layer arrangement of the main and exciting stator windings. The value of magnetic flux density in the stator tooth zones is 2 T, which leads to an increase in losses in the magnetic core. A similar analysis of the distribution of currents in the winding is presented in [19].

Figure 5 shows the graphs of the SRG torque and the output phase voltage.

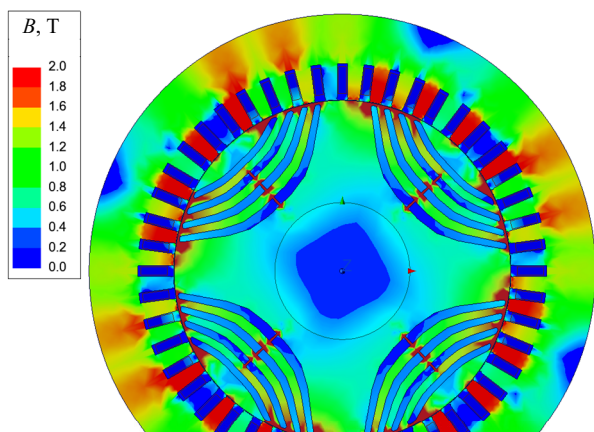


Fig. 4. Distribution of magnetic flux density in the magnetic core with a single-layer arrangement of the main and exciting windings of the SRG stator

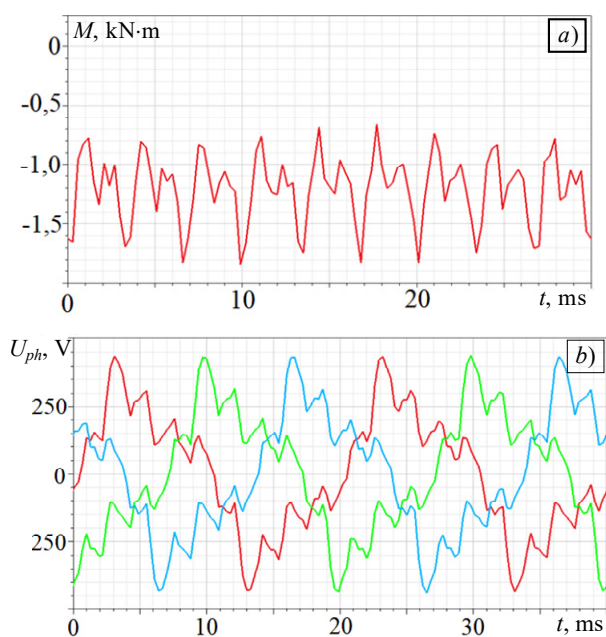


Fig. 5. Torque (a) and output phase voltage (b)

The « \leftrightarrow » sign of the torque indicates that it is an external torque from the diesel engine rotating the generator rotor. Large torque pulsations can be observed, which indicate a significant change in the stator inductances along the d and q axes during rotor rotation.

The bearings of the generator mechanical system will experience large pulsating loads, which will affect their performance. The rated value of the output phase voltage is 222 V, which corresponds to 385 V of line voltage at an electrical load of 158 kW. The efficiency of the generator with such a stator winding was 91.2 %.

The option of a two-layer stator winding was considered (Fig. 6). Two-layer windings are very widely used as stator windings in modern production of high-power electric motors and the process of their manufacture is technologically advanced.

The main three-phase winding is located closer to the outer diameter of the stator, and the excitation winding is closer to the rotor surface. A study was conducted of four options for the mutual arrangement of the phases of the main and exciting windings with their two-layer arrangement (Fig. 7, a–d).

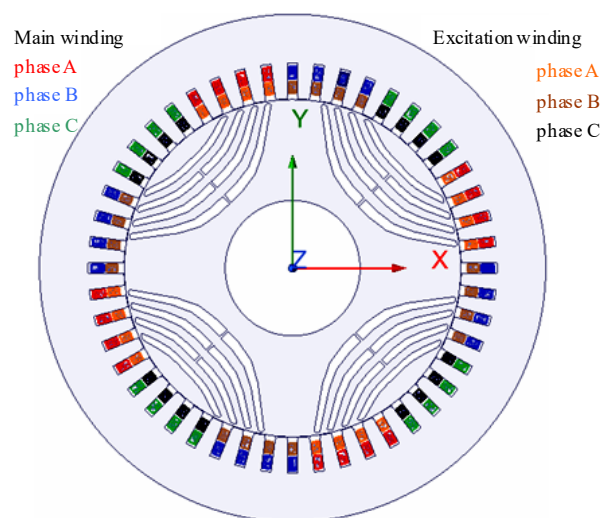


Fig. 6. Two-layer arrangement of the main and excitation windings of the SRG stator

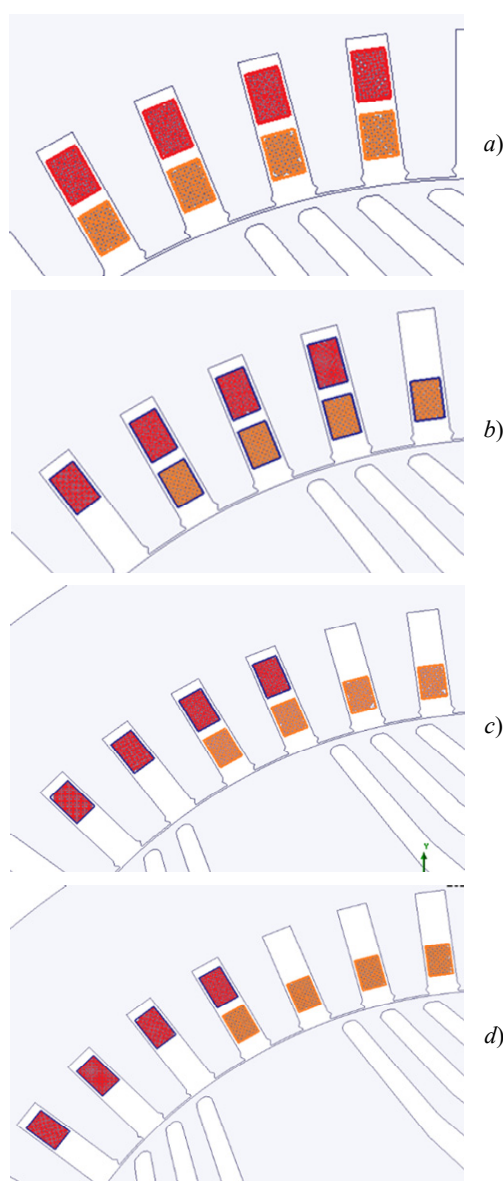


Fig. 7. Variants of the mutual arrangement of the phases of the main and exciting windings of the stator of the SRG: a) without phase shift; b) shift by 1 slot; c) shift by 2 slots; d) shift by 3 slots

The results of studies of the characteristics of the SRG with a two-layer arrangement of stator windings are shown in Fig. 8,a–d.

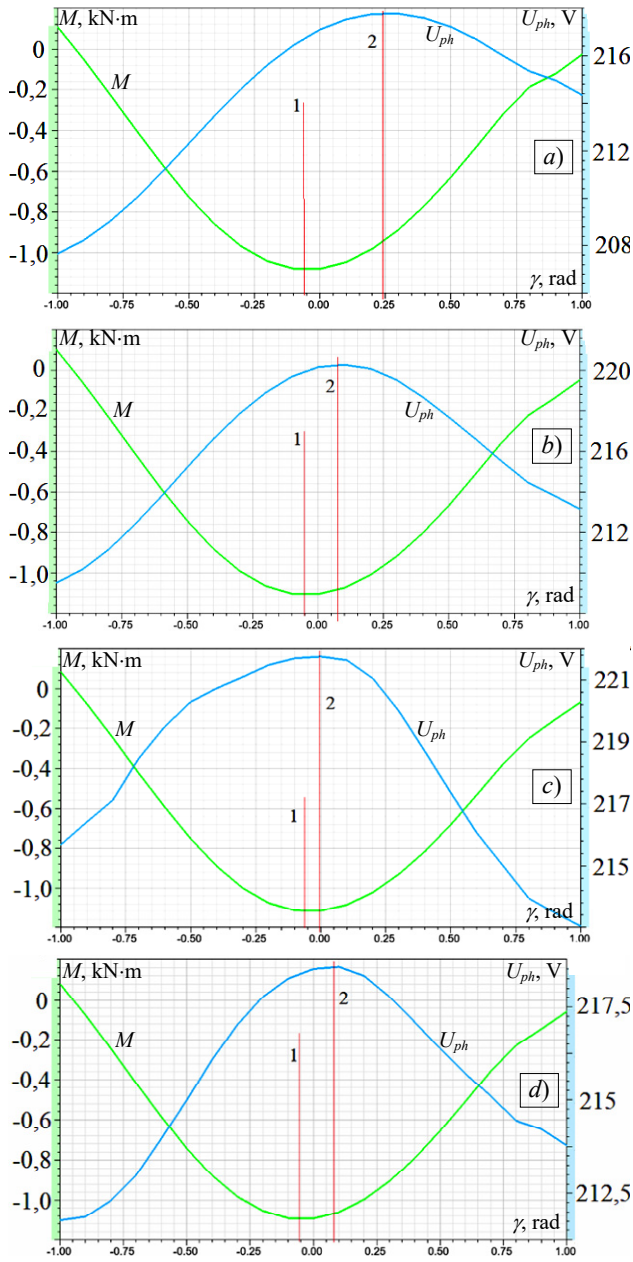


Fig. 8. Dependencies of external torque and output phase voltage on the angle γ at different mutual arrangements of the windings: a) without phase shift; b) shift by 1 slot; c) shift by 2 slots; d) shift by 3 slots

The SRG with a phase shift of the main and exciting windings by 2 slots practically has the coincidence of the maximum induced voltage and torque by the angle γ (Fig. 8,c). With this design of the stator windings, the largest phase voltage is also observed at the generator output (221.7 V) compared to other options.

The distribution of magnetic flux density in the magnetic core with a phase shift of the main and exciting windings by 2 slots is shown in Fig. 9.

The reduction in magnetic flux density in the tooth zones and the stator yoke compared to the single-layer winding option reduces losses in the magnetic core by 24 % (Fig. 10).

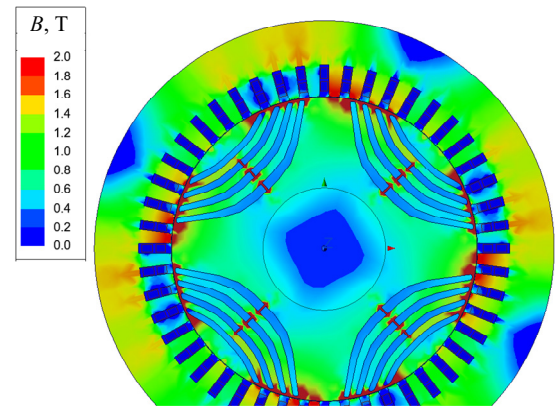


Fig. 9. Distribution of magnetic flux density in the magnetic core when the phases of the main and exciting windings are shifted by 2 slots

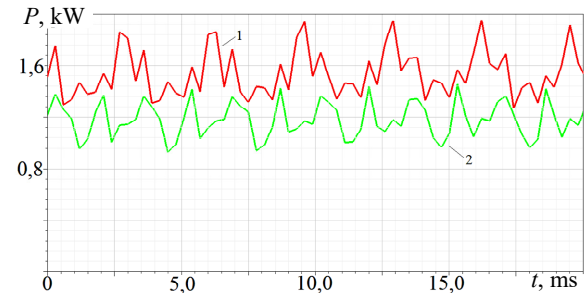


Fig. 10. Losses in the stator magnetic core with a single-layer stator winding (1) and with a double-layer winding with a phase shift of the main and excitation windings by 2 slots (2)

The conducted studies of the torque on the SRG rotor and the shape of the output voltage for the best option of a two-layer design of the stator windings show a reduction in pulsations compared to a single-layer design (Fig. 11).

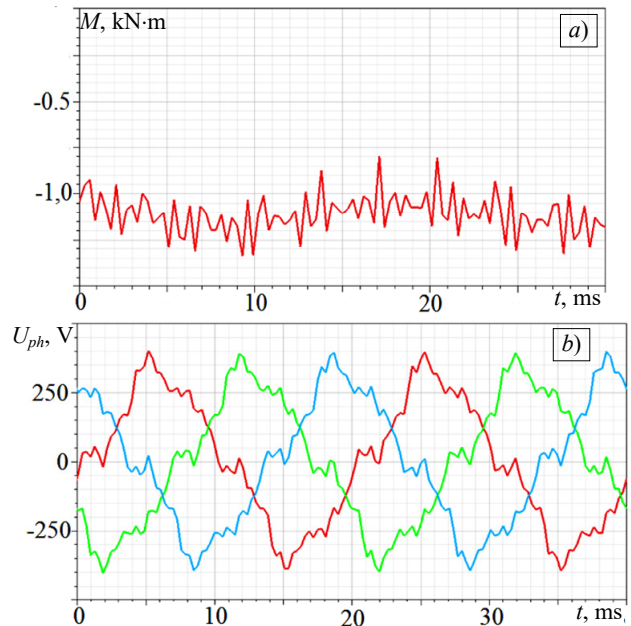


Fig. 11. Torque (a) and output phase voltage (b) for a SRG with a two-layer arrangement of the main and excitation windings and a mutual displacement of 2 slots

To compare the oscillations of the torque of the SRG with a single-layer stator winding and with a double-layer

winding when the phases of the main and exciting windings are shifted by 2 slots, spectrograms were created with the determination of amplitudes in the frequency range of 0–1 kHz (Fig. 12).

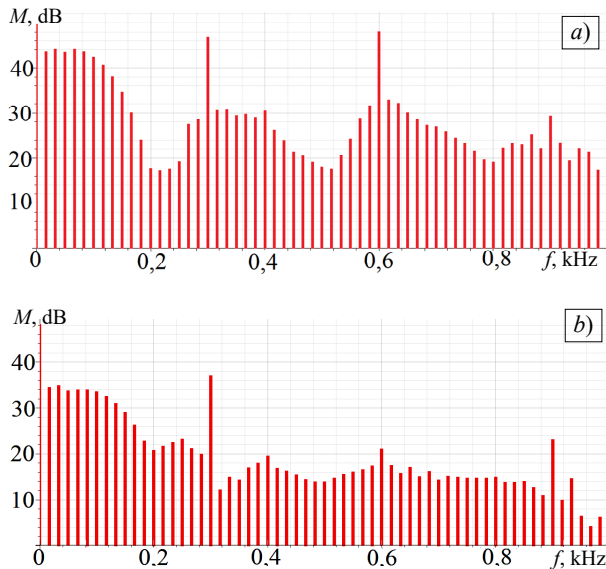


Fig. 12. Spectrograms of the torque with a single-layer stator winding (a) and with a double-layer winding with a phase shift of the main and exciting windings by 2 slots (b)

Comparison of the spectrograms of the SRG with a single-layer winding and a double-layer stator winding showed a decrease in amplitude at a frequency of 100 Hz by 26 %; for a frequency of 150 Hz – by 14 %. For both variants at a frequency of 300 Hz, a sharp increase in amplitude is observed, but for the SRG with a double-layer winding the amplitude is 53 % less than for the SRG variant with a single-layer winding. Reducing torque ripples will have a positive effect on the performance of bearing units and will lead to a decrease in vibrations during the operation of the SRG.

The results of determining losses and efficiency for the selected variant of the SRG with a double-layer stator winding with a phase shift of 2 slots are given in Table 1.

Table 1
Losses and efficiency of the SRG with a two-layer stator winding with a phase shift of 2 slots

No.	Parameter	Values
1	Electrical losses in stator windings, W	7152
2	Losses in the magnetic core steel, W	1621
3	Mechanical losses, W	2600
4	Additional losses, W	1600
5	Total losses, W	12973
6	Efficiency, %	92,5

Conclusions. The conducted studies of the SRG with the main and excitation windings of the stator showed that there is a significant dependence of the characteristics on the design of these windings. The considered variant with a single-layer arrangement of both windings in the stator slots is characterized by the fact that there are large torque pulsations (with an amplitude of 0.6 kN·m) and lower efficiency than in the other considered variants.

The two-layer arrangement of the main and exciting windings of the stator showed the best results in the analysis of the SRG. However, the research has established that the mutual arrangement of the phases of the main and exciting windings also has a significant impact on the SRG parameters. The results of the calculation experiments have determined the best option for the implementation of the two-layer SRG winding, namely with a phase shift of 2 slots from each other. This provides a significant reduction in torque fluctuations and an increase in the energy characteristics of the SRG and allows to obtain high efficiency (92.5 %) with a useful electric power of 160 kW at the SRG output.

Conflict of interest. The authors declare no conflict of interest.

REFERENCES

1. Mazurenko L.I., Dzhura O.V., Popovych O.M., Hrebenikov V.V., Holovan I.V. Electric generators and AC motors. Electromechatronic energy converters. *Proceedings of the Institute of Electrodynamics of the National Academy of Sciences of Ukraine*, 2013, no. 35, pp. 58-66. (Ukr).
2. Choe Wei Chang C., Jian Ding T., Jian Ping T., Chia Chao K., Bhuiyan M.A.S. Getting more from the wind: Recent advancements and challenges in generators development for wind turbines. *Sustainable Energy Technologies and Assessments*, 2022, vol. 53, art. no. 102731. doi: <https://doi.org/10.1016/j.seta.2022.102731>.
3. Wang H., Lamichhane T.N., Paranthaman M.P. Review of additive manufacturing of permanent magnets for electrical machines: A prospective on wind turbine. *Materials Today Physics*, 2022, vol. 24, art. no. 100675. doi: <https://doi.org/10.1016/j.mtphys.2022.100675>.
4. Tezcan M.M., Ayaz M. Performance analysis of aluminium wound double fed induction generator for cost-efficient wind energy conversion systems. *Engineering Research Express*, 2023, vol. 5, no. 4, art. no. 045037. doi: <https://doi.org/10.1088/2631-8695/ad061b>.
5. Zachepa I., Zachepa N., Khrebtova O., Serhiienko I., Shokarov D., Mykhalchenko G. Guaranteed and Reliable Excitation of Asynchronous Generator Coupled to Shaft of Vehicle. *2021 IEEE International Conference on Modern Electrical and Energy Systems (MEES)*, 2021, pp. 1-5. doi: <https://doi.org/10.1109/MEES52427.2021.9598649>.
6. Iegorov O., Iegorova O., Kundenko M., Andriy M. The Influence of the Phase Angle Between the Rotor Magnetic Axis and the Stator Winding Current Vector on the Synchronous Reluctance Motor Efficiency. *2019 IEEE International Conference on Modern Electrical and Energy Systems (MEES)*, 2019, pp. 62-65. doi: <https://doi.org/10.1109/MEES.2019.8896480>.
7. Adjei-Frimpong S., Muteba M. Performance Analysis of a Synchronous Reluctance Generator with a Slitted-Rotor Core for Off-Grid Wind Power Generation. *Electricity*, 2025, vol. 6, no. 1, art. no. 2. doi: <https://doi.org/10.3390/electricity6010002>.
8. Livutse Amuhaya L., Simon Obe E., Murtala Zungeru A., Ijeoma Obe P. Performance of Synchronous Reluctance Generators with Series and Shunt Stator Connections. *International Journal of Electrical and Computer Engineering Systems*, 2023, vol. 14, no. 5, pp. 589-592. doi: <https://doi.org/10.32985/ijeces.14.5.10>.
9. Iegorov O., Iegorova O., Kundenko M., Potryvaieva N. Ripple Torque Synchronous Reluctance Motor with Different Rotor Designs. *2020 IEEE Problems of Automated Electrodynamics. Theory and Practice (PAEP)*, 2020, pp. 1-4. doi: <https://doi.org/10.1109/PAEP49887.2020.9240820>.

10. Enemor C.G., Idoniboyeobu D.C., Braide S.L. Performance Analysis of Synchronous Reluctance Generator. *International Journal for Research in Applied Science and Engineering Technology*, 2022, vol. 10, no. 5, pp. 765-774. doi: <https://doi.org/10.22214/ijraset.2022.41501>.
11. Štumberger B., Igrec D., Chowdhury A., Hadžiselimovic M. Design of synchronous reluctance generator with dual stator windings and anisotropic rotor with flux barriers. *Przeglad Elektrotechniczny*, 2012, vol. 88, no. 12 B, pp. 16-19.
12. Cupertino F., Pellegrino G., Gerada C. Design of Synchronous Reluctance Motors With Multiobjective Optimization Algorithms. *IEEE Transactions on Industry Applications*, 2014, vol. 50, no. 6, pp. 3617-3627. doi: <https://doi.org/10.1109/TIA.2014.2312540>.
13. Iegorov O., Iegorova O. Influence of the geometric parameters of a synchronous reluctance motor rotor on its energy characteristics. *Bulletin of the Kharkiv National Technical University of Agriculture named after Peter Vasylenko*, 2019, vol. 161, pp. 99-101.
14. Cui J. Optimal control of maximum torque current ratio for synchronous reluctance motor based on virtual signal injection algorithm. *Archives of Electrical Engineering*, 2024, vol. 73, no. 2, pp. 451-466. doi: <https://doi.org/10.24425/ae.2024.149926>.
15. Lavinsky D.V., Zaitsev Y.I. Computational studies of electromagnetic field propagation and deforming of structural elements for a thin-walled curved workpiece and an inductor. *Electrical Engineering & Electromechanics*, 2024, no. 2, pp. 55-60. doi: <https://doi.org/10.20998/2074-272X.2024.2.08>.
16. Mynar Z., Vaclavek P., Blaha P. Synchronous Reluctance Motor Parameter and State Estimation Using Extended Kalman Filter and Current Derivative Measurement. *IEEE Transactions on Industrial Electronics*, 2021, vol. 68, no. 3, pp. 1972-1981. doi: <https://doi.org/10.1109/TIE.2020.2973897>.
17. Kuznetsov B.I., Nikitina T.B., Bovdii I.V., Chunikhin K.V., Kolomiets V.V., Kobylanskyi B.B. Method for reduction of

magnetic field of uncertain extended technical objects based on their multyspheroidal model and compensating magnetic dipoles. *Electrical Engineering & Electromechanics*, 2025, no. 2, pp. 48-58. doi: <https://doi.org/10.20998/2074-272X.2025.2.07>.

18. Kuznetsov B.I., Kutsenko A.S., Nikitina T.B., Bovdii I.V., Chunikhin K.V., Kolomiets V.V. Method for prediction magnetic silencing of uncertain energy-saturated extended technical objects in prolate spheroidal coordinate system. *Electrical Engineering & Electromechanics*, 2024, no. 6, pp. 57-66. doi: <https://doi.org/10.20998/2074-272X.2024.6.08>.
19. Milykh V.I. Numerical-field analysis of differential leakage reactance of stator winding in three-phase induction motors. *Electrical Engineering & Electromechanics*, 2025, no. 2, pp. 7-18. doi: <https://doi.org/10.20998/2074-272X.2025.2.02>.

Received 23.02.2025

Accepted 29.04.2025

Published 02.09.2025

O.B. Iegorov¹, PhD, Associate Professor,
M.P. Kundenko², Doctor of Technical Science, Professor,
O.Yu. Iegorova³, PhD, Associate Professor,
V.A. Mardziavko³, Assistant Lecturer,
A.Yu. Rudenko³, Assistant Lecturer,
¹ O.M. Beketov National University of Urban Economy in Kharkiv,
17, Chornoglazivska Str., Kharkiv, 61002, Ukraine.
² National Technical University «Kharkiv Polytechnic Institute»,
2, Kyrpychova Str., Kharkiv, 61002, Ukraine.
³ Mykolaiv National Agrarian University,
9, Georgy Gongadze Str., Mykolaiv, 54000, Ukraine,
e-mail: vitalijmardzavko@gmail.com (Corresponding Author)

How to cite this article:

Iegorov O.B., Kundenko M.P., Iegorova O.Yu., Mardziavko V.A., Rudenko A.Yu. The influence of the design of the stator winding of a synchronous-reactive generator on increasing its energy efficiency. *Electrical Engineering & Electromechanics*, 2025, no. 5, pp. 3-9. doi: <https://doi.org/10.20998/2074-272X.2025.5.01>

H. Hafaiedh, Y. Saoudi, A. Benamor, L. Chrifi-Alaoui

Wind farms integration into power system with improved location and stability problem solving

Problem. This article investigates as a consistent supply to satisfy rising world energy consumption, wind energy is becoming more and more important. Correct evaluation of the stability and performance of wind induction generators inside power systems remains difficult, particularly in regard to ensuring compliance with grid rules and best location. **Goal.** To evaluate and compare the dynamic behavior and grid compatibility of the squirrel cage induction generator (SCIG) and the doubly fed induction generator (DFIG) wind generators in various locations within the IEEE 14 bus network, and to determine the improved generator type and location. **Methodology.** The investigation adopts the small signal stability analysis for modeling the wind induction turbines due to its capability to assess system stability, controllability and observability. The IEEE 14 bus distribution network is modeled with wind generators interconnected at buses 10 through 14. Several parameters are analyzed under different operating conditions, including voltage, rotor angle, active power, reactive power and frequency. **Results.** DFIG exhibits superior performance across all analyzed parameters, particularly in maintaining grid stability and meeting grid code requirements. Bus 13 was identified as the improved integration point for wind farms using DFIG technology. **Scientific novelty.** The study offers a structured comparison of SCIG and DFIG using state space modeling rarely applied in a direct bus by bus comparative study within a standard distribution network. **Practical value.** The results help system planners choose the right wind turbine type and location, which promotes a more reliable and effective integration of renewable energy sources into power networks. References 51, tables 5, figures 7.

Key words: squirrel cage induction generator, doubly fed induction generator, best location of wind farms, IEEE 14 bus network.

Проблема. У статті розглядається вітряна енергія як джерело безперебійного живлення для задоволення світового споживання енергії, що зростає, і її роль у цьому процесі. Коректна оцінка стабільності та продуктивності вітрогенераторів в енергосистемах залишається складним завданням, особливо з точки зору забезпечення відповідності вимогам електромережі та вибору оптимального розташування. **Мета.** Оцінка та порівняння динамічної поведінки і мережевої сумісності вітрогенераторів з короткозамкненим ротором (SCIG) та асинхронним генератором з подвійним живленням (DFIG) у різних місцях мережі IEEE 14, а також визначення покращеного типу та міста розташування генератора. **Методологія.** У дослідженні для моделювання вітрогенераторів використовується аналіз стійкості при малих сигналах завдяки його здатності оцінювати стійкість, керованість та спостережливість системи. Розподільна мережа IEEE 14 моделюється з вітрогенераторами, з'єднаними між собою на шинах 10-14. Аналізуються різні параметри за різних робочих умов, включаючи напругу, кут ротора, активну потужність, реактивну потужність та частоту. **Результати.** DFIG демонструє кращі характеристики за всіма проаналізованими параметрами, особливо щодо підтримки стабільності мережі та відповідності вимогам мережевого кодексу. Шина 13 була визначена як покращена точка інтеграції для вітропарків, які використовують DFIG. **Наукова новизна.** Дослідження пропонує структуроване порівняння SCIG та DFIG з використанням моделювання простору станів, що рідко застосовується при прямому порівняльному дослідженні шин у стандартній розподільній мережі. **Практична значимість.** Результати допомагають системним планувальникам вибрати правильний тип та місцезнаходження вітрогенератора, що сприяє більш надійній та ефективній інтеграції відновлюваних джерел енергії в енергомережі. Бібл. 51, табл. 5, рис. 7.

Ключові слова: асинхронний генератор з короткозамкненим ротором, асинхронний генератор з подвійним живленням, найкраще розташування вітряних станцій, шина живлення IEEE 14.

Introduction. Wind energy is seen as an endless supply of clean energy as compared to other energy sources like nuclear, coal, gas and oil. When it was adopted, the use of fossil fuels greatly decreased. Globally, wind power plant construction has increased dramatically during the last twenty years [1–4].

Globally, installed wind energy capacity exceeded 100 GW by the end of 2023, as stated by the Global Wind Energy Council [5]. This is a 15 % increase globally over 2022 in installed capacity [6]. It's also the year with the most wind energy of all time. As of 2022, there were 906 GW of installed capacity for wind energy globally, a 9 % growth. One major problem for wind energy is the constant variations in temperature, density, and wind speed. To prevent unfavorable effects on grid electricity, the integration of wind turbines into the grid must be supervised by specific laws or grid codes [1, 7–9]. The operational restrictions and environmental variables of different countries influence the grid codes produced [10, 11]. Like a traditional power plant, wind farms need a connection to the grid that minimizes interruptions.

In wind turbines, 3 different kinds of power generation devices are typically utilized to transform electrical energy from wind: doubly fed induction generator (DFIG), permanent magnet synchronous generator (PMSG), squirrel cage induction generator (SCIG). Among these generators, DFIG has stayed connected to the power system and has demonstrated good performance in low

voltage ride through incidents [12]. Because of their significant advantages, such as increased energy efficiency, improved power quality, ease of control and variable speed handling, DFIGs are frequently utilized in systems that convert wind energy [13]. However, due to their robustness, affordability and ease of use [14], wind power conversion systems equipped with SCIGs also use reactive power compensators.

Consequently, precise modeling of induction generator is needed for research utilizing computer simulations, investigations, and research in order to effectively handle their major issues, especially with relation to the grid installation of wind energy conversion technologies. Understanding the utilization of wind power and how it integrates with the grid has thus become crucial research [15].

It is vital to do in depth research to comprehend how wind farms and the power grid interact. A wind farm in the design phase involves a number of research projects, which are carried out in a manner akin to that of other new technological facilities [13, 15]. Model planning, which takes into account variables like voltage, electricity flow, reactive power capability, short-circuit currents and the transient stability, is typically used to assess the effects of wind technology [16–19]. It is common practice to take into account a thorough depiction of every single unit as well as the relationships between units and the system.

© H. Hafaiedh, Y. Saoudi, A. Benamor, L. Chrifi-Alaoui

As an alternative, when considering the wind farm from the standpoint of the system, it can be treated as a lumped equivalent model [17]. Additional related research focuses on improving transient stability and dispatching spinning reserves in wind-thermal power systems [20, 21].

The authors of [22] examined the differences in performance between wind turbines connected to the power system that were induction generators, DFIG and PMSG. By taking into account a 3-phase defect at the end of a transmission line, the machines efficiency are assessed. Using MATLAB software, the performance of grid connected 5-phase modular PMSG with various slot and pole number combinations is assessed in [23].

Additionally, the technological difficulties of integrating wind were covered in earlier studies [24] energy into the grid. The primary obstacles to wind energy grid integration are discussed in [4], including the consequences of power quality, power imbalances, wind power on the power system and operating costs. The comparison of the grid integration impact of DFIG and SCIG is examined in [25]. This research [26] compares the performance of SCIG and DFIG wind turbines under various conditions through MATLAB/Simulink. The results indicate that DFIG is more efficient, especially in variable speed generation and power regulation, making it more compatible with large wind farms connected to weak grids.

The **goal** of this work is to evaluate and compare the dynamic behavior and grid compatibility of SCIG and DFIG wind generators in various locations within the IEEE 14 bus network, and to determine the improved generator type and location. The working conditions for producing reactive and active power, as well as voltage, angle theta, industrial frequency, and stability, were the primary subjects of the analysis. Numerous simulation programs have been examined for the analysis and modeling of wind farms, as well as for improved location and stability problem solving. The Power System Analysis Toolbox (PSAT) was selected because it offered sophisticated simulation tools and could be used for the necessary analysis.

1. Modeling of wind energy. The wind turbines capture wind energy through their blades and convert it into mechanical power. This process is influenced by various factors such as wind speed, blade design, and the area swept by the blades. To assess the efficiency of energy conversion, specific mathematical models that incorporate these elements can be applied. By optimizing turbine performance, wind energy can be effectively harnessed and used for power generation. Through the turbine blades, wind energy is converted to power, which is given as follows:

$$P_{wi} = T_{me} \cdot \omega_m; \quad (1)$$

$$T_{me} = P_{wi} / \omega_m, \quad (2)$$

where P_{wi} , T_{me} are the generated power and mechanical torque respectively; ω_m is the rotor angular speed.

The power generated by the wind is expressed as follows [27–30]:

$$P_{wi} = 0.5 \zeta_p(\lambda, \beta) \rho \pi R^2 V^3, \quad (3)$$

where ζ_p is the power coefficient; λ , β are the blade pitch angle and the tip speed ratio respectively; ρ is the air density; R is the radius of the turbine blades; V is the wind speed.

The tip speed ratio λ is determined as:

$$\lambda = \omega_m R / V. \quad (4)$$

The rotor angular speed ω_m is:

$$\omega_m = 2\pi n / 60, \quad (5)$$

where n is the rotational speed.

The power coefficient ζ_p is [5]:

$$\zeta_p = 0.44 \left(\frac{125}{\lambda_j} - 6.94 \right) e^{16.5/\lambda_j}, \quad (6)$$

where λ_j is the tip speed ratio coefficient at the j^{th} element of the turbine blade:

$$\lambda_j = \frac{1}{1/\lambda + 0.002}. \quad (7)$$

2. Configuration induction generator. Wind turbines can be classified into different types, with 2 common ones using induction generators. These turbines use induction generators to convert wind energy into electrical power. In an induction generator, the rotor is driven by the wind, creating a rotating magnetic field that induces electrical current in the stator. The key advantage of these turbines is their simplicity and cost effectiveness, as they can operate asynchronously with the grid. They are reliable and require minimal maintenance, making them suitable for various wind conditions and widely used in both small and large scale energy projects. In this section, the configurations of these turbines will be explored, detailing their design and operation. Additionally, the mathematical models associated with each type will be presented. A comparison will then be made, evaluating their performance, power quality, and reliability.

2.1. Modeling of induction generator. Induction generators are commonly used in wind energy systems due to their simplicity and reliability. These generators convert mechanical energy from the turbine into electrical power through electromagnetic induction. Modeling an induction generator involves understanding key parameters like rotor and stator voltages, which directly impact performance and efficiency. The mathematical formulas for modeling an induction generator by the rotor and stator voltage in d - q (direct and quadrature) axis [17–19] are:

$$\begin{cases} v_{dr} = R_r i_{dr} + \frac{d\phi_{dr}}{dt} + \omega_s \phi_{qr}; \\ v_{qr} = R_r i_{qr} + \frac{d\phi_{qr}}{dt} - \omega_s \phi_{dr}; \\ v_{ds} = R_s i_{ds} + \frac{d\phi_{ds}}{dt} + \omega_s \phi_{qs}; \\ v_{qs} = R_s i_{qs} + \frac{d\phi_{qs}}{dt} - \omega_s \phi_{ds}, \end{cases} \quad (8)$$

where v_{dr} , v_{ds} , v_{qr} , v_{qs} are the rotor and stator voltages respectively; i_{dr} , i_{qr} are the current of the rotor; i_{ds} , i_{qs} are the current of the stator; ϕ_{dr} , ϕ_{qr} are the flux of the rotor; ϕ_{ds} , ϕ_{qs} are the flux of the stator; v_s , v_r are the voltage of stator and rotor respectively.

The equations below present the flux linkage and electromagnetic torque:

$$\begin{cases} \phi_{dr} = L_m i_{ds} + L_{ro} i_{dr}; \\ \phi_{qr} = L_m i_{qs} + L_{ro} i_{qr}; \\ \phi_{ds} = L_m i_{dr} + L_{so} i_{ds}; \\ \phi_{qs} = L_m i_{qr} + L_{so} i_{qs}, \end{cases} \quad (9)$$

$$T_{el} = \phi_{qr} i_{dr} - \phi_{dr} i_{qr}, \quad (10)$$

where L_m is the mutual inductance; L_{so} , L_{ro} are the stator and rotor leakage inductance respectively; T_{el} is the electrical torque.

The mechanical equations are as follows:

$$\begin{cases} T_{el} = -\frac{3}{2} P_{wi} \frac{L_m}{L_{so}} (\phi_{ds} i_{qr} - \phi_{qs} i_{ds}) \\ \frac{d\Omega_{me}}{dt} = \frac{1}{J} (T_{me} - T_{el} - f \cdot \Omega_{me}) \end{cases} \quad (11)$$

where Ω_{me} is the angular acceleration; $d\Omega_{me}$ is the angular velocity; f is the setting in the system; J is the inertia moment of the rotor.

These equations are used to limit how powers variation affects voltage amplitude and frequency [31–33]:

$$P = P_0 \left(1 + D_p \frac{f - f_n}{f_n} \right) \cdot \left(\frac{V}{V_0} \right)^\alpha \quad (12)$$

where P is the active power; P_0 is the reference active power; D_p is the active power sensitivity factor; V_0 is the voltage amplitude; α may indicate a load model parameter, potentially connected to the active power and another parameter, possibly related to the load dependency on voltage or frequency respectively.

Table 1 shows the different values of the constants for each load category. These load category parameters vary depending on the network. The coefficient D_p is used to illustrate the frequency bearing evolution of each electrical bus. Therefore, it is essential to introduce (12) to show the development of a significant dynamic grid element. In reality, there is a close connection between these variables and the installed loads.

Table 1
Parameters of the different load category

Load category	α	D_p
Winter	1.02	1.000
Summer	1.20	0.999
Industrial	0.80	1.000

2.2. The squirrel cage induction generator. The SCIG running at a steady pace is used in wind energy turbines that are directly linked to the grid [34, 35]. The generator is connected directly to the grid, much like in other wind energy conversion systems, while the turbine is associated with the SCIG through a gearbox to reach the necessary speed for power generation (Fig. 1). Since rotor slip is the primary cause of speed variations, variations in rotor speed are minimal, wind turbines usually run at a set speed. The SCIG absorbs reactive power by acting as an induction motor during changes in grid voltage. Pitch angle control is used to adjust generator rotor speed instabilities when wind speeds change, maximizing wind power output. Wind energy systems with varying speeds also use squirrel cage technology [36–42]. The SCIG data are presented in Table 2.

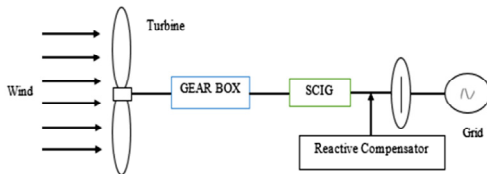


Fig. 1. The classic method of integrating SCIGs with the grid

Table 2
Wind turbine data for SCIG

Parameters	Value	Parameters	Value
Rated power, MVA	10	Stator reactance, p.u.	0.01
Rated voltage, kV	13.8	Rotor reactance, p.u.	0.08
Rated frequency, Hz	50	Mutual reactance, p.u.	3
Stator resistance, p.u.	0.01	Inertia constants [kW/kVA, kW/kVA, p.u.]	2.5, 0.5, 0.3
Rotor resistance, p.u.	0.1	Number of poles pairs	4

2.3. The double fed induction generator. Figure 2 shows the integrating DFIGs into the grid.

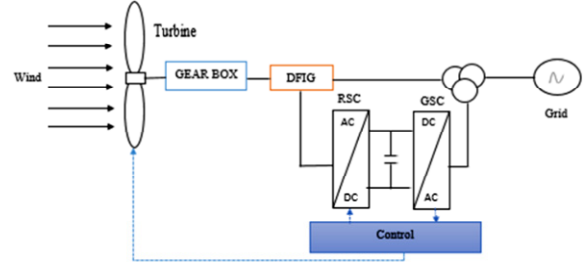


Fig. 2. Traditional integration of a DFIG with the grid

The rotor of the DFIG is associated with the wind turbines low speed shaft by a gearbox, which increases the speed to the necessary level so that the generator can generate electricity [34]. With 2 voltages source converters placed back-to-back and using a wound type rotor, the DFIG configures a grid-connected AC-DC-AC [41–46]. Normally, each converter runs at 30 % of the specified rated power of the generator. The converter connected to the rotor is known as rotor side converter (RSC), while the converter connected to the grid is known as grid side converter (GSC). These converters handle varying wind speeds well, making sure that the output frequency remains constant and in line with grid needs. They are divided using a DC capacitor in the intermediate circuit that works as an energy stock management device [16]. The step up transformer is a device that connects the stator to the network [13]. An integrated control system at the wind turbine shaft manages precise power, reactive power and voltage across the network. Different voltage commands are generated by this system for the RSC and GSC. The RSC ensures control of active and reactive powers, and the GSC ensures their operation at a unity power factor. The GSC also controls the voltage at the DC link capacitor between the RSC and the GSC. Table 3 shows the wind turbine data for DFIG used in the model.

Table 3

Wind turbine data for DFIG

Parameters	Value	Parameters	Value
Rated power, MVA	10	Mutual reactance, p.u.	3
Rated voltage, kV	13.8	Inertia constants, kW/kVA	3
Rated frequency, Hz	50	Pitch control gain, p.u.	10
Stator resistance, p.u.	0.01	Time constant, s	3
Rotor resistance, p.u.	0.1	Voltage control gain, p.u.	10
Stator reactance, p.u.	0.01	Power control gain, s	0.01
Rotor reactance, p.u.	0.08	Number of poles pairs	4

3. Small signal stability analysis is a crucial aspect of power system dynamics, used to assess the stability of the system when subjected to small disturbances. It helps to understand how the system responds to minor fluctuations and ensures that the system remains stable under normal operating conditions. The eigenvalue method can be used to analyze the small signal stability. This method is essential for identifying potential instabilities and improving system performance.

This approach works with linear models via examining where the poles are located inside the complex plane. The characteristic polynomial described by the following equation has poles as its solutions [47]:

$$\det(A - \lambda I) = 0, \quad (13)$$

where \det is the determinant of the matrix $(A - \lambda I)$; A is the state matrix; I is the identity matrix of the same size as A ; λ is the eigenvalue.

In the latter, there is an imaginary portion and a real part. The real portion determines the analyzed system's convergence, whereas the oscillating behavior is correlated with the imaginary part. If every pole is in the complex plane's negative real portion, the system is considered stable.

The system model or its parameters determine the values of the poles. One may verify the model's stability domain by examining how the positions of the poles change with respect to the parameter values.

4. Results and discussion. In this section devoted to the results of the experiment and its analysis, one examines 3 key elements. First, one examines the performance of 2 types of generators employed in wind power systems: the SCIG and the DFIG. The disparities in stability, efficiency, and resistance to disruption between these 2 technologies are highlighted by this comparison. Subsequently, one examines the stability of the electricity network when integrating these generators. The basis of this analysis is the eigenvalue analysis of the system, which allows determining the conditions under which the network remains stable or can become unstable. Finally, one compares the results with those of other studies in order to evaluate the relevance of the findings and to place the study within the broader framework of existing research. The analysis highlights the methodological disparities and the obtained results, which allows having a more exhaustive vision of the consequences of integrating these generators into the electricity network.

4.1. Evaluation of 2 different types of generators.

This section compares 2 types of wind power systems, including their performance and the market share each type currently enjoys. The influence of wind generation on the transient stability of the system is examined for wind farms using an aggregated model [48]. PSAT is utilized in this work to perform the transient stability analysis [49, 50]. There are 16 lines, 14 buses, 5 generators, 4 transformers and 11 loads in this system. The standard IEEE 14 bus data format has been used to load the buses and lines [48].

The following figures show several graphs comparing the performance of 2 types of wind turbine generators: the SCIG and the DFIG. Each graph shows different electrical parameters as a function of time for buses 10–14 of the network. Figure 3 presents the variation of the voltage profile for 2 types of wind turbines. It shows that the rotor inductance of DFIG is higher, which results in less variation in the magnetic field. Therefore, the voltage fluctuations are reduced, which decreases the voltage ripple compared to the other case and makes the voltage smoother.

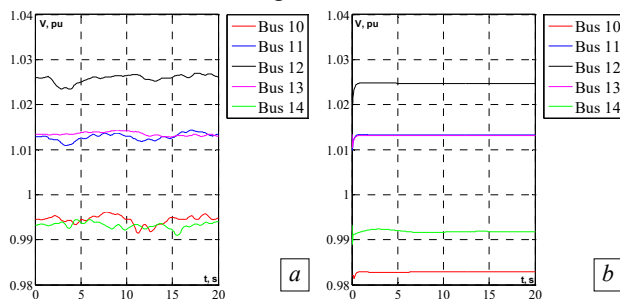


Fig. 3. The voltage for 2 different type of wind turbine: a – for SCIG; b – for DFIG

The following figure shows the variation of angle θ for the 2 types of wind turbines. The phase angle curves in Fig. 4 show that the phase angle ripples in DFIG are more stable and converge to a constant value. This is explained by the higher inertia compared to SCIG, which favors a better network synchronization with this type of generators.

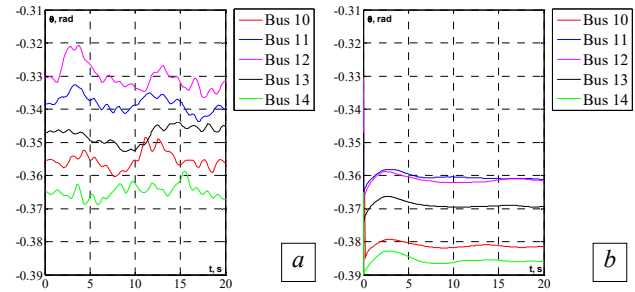


Fig. 4. The angle for 2 different type of wind turbine: a – for SCIG; b – for DFIG

Figures 5, 6 depict the variation of active and reactive power respectively over time for the 2 types of wind turbines. From the presented Fig. 5, the active power of the DFIG is more stable, with only slight fluctuations, indicating its better ability to provide constant active power. On the other hand, for the SCIG, oscillations are recorded on all critical buses, with less significant variations at bus 14.

For both types of wind turbines, Fig. 6 shows that the same reactive power is consumed to create the internal magnetic field. This reactive power is essential for the proper functioning of the generators, allowing them to produce the active power.

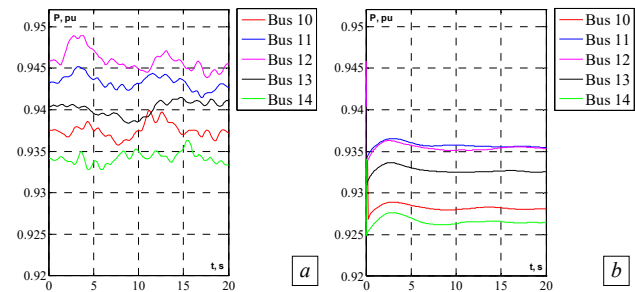


Fig. 5. The active power for 2 different type of wind turbine: a – for SCIG; b – for DFIG

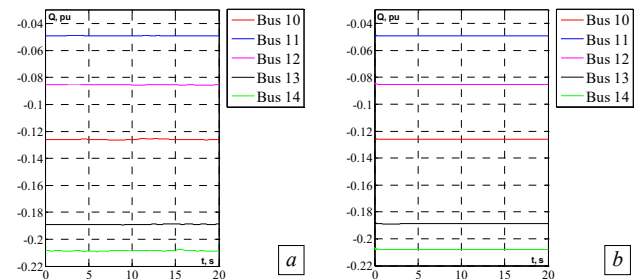


Fig. 6. The reactive power for 2 different type of wind turbine: a – for SCIG; b – for DFIG

Figure 7 shows the variation of frequency versus time for both types of SCIG and DFIG wind turbines under 3 conditions, represented by (12). This study examines the effect of wind turbine integration on frequency stability.

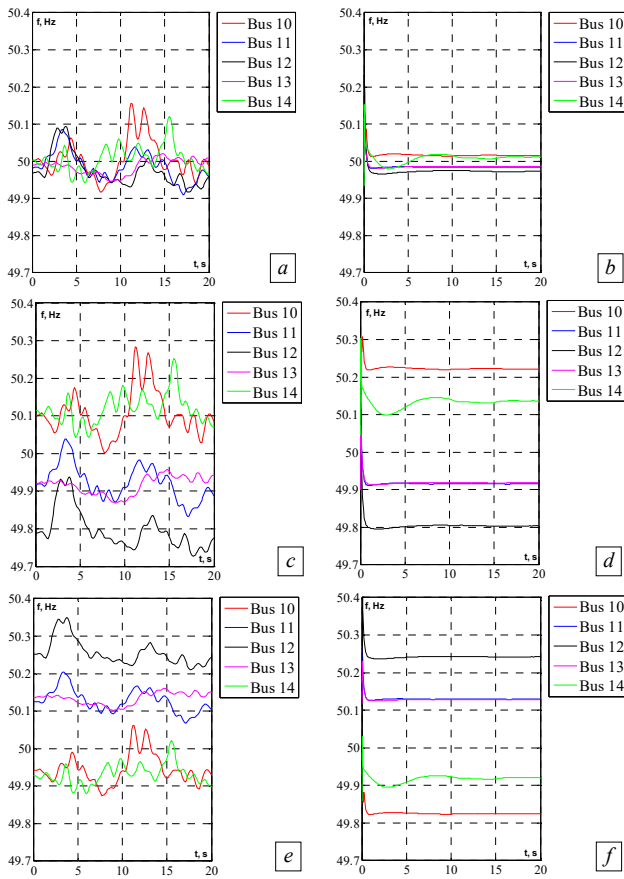


Fig. 7. Frequency performance analysis graphs of 2 types of wind turbines under different grid conditions: *a* – SCIG under winter conditions; *b* – DFIG under winter conditions; *c* – SCIG under summer conditions; *d* – DFIG under summer conditions; *e* – SCIG under industrial conditions; *f* – DFIG under industrial condition

According to Fig. 7, the system is strongly influenced by both grid and climatic conditions. It is affected by climatic variations, particularly in winter and summer, as well as by industrial factors and the type of equipment installed on the grid.

The grid integrated wind turbine is a DFIG type, which contributes to greater grid stability. Indeed, this figure generally illustrates frequency variation, which is influenced by the inertia of the DFIG. Since the inertia of the DFIG is higher than that of the SCIG, disturbances are more difficult to induce. Consequently, the DFIG provides greater grid stability. Furthermore, it is possible to produce approximately 2/3 of the power via the stator, while approximately 1/3 of the power can be recovered by the rotor thanks to the addition of a power electronics stage. This configuration allows power to be distributed between the rotor and stator, while minimizing overload on the stator windings.

4.2. Examination of the stability of the electrical network. Tables 4, 5 show the eigenvalue evaluation curves for 2 types of generators: the SCIG and the DFIG, in an electrical network, for buses 10–14. Table 4 shows that our network is more stable when DFIG is installed, because in case of SCIG, the minimum value of the eigenvalues is -0.25 p.u., while for DFIG it is -1 p.u. Thus, SCIG is very sensitive to instability, which can cause disturbances in the system and it causes a blackout phenomenon. In conclusion, bus 13 appears to be the

most suitable location for wind turbine integration particularly with DFIG and SCIG technologies due to its ability to maintain voltage levels, phase angle, power flow, and frequency stability, thereby enhancing the overall stability of the network.

Table 4
Network eigenvalues with integration of a wind turbine to the buses

Bus	Eigenvalues of network with SCIG	Eigenvalues of network with DFIG
10	$-7.5427+35.4824j$ $-7.5427-35.4824j$ $-10.1091+0j$ $-0.89032+4.1965j$ $-0.89032-4.1965j$ $-0.25+0j$	$-100.9781+0j$ $-0.6524+0j$ $-0.25+0j$ $-0.33333+0j$ $-1+0j$
11	$-7.5704+35.2617j$ $-7.5704-35.2617j$ $-9.8834+0j$ $-0.91571+4.2364j$ $-0.91571-4.2364j$ $-0.25+0j$	$-100.9315+0j$ $-6.2085+0j$ $-0.64742+0j$ $-0.33333+0j$ $-1+0j$
12	$-7.5704+35.2617j$ $-7.5704-35.2617j$ $-9.8834+0j$ $-0.91571+4.2364j$ $-0.91571-4.2364j$ $-0.25+0j$	$-100.9315+0j$ $-6.2085+0j$ $-0.64742+0j$ $-0.33333+0j$ $-1+0j$
13	$-7.5178+35.3704j$ $-7.5178-35.3704j$ $-10.3942+0j$ $-0.89366+4.2294j$ $-0.89366-4.2294j$ $-0.25+0j$	$-100.8581+0j$ $-5.7772+0j$ $-0.64476+0j$ $-0.33333+0j$ $-1+0j$
14	$-7.4181+34.68222j$ $-7.4181-34.68222j$ $-9.3169+0j$ $-0.92836+4.2348j$ $-0.92836-4.2348j$ $-0.25+0j$	$-101.282+0j$ $-0.64034+0j$ $-0.25+0j$ $-0.33333+0j$ $-1+0j$

4.3. Comparative study. Table 5 contrasts the advised approaches with the current state of the art approaches. One has extended the approach from [51], which just uses an IEEE 14 bus network for voltage analysis. However, this approach is flawed since it fails to account for network frequency. One tested both voltage and frequency during the investigation because they are complementary.

Table 5
Comparison with the existing state of art methods

Bus number	Work [51]		Proposed work	
	V , p.u.	θ , rad	V , p.u.	θ , rad
1	1.06200	0.00000	1.06000	0.00000
2	1.04500	-0.13560	1.04500	-0.13451
3	1.01300	-0.33210	1.01000	-0.32979
4	0.99700	-0.26440	0.99800	-0.26152
5	1.00200	-0.22690	1.00300	-0.22553
6	1.07400	-0.36950	1.07000	-0.37431
7	1.03600	-0.33930	1.03700	-0.35054
8	1.09300	-0.33930	1.09000	-0.35054
9	1.01200	-0.37900	1.01600	-0.39755
10	1.01200	-0.38440	1.01500	-0.40046
11	1.03500	-0.37980	1.03600	-0.39025
12	1.04600	-0.90590	1.04800	-0.39615
13	1.03600	-0.39140	1.04000	-0.39863
14	0.99600	-0.41050	1.01300	-0.42544

In contrast to work [51], in which were used automatic voltage regulators (AVRs) and turbine

governors (TGs) in the network IEEE 14 bus, only TGs are used, which enables one to drastically cut costs. In contrast to [51], which compares the power factor (PF) on a single bus 14 when a wind turbine is integrated into the IEEE 14 network versus not, this work first compares the integration of 2 different kinds of wind turbines before calculating the PF on multiple buses (10–14) to identify the best wind turbine and where to put it.

Conclusions. Concretely, the integration of renewable energies is essential today in the face of the continuous increase in electricity consumption. Renewable energies, such as wind power, are inexhaustible, sustainable, and profitable. However, their production is highly dependent on natural conditions, making grid stability more difficult to ensure without appropriate monitoring mechanisms.

In this study, we modeled the integration of SCIG and DFIG generators into the IEEE 14 standard bus network using the small signal stability analysis approach to analyze their dynamic behavior and grid compatibility. The results show that DFIG offers better performance in terms of stability, voltage, frequency, and compliance with grid requirements. Bus 13 was identified as the optimal location for connecting a DFIG based wind farm.

Thus, the objective of this research, which was to evaluate and compare the dynamic performance of SCIG and DFIG generators and to determine their improved placement within the IEEE 14 bus network, was fully achieved.

Future research will focus on improving existing wind turbine technologies and jointly optimizing the placement of wind turbines and FACTS devices to improve the overall performance of the power grid.

Conflict of interest. The authors declare that they have no conflicts of interest.

REFERENCES

- Giefer L.A., Staar B., Freitag M. FPGA-Based Optical Surface Inspection of Wind Turbine Rotor Blades Using Quantized Neural Networks. *Electronics*, 2020, vol. 9, no. 11, art. no. 1824. doi: <https://doi.org/10.3390/electronics9111824>.
- Villena-Ruiz R., Honrubia-Escribano A., Jiménez-Buendía F., Molina-García A., Gómez-Lázaro E. Requirements for Validation of Dynamic Wind Turbine Models: An International Grid Code Review. *Electronics*, 2020, vol. 9, no. 10, art. no. 1707. doi: <https://doi.org/10.3390/electronics9101707>.
- Sahragard A., Falaghi H., Farhadi M., Mosavi A., Estebsari A. Generation Expansion Planning in the Presence of Wind Power Plants Using a Genetic Algorithm Model. *Electronics*, 2020, vol. 9, no. 7, art. no. 1143. doi: <https://doi.org/10.3390/electronics9071143>.
- Abdollahi A., Ghadimi A., Miveh M., Mohammadi F., Jurado F. Optimal Power Flow Incorporating FACTS Devices and Stochastic Wind Power Generation Using Krill Herd Algorithm. *Electronics*, 2020, vol. 9, no. 6, art. no. 1043. doi: <https://doi.org/10.3390/electronics9061043>.
- Global Wind Energy Council. *Global Wind Report 2023*. 120 p. Available at: <https://www.gwec.net/reports/globalwindreport2023> (accessed on 27 March 2023).
- Global Wind Energy Council. *Global Wind Report 2022*. 158 p. Available at: <https://www.gwec.net/reports/globalwindreport2022> (accessed on 27 March 2022).
- Mlecnik E., Parker J., Ma Z., Corchero C., Knotzer A., Perneti R. Policy challenges for the development of energy flexibility services. *Energy Policy*, 2020, vol. 137, art. no. 111147. doi: <https://doi.org/10.1016/j.enpol.2019.111147>.
- Lu Y., Khan Z.A., Alvarez-Alvarado M.S., Zhang Y., Huang Z., Imran M. A Critical Review of Sustainable Energy Policies for the Promotion of Renewable Energy Sources. *Sustainability*, 2020, vol. 12, no. 12, art. no. 5078. doi: <https://doi.org/10.3390/su12125078>.
- Schwarz M., Nakhle C., Knoeri C. Innovative designs of building energy codes for building decarbonization and their implementation challenges. *Journal of Cleaner Production*, 2020, vol. 248, art. no. 119260. doi: <https://doi.org/10.1016/j.jclepro.2019.119260>.
- Nazir M.S., Mahdi A.J., Bilal M., Sohail H.M., Ali N., Iqbal H.M.N. Environmental impact and pollution-related challenges of renewable wind energy paradigm – A review. *Science of The Total Environment*, 2019, vol. 683, pp. 436–444. doi: <https://doi.org/10.1016/j.scitotenv.2019.05.274>.
- Andrić I., Koc M., Al-Ghamdi S.G. A review of climate change implications for built environment: Impacts, mitigation measures and associated challenges in developed and developing countries. *Journal of Cleaner Production*, 2019, vol. 211, pp. 83–102. doi: <https://doi.org/10.1016/j.jclepro.2018.11.128>.
- Bourouina A., Taleb R., Bachir G., Boudjema Z., Bessaad T., Saidi H. Comparative analysis between classical and third-order sliding mode controllers for maximum power extraction in wind turbine system. *Electrical Engineering & Electromechanics*, 2025, no. 3, pp. 18–22. doi: <https://doi.org/10.20998/2074-272X.2025.3.03>.
- Belayneh B.A., Tuka M.B. Performance analysis of doubly fed induction generator in wind energy conversion system by controlling active and reactive power. *Research Square*, 2022. pp. 1–14. doi: <https://doi.org/10.21203/rs.3.rs-2152568/v1>.
- Son J.-Y., Ma K. Wind Energy Systems. *Proceedings of the IEEE*, 2017, vol. 105, no. 11, pp. 2116–2131. doi: <https://doi.org/10.1109/JPROC.2017.2695485>.
- Yang B., Jiang L., Wang L., Yao W., Wu Q.H. Nonlinear maximum power point tracking control and modal analysis of DFIG based wind turbine. *International Journal of Electrical Power & Energy Systems*, 2016, vol. 74, pp. 429–436. doi: <https://doi.org/10.1016/j.ijepes.2015.07.036>.
- Holtinen H., Hirvonen R. Power System Requirements for Wind Power. *Wind Power in Power Systems*, 2005, pp. 143–167. doi: <https://doi.org/10.1002/0470012684.ch8>.
- Kazachkov Y.A., Feltes J.W., Zavdil R. Modeling wind farms for power system stability studies. *2003 IEEE Power Engineering Society General Meeting*, 2003, pp. 1526–1533. doi: <https://doi.org/10.1109/PES.2003.1267382>.
- Rodríguez J.M., Fernández J.L., Beato D., Iturbe R., Usaola J., Ledesma P., Wilhelmi J.R. Incidence on power system dynamics of high penetration of fixed speed and doubly fed wind energy systems: study of the Spanish case. *IEEE Transactions on Power Systems*, 2002, vol. 17, no. 4, pp. 1089–1095. doi: <https://doi.org/10.1109/TPWRS.2002.804971>.
- Beainy A., Maatouk C., Moubayed N., Kaddah F. Comparison of different types of generator for wind energy conversion system topologies. *2016 3rd International Conference on Renewable Energies for Developing Countries (REDEC)*, 2016, pp. 1–6. doi: <https://doi.org/10.1109/REDEC.2016.7577535>.
- Reddy S.S., Prathipati K., Lho Y.H. Transient Stability Improvement of a System Connected with Wind Energy Generators. *International Journal of Emerging Electric Power Systems*, 2017, vol. 18, no. 5, pp. 20170063. doi: <https://doi.org/10.1515/ijeeps-2017-0063>.
- Maity D., Chowdhury A., Reddy S.S., Panigrahi B.K., Abhyankar A.R., Mallick M.K. Joint energy and spinning reserve dispatch in wind-thermal power system using IDE-SAR technique. *2013 IEEE Symposium on Swarm Intelligence (SIS)*, 2013, pp. 284–290. doi: <https://doi.org/10.1109/SIS.2013.6615191>.
- Yi Zhang, Ula S. Comparison and evaluation of three main types of wind turbines. *2008 IEEE/PES Transmission and Distribution Conference and Exposition*, 2008, pp. 1–6. doi: <https://doi.org/10.1109/TDC.2008.4517282>.
- Abdel-Khalik A.S., Ahmed K.H. Performance evaluation of grid connected wind energy conversion systems with five-phase modular permanent magnet synchronous generators having different slot and pole number combinations. *2011 IEEE International Electric Machines & Drives Conference (IEMDC)*, 2011, pp. 1119–1124. doi: <https://doi.org/10.1109/IEMDC.2011.5994758>.
- Chowdhury M.M., Haque M.E., Aktarujjaman M., Negnevitsky M., Gargoom A. Grid integration impacts and energy storage systems for wind energy applications – A review. *2011 IEEE Power and Energy Society General Meeting*, 2011, pp. 1–8. doi: <https://doi.org/10.1109/PES.2011.6039798>.
- Duan J.D., Li R., An L. Study of Voltage Stability in Grid-Connected Large Wind Farms. *Advanced Materials Research*, 2012, vol. 433–440, pp. 1794–1801. doi: <https://doi.org/10.4028/www.scientific.net/AMR.433-440.1794>.
- Behabtu H.A., Coosemans T., Bercebar M., Fante K.A., Kebede A.A., Mierlo J.V., Messagie M. Performance Evaluation of Grid-

- Connected Wind Turbine Generators. *Energies*, 2021, vol. 14, no. 20, art. no. 6807. doi: <https://doi.org/10.3390/en14206807>.
27. Nid A., Sayah S., Zabar A. Power fluctuation suppression for grid connected permanent magnet synchronous generator type wind power generation system. *Electrical Engineering & Electromechanics*, 2024, no. 5, pp. 70–76. doi: <https://doi.org/10.20998/2074-272X.2024.5.10>.
28. Zine H.K.E., Abed K. Smart current control of the wind energy conversion system based permanent magnet synchronous generator using predictive and hysteresis model. *Electrical Engineering & Electromechanics*, 2024, no. 2, pp. 40–47. doi: <https://doi.org/10.20998/2074-272X.2024.2.06>.
29. Manikandan K., Sasikumar S., Arulraj R. A novelty approach to solve an economic dispatch problem for a renewable integrated micro-grid using optimization techniques. *Electrical Engineering & Electromechanics*, 2023, no. 4, pp. 83–89. doi: <https://doi.org/10.20998/2074-272X.2023.4.12>.
30. Oualah O., Kerdoun D., Boumassata A. Super-twisting sliding mode control for brushless doubly fed reluctance generator based on wind energy conversion system. *Electrical Engineering & Electromechanics*, 2023, no. 2, pp. 86–92. doi: <https://doi.org/10.20998/2074-272X.2023.2.13>.
31. Ekanayake J.B., Holdsworth L., XueGuang Wu, Jenkins N. Dynamic modeling of doubly fed induction generator wind turbines. *IEEE Transactions on Power Systems*, 2003, vol. 18, no. 2, pp. 803–809. doi: <https://doi.org/10.1109/TPWRS.2003.811178>.
32. Hannan M.A., Al-Shetwi A.Q., Mollik M.S., Ker P.J., Mannan M., Mansor M., Al-Masri H.M.K., Mahlia T.M.I. Wind Energy Conversions, Controls, and Applications: A Review for Sustainable Technologies and Directions. *Sustainability*, 2023, vol. 15, no. 5, art. no. 3986. doi: <https://doi.org/10.3390/su15053986>.
33. Saoudi Y., Abdallah H.H. Contribution of FACTS Device for Persisting Optimal Grid Performance Despite Wind Farm Integration. *International Review on Modelling and Simulations*, 2015, vol. 8, no. 2, pp. 147–153. doi: <https://doi.org/10.15866/iremos.v8i2.3033>.
34. Hajer H., Yahia S., Anouar B., Larbi C.-A., Taouali O. The Dynamic of the Grid with the Presence of WF and the AVR for Power Quality Enhancement. *2025 4th International Conference on Computing and Information Technology (ICCIT)*, 2025, pp. 629–632. doi: <https://doi.org/10.1109/ICCIT63348.2025.10989368>.
35. Milykh V.I. Numerical-field analysis of active and reactive winding parameters and mechanical characteristics of a squirrel-cage induction motor. *Electrical Engineering & Electromechanics*, 2023, no. 4, pp. 3–13. doi: <https://doi.org/10.20998/2074-272X.2023.4.01>.
36. Ramos T., Medeiros Júnior M.F., Pinheiro R., Medeiros A. Slip Control of a Squirrel Cage Induction Generator Driven by an Electromagnetic Frequency Regulator to Achieve the Maximum Power Point Tracking. *Energies*, 2019, vol. 12, no. 11, art. no. 2100. doi: <https://doi.org/10.3390/en12112100>.
37. García H., Segundo J., Rodríguez-Hernández O., Campos-Amezcuza R., Jaramillo O. Harmonic Modelling of the Wind Turbine Induction Generator for Dynamic Analysis of Power Quality. *Energies*, 2018, vol. 11, no. 1, art. no. 104. doi: <https://doi.org/10.3390/en11010104>.
38. Patil N.S., Bhosle Y.N. A review on wind turbine generator topologies. *2013 International Conference on Power, Energy and Control (ICPEC)*, 2013, pp. 625–629. doi: <https://doi.org/10.1109/ICPEC.2013.6527733>.
39. Osman S.H.E., Irungu G.K., Murage D.K. Impact of Different Locations of Integrating SCIG Wind Turbine into Distributed Network Using Continuation Power Flow Method. *2019 International Conference on Computer, Control, Electrical, and Electronics Engineering (ICCCEE)*, 2019, pp. 01–05. doi: <https://doi.org/10.1109/ICCCEE46830.2019.9071040>.
40. Anusri P., Sindhu K.C. Mathematical Modeling of the Squirrel Cage Induction Generator based Wind Farm for Sub-Synchronous Resonance Analysis. *Indian Journal of Science and Technology*, 2016, vol. 9, no. 38, pp. 1–7. doi: <https://doi.org/10.17485/ijst/2016/v9i38/101943>.
41. Hafaiedh H., Saoudi Y., Benamor A., Chrifi Alaoui L. Study of the impact of SCIG Wind farm integration and the effect of the location bus in dynamic grid enhancement. *2022 10th International Conference on Systems and Control (ICSC)*, 2022, pp. 114–118. doi: <https://doi.org/10.1109/ICSC57768.2022.9993873>.
42. Hannan M.A., Al-Shetwi A.Q., Mollik M.S., Ker P.J., Mannan M., Mansor M., Al-Masri H.M.K., Mahlia T.M.I. Wind Energy Conversions, Controls, and Applications: A Review for Sustainable Technologies and Directions. *Sustainability*, 2023, vol. 15, no. 5, art. no. 3986. doi: <https://doi.org/10.3390/su15053986>.
43. Yang W., Yang J. Advantage of variable-speed pumped storage plants for mitigating wind power variations: Integrated modelling and performance assessment. *Applied Energy*, 2019, vol. 237, pp. 720–732. doi: <https://doi.org/10.1016/j.apenergy.2018.12.090>.
44. El Amine B.B.M., Ahmed A., Houari M.B., Mouloud D. Modeling, simulation and control of a doubly-fed induction generator for wind energy conversion systems. *International Journal of Power Electronics and Drive Systems*, 2020, vol. 11, no. 3, pp. 1197–1210. doi: <https://doi.org/10.11591/ijpeds.v11.i3.pp1197-1210>.
45. Pandikumar M. A Control Methodology of Doubly Fed Induction Generator for Wind Energy Generation. *IOP Conference Series: Materials Science and Engineering*, 2020, vol. 937, no. 1, art. no. 012056. doi: <https://doi.org/10.1088/1757-899X/937/1/012056>.
46. Saoudi Y., Abdallah H.H. The effect of the injected active and reactive powers for the improvement of voltage amplitude and frequency qualities. *14th International Conference on Sciences and Techniques of Automatic Control & Computer Engineering – STA'2013*, 2013, pp. 47–51. doi: <https://doi.org/10.1109/STA.2013.6783104>.
47. Boukadoum A., Bouguerne A., Bahi T. Direct power control using space vector modulation strategy control for wind energy conversion system using three-phase matrix converter. *Electrical Engineering & Electromechanics*, 2023, no. 3, pp. 40–46. doi: <https://doi.org/10.20998/2074-272X.2023.3.06>.
48. Hatziaargyriou N., Milanovic J., Rahmann C., Ajarapu V., Canizares C., Erlich I., Hill D., Hiskens I., Kamwa I., Pal B., Pourbeik P., Sanchez-Gasca J., Stankovic A., Van Cutsem T., Vittal V., Vournas C. Definition and Classification of Power System Stability – Revisited & Extended. *IEEE Transactions on Power Systems*, 2021, vol. 36, no. 4, pp. 3271–3281. doi: <https://doi.org/10.1109/TPWRS.2020.3041774>.
49. Chi Y., Liu Y., Wang W., Dai H. Voltage Stability Analysis of Wind Farm Integration into Transmission Network. *2006 International Conference on Power System Technology*, 2006, pp. 1–7. doi: <https://doi.org/10.1109/ICPST.2006.321661>.
50. Sauer P.W., Pai M.A., Chow J.H. Power System Toolbox. *Power System Dynamics and Stability: With Synchrophasor Measurement and Power System Toolbox 2nd edition*, 2017, pp. 305–325. doi: <https://doi.org/10.1002/9781119355755.ch11>.
51. Kumar S., Kumar A., Sharma N.K. A novel method to investigate voltage stability of IEEE-14 bus wind integrated system using PSAT. *Frontiers in Energy*, 2020, vol. 14, no. 2, pp. 410–418. doi: <https://doi.org/10.1007/s11708-016-0440-8>.

Received 28.02.2025

Accepted 25.04.2025

Published 02.09.2025

H. Hafaiedh¹, PhD,

Y. Saoudi², Doctor of Electrical Engineering,

A. Benamor³, Associate Professor,

L. Chrifi-Alaoui⁴, Associate Professor,

¹ Higher National School of Engineering of Tunis,

University of Tunis, Tunisia,

e-mail: hajer.hafayedh@gmail.com (Corresponding Author)

² Laboratory of Control and Energy Management Laboratory,

National School of Engineering of Sfax, Tunisia.

³ National School of Engineers of Monastir,

Laboratory of Automatic Signal and Image Processing,

University of Monastir, Tunisia.

⁴ Laboratory of Innovative Technologies,

University of Picardy Jules Verne, France.

How to cite this article:

Hafaiedh H., Saoudi Y., Benamor A., Chrifi-Alaoui L. Wind farms integration into power system with improved location and stability problem solving. *Electrical Engineering & Electromechanics*, 2025, no. 5, pp. 10–16. doi: <https://doi.org/10.20998/2074-272X.2025.5.02>

Maximum power point tracking improving of photovoltaic systems based on hybrid triangulation topology aggregation optimizer and incremental conductance algorithm

Introduction. Maximum power point tracking (MPPT) in photovoltaic (PV) systems has been a key research focus in recent years. While numerous techniques have been proposed to optimize power extraction, each suffers from inherent limitations that hinder their effectiveness.

Problem. Environmental factors such as shading, partial shading, and low irradiance levels significantly impact PV system performance, with partial shading being the most critical and complex challenge due to its creation of multiple local power maxima. **Goal.** This study aims to improve MPPT in PV systems under partial shading conditions by developing a hybrid approach that integrates a Triangulation Topology Aggregation Optimizer (TTAO) with the Incremental Conductance (IC) algorithm. **Methodology.** Simulations were conducted in MATLAB/Simulink under four static partial shading scenarios, comparing the hybrid TTAO-IC algorithm against traditional methods like Perturb and Observe (P&O), IC and metaheuristic algorithms. **Scientific novelty** of this work lies in the hybrid TTAO-IC algorithm, which combines the global optimization strength of TTAO with the precision of IC, addressing the shortcomings of conventional methods. **Practical value.** The results show that the hybrid TTAO-IC algorithm achieves tracking efficiencies exceeding 99 %, outperforming existing methods and demonstrating robust adaptability to varying environmental conditions. References 31, tables 5, figures 15.

Key words: solar photovoltaic system, triangulation topology aggregation optimizer, maximum power point tracking, global maximum power point, partial shading conditions.

Вступ. Відстеження точки максимальної потужності (MPPT) у фотоелектричних (PV) системах є ключовим напрямком досліджень в останні роки. Хоча було запропоновано численні методи оптимізації отримання енергії, кожен з них має певні обмеження, що зменшують їх ефективність. **Проблема.** Фактори навколишнього середовища, такі як затінення, часткове затінення та низький рівень опромінення, суттєво впливають на продуктивність PV системи, причому часткове затінення є найбільш критичною та складною проблемою через створення кількох локальних максимумів потужності. **Мета.** Це дослідження спрямоване на покращення MPPT у PV системах в умовах часткового затінення шляхом розробки гібридного підходу, який інтегрує оптимізатор агрегації топології триангуляції (TTAO) з алгоритмом інкрементальної провідності (IC). **Методологія.** Моделювання проводилося в MATLAB/Simulink за чотирма статичними сценаріями часткового затінення, порівнюючи гібридний алгоритм TTAO-IC з традиційними методами, такими як метод збурень та спостережень (P&O), IC та метаевристичними алгоритмами. **Наукова новизна** роботи полягає в гібридному алгоритмі TTAO-IC, який поєднує глобальну оптимізаційну силу TTAO з точністю IC, усуваючи недоліки традиційних методів. **Практична цінність.** Результати показують, що гібридний алгоритм TTAO-IC досягає ефективності відстеження, що перевищує 99 %, перевершуючи існуючі методи та демонструючи надійну адаптивність до різних умов навколишнього середовища. Бібл. 31, табл. 5, рис. 15.

Ключові слова: сонячна фотоелектрична система, оптимізатор агрегації топології триангуляції, відстеження точки максимальної потужності, глобальна точка максимальної потужності, умови часткового затінення.

Introduction. Photovoltaic (PV) systems play a key role in the global energy transition by harnessing solar energy to generate electricity. Using semiconductor devices, these systems directly convert solar energy into electricity. However, the conversion efficiency typically ranges from 10 % to 25 % of the total incident solar power, highlighting the importance of optimizing power extraction to maximize energy efficiency. In this context, Maximum Power Point Tracking (MPPT) algorithms have become essential tools for achieving this goal. Since their inception in the 1950s, MPPT strategies have continuously evolved to address growing challenges, such as irradiance fluctuations, temperature variations, and partial shading effects [1]. Traditional approaches, particularly the Perturb and Observe (P&O) and Incremental Conductance (IC) methods, dominated early generations of MPPT systems due to their simplicity and effectiveness under stable conditions. However, these methods have significant limitations when applied to dynamic or complex environments. These limitations include slow convergence, inadequate tracking accuracy, and an inability to effectively manage partial shading scenarios [2–4]. To overcome these challenges, innovative approaches based on metaheuristic and hybrid algorithms have been developed. Methods such as Particle Swarm Optimization (PSO), Cuckoo Search (CS) [5] and Grey Wolf Optimization (GWO) [6] have proven to be particularly promising. These algorithms allow for a more accurate localization of the Global Maximum Power Point (GMPP), while improving convergence speed and reducing steady-state oscillations [7, 8]. Additionally, advanced variants, such as modified PSO, Plant

Propagation Algorithm (PPA), and hybrid solutions like Radial Basis Function Neural Network based on PSO (PSO-RBFNN), have demonstrated their ability to achieve energy yields above 99 %, even in variable and complex weather conditions [9–12]. The emergence of artificial intelligence in MPPT strategies has marked the beginning of a new era of innovation. Algorithms based on artificial neural networks, combined with hybrid techniques like PSO-RBFNN, help address complex challenges while enhancing the reliability and speed of systems [13, 14]. Previous work, such as the study by [15], introduced improvements to traditional methods. For instance, an optimized version of the P&O algorithm achieved an energy efficiency of 96 % under uniform atmospheric conditions, but it did not account for the effects of non-uniform conditions. Simultaneously, advancements in DC-DC converter design, such as high-voltage gain converters with soft switching, have significantly contributed to improving the energy efficiency of grid-connected PV systems [16].

Moreover, advanced control strategies, such as Terminal Sliding Mode Controllers (TSMC), hybrid PSO-TSMC algorithms, and approaches utilizing fuzzy logic and fractional-order controllers, offer enhanced robustness. These solutions stand out for their ability to reduce oscillations, improve system stability, and provide a quick response to environmental changes [17–20]. Given the variety of available methods and the rapid advancements in the field, it is crucial to evaluate and compare these approaches to determine the most suitable solutions for current challenges. A detailed analysis of

existing MPPT techniques is provided, highlighting innovative strategies that integrate metaheuristic algorithms, artificial intelligence, and innovations in converter design, as evidenced by [21–23]. Other efforts, such as those by [24], have proposed variants of the IC algorithm adapted to changing irradiance profiles. Although these approaches have demonstrated promising performance, they remain limited by the lack of experimental validation or their inability to effectively address partial shading scenarios and rapid irradiance variations. A hybrid algorithm combining a wavelet neural network and a cuckoo search algorithm has demonstrated superior performance in predicting PV production, better capturing the chaotic variations of solar radiation [25]. Furthermore, optimizations of the flower pollination algorithm for MPPT under partial shading have led to reduced tracking time and increased efficiency [26]. Another hybrid control approach abbreviated as ACO-ANN, based on a neural network and ant colony optimization, has enhanced MPPT and energy quality in industrial applications [27]. Strategies such as the improved grey wolf optimizer and the super-twisting sliding mode controller have also contributed to significant improvements in robustness and response time under shading conditions [28, 29]. Additionally, a strategy for quickly locating the global peak in PV systems under partial shading conditions, without particle reset, has been introduced, reducing convergence time by 650 % compared to traditional PSO reset methods and avoiding premature convergence [30]. However, despite the progress made, a major limitation remains for many MPPT techniques: their inefficiency in the face of slow or sudden changes in ambient temperature and solar irradiance. This highlights the need for even more robust and adaptive algorithms.

Goal. This study aims to improve MPPT in PV systems under partial shading conditions by developing a hybrid approach that integrates a Triangulation Topology Aggregation Optimizer (TTAO) with the IC algorithm. By integrating the global optimization capabilities of TTAO with the precision of the IC method, the proposed TTAO-IC algorithm addresses the limitations of traditional MPPT techniques, such as P&O and standalone IC, which often struggle with local optima, oscillations, and slow convergence under non-uniform irradiance. The goal is to provide a robust, efficient, and reliable solution for improving energy extraction in PV systems, particularly in large-scale deployments where partial shading is a common challenge. Simulation results demonstrate the superior performance of TTAO-IC, particularly in cases where conventional methods fail to converge to GMPP. The algorithm achieves tracking efficiencies exceeding 99 % across diverse partial shading conditions, highlighting its robustness and reliability. Key advantages of the TTAO-IC algorithm include:

- Rapid convergence to the GMPP, ensuring minimal energy loss during the tracking process.
- Significant reduction in oscillations around the MPP, even under dynamic and non-uniform irradiance conditions.
- Consistently high tracking efficiency, leading to enhanced energy yield and improved overall system performance.

The results from simulations demonstrate the effectiveness of this hybrid algorithm, which combines precision, speed, and robustness. This advancement opens

new perspectives for optimizing solar systems, ensuring optimal and reliable energy exploitation.

1. Modelling and analysis.

1.1. PV conversion chain. The MPP is achieved by controlling a DC-DC converter with an MPPT controller (Fig. 1). The MPPT controller optimizes power transfer from the PV system to the load, adapting to varying weather conditions to ensure maximum efficiency.

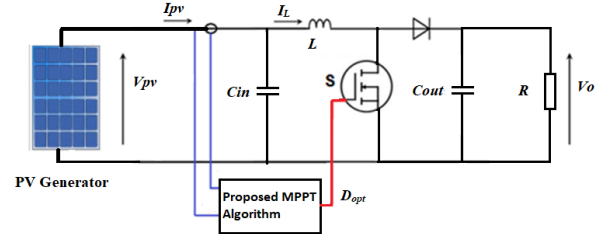


Fig. 1. DC-DC boost converter

PV system is made up of two identical solar panels connected in series, with their electrical specifications (Table 1). Connecting panels in series combines their voltages while maintaining the same current, enabling the system to achieve a higher output voltage. This configuration is particularly useful for applications requiring higher voltage levels, as it reduces the need for voltage amplification by the DC-DC converter.

Table 1

PV panel specifications

Parameter	PV module	PV installation
Maximum power output P_{\max} under standard test conditions (STC), W	213.15	426.3
Open-circuit voltage V_{oc} under STC, V	36.3	72.6
Short-circuit current I_{sc} under STC, A	7.84	7.84
Voltage at the MPP V_{mp} under STC, V	29	58
Current at the MPP I_{mp} under STC, A	7.35	7.35

The electrical parameters of the DC-DC boost converter used in the simulation are provided in Table 2.

Table 2

Boost converter component specifications

Parameter	Value
Inductance L , mH	1.1478
Input capacitor C_{in} , μ F	6800
Output capacitor C_{out} , μ F	3300
PWM frequency f , kHz	10
Resistive load R , Ω	100

The components of the boost converter are essential to the system's operation and have a direct impact on the performance of the TTAO-IC algorithm. The inductor (L) reduces current ripple, providing a stable power supply, while the input (C_{in}) and output (C_{out}) capacitors ensure smooth voltage levels on both sides of the converter, minimizing disturbances during MPPT. The load resistance (R) simulates power consumption and is crucial for evaluating the converter's energy efficiency. Additionally, the switching frequency (f) influences system responsiveness: a higher frequency allows for faster MPPT adjustments but can increase switching losses. Optimizing these parameters is essential for stable converter operation, which in turn improves the accuracy and convergence speed of the TTAO-IC algorithm. This is particularly valuable under challenging conditions, such as partial shading and rapid changes in irradiance.

1.2. PV panel model. A PV cell is represented by the single-diode model. This model can be extended to a PV module by treating it as a group of identical cells connected in series and/or parallel. The model of an individual cell is developed using the widely adopted equivalent electrical circuit (Fig. 2).

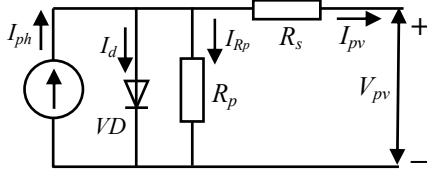


Fig. 2. Equivalent circuit diagram of a single-diode solar cell model

A PV system consists of multiple PV modules that are connected in series and parallel configurations to increase overall power output. The series connection of modules helps increase the system's voltage, while the parallel connection raises the current output [23]. The mathematical model of a PV system is described by a set of equations that represent the electrical behavior and characteristics of the modules under different conditions. These equations consider factors such as the irradiance, temperature, internal resistances, and electrical parameters of the PV cells:

$$I_{pv} = I_{ph}N_p - I_d N_p \times \exp\left(\frac{q(V_{pv} + \frac{I_{pv}R_s N_s}{N_p})}{nN_s k_b T}\right) - 1 - \frac{V_{pv} + \frac{I_{pv}R_s N_s}{N_p}}{R_p \frac{N_s}{N_p}} \quad (1)$$

with $V_t = k_b T / q$; (2)

$$I_{ph} = (I_{sc} + k_i(T - 270)) \frac{G}{1000}; \quad (3)$$

$$I_d = (I_{dr} \left(\frac{T}{298}\right)^3 \exp\left[\frac{qE_q}{N_s k_b V_t} \left(\frac{1}{298} - \frac{1}{T}\right)\right]), \quad (4)$$

where I_{ph} is the photocurrent; I_{sc} is the short-circuit current; I_{dr} is the dark saturation current; N_s is the number of series cells; N_p is the number of parallel cells; R_s is the series resistance; R_p is the shunt resistance; V_t is the thermal voltage; q is the electron charge; E_q is the photon energy; k_i is the short-circuit coefficient; k_b is the Boltzmann constant; T is the temperature; G is the irradiance.

1.3. Boost converter. In PV systems, the DC-DC converter is essential for implementing MPPT, ensuring maximum energy capture and enhancing system efficiency, especially in fluctuating environmental conditions. MPPT algorithms work in conjunction with DC-DC converters to fine-tune the system's electrical parameters for optimal power conversion. A widely used DC-DC converter for this purpose is the boost converter, which steps up the output voltage in comparison to the input voltage. The power produced by the PV panel is fed to this boost converter, which is regulated using a PWM signal generated by the MPPT controller. To ensure maximum power extraction from the PV system, the duty cycle (D) of the boost converter is continuously adjusted based on changes in solar irradiation, temperature, and other environmental factors [17]. This dynamic adjustment enables the PV system to maintain operation

at or near its MPP. An input capacitor is typically placed on the PV panel side to filter out high-frequency variations and stabilize the current. The optimal duty cycle for the boost converter, which allows maximum power extraction from the PV generator, is determined using specific mathematical relationships and control strategies, based on system parameters and environmental inputs:

$$D_{opt} = 1 - V_{mpp} / \sqrt{P_{mpp} R}, \quad (5)$$

where P_{mpp} is the peak power a PV system can generate while functioning at its MPP; V_{mpp} is the voltage level at which the PV panel operates to achieve maximum power output at the MPP; R is the load's equivalent resistance at the output of the DC-DC boost converter plays a crucial role in determining the efficiency of power transfer; D_{opt} is the ideal duty cycle configuration for the boost converter is essential for efficient MPPT, enabling the PV system to achieve maximum power output.

The MPPT block produces a duty cycle signal to regulate the switching element of the boost converter, which typically functions at an operating frequency of 10 kHz. A boost converter is employed in PV systems to increase the output voltage to a higher level, meeting system requirements. Its straightforward design and ease of control further contribute to its widespread use, as highlighted in [22]. In continuous conduction mode the inductor current and capacitor voltage are typically chosen as state variables. These variables are utilized to derive the averaged model of the boost converter, which can be represented by a set of equations, as illustrated in Fig. 1:

$$\frac{dI_L(t)}{dt} = -(1-D)\frac{1}{L}V_0(t) + \frac{1}{L}V_{pv}(t); \quad (6)$$

$$\frac{dV_0(t)}{dt} = (1-D)\frac{1}{C_{out}}I_L(t) + \frac{1}{RC_{out}}V_0(t), \quad (7)$$

where I_L is the current through the inductor; V_0 is the output voltage across the capacitor C_{out} ; V_{pv} is the supply voltage; D is the duty cycle ($\in [0, 1]$). In the boost converter circuit, the parameters R , L , C_{out} are the load resistance, the input circuit inductance, and the output filter capacitance, respectively.

1.4. Configuration of PV modules under static partial shading conditions. In non-uniform irradiance scenarios, such as shading caused by obstacles like trees, buildings, or passing clouds, PV generator systems may experience partial shading. As illustrated in Fig. 3, this phenomenon leads to a power-voltage (P - V) curve with multiple peaks, representing different maximum power points (MPPs). Among these, one is the GMPP, while the others are classified as local maximum power points (LMPPs). To replicate partial shading conditions, PV panels are exposed to varying irradiance levels, resulting in P - V curves with multiple peaks. To validate our method, a case study under static partial shading conditions is provided, including 4 practical test scenarios for simulation:

1. Scenario 1: a test under STC (1000 W/m² at 25 °C).
2. Scenario 2: $G_1 = 1000$ W/m², $G_2 = 400$ W/m² at 25 °C.
3. Scenario 3: $G_1 = 800$ W/m², $G_2 = 400$ W/m² at 25 °C.
4. Scenario 4: $G_1 = 600$ W/m², $G_2 = 400$ W/m² at 25 °C.

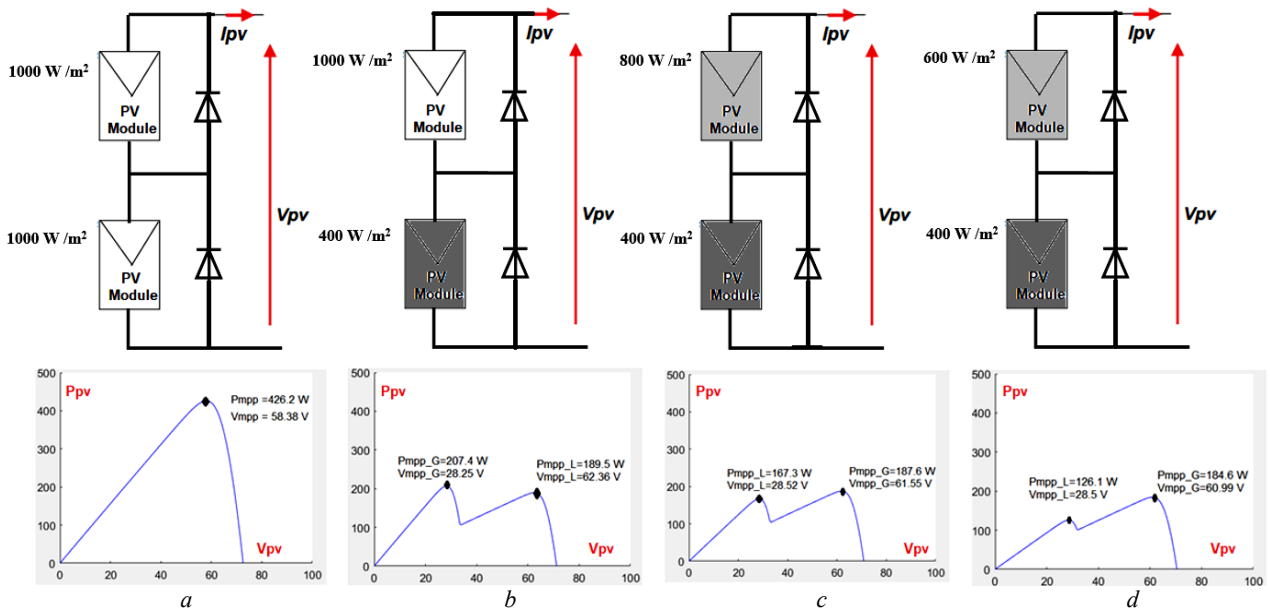


Fig. 3. Arrangement of PV modules across various static partial shading scenarios:
a) scenario 1 (STC); b) scenario 2; c) scenario 3; d) scenario 4

The optimal duty cycles for each scenario, as determined by (5), are provided in Table 3.

Table 3
Optimal duty cycle calculated for each scenario

Scenario	P_{mpp} , W	D_{opt}
Scenario 1	$P_{mpp} = 426.3$	$D_{opt_G} = 0.71721425$
Scenario 2	$P_{mpp_G} = 207.4$ $P_{mpp_L} = 189.5$	$D_{opt_G} = 0.80383836$ $D_{opt_L} = 0.54699656$
Scenario 3	$P_{mpp_G} = 187.6$ $P_{mpp_L} = 167.3$	$D_{opt_G} = 0.55062217$ $D_{opt_L} = 0.77950357$
Scenario 4	$P_{mpp_G} = 184.6$ $P_{mpp_L} = 126.1$	$D_{opt_G} = 0.55110705$ $D_{opt_L} = 0.74620251$

Note. P_{mpp_G} is the output power at the GMPP; P_{mpp_L} is the output power at LMPP; D_{opt_G} is the optimal duty cycle corresponding to the GMPP; D_{opt_L} : is the optimal duty cycle corresponding to the LMPP.

MATLAB/Simulink simulations were carried out to evaluate the performance of the hybrid TTAO-IC algorithm under defined static partial shading conditions. The outcomes were benchmarked against those of two conventional MPPT techniques: P&O and IC.

2. Enhanced MPPT based on hybrid TTAO-IC algorithm. In PV systems, optimizing efficiency requires identifying the ideal operating point where power output is maximized, a process achieved through advanced strategies. Given the non-linear characteristics of PV systems and the variability of environmental conditions, sophisticated algorithms are essential to consistently locate and maintain this optimal point. Hybrid metaheuristic algorithms, which combine the strengths of multiple optimization techniques, have proven particularly effective in enhancing this process. These approaches are especially adept at addressing complex challenges, such as partial shading conditions, and adapting to dynamic environmental changes, making them a robust solution for improving the performance and reliability of PV systems.

2.1. TTAO algorithm.

The TTAO is a global optimization algorithm based on mathematical principles, designed to solve continuous and engineering problems [31]. This algorithm leverages triangular topological similarity to develop 2 main strategies: generic aggregation and local aggregation. These strategies enable the TTAO to effectively explore the search space, avoid local optima, and converge toward the global optimum. The detailed functioning of this algorithm is described by the flowchart (Fig. 4) and the corresponding pseudocode (Fig. 5).

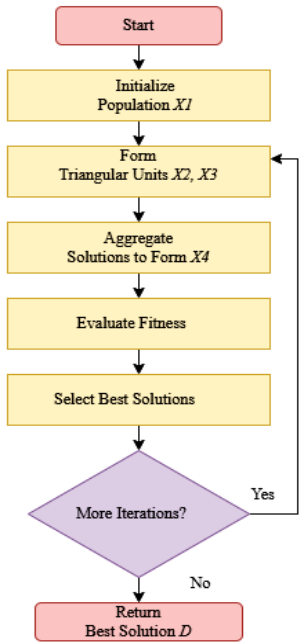


Fig. 4. Flowchart of TTAO algorithm

Algorithm 1: TTAO algorithm

```

1: Input:  $V_{pv}$ ,  $I_{pv}$  (voltage and current from PV panel)
2: Parameters:
   Population size  $Pop\ Size = 30$ , Iterations  $T = 100$ 
   Dimension  $Dim = 1$ , Bounds ( $Low = 0$ ,  $Up = 1$ )
    $X1$ ,  $X2$ ,  $X3$  and  $X4$ : populations
3: Initialize population  $X1$  randomly within the bounds.
4: For  $t = 1$  to  $T$  do
5:   Form triangular units  $X2$ ,  $X3$  based on  $X1$ .
6:   Aggregate solutions to form  $X4$ .
7:   Evaluate fitness of  $X1$ ,  $X2$ ,  $X3$ ,  $X4$ .
8:   Select the best solutions and update  $X1$ .
9: End for
10: Return the best solution  $D$ 

```

Fig. 5. TTAO algorithm

2.2. IC algorithm. The IC algorithm is a popular MPPT method for PV systems, aimed at maximizing energy extraction by dynamically comparing the

instantaneous conductance (I/V) with the incremental conductance (dI/dV) in relation to the voltage. The IC algorithm enhances efficiency by continuously fine-tuning the operating voltage to keep the system close to the MPP while minimizing oscillations. It adjusts the duty cycle (D) of the power converter in response to real-time variations in voltage (V) and current (I), ensuring optimal operation. The MPP condition is mathematically described as follows:

$$dP/dV = 0 \text{ where } P = V \cdot I. \quad (8)$$

Expanding this gives:

$$\frac{d(V \cdot I)}{dV} = I + V \frac{dI}{dV}. \quad (9)$$

The detailed functioning of this algorithm is described by the pseudocode (Fig. 6).

Algorithm 2: IC algorithm
1: Initialize $D_{prev} = 0.5$, $V_{pv, prev} = V_{pv}$, $I_{pv, prev} = I_{pv}$
2: Set step size $\Delta D = 0.0001$
3: while system is running do
4: Measure current voltage V_{pv} and current I_{pv}
5: Calculate the change in voltage: $\Delta V = V_{pv} - V_{pv, prev}$
6: Calculate the change in current: $\Delta I = I_{pv} - I_{pv, prev}$
7: if ($\Delta V \neq 0$) then
if ($\Delta I/\Delta V > -I_{pv}/V_{pv}$) then
8: Decrease duty cycle : $D = D_{prev} - \Delta D$
9: else if ($\Delta I/\Delta V < -I_{pv}/V_{pv}$) then
10: Increase duty cycle: $D = D_{prev} + \Delta D$
11: else
12: No change in duty cycle : $D = D_{prev}$
13: end if
14: else if ($\Delta V = 0$) then
15: if ($\Delta I \neq 0$) then
16: Decrease duty cycle : $D = D_{prev} - \Delta D$
17: end if
18: end if
19: Update previous values: $V_{pv, prev} = V_{pv}$, $I_{pv, prev} = I_{pv}$
20: Set $D_{prev} = D$
21: end while

Fig. 6. IC algorithm

2.3. Hybrid TTAO-IC algorithm. The hybrid TTAO-IC algorithm is a method combining the global search capabilities of the TTAO with the local refinement provided by the IC algorithm. This hybrid approach is designed to optimize MPPT in PV systems. TTAO is used to explore the search space globally and identify regions close to the MPP, while IC refines the duty cycle to achieve precise MPPT. The power generated by the PV system is given as:

$$P_{pv} = V_{pv} I_{pv}, \quad (10)$$

where V_{pv} , I_{pv} are the PV panel voltage and current.

To maximize the power P_{pv} the derivative of power with respect to voltage must be zero:

$$dP_{pv}/dV_{pv} = 0; \quad (11)$$

$$dP_{pv}/dV_{pv} = I_{pv} + V_{pv} \frac{dI_{pv}}{dV_{pv}}. \quad (12)$$

The hybrid TTAO-IC algorithm can be broken down into the following steps:

- **Initialization:** the algorithm starts by generating a random initial population for the TTAO phase. The initial duty cycle is set to $D_{prev} = 0.5$.

- **Global exploration (TTAO):** during each iteration of TTAO, triangular units are formed from the population, and solutions are aggregated and evaluated. The best

solution from this phase, denoted D_{TTAO} , represents a candidate duty cycle near the MPP.

- **Local refinement (IC):** the best solution from TTAO is refined using the IC method. IC adjusts the duty cycle based on the change in power relative to voltage, following the conditions:

$$dI_{pv}/dV_{pv} = -I_{pv}/V_{pv}; \quad (13)$$

$$D_{prev} = \alpha D_{IC} + (1 - \alpha) D_{prev}, \quad (14)$$

where α is the smoothing factor.

- **Termination:** after a predefined number of iterations, or once the duty cycle converges, the final value of D is returned, optimizing the PV system's operation.

The algorithm's detailed operation is visually represented through the flowchart in Fig. 7 and clearly outlined in the pseudocode shown in Fig. 8.

The hybrid TTAO-IC algorithm improves MPPT efficiency in PV systems by combining the global exploration of TTAO with the precision of IC, thus optimizing maximum power tracking. This hybrid approach ensures the system does not get stuck in local optima, while accurately tracking the MPP under varying environmental conditions (e.g., static partial shading conditions).

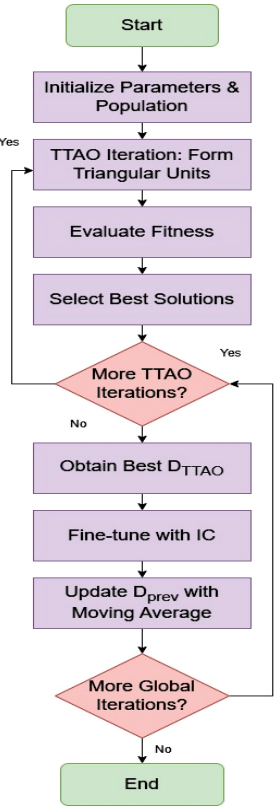


Fig. 7. Flowchart of hybrid TTAO-IC algorithm

Algorithm 3: Hybrid TTAO-IC Algorithm
1: Input: V_{pv} , I_{pv}
2: Parameters: Population size $PopSize = 10$, TTAO iterations $T = 10$, maximum iterations $MaxIter = 100$, dimension $Dim = 1$, $\Delta D = 0.0001$
3: Initialize population for TTAO
4: Initialize persistent variables: $V_{pv, prev} = 0$, $I_{pv, prev} = 0$, $D_{prev} = 0.5$
5: for iteration = 1 to $MaxIter$ do
6: for $t = 1$ to T do
7: Form triangular units and aggregate solutions in TTAO
8: Evaluate the fitness and update the population
9: end for
10: Obtain the best solution D_{TTAO}
11: Fine-tune using the IC algorithm to get D_{IC}
12: Update $D_{prev} = \alpha D_{IC} + (1 - \alpha) D_{prev}$ (apply moving average filter)
13: end for
14: Output: Final duty cycle $D = D_{prev}$

Fig. 8. Hybrid TTAO-IC algorithm

3. Simulation results and discussion.

3.1. Simulation results. To assess the performance of the proposed MPPT control algorithm, a series of simulations were conducted in the MATLAB/Simulink environment. The control architecture used in these simulations is shown in Fig. 9. In this setup, a DC-DC boost converter acts as the interface between the simulated PV system and a DC load. This boost converter is crucial

as it regulates the voltage and current, ensuring that the PV system operates at its MPP. Four distinct MPPT algorithm blocks were incorporated into the simulation environment, each tested individually to evaluate their respective performances. The main goal of this study is to evaluate the efficiency and accuracy of 4 different algorithms for tracking the GMPP in a PV system under static partial shading conditions. The algorithms analyzed include IC, P&O, TTAO and a hybrid TTAO-IC approach. The aim of the hybrid algorithm is to optimize the precision and speed of the search process, ensuring reliable and efficient tracking of the GMPP. The selection of these algorithms is based on their complementary characteristics:

- P&O is known for its simplicity and widespread use, though it may struggle to maintain accuracy under variable irradiance.

- IC offers improved precision, particularly in dynamic conditions, as it adjusts to changes in irradiance more effectively.

- TTAO, a metaheuristic optimization technique, excels in locating global maxima in complex search spaces, such as those introduced by partial shading effects.

- The hybrid TTAO-IC algorithm combines the global search capability of TTAO with the local precision of IC, aiming to reduce convergence time and improve tracking accuracy. Efficient MPPT control also directly affects the efficiency of the DC-DC boost converter. Algorithms that minimize oscillations around the MPP reduce switching losses, thereby optimizing the overall system performance. Conversely, slower or less accurate algorithms can lead to higher power losses due to increased switching activity.

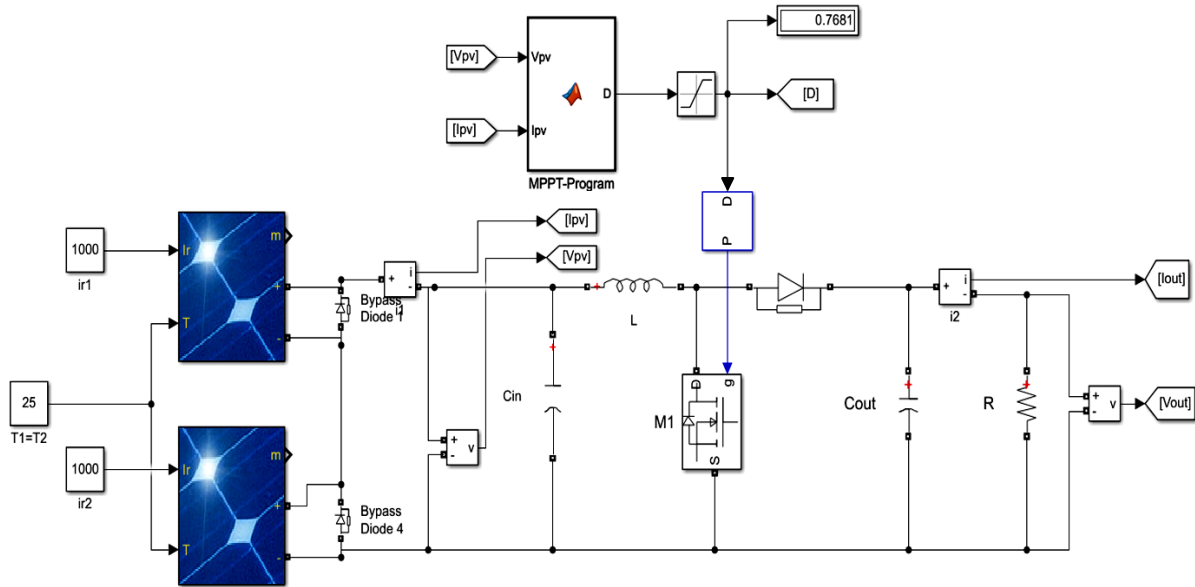


Fig. 9. Schematic representation of the PV system simulated in MATLAB/Simulink

The comparative performance of the algorithms is assessed based on 3 key parameters:

- *Time*. These measures the time required for each algorithm to converge to the MPP (P_{pv}). A shorter tracking time indicates faster adaptation to the MPP.

- *Tracking error*. This parameter evaluates how accurately the algorithm identifies the MPP. It is computed as the percentage difference between the duty cycle determined by the algorithm and the actual global duty cycle, which is obtained from the reference values (Table 3).

- *System efficiency*. This evaluates the overall efficiency of the PV system by computing the ratio of the extracted power to the maximum available power under the given conditions.

3.2. Simulation observations. The simulation results are illustrated in Fig. 10–13, which correspond to 4 scenarios, each highlighting the power (P_{pv}) and duty cycle achieved by the algorithms (IC, P&O, TTAO, and TTAO-IC). According to the simulation results presented in Table 4, the performance of the algorithms is evaluated under various scenarios:

- *Scenario 1*. Both TTAO and TTAO-IC exhibit minimal tracking errors, significantly outperforming the IC and P&O methods, which display much higher error rates.

- *Scenarios 2 and 3*. The IC and P&O techniques show considerable limitations, with tracking errors exceeding 30 %, emphasizing their reduced effectiveness

in these conditions. In contrast, TTAO and TTAO-IC maintain notably lower error levels, with TTAO-IC achieving superior performance.

- *Scenario 4*. The same trend is observed, where TTAO-IC consistently records the lowest tracking error, demonstrating its robustness and accuracy across varying conditions.

The results highlight the superior performance of the hybrid TTAO-IC algorithm compared to other methods. This algorithm demonstrates rapid convergence to the GMPP with minimal tracking error, ensuring high efficiency in power extraction. Moreover, it eliminates persistent steady-state oscillations, making it a robust and reliable solution for MPPT under partial shading conditions. The comparative analysis confirms the hybrid TTAO-IC algorithm as the most effective solution for tracking the GMPP in PV systems, particularly under partial shading. By combining global optimization capabilities with precise local adjustments, it ensures rapid convergence, minimal error, and enhanced system efficiency. These findings underscore the critical importance of adopting advanced MPPT methods like TTAO-IC to maximize energy yield and optimize the overall performance of PV systems. The TTAO-IC method excels in maintaining minimal tracking errors across all scenarios, showcasing its superior precision in accurately determining the GMPP.

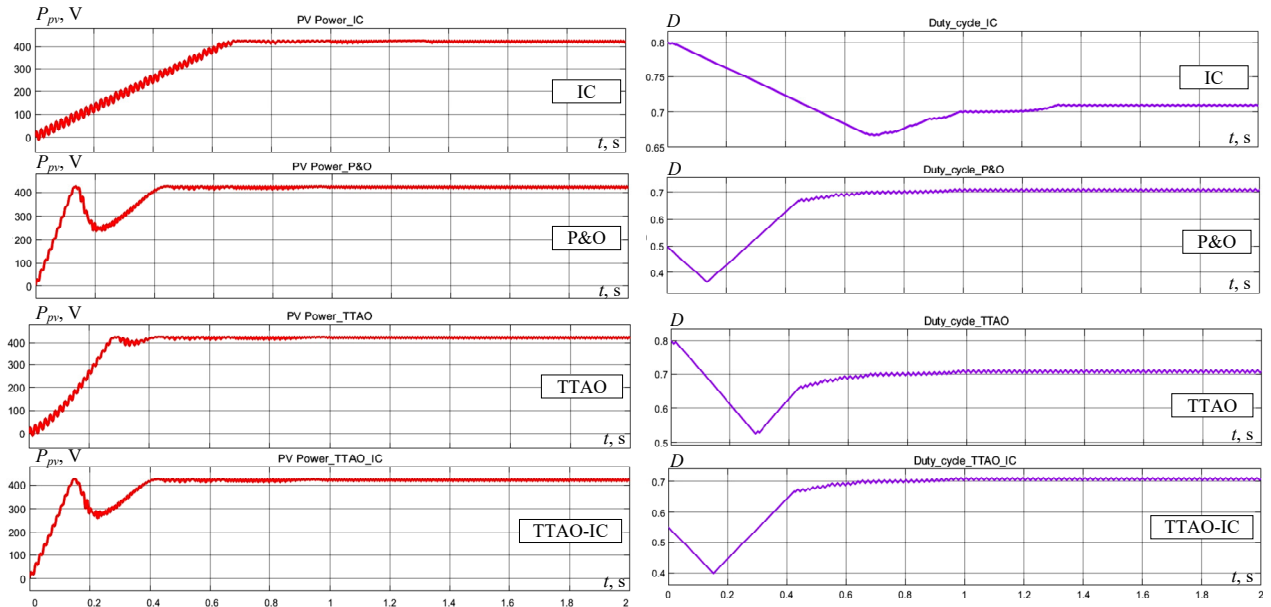


Fig. 10. Power P_{pv} and duty cycle D in scenario 1

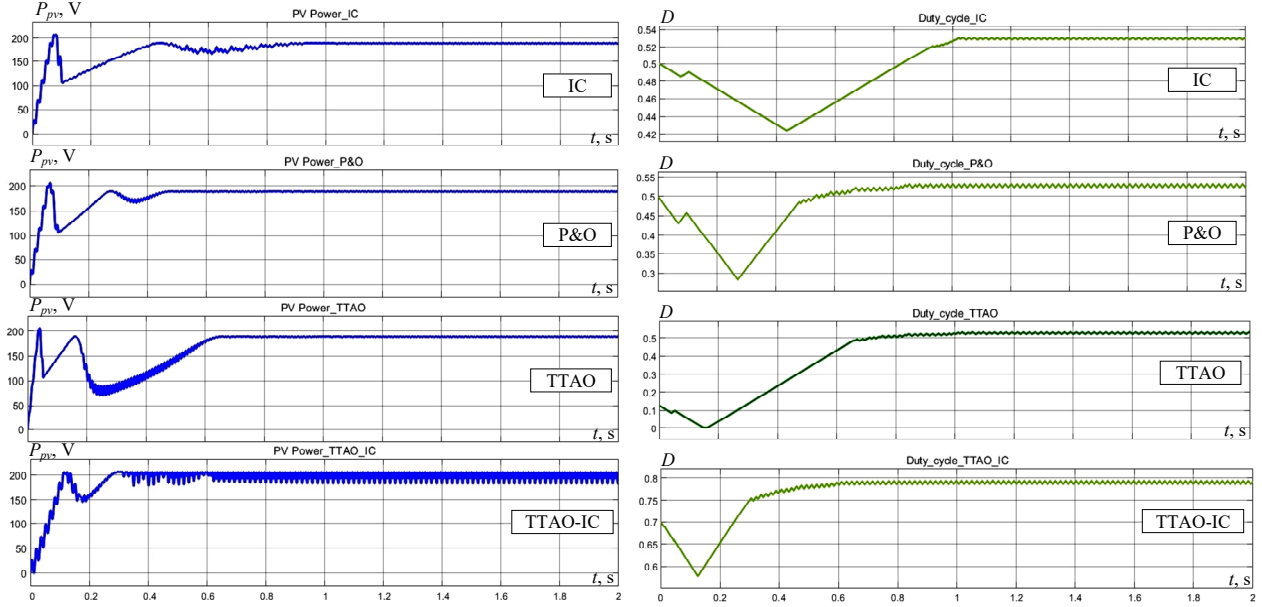


Fig. 11. Power P_{pv} and duty cycle D in scenario 2

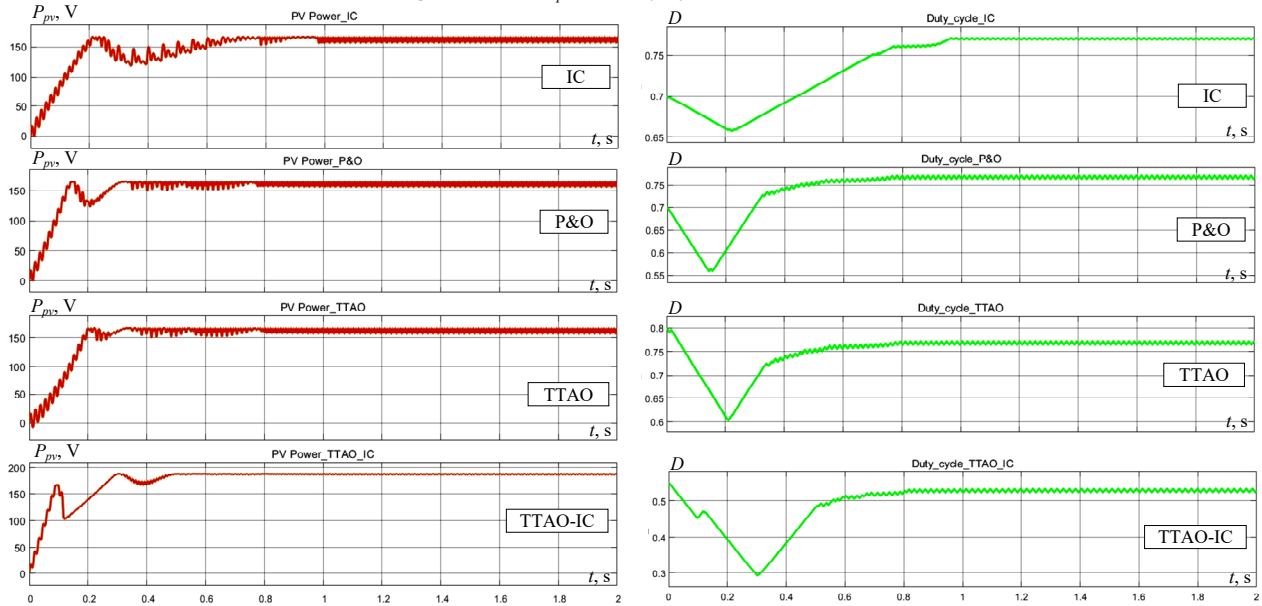


Fig. 12. Power P_{pv} and duty cycle D in scenario 3

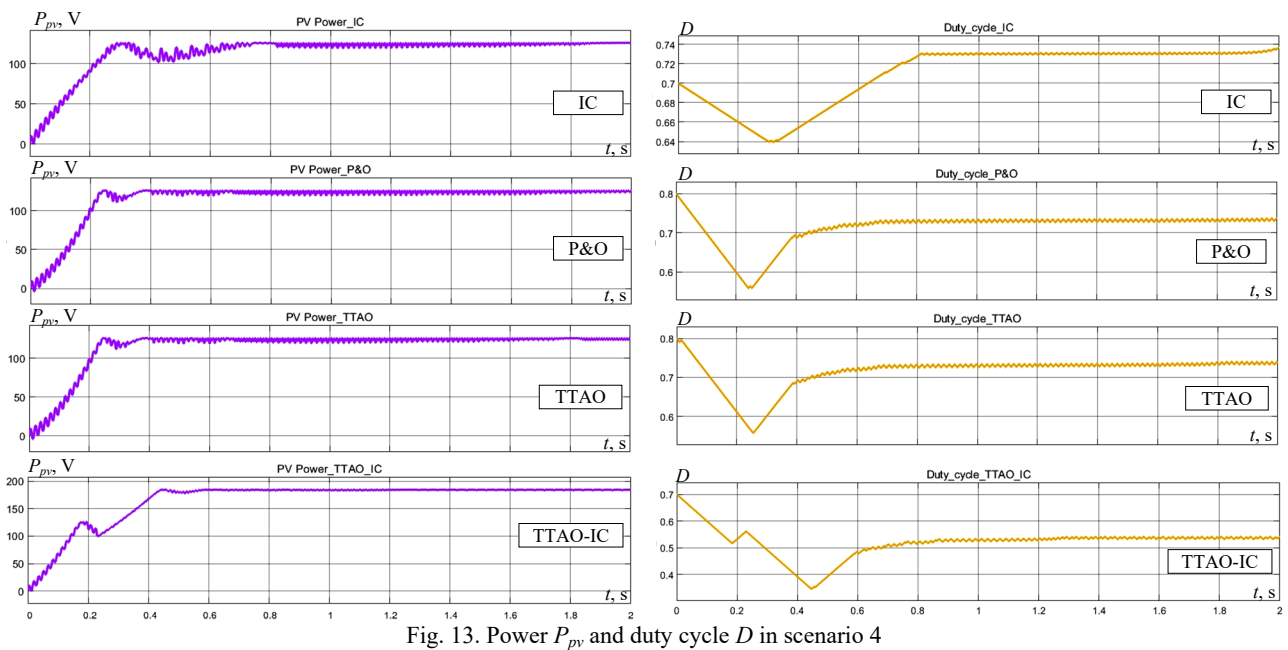


Fig. 13. Power P_{pv} and duty cycle D in scenario 4

Table 4

Performance comparison of algorithms in various scenarios

Algorithm	Convergence time	Duty cycle	Tracking error, %	P_{pv} , W	Efficiency, %
Scenario 1: $G_1 = G_2 = 1000 \text{ W/m}^2$, $T_1 = T_2 = 25 \text{ }^\circ\text{C}$, $P_{mpp} = 426.3 \text{ W}$, $D_{optG} = 0.71721435$					
IC	648.689	0.7103	0.9641	426.130	99.96
P&O	628.276	0.7108	0.8943	426.124	99.96
TTAO	352.368	0.7101	0.9919	426.106	99.95
TTAO-IC	397.775	0.7101	0.7808	426.130	99.96
Scenario 2: $G_1 = 1000 \text{ W/m}^2$, $G_2 = 400 \text{ W/m}^2$, $T_1 = T_2 = 25 \text{ }^\circ\text{C}$, $P_{mppG} = 207.4 \text{ W}$, $D_{optG} = 0.80383836$					
IC	768.902	0.5305	34.0041	189.453	91.35
P&O	517.483	0.5308	33.9668	189.450	91.35
TTAO	254.545	0.7925	1.4105	204.705	98.70
TTAO-IC	265.734	0.7943	1.1866	206.400	99.75
Scenario 3: $G_1 = 800 \text{ W/m}^2$, $G_2 = 400 \text{ W/m}^2$, $T_1 = T_2 = 25 \text{ }^\circ\text{C}$, $P_{mppG} = 187.6 \text{ W}$, $D_{optG} = 0.55062217$					
IC	567.832	0.7704	39.9145	167.000	89.02
P&O	405.594	0.7699	39.8236	167.200	89.13
TTAO	271.329	0.7714	40.0961	167.200	89.13
TTAO-IC	442.281	0.5378	2.3287	187.600	100.00
Scenario 4: $G_1 = 600 \text{ W/m}^2$, $G_2 = 400 \text{ W/m}^2$, $T_1 = T_2 = 25 \text{ }^\circ\text{C}$, $P_{mppG} = 184.6 \text{ W}$, $D_{optG} = 0.55110705$					
IC	623.776	0.7401	34.2933	125.800	68.15
P&O	433.566	0.7400	34.2752	125.900	68.20
TTAO	338.462	0.7391	34.1119	125.700	68.09
TTAO-IC	443.477	0.5311	3.3631	184.500	99.95

3.3. Statistical analysis. The tracking error of the duty cycle measures how accurately each algorithm identifies the GMPP. Figure 14 presents a comparison of the 4 algorithms' performance across the 4 scenarios.

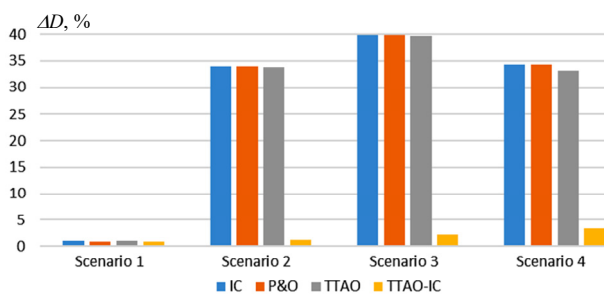


Fig. 14. Duty cycle tracking error

The power extraction efficiency evaluates the capability of each algorithm to maximize the output

power from the PV system. The results for the 4 algorithms under the 4 scenarios are shown in Fig. 15. Scenario 1 – all algorithms demonstrate high efficiency ($\approx 99\%$) under uniform shading conditions. However, TTAO-IC consistently achieves slightly higher efficiency compared to the other methods. Scenario 2–4: under partial shading conditions, the performance of IC and P&O deteriorates significantly, with efficiency dropping below 70% . Conversely, TTAO-IC sustains efficiencies close to 100% with showing a slight edge. The TTAO-IC algorithm achieves near-perfect power extraction efficiency under all conditions, outperforming other methods, especially under partial shading scenarios.

The findings presented in Table 5 highlight the exceptional performance of the TTAO-IC algorithm across several critical metrics. Simulation results were used to calculate the efficiency percentage for each

method, showing that the TTAO-IC algorithm delivers substantially higher efficiency compared to the techniques detailed in [11, 12, 29].

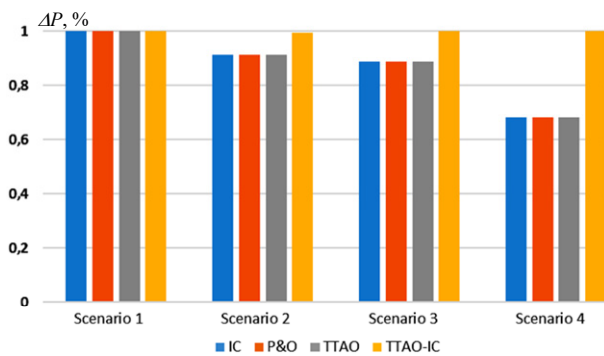


Fig. 15. Power extraction efficiency

Furthermore, the TTAO-IC controller demonstrates a significantly faster response time than PSO, PPA, PSO-OBL, ABC and SSA-GWO when subjected to static shading conditions, emphasizing its capability to quickly reach the GMPP. This enhanced efficiency reduces energy losses by ensuring precise and rapid tracking of the GMPP. These results highlight the exceptional effectiveness and superiority of the TTAO-IC algorithm in optimizing the MPPT process for PV systems. With its accelerated convergence rate and improved efficiency, the algorithm emerges as a highly effective solution for maximizing energy production while addressing shading challenges in PV applications.

Table 5

Comparative performance analysis of the proposed TTAO-IC algorithm and other MPPT techniques

MPPT algorithm	Efficiency, %	Tracking time, s
Particle Swarm Optimization (PSO) [29]	99.71	0.46
Plant Propagation Algorithm (PPA) [11]	99.91	0.68
PSO-Optimization Based Learning (OBL) [12]	99.72	0.69
Artificial Bee Colony (ABC) algorithm [29]	99.54	0.47
Salp Swarm Algorithm with Grey Wolf Optimizer (SSA-GWO) [29]	99.84	0.43
Proposed TTAO-IC	99.96	0.398

Conclusions. This research has conducted an in-depth exploration of various MPPT techniques, emphasizing their essential role in optimizing the efficiency of PV systems. By evaluating both individual and hybrid MPPT algorithms, we have provided valuable insights into their performance under different operational conditions. The study focused on key parameters such as response time, stability, performance under partial shading and accuracy, offering a holistic view of the effectiveness of these techniques.

The study successfully achieves the goal through the development of the TTAO-IC algorithm, which combines the global optimization capabilities of TTAO with the precision of the IC method. Simulation results demonstrate that the TTAO-IC algorithm significantly enhances MPPT performance under partial shading conditions, achieving tracking efficiencies exceeding 99 % and outperforming

traditional methods like P&O and IC, as well as other hybrid techniques such as PSO, GWO, PSO-OBL, PPA, and ABC.

The algorithm addresses the limitations of conventional methods by delivering faster convergence to GMPP, reducing oscillations around the MPP, and maintaining high tracking efficiency even under non-uniform shading conditions. In conclusion, the TTAO-IC algorithm stands out as a highly efficient and reliable solution for MPPT in PV systems, offering a balance between performance and high efficiency even under challenging conditions makes it a strong contender for large-scale solar energy applications.

Future research should focus on further refining this hybrid approach and validating its performance in real-world scenarios, aiming to enhance the global adoption of solar energy. For further studies, we suggest adjusting key parameters to optimize performance across various PV generator architectures, possibly using advanced optimization techniques. Specifically, we aim to implement the methodology in centralized, decentralized, and hybrid PV systems, as well as with different types of solar panels, including monocrystalline and polycrystalline varieties. Additionally, we plan to evaluate the algorithm under a range of conditions, such as varying irradiance levels and dynamic partial shading situations. By applying the methodology across these different system designs and environmental contexts, we seek to enhance our understanding of its performance and potential adaptations.

Conflict of interest. The authors declare that they have no conflicts of interest.

REFERENCES

1. Abdel-Salam M., EL-Mohandes M.-T., Goda M. History of Maximum Power Point Tracking. Book Chapter in *Green Energy and Technology*, Springer, 2020, pp. 1-29. doi: https://doi.org/10.1007/978-3-030-05578-3_1.
2. Mohamed S.A., Abd El Sattar M. A comparative study of P&O and INC maximum power point tracking techniques for grid-connected PV systems. *SN Applied Sciences*, 2019, vol. 1, no. 2, art. no. 174. doi: <https://doi.org/10.1007/s42452-018-0134-4>.
3. Abd H.M., Abdo E.A., Jasim A.M., Sabaawi A.M.A. Incremental Conductance Algorithm Optimization for a Photovoltaic System with Fast Response Under Fast-Varying of Solar Power. *2019 10th International Renewable Energy Congress (IREC)*, 2019, pp. 1-6. doi: <https://doi.org/10.1109/IREC.2019.8754600>.
4. Hadjidi N., Benbrahim M., Ounnas D., Mouss L.H. Global maximum power point tracking method for photovoltaic systems using Takagi-Sugeno fuzzy models and ANFIS approach. *Electrical Engineering & Electromechanics*, 2025, no. 2, pp. 31-38. doi: <https://doi.org/10.20998/2074-272X.2025.2.05>.
5. Abo-Elyousr F.K., Abdelshafy A.M., Abdelaziz A.Y. MPPT-Based Particle Swarm and Cuckoo Search Algorithms for PV Systems. Book Chapter in *Green Energy and Technology*, Springer, 2020, pp. 379-400. doi: https://doi.org/10.1007/978-3-030-05578-3_14.
6. Laouafi F. Improved grey wolf optimizer for optimal reactive power dispatch with integration of wind and solar energy. *Electrical Engineering & Electromechanics*, 2025, no. 1, pp. 23-30. doi: <https://doi.org/10.20998/2074-272X.2025.1.04>.
7. Mohamed M.A., Zaki Diab A.A., Rezk H. Partial shading mitigation of PV systems via different meta-heuristic techniques. *Renewable Energy*, 2019, vol. 130, pp. 1159-1175. doi: <https://doi.org/10.1016/j.renene.2018.08.077>.
8. Bertahar F., Abdeddaim S., Betka A., Omar C. A Comparative Study of PSO, GWO, and HOA Algorithms for Maximum Power Point Tracking in Partially Shaded Photovoltaic Systems. *Power Electronics and Drives*, 2024, vol. 9, no. 1, pp. 86-105. doi: <https://doi.org/10.2478/pead-2024-0006>.

9. Hamdi H., Ben Regaya C., Zaafour A. Real-time study of a photovoltaic system with boost converter using the PSO-RBF neural network algorithms in a MyRio controller. *Solar Energy*, 2019, vol. 183, pp. 1-16. doi: <https://doi.org/10.1016/j.solener.2019.02.064>.
10. Singh Chawda G., Prakash Mahela O., Gupta N., Khosrav M., Senjyu T. Incremental Conductance Based Particle Swarm Optimization Algorithm for Global Maximum Power Tracking of Solar-PV under Nonuniform Operating Conditions. *Applied Sciences*, 2020, vol. 10, no. 13, art. no. 4575. doi: <https://doi.org/10.3390/app10134575>.
11. Khaterchi H., Moulahi M.H., Jeridi A., Ben Messaoud R., Zaafour A. Improvement teaching-learning-based optimization algorithm for solar cell parameter extraction in photovoltaic systems. *Electrical Engineering & Electromechanics*, 2025, no. 3, pp. 37-44. doi: <https://doi.org/10.20998/2074-272X.2025.3.06>.
12. Saeed H., Mehmood T., Khan F.A., Shah M.S., Ullah M.F., Ali H. An improved search ability of particle swarm optimization algorithm for tracking maximum power point under shading conditions. *Electrical Engineering & Electromechanics*, 2022, no. 2, pp. 23-28. doi: <https://doi.org/10.20998/2074-272X.2022.2.04>.
13. Jyothy L.P.N., Sindhu M.R. An Artificial Neural Network based MPPT Algorithm For Solar PV System. *2018 4th International Conference on Electrical Energy Systems (ICEES)*, 2018, pp. 375-380. doi: <https://doi.org/10.1109/ICEES.2018.8443277>.
14. Khatib T., Muhsen D.H. Optimal Sizing of Standalone Photovoltaic System Using Improved Performance Model and Optimization Algorithm. *Sustainability*, 2020, vol. 12, no. 6, art. no. 2233. doi: <https://doi.org/10.3390/su12062233>.
15. Mosaad M.I., Abed el-Raouf M.O., Al-Ahmar M.A., Banakher F.A. Maximum Power Point Tracking of PV system Based Cuckoo Search Algorithm; review and comparison. *Energy Procedia*, 2019, vol. 162, pp. 117-126. doi: <https://doi.org/10.1016/j.egypro.2019.04.013>.
16. Louarem S., Kebbab F.Z., Salhi H., Nouri H. A comparative study of maximum power point tracking techniques for a photovoltaic grid-connected system. *Electrical Engineering & Electromechanics*, 2022, no. 4, pp. 27-33. doi: <https://doi.org/10.20998/2074-272X.2022.4.04>.
17. Al-Dhaifallah M., Nassef A.M., Rezk H., Nisar K.S. Optimal parameter design of fractional order control based INC-MPPT for PV system. *Solar Energy*, 2018, vol. 159, pp. 650-664. doi: <https://doi.org/10.1016/j.solener.2017.11.040>.
18. Lamzouri F.-E., Boufounas E.-M., Brahmi A., Amrani A.E. Optimized TSMC Control Based MPPT for PV System under Variable Atmospheric Conditions Using PSO Algorithm. *Procedia Computer Science*, 2020, vol. 170, pp. 887-892. doi: <https://doi.org/10.1016/j.procs.2020.03.116>.
19. Saad W., Sellami A., Garcia G. Terminal sliding mode control-based MPPT for a photovoltaic system with uncertainties. *International Journal of Modelling, Identification and Control*, 2018, vol. 29, no. 2, pp. 118-126. doi: <https://doi.org/10.1504/IJMIC.2018.090478>.
20. Zerzouri N., Ben Si Ali N., Benalia N. A maximum power point tracking of a photovoltaic system connected to a three-phase grid using a variable step size perturb and observe algorithm. *Electrical Engineering & Electromechanics*, 2023, no. 5, pp. 37-46. doi: <https://doi.org/10.20998/2074-272X.2023.5.06>.
21. Eltamaly A.M., Farh H.M.H., Al-Saud M.S. Grade point average assessment for metaheuristic GMPP techniques of partial shaded PV systems. *IET Renewable Power Generation*, 2019, vol. 13, no. 8, pp. 1215-1231. doi: <https://doi.org/10.1049/iet-rpg.2018.5336>.
22. Mao M., Zhou L., Yang Z., Zhang Q., Zheng C., Xie B., Wan Y. A hybrid intelligent GMPPT algorithm for partial shading PV system. *Control Engineering Practice*, 2019, vol. 83, pp. 108-115. doi: <https://doi.org/10.1016/j.conengprac.2018.10.013>.
23. Mosaad M.I., Abed el-Raouf M.O., Al-Ahmar M.A., Banakher F.A. Maximum Power Point Tracking of PV system Based Cuckoo Search Algorithm; review and comparison. *Energy Procedia*, 2019, vol. 162, pp. 117-126. doi: <https://doi.org/10.1016/j.egypro.2019.04.013>.
24. Ali A.I.M., Mohamed H.R.A. Improved P&O MPPT algorithm with efficient open-circuit voltage estimation for two-stage grid-integrated PV system under realistic solar radiation. *International Journal of Electrical Power & Energy Systems*, 2022, vol. 137, art. no. 107805. doi: <https://doi.org/10.1016/j.ijepes.2021.107805>.
25. Alsafasfeh Q. An Efficient Algorithm for Power Prediction in PV Generation System. *International Journal of Renewable Energy Development*, 2020, vol. 9, no. 2, pp. 207-216. doi: <https://doi.org/10.14710/ijred.9.2.207-216>.
26. Awan M.M.A., Mahmood T. Optimization of Maximum Power Point Tracking Flower Pollination Algorithm for a Standalone Solar Photovoltaic System. *Mehran University Research Journal of Engineering and Technology*, 2020, vol. 39, no. 2, pp. 267-278. doi: <https://doi.org/10.22581/muet1982.2002.05>.
27. Babes B., Boutaghane A., Hamouda N. A novel nature-inspired maximum power point tracking (MPPT) controller based on ACO-ANN algorithm for photovoltaic (PV) system fed arc welding machines. *Neural Computing and Applications*, 2022, vol. 34, no. 1, pp. 299-317. doi: <https://doi.org/10.1007/s00521-021-06393-w>.
28. Ahmed S., Muhammad Adil H.M., Ahmad I., Azeem M.K., E Huma Z., Abbas Khan S. Supertwisting Sliding Mode Algorithm Based Nonlinear MPPT Control for a Solar PV System with Artificial Neural Networks Based Reference Generation. *Energies*, 2020, vol. 13, no. 14, art. no. 3695. doi: <https://doi.org/10.3390/en13143695>.
29. Guo K., Cui L., Mao M., Zhou L., Zhang Q. An Improved Gray Wolf Optimizer MPPT Algorithm for PV System With BFBIC Converter Under Partial Shading. *IEEE Access*, 2020, vol. 8, pp. 103476-103490. doi: <https://doi.org/10.1109/ACCESS.2020.2999311>.
30. Eltamaly A.M., Al-Saud M.S., Abo-Khalil A.G. Performance Improvement of PV Systems' Maximum Power Point Tracker Based on a Scanning PSO Particle Strategy. *Sustainability*, 2020, vol. 12, no. 3, art. no. 1185. doi: <https://doi.org/10.3390/su12031185>.
31. Zhao S., Zhang T., Cai L., Yang R. Triangulation topology aggregation optimizer: A novel mathematics-based meta-heuristic algorithm for continuous optimization and engineering applications. *Expert Systems with Applications*, 2024, vol. 238, art. no. 121744. doi: <https://doi.org/10.1016/j.eswa.2023.121744>.

Received 06.01.2025
Accepted 04.04.2025
Published 02.09.2025

A. Jeridi ¹, PhD,
M.H. Moulahi ¹, Associate Professor,
H. Khaterchi ¹, PhD,
A. Zaafour ¹, Professor of Electrical Engineering,
¹ University of Tunis, Higher National Engineering School of Tunis,
Industrial Systems Engineering and Renewable Energies Research
Laboratory, Tunisia,
e-mail: ahmed.jeridi@ensit.u-tunis.tn (Corresponding Author);
mohamedheddia.moulahi@isetn.mu.tn;
hechmi.khaterchi@uvt.tn;
abdou.zaaaf@ensit.rnu.tn

How to cite this article:

Jeridi A., Moulahi M.H., Khaterchi H., Zaafour A. Maximum power point tracking improving of photovoltaic systems based on hybrid triangulation topology aggregation optimizer and incremental conductance algorithm. *Electrical Engineering & Electromechanics*, 2025, no. 5, pp. 17-26. doi: <https://doi.org/10.20998/2074-272X.2025.5.03>

B.I. Kuznetsov, T.B. Nikitina, I.V. Bovdii, K.V. Chunikhin, V.V. Kolomiets, B.B. Kobylanskyi

Optimization of combined active-passive electromagnetic shielding system for overhead power lines magnetic field normalization in residential building space

Problem. Normalization of overhead power lines magnetic field level in residential building. **Goal.** Normalization of overhead power line magnetic field by optimization of combined electromagnetic shielding system, consisting of active and passive parts, in residential building space based on magnetic field three-dimensional model. **Methodology.** Optimization of combined electromagnetic shielding system for initial magnetic field three-dimensional model solved based on multi-criteria two-player antagonistic game solution. Game payoff vector calculated based on finite element calculations system COMSOL Multiphysics package. Game solution calculated based on particles multiswarm optimization algorithms. **Results.** The results of theoretical and experimental studies of combined electromagnetic passive and active shielding system for magnetic field three-dimensional model in residential building from two-circuit overhead power transmission line with wires «Barrel» type arrangement presented. **Scientific novelty.** For the first time the method for normalization of overhead power lines magnetic field in residential building space based on optimization of combined active-passive electromagnetic shielding system for magnetic field three-dimensional model developed. **Practical value.** Spatial location coordinates of shielding winding, currents and phases in shielding winding of robust active shielding system, geometric dimensions and thickness of electromagnetic passive shield calculated during optimization of combined electromagnetic shielding system for magnetic field three-dimensional model. References 49, figures 13.

Key words: overhead power line, magnetic field, combined electromagnetic active and passive shielding system, computer simulation, experimental research.

Проблема. Нормалізація рівня магнітного поля повітряних ліній електропередачі в житлових будинках. **Мета.** Нормалізація рівня магнітного поля повітряних ліній електропередачі шляхом оптимізації комбінованої електромагнітної екрануючої системи, що складається з активної та пасивної частин, у просторі житлових приміщень на основі тривимірної моделі магнітного поля. **Методологія.** Оптимізація комбінованої електромагнітної екрануючої системи тривимірної моделі вихідного магнітного поля розраховується на основі рішення багатокритеріальної антагоністичної гри двох гравців. Вектор виграшів гри розраховується на основі кінцево-елементної системи обчислень COMSOL Multiphysics. Рішення гри розраховується на основі алгоритмів оптимізації мультироїв частинок. **Результати.** Наведено результати теоретичних та експериментальних досліджень комбінованої електромагнітної системи пасивного та активного екранування тривимірної моделі магнітного поля в житловому будинку від доволанцюгової повітряної лінії електропередач із розташуванням проводів типу «бочка». **Наукова новизна.** Вперше розроблено метод нормалізації магнітного поля повітряних ліній електропередачі в житловому приміщенні на основі оптимізації комбінованої активно-пасивної системи електромагнітного екранування тривимірної моделі магнітного поля. **Практична значимість.** Координати розташування екрануючих обмоток, струм і фаза в екрануючих обмотках робастної системи активного екранування, та геометричні розміри і товщина електромагнітного пасивного екрану розраховуються при оптимізації комбінованих електромагнітних екрануючих систем тривимірної моделі магнітного поля. Бібл. 49, рис. 13.

Ключові слова: повітряна лінія електропередачі, магнітне поле, комбінована електромагнітна активна та пасивна система екранування, комп'ютерне моделювання, експериментальні дослідження.

Introduction. Many residential buildings in Ukraine are located in close proximity to overhead power lines. Induction level in such houses is many times higher than modern standards for industrial frequency magnetic induction level for safe living [1–3].

Most often, single-circuit power lines with a triangular arrangement of wires located near single-story old buildings. Double-circuit power lines with a «Barrel» type of wire arrangement also often located near single-story and multi-story residential buildings of old construction, as shown in Fig. 1.



Fig. 1. A multi-storeys residential building located near a double-circuit power line

One of most economically justified approaches to further operation of high-grade residential buildings without eviction of population or replacement of existing overhead power lines with underground cable power lines used of original magnetic field modeling and shielding to safe level for habitation [4–7].

To implement necessary shielding factor of initial magnetic field, it is necessary to use active shielding [8–18]. To increase the effectiveness of shielding, especially in long-distance residential buildings, it is advisable to use combined shielding of the initial magnetic field, including active and passive shielding [19].

The diagram of such combined electromagnetic active-passive shielding system shown in Fig. 2.

The active shielding system contains shielding windings, amplifier, control system and a magnetic field sensor installed inside the shielding space. An external power source used to power the active shielding system.

This magnetic field sensor, which installed inside the shielding space, measured resulting magnetic field generated by power line and combined electromagnetic active-passive shielding system inside shielding space.

The source of energy for passive shielding system is the external electromagnetic field acting on the passive electromagnetic shield. This external magnetic field for

the passive shield generated by power transmission line wires and compensation windings of electromagnetic active shielding system. Under the influence of this primary magnetic field, currents induced in the passive electromagnetic shield, which create a secondary magnetic field. This secondary magnetic field directed opposite to the original primary field.

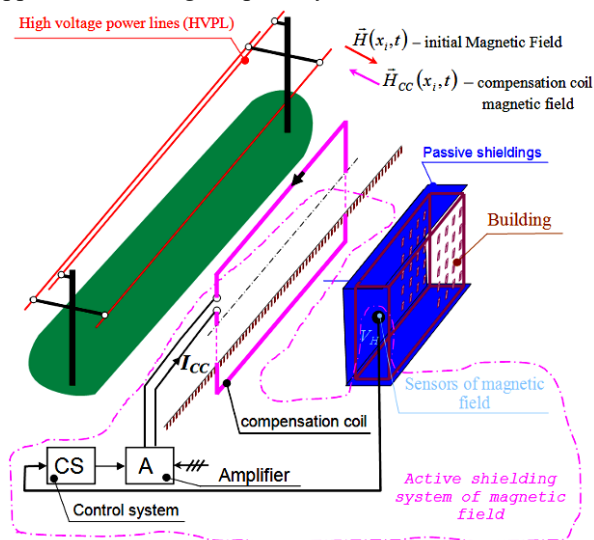


Fig. 2. Combined electromagnetic active-passive shielding system diagram

The resulting magnetic field, which is equal to the sum of the primary magnetic field generated by power transmission line wires and compensation windings, and the secondary magnetic field generated by the passive screen, will be less than the initial magnetic field. Due to this reduction in the resulting magnetic field, the shielding effect of the combined active-passive electromagnetic shielding system achieved.

Note that since the active and passive shielding systems influence each other, when optimizing the combined active-passive electromagnetic shielding system, it is necessary simultaneously optimize both the parameters of the active and the parameters of the passive electromagnetic system to achieve the minimum resulting magnetic field in the shielding space.

Often, to increase the efficiency of shielding the original magnetic field using such hybrid electromagnetic active-passive shielding system, the active shielding system designed as a system with two degrees of freedom. In this case, two closed and open control loops used simultaneously. To implement open-loop control, another magnetic field sensor used to measure the initial magnetic field, which installed outside the shielding space. This magnetic field sensor usually installed away from the shielding space but close to power transmission line wires in order to reduce the influence of compensation winding currents of active shielding system.

When designing electromagnetic shielding systems, two geometric problems of magnetostatic's solved [12, 13]. First, a geometric forward problem of magnetostatics solved when, for given values and geometric arrangement of sources of industrial frequency magnetic field, the magnetic field induction calculated at given points of the shielding space. This geometric forward problem calculated effect from magnetic field source of a given power and located in a given «geometric» position at points in the shielding space.

The geometric inverse problem of magnetostatics calculate the power and «geometric» position of industrial frequency magnetic field sources that generate a given magnetic field at given points in the shielding space. Thus, in the course of solving a geometric inverse problem, it is necessary to calculate not the result, but the cause that leads to a given result. Naturally, a geometric inverse problem is an uncorrected problem and can have many solutions. As a rule, solving a geometric inverse problem reduced to solving an optimization problem [20–23].

The work [19] considered issues of synthesis of systems for combined magnetic field shielding in a two-dimensional formulation. In this case, shielding is assumed in the central section of residential buildings.

However, when magnetic field shielding in residential buildings, it is necessary to reduce magnetic field induction level to a safe level in apartments located at edges of house.

Most studies carried out based on two-dimensional magnetic field model, which does not allow studying effectiveness decrease of original field shielding in residential building edges [8–18]. This determines the formulation and solution of problem of design of combined electromagnetic active-passive shielding system in three-dimensional formulation.

The goal of the work is normalization of overhead power line magnetic field by optimization of combined electromagnetic shielding system, consisting of active and passive parts, in residential building space based on magnetic field three-dimensional model.

Definition of geometric forward magnetostatic problem for overhead power lines and compensating winding magnetic field. Geometric forward magnetostatic problem calculates the consequence – the magnetic field at a given point in space, generated by a given source of magnetic field located at a given «geometric» point in space. This problem is solved on basis of Maxwell's law is a mathematically correct problem and calculated exactly.

Geometric forward magnetostatic problem for overhead power lines and compensating winding magnetic field is to calculate magnetic field at any point in space for given magnetic field sources. Mathematical modeling of magnetic field reduced to boundary value problem solution for electromagnetic field with a known distribution of its sources in the volume or on the surface of the given area [4–6]. To correctly solve this problem, it is necessary, first of all, to choose a physical model of this process, which covers its main aspects. Physical model should be one of Maxwell equations full system simplifications. Maxwell equations describing electromagnetic fields in media with continuous or piecewise-continuously changing properties are the basis for analytical and numerical modeling of any electromagnetic processes, both in vacuum and in material media [7].

To simplify high-voltage power transmission lines magnetic field mathematical mode, the phase's wires taken in infinite long form and thin straight conductors, which allows two-dimensional magnetic field model used which contains two spatial components along axes and does not depend on coordinate along which power line wires conductors located. However, in this task, controlled windings vertical sections of active shielding system create significant projections of magnetic field intensity vector, which constitute, along coordinate, which determines

three-dimensional magnetic field model used. Such model, in addition, also allows take into account magnetic field intensity vector component along coordinate, created by power lines due to their sagging between supports.

When calculating current magnetic field quasi-static approximation of Maxwell equations system [4–7] is equivalent to Biot-Savart's law, which can be written in form [4]:

$$\mathbf{B}(P) = \frac{\mu_0 I_m}{4\pi} \int_L \frac{[d\mathbf{l} \times \mathbf{R}]}{R^3}, \quad (1)$$

where $\mathbf{B}(P)$ – magnetic field induction at observation point P ; $d\mathbf{l}$ – circuit element with current I_m ; \mathbf{R} – vector directed from contour element $d\mathbf{l}$ to observation point P .

Definition of forward quasi-static magnetic field active shielding system design problem. Let us consider definition of forward quasi-static magnetic field active shielding system design problem. Forward magnetic field active shielding system design problem calculated magnetic field induction generated by the compensation windings in shielding space given point for given compensation windings spatial location coordinates of active shielding system.

First, consider geometric direct problem solution for power lines – mathematical model design of initial magnetic field generated by power transmission line. Power lines wires position initially known. Power lines wires instantaneous values currents set in dependences sinusoidal form. We set amplitudes A_i and phases φ_i of industrial frequency currents of power line wires. Let's set power transmission lines wire currents in complex form

$$I_i(t) = A_i \exp j(\omega t + \varphi_i). \quad (2)$$

Then, based on relation (1), initial magnetic field induction $\mathbf{B}_0(P, I_0(t), t)$ at point P created by power transmission lines currents calculated in following form

$$\mathbf{B}_0(P, I_0(t), t) = \sum_{l=1}^L \mathbf{B}_{0l}(P, I_l(t)). \quad (3)$$

Power line currents vector $I_0(t)$ introduced components of which are power line wires currents

$$I_0(t) = \{I_l(t)\}.$$

Note that when transmission line resulting magnetic field calculating according to (1) for 3D modeling, it is necessary to take into account the real sagging of transmission line wires, and elementary sections number of transmission line conductors at ends of considered sections of transmission lines must be determined from required accuracy of resulting magnetic field induction calculation, which generated by all power lines at given point in shielding space.

Let us now consider forward problem solution for calculating magnetic field generated by compensation windings at shielding space points. Let us set compensating windings location coordinates of active shielding system in form of initial geometric values vector of compensating windings dimensions of active protection, as well as amplitude A_i and phase φ_i of compensating windings currents [12–14]. Let's set compensating windings currents in complex form

$$I_{ai}(t) = A_{ai} \exp j(\omega t + \varphi_{wi}). \quad (4)$$

Then, based on (1) similar to (3) magnetic field induction at point P_i created by windings currents at time moment t calculated in the following form

$$\mathbf{B}_y(P_i, I_y(t), t) = \sum_{m=1}^M \mathbf{B}_{ym}(P_i, I_{ym}(t), t), \quad (5)$$

here currents vector $I_y(t)$ in compensating windings introduced with windings currents components

$$I_y(t) = \{I_{ym}(t)\}.$$

Note that when calculating resulting magnetic field generated by all compensating windings wires, according to formula (5), for 3D modeling, it is necessary to take into account not only real dimensions of horizontal parts of compensating windings, but also real length of compensating windings, since it is near ends of horizontal sections of compensating windings that greatest change in magnetic field induction level generated by compensating windings is observed.

Naturally, that in 3D modeling in (5) it is necessary to take into account vertical parts of compensating windings, since it is these vertical parts that generate main part of the of the magnetic field induction level.

Then, based on superposition principle, the resulting magnetic field induction vector $\mathbf{B}(P_i, I_0(t), I_y(t), t)$ at the point P_i , created by power line wires currents (1) and controlling windings currents (5), is equal to vectors sum [4]

$$\mathbf{B}(P_i, I_0(t), I_y(t), t) = \mathbf{B}_0(P_i, I_0(t), t) + \dots + \mathbf{B}_y(P_i, I_y(t), t). \quad (6)$$

Definition of forward dynamic problem of magnetic field active shielding system design. The calculation of the magnetic field generated by the transmission line wires and compensation windings calculated based on the Biot-Savart's law [4–7]. In this case, the magnetic field induction is a static dependence (1) on the current of the transmission line wires or compensation windings. Thus, the magnetic field is practically «instantaneously» generated by currents and the speed of propagation of the electromagnetic field of industrial frequency is neglected.

However, the active shielding system is a dynamic system, the processes in which are commensurate with the industrial frequency. Moreover, the design of the active shielding system performed taking into account the dynamic characteristics of its elements - the presence of inductances of compensating windings, the presence of time delay of magnetic field sensors and other. In the active shielding system with two degrees of freedom, open-loop control by disturbance and closed-loop control by deviation with the help of feedback used simultaneously.

The forward problem of dynamic magnetic field active shielding system is the calculation of the dynamic characteristics of the active shielding system with two degrees of freedom for the given values of the parameters of the open-loop and closed-loop control regulators and for the given values of the parameters of the disturbing effects and interference measurements of the sensors of the initial and resulting magnetic field, with the help of which the open-loop and closed-loop control is implemented. This forward dynamics problem of an active shielding system is a correct mathematical problem and solved «exactly», for example, by direct modeling of processes in such a dynamic system with two degrees of freedom.

The inverse dynamics problem of an active shielding system consists in calculating the values of the parameters of the open-loop and closed-loop control regulators for the given values of the parameters of the disturbing effects and the interference of the measurements of

magnetic field sensors of initial and resulting magnetic field for implementation of specified dynamic characteristics in designed system. The solution of the inverse problem of the dynamics of an active shielding system reduced to an optimization problem.

In this case, the open and closed control channel regulators synthesized from the condition of minimizing the error of compensation of the initial magnetic field, caused by the disturbing effect in the form of induction of the initial magnetic field. In this case, with the help of these same open and closed control regulators, the noise of the magnetic field sensors measuring the initial magnetic field and the resulting magnetic field in the shielding space filtered.

The inverse dynamics problem of active shielding system is an uncorrected mathematical problem, and its solution is also found approximately by numerical methods. One of the possible approaches to solving the inverse problem of dynamics for active shielding system with two degrees of freedom control used of robust optimal control based on four Riccati equations solutions [24–26]. To implement such robust optimal control, robust optimal Kalman's filters used, which also synthesized based on four Riccati equations solutions [26–28].

Such a robust optimal solution to the inverse dynamics problem for active shielding system with two degrees of freedom control allows obtained the highest accuracy of the active shielding system; however, the implementation of such a system presents certain difficulties. Therefore, the overwhelming majority of industrial control systems built on the principle of subordinate regulation and implemented using standard PID controllers.

Let us accept the structure of the active shielding system as two-loop subordinate control system. The internal loop of such a system is the current control loop of the compensation winding. With the help of the PI controller of the current loop, the «large» time constant of the current loop, caused by the inductance of the compensation winding, compensated. The external loop of this two-loop subordinate control system is the loop for regulating the induction of the resulting magnetic field.

A delay link used to form open-loop control for active shielding system with two degrees of freedom control over the initial magnetic field. The magnitude of the gain and delay coefficients experimentally adjusted during the system setup from the condition of minimizing the space-time characteristic of the resulting magnetic field in the shielding space.

Let us consider definition of forward magnetic field active shielding dynamic system design problem. Forward dynamic magnetic field active shielding system design problem calculated magnetic field induction generated by the compensation windings in shielding space given point not for given compensation windings spatial location coordinates but and for given structure and parameters of active shielding system regulators as closed loop and open loop dynamic system [20–23]. This dynamic active shielding system is two degrees of freedom dynamic system. This dynamic system combines both open loop and closed-loop control. However, in contrast to classical synthesis of robust control system with two degrees of freedom, in the developed method, the synthesis of open-loop coarse control performed based on quasi-static model of magnetic field. Synthesis of closed-loop refinement control carried out based on closed system dynamics

equations, taking into account plant models and measuring equations devices, disturbances and measurement noise.

First, consider the possible structures of dynamic magnetic field active shielding system design problem. If it is possible to measure the of the power line wires current of three-phase power lines or directly measure magnetic field induction near power line wires, then can design open loop system of dynamic magnetic field active shielding system as follows.

Initial magnetic field model in considered space can be taken in form of magnetic field generated by three, six, and etc. conductors of three-phase current of industrial frequency, located in known position relative to considered space, in which it is necessary shielded magnetic field.

To design open loop control circuit of magnetic field active shielding system sufficient measured current wires current line one phase and used some reference voltage

$$u_u(t) = A_u \sin(\omega t + \varphi_u). \quad (7)$$

Based on measured wires current line as reference voltage, we will form open loop control by compensation windings current at following form

$$u_i(t) = A_i \sin(\omega t + \varphi_i) + f_{ui}, \quad (8)$$

where A_i – the sought amplitudes and φ_i – control phases in the i -th compensation windings current with respect to the measured current in the phase of the current line or reference voltage; f_{ui} – equivalent noise of current or reference voltage measurement.

It is advisable to supplement such open loop control circuit with feedback control circuit, so that the active shielding system becomes two degrees of freedom dynamic system one based on control principle.

To design closed loop control by active shielding system, it is necessary to have magnetic field induction measuring devices – magnetometers installed at certain points in space to measure resulting magnetic field induction created by both power line wires current and compensation windings current of active shielding system. Let's form a vector $\mathbf{y}(t)$ of measured components of resulting magnetic field induction vector at some points P_j

$$\mathbf{v}(t) = \{ \mathbf{B}_0(P_j, \mathbf{I}_0(t), t) + \mathbf{B}_y(P_j, \mathbf{I}_y(t), t) \} \quad (9)$$

at time moment t at magnetometers installation points P_j in following form

$$\mathbf{y}(t) = \mathbf{v}(t) + \mathbf{w}(t), \quad (10)$$

where $\mathbf{w}(t)$ – magnetometer noise vector.

Note that when using combined shielding resulting magnetic field, simultaneously generated by power line wires, compensation windings wires of active shielding system and passive shield, measured by magnetometer installed in shielding space point [19].

Let's take structure of closed loop control by active shielding system of magnetic field in following form: we will apply corresponding magnetometer output voltage to each channel PID controller input.

Let's write down state differential equation of discrete PID regulators, the input of which is vector $\mathbf{y}(t)$ of measured magnetic field induction components, and output is closed-loop control vector $\mathbf{u}_3(t)$ of compensation windings wires in the following form

$$\mathbf{x}_p(t+1) = A_p \mathbf{x}_p(t) + B_p \mathbf{y}(t); \quad (11)$$

$$\mathbf{u}_3(t) = C_p \mathbf{x}_p(t) + D_p \mathbf{y}(t), \quad (12)$$

in which elements of matrices A_p, B_p, C_p, D_p calculated by PID regulators parameters.

Then design of two degrees of freedom dynamic system of active shielding of magnetic field, which includes open and closed control loops reduced to calculated regulators parameters vector, components of which are sought elements of matrices A_p , B_p , C_p , D_p , determined by closed control channels PID regulators gain coefficients, as well as vector of sought amplitudes $A = \{A_i\}$ and phases $\varphi = \{\varphi_i\}$ of compensation windings wires currents, components of which are amplitudes A_i and currents φ_i of components of compensation windings wires currents open loop control regulators [24–26].

Definition of geometric forward magnetostatic problem for passive electromagnetic shielding magnetic field. Let us now consider geometric forward problem of magnetostatics for a continuous electromagnetic passive shield. The geometric forward problem for a passive electromagnetic shield also calculates the consequence – the magnetic field at a given point in space, generated by a given source of magnetic field in form of passive shield, located at a given «geometric» point in space. This problem is also solved on basis of Maxwell's law and is mathematically correct problem and calculated exactly [4–7].

The principle of operation of a passive electromagnetic shield based on action of the initial primary magnetic field, as a result of which conduction currents induced in the passive screen. These currents create a secondary magnetic field, which, according to Faraday's law, directed opposite to the initial magnetic field. The resulting magnetic field, equal to the sum of the primary and secondary fields, is weaker than the primary field in the protected area, due to which the initial magnetic field shielded.

The general approach to solving magnetic field shielding problems using a passive electromagnetic shield also comes down to integrating Maxwell's equations in all areas: both inside the shield volume and in the external environment. When considering the problems of shielding industrial frequency magnetic field, Maxwell's equations solved in a quasi-stationary approximation. In the numerical solution, the space divided into simply connected dielectric regions, the boundaries of which are conducting shells. The finite element method has received the greatest distribution for numerical study of electromagnetic field.

The numerical procedure reduced to compiling and solving a system of linear equations. The computational domain divided into a set of polygons, which in the simplest case have triangular cells. The geometric inverse problem of magnetostatics for electromagnetic passive shield calculated not only «geometric» position of passive screen, but also the thickness and conductivity characteristics of the passive screen. Naturally, geometric inverse problem of magnetostatics for electromagnetic passive shield is an uncorrected problem and can have many solutions. As a rule, the solution of this geometric inverse problem also comes down to solving an optimization problem and solved approximately.

Definition of geometric inverse magnetostatic problem for magnetic field combined electromagnetic silence design. Geometric inverse magnetostatic problem calculates the cause – the magnitude of source of initial magnetic field and coordinates of «geometric» location of this source at a given «geometric» point in space in such a way as to realize the effect – a given magnetic field at a given point in space. Naturally, this problem is a mathematically uncorrected problem and can have many solutions. The same given magnetic field at a given point

in space can be realized using different sources of the initial magnetic field and these sources can be located at different «geometric» points in space. This problem is always solved approximately, as a rule, based on the solution of the optimization problem.

In fact, geometric inverse problem is the problem of approximating a given distribution of a magnetic field using a finite number of sought sources of a magnetic field, so that the approximation problem is parameterized in the form of power values and coordinates of the «geometric» location of the sought sources of a magnetic field.

Geometric inverse magnetostatics problem for combined electromagnetic shielding system design problem calculated spatial location and parameters of magnetic field sources to generate compensating magnetic field directed opposite to original magnetic field [20–22]. Initial magnetic field generated by power line wires and the compensating magnetic field simultaneously generated by compensating windings of active shielding system and continuous passive shield.

Consider geometrical inverse problem of magnetostatics for task of designing a combined electromagnetic screen, which consists in calculating the spatial location and parameters of magnetic field sources to generate a compensating magnetic field directed opposite to initial magnetic field [27–32]. At the same time, initial magnetic field generated by power line wires, and compensating magnetic field simultaneously generated by compensating windings of active shielding system and solid passive shield.

Consider desired parameters vector X for design of combined shielding system, components of which are geometric dimensions values vector X_a of compensating windings, as well as currents A_{oi} and phases φ_{oi} in compensating windings: as well as geometric dimensions vector X_p , thickness and material of passive shield [33–35]. In addition, we also include in desired parameters vector X sought elements of matrices A_p , B_p , C_p , D_p , determined by closed control channels PID regulators gain coefficients [36, 37].

Then, for given initial values of sought parameters vector X and uncertainty parameters vector δ of combined shielding system designing task resulting magnetic field induction effective value $B_R(X, \delta, P_i)$ at shielding space point Q_i calculated, based on finite element calculation system of COMSOL Multiphysics [38–41]. Then combined shielding system designing task reduced to vector game solution calculating

$$B_R(X, \delta) = \langle B_R(X, \delta, P_i) \rangle. \quad (13)$$

Game payoff vector components $B_R(X, \delta, P_i)$ are effective values of resulting magnetic field induction at all given points P_i of shielding space. In this vector game, it is necessary to calculated payoff vector game minimum along vector X , but same payoff vector game maximum along the vector δ [42–44].

At the same time, it is necessary to take into account restrictions on desired parameters vector X of combined shielding system in form of vector inequality and, possibly, vector equality.

$$G(X) \leq G_{\max}, \quad H(X) = 0. \quad (14)$$

Solving problem algorithm. Components of the vector game (13) and vector constraints (14) are nonlinear functions of required parameters vector X and calculated based on finite element system of COMSOL Multiphysics.

Consider *method of solving formulated problem*. Local minimum task calculation at one point of considered space is, as a rule, multi-extreme, containing local minima and maxima, therefore, it is advisable to use stochastic multi-agent optimization algorithms for its solution. Consider calculation algorithm for Pareto-optimal solutions set of multi-criteria nonlinear programming problems based on stochastic multi-agent optimization [45]. Particle swarm optimization algorithms – PSO algorithms have been developed based on collective intelligence idea of particle swarm, such as gbest PSO and lbest PSO algorithms.

Stochastic multi-agent optimization methods application for multi-criteria problems solving causes certain difficulties and this direction continues to develop intensively. To solve original multi-criteria problem of nonlinear programming with constraints stochastic multi-agent optimization algorithm design based on particle swarms set, which number is equal to vector optimization criterion components number [46].

To increase global solution calculation speed stochastic multi-agent optimization nonlinear algorithms used, in which particle i swarm j movement described by following expressions [47]

$$\begin{aligned} v_{ij}(t+1) &= w_j v_{ij}(t) + c_{1j} r_{1j}(t) H(p_{1j} - \varepsilon_{1j}(t)) \times \dots \\ &\dots \times [v_{ij}(t) - x_{ij}(t)] + c_{2j} r_{2j}(t) H(p_{2j} - \varepsilon_{2j}(t)) \times \dots \quad (15) \\ &\dots \times [v_j^*(t) - x_{ij}(t)] \end{aligned}$$

$$x_{ij}(t+1) = x_{ij}(t) + v_{ij}(t+1), \quad (16)$$

where position $x_{ij}(t)$ and speed $v_{ij}(t)$ of particle i swarm j .

To global solution calculation of initial multi-criteria problem, individual swarms exchanged information among themselves during local criteria optimal solutions calculation [48]. Information about global optimum calculated by another swarm particles used to particles movement speed calculated of one swarm, which allows all potential Pareto-optimal solutions identified.

At each step t particle i swarm j movement of local solutions advantages functions calculated by all swarms used. Solution $X_j^*(t)$ calculated during objective function $B(X(t), P_j)$ optimization by swarm j is better in relation to solution $X_k^*(t)$ calculated during objective function $B(X(t), P_k)$ optimization by swarm k , i.e. $X_j^*(t) > X_k^*(t)$, if condition fulfilled

$$\max_{i=1,m} B(P_i, X_j^*(t)) < \max_{i=1,m} B(P_i, X_k^*(t)). \quad (17)$$

Global solution $X_k^*(t)$ calculated by swarm k used as global optimal solution $X_j^*(t)$ for swarm k , which is better in relation to global solution $X_k^*(t)$ by swarm k based on preference relationship (17).

Simulation results. Let us consider the results of calculations of resulting magnetic field in the designed combined electromagnetic combined shielding system during 3D modeling. The initial magnetic field generated by «Barrel» type double-circuit power line with wires currents $I = 26.79$ A. As result of designing combined electromagnetic shield for this power line, coordinates of two compensation windings location of active shielding

system, as well as currents magnitudes and phases in these windings, were calculated. Figure 3 shows diagram of power line wires arrangement, residential building and two compensation windings.

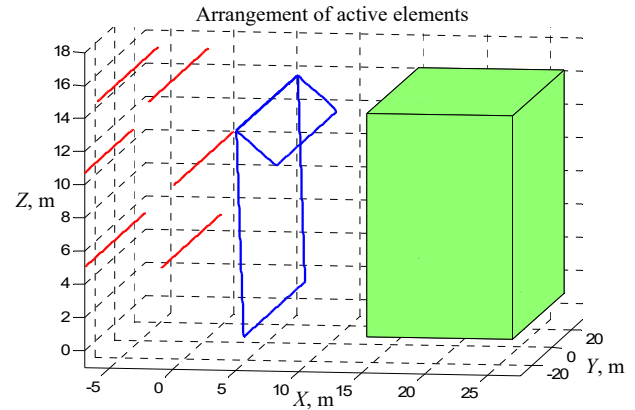


Fig. 3. Layout of power lines, residential buildings and two compensation windings

First, let's look results of 3D modeling of resulting magnetic field when combined shield operates without side plates. Figure 4 shows distribution of resulting magnetic field induction along passive screen length for various coordinates along passive shield height.

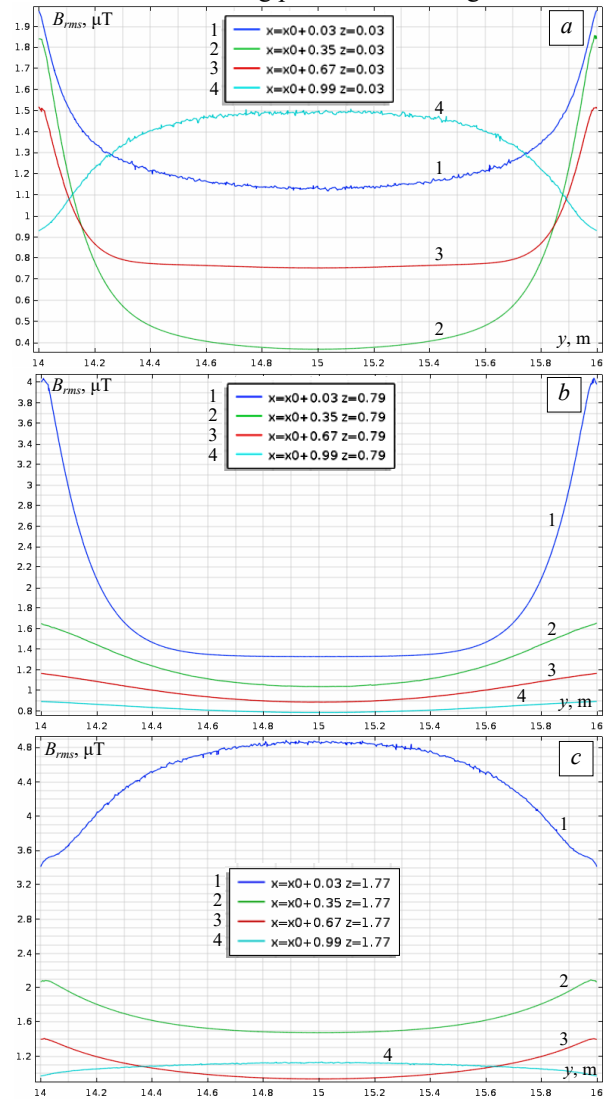


Fig. 4. Resulting magnetic field induction distribution along passive shield length

As follows from Fig. 4, *a* initial magnetic field is most effectively shield at 0.3 m height and a width of 0.35 m at center of passive shield length so that resulting magnetic field induction is 0.4 μT . At the same time, along edges of passive screen length, induction level of resulting magnetic field further increases by 4.6 times and amounts to 1.85 μT .

When approaching passive shield width to 0.03 m distance resulting magnetic induction level field increases by 2.8 times and amounts to 1.12 μT . This occurs due to an increase resulting magnetic field induction level near passive screen. At the same time, along edges of passive shield length resulting magnetic field induction level further increases by 1.7 times and amounts to 2 μT .

When moving away from passive shield by 0.99 m distance in width resulting magnetic field induction level also increases by 3.75 times and amounts to 1.5 μT . However, at passive shield length edges resulting magnetic field induction level decreases by 1.57 times and amounts to 0.92 μT .

As follows from Fig. 4, *c* highest value of resulting magnetic field induction level of 4.8 μT observed near passive shield at 0.03 m distance and at 1.17 m height. Firstly, at this height highest value of initial magnetic field induction is 2.55 μT , and, secondly, near passive screen there is an increase in initial magnetic field induction level by 1.88 times.

However, at passive screen length edges resulting magnetic field induction level decreases by 1.41 times and amounts to 3.4 μT .

Let us now consider calculations results of magnetic field generated by a double-circuit power line of the «Barrel» type with wires currents $I = 26.79$ A for combined screen in which of the passive screen side surfaces are covered with aluminum sheets.

Figure 5 shows resulting magnetic field induction distribution along the length of passive screen with side plates for various coordinates along height and width of passive screen.

Comparison resulting magnetic field induction distributions with side surfaces combined shield (Fig. 5) and without side surfaces (Fig. 4) shown that resulting magnetic field induction levels in central subsection of passive shield for these combined shield are almost the same.

However, at passive shield length edges when using side plates induction level is slightly lower. So, for example, for section at 0.3 m height and 0.35 m width at passive shield length center, where initial magnetic field is screened most effectively so that of the resulting magnetic field induction is 0.4 μT for both combination shield types.

Moreover, for combined shield without side surfaces along passive shield length edges resulting magnetic field induction level increases by 4.6 times and amounts to 1.85 μT , and when using side surfaces resulting magnetic field induction level increases only by 3.87 times and amounts to 1.55 μT .

Combined shield experimental setup. To conduct experimental studies experimental setup of combined shielding system under consideration developed. All experimental studies carried out on the magnetodynamic measuring stand at the Anatolii Pidhornyi Institute of Power Machines and Systems of the National Academy of Sciences of Ukraine [49].

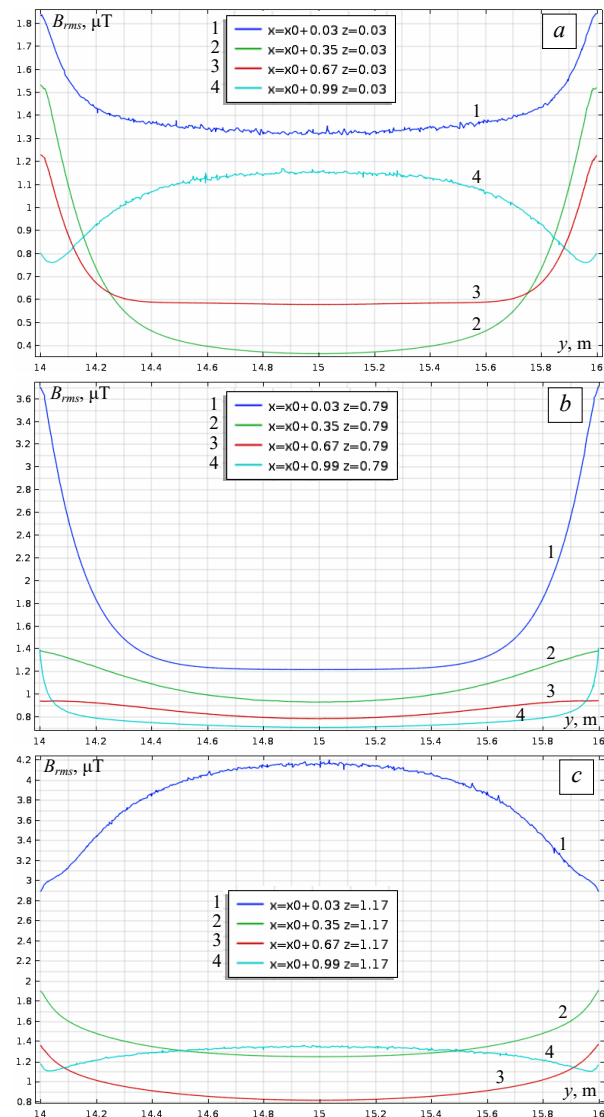


Fig. 5. Resulting magnetic field induction distribution along passive shield length with side plates

The experimental setup contains setup of double-circuit power line with six wires «Barrel» arrangement, two compensation windings of active shielding system and electromagnetic passive shield made of solid aluminum.

To conduct experimental studies of a combined shielding system, in which the side surfaces of the passive shield are open experimental setup was developed (Fig. 6).



Fig. 6. Passive shield without side plates

Two magnetic field sensors installed inside passive screen to implement two closed-loop control loops for two compensation windings of active shielding system with feedback on resulting magnetic field.

During process of adjusting control loops axes of these sensors set in such a way as to measure magnetic field induction maximum value generated by compensation winding of corresponding compensating channel. This installation of magnetic field sensors axes makes it possible to minimize the influence of channels on each other when they work together.

Two more magnetic field sensors are also installed inside passive shield, axes of which directed parallel to coordinate axes. These two sensors used in system for measuring space-time characteristics of resulting magnetic field. This measuring system used to adjust control loops of active shielding system of combined magnetic field shielding.

To power compensation windings power amplifiers used (Fig. 7).

In Fig. 8 shown combined shielding control system. To measure resulting magnetic field inside shielding space three-coordinate magnetometer type «TES 1394S triaxial ELF magnetic field meter» used with shown in Fig. 9.

This magnetometer measures three components of magnetic field induction vector using three orthogonal measuring coils (Fig. 10). Axes of these three measuring coils are orthogonal to each other and form an orthogonal coordinate system for measuring magnetic field.



Fig. 7. Power amplifiers for powering compensation windings



Fig. 8. Combination screen control system

To conduct experimental studies of combined shield, in which the side surfaces of the passive shield are covered with aluminum sheets experimental setup was developed (Fig. 11).



Fig. 9. Three-coordinate magnetometer for measuring resulting magnetic field

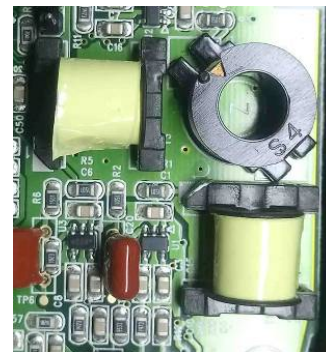


Fig. 10. Measuring coils of triaxial magnetometer



Fig. 11. Experimental installation of passive shield with side plates

Experimental studies results. Let us now consider experimental studies of resulting magnetic field distributions with combined electromagnetic shield consisting of two compensation windings of active shield and electromagnetic continuous passive shield.

First, let us consider experimental studies results of resulting magnetic field when operating combined shield without side plates. Figure 12 shows experimentally measured distributions of magnetic field induction along passive shield length for various coordinates along height and width of passive shield.

By analogy with calculations results of resulting magnetic field induction shown in Fig. 4,*a*, as follows from Fig. 10,*a* initial magnetic field is most effectively shield at 0.3 m height and 0.35 m width at passive shield length center so that resulting magnetic field induction is 0.27 μT .

At the same time, along passive shield length edges resulting magnetic field induction level increases by 2.59 times and amounts to 0.7 μT .

When passive shield width approaching to 0.03 m distance resulting magnetic field induction level increases by 1.22 times and amounts to 0.33 μT . This occurs due to an increase in resulting magnetic field induction level near passive shield.

At the same time, along passive shield length edges resulting magnetic field induction level further increases by 2.12 times and amounts to 0.7 μT . When moving away from passive shield by 0.99 m distance in width resulting magnetic field induction level also increases by 2.59 times and amounts to 0.7 μT . However, at passive shield length resulting magnetic field induction level decreases edges by 1.57 times and amounts to 0.455 μT .

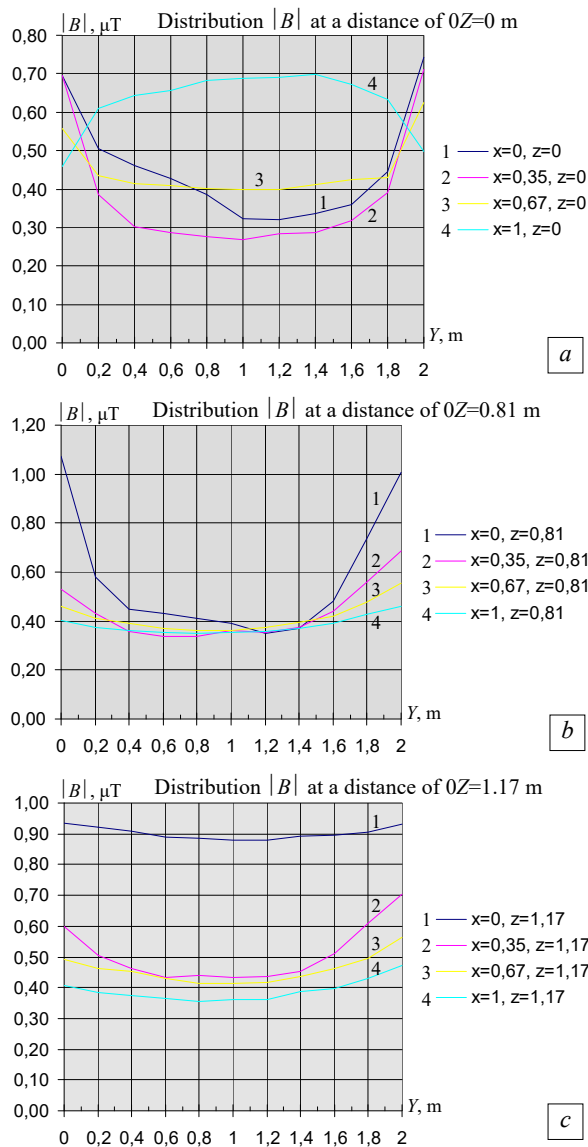


Fig. 12. Experimentally measured distributions of magnetic field induction of passive shield without side plates

As follows from Fig. 12,c resulting magnetic field induction level highest value of $0.88 \mu\text{T}$ observed near passive shield at 0.03 m distance and at 1.17 m height. Firstly, at this height initial magnetic field induction level is highest and, secondly, near passive shield initial magnetic field induction level increase observed.

However, at passive screen length edges resulting magnetic field induction level increases by 1.05 times and amounts to $0.93 \mu\text{T}$.

Thus, magnetic field induction distribution change nature experimentally measured on combined shielding system installation corresponds to calculated values of resulting magnetic field induction distribution during operation of combined shield.

Let us now consider experimental measurements results of magnetic field induction on experimental installation of combined shield, in which passive shield side surfaces covered by aluminum sheets. Figure 13 shows experimentally measured distribution of resulting magnetic field induction level on experimental installation of combined shield, in which passive shield side surfaces covered by aluminum sheets.

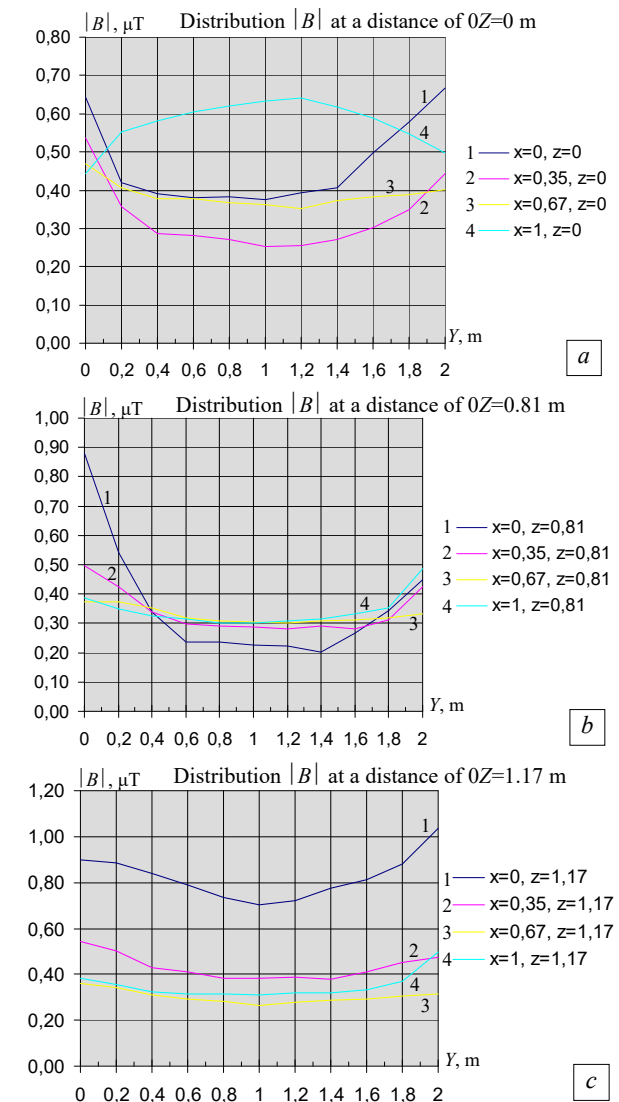


Fig. 13. Experimentally measured distributions of magnetic field induction along passive shield length with side plates

Comparison of experimentally measured distributions of resulting magnetic field induction with combined shield without side surfaces (Fig. 12) and with the side surfaces (Fig. 13) shows that resulting magnetic field induction levels in passive shield central section for these combined shield are almost the same.

However, at passive shield length edges when using side plates induction level is slightly lower. So, for example, for 0.3 m height section and for 0.35 m width at passive shield length center, where initial magnetic field is screened most effectively so that the experimentally measured resulting magnetic field induction is $0.27 \mu\text{T}$ for combination shield both types.

Moreover, for a combined shield without side surfaces along of passive shield length edges, resulting magnetic field induction level increases by 2.59 times and amounts to $0.7 \mu\text{T}$, and when using side surfaces resulting magnetic field induction level increases only by 2.4 times and amounts to $0.65 \mu\text{T}$.

Conclusions.

1. For the first time the method for normalization of overhead power lines magnetic field in residential building space based on optimization of combined active-passive electromagnetic shielding system for magnetic field three-dimensional model developed.

2. Optimization of combined electromagnetic shielding system for initial magnetic field three-dimensional model solved based on multi-criteria two-player antagonistic game solution. Game payoff vector calculated based on finite element calculations system COMSOL Multiphysics package. Game solution calculated based on particles multiswarm optimization algorithms.

3. During optimization of combined electromagnetic shielding system for magnetic field three-dimensional model Spatial location coordinates of shielding winding, currents and phases in shielding winding of robust active shielding system, geometric dimensions and thickness of electromagnetic passive shield calculated.

4. The results of theoretical and experimental studies of normalization for overhead power lines magnetic field by combined electromagnetic passive and active shielding system for magnetic field three-dimensional model in residential building from two-circuit overhead power transmission line with wires «Barrel» type arrangement presented. In the future, it is necessary to implement such combined electromagnetic passive and active shielding systems to normalize the field in real residential building.

Acknowledgments. The authors express their gratitude to PhD, Senior Research Scientist Tkachenko O.O., Engineers Sokol A.V. and Shevchenko A.P. of the Department of Magnetism of Technical Objects of Anatolii Pidhornyi Institute of Power Machines and Systems of the National Academy of Sciences of Ukraine for your help in designing and experimental testing of combined electromagnetic shielding system.

Conflict of interest. The authors declare that they have no conflicts of interest.

REFERENCES

1. Sung H., Ferlay J., Siegel R.L., Laversanne M., Soerjomataram I., Jemal A., Bray F. Global Cancer Statistics 2020: GLOBOCAN Estimates of Incidence and Mortality Worldwide for 36 Cancers in 185 Countries. *CA: A Cancer Journal for Clinicians*, 2021, vol. 71, no. 3, pp. 209-249. doi: <https://doi.org/10.3322/caac.21660>.
2. Directive 2013/35/EU of the European Parliament and of the Council of 26 June 2013 on the minimum health and safety requirements regarding the exposure of workers to the risks arising from physical agents (electromagnetic fields). Available at: <http://data.europa.eu/eli/dir/2013/35/oj> (Accessed 20 February 2025).
3. The International EMF Project. *Radiation & Environmental Health Protection of the Human Environment* World Health Organization. Geneva, Switzerland, 1996. 2 p. Available at: <https://www.who.int/initiatives/the-international-emf-project> (Accessed 20 February 2025).
4. Rozov V., Grinchenko V., Tkachenko O., Yerisov A. Analytical Calculation of Magnetic Field Shielding Factor for Cable Line with Two-Point Bonded Shields. *2018 IEEE 17th International Conference on Mathematical Methods in Electromagnetic Theory (MMET)*, 2018, pp. 358-361. doi: <https://doi.org/10.1109/MMET.2018.8460425>.
5. Rozov V.Y., Pelevin D.Y., Kundius K.D. Simulation of the magnetic field in residential buildings with built-in substations based on a two-phase multi-dipole model of a three-phase current conductor. *Electrical Engineering & Electromechanics*, 2023, no. 5, pp. 87-93. doi: <https://doi.org/10.20998/2074-272X.2023.5.13>.
6. Rozov V.Y., Zavalnyi A.V., Zolotov S.M., Gretsikh S.V. The normalization methods of the static geomagnetic field inside houses. *Electrical Engineering & Electromechanics*, 2015, no. 2, pp. 35-40. doi: <https://doi.org/10.20998/2074-272X.2015.2.07>.
7. Rozov V.Yu., Reutsky S.Yu., Pelevin D.Ye., Kundius K.D. Approximate method for calculating the magnetic field of 330-750 kV high-voltage power line in maintenance area under voltage. *Electrical Engineering & Electromechanics*, 2022, no. 5, pp. 71-77. doi: <https://doi.org/10.20998/2074-272X.2022.5.12>.
8. Salceanu A., Paulet M., Alistar B.D., Asimincesei O. Upon the contribution of image currents on the magnetic fields generated by overhead power lines. *2019 International Conference on Electromechanical and Energy Systems (SIEMEN)*. 2019. doi: <https://doi.org/10.1109/siemen.2019.8905880>.
9. Del Pino Lopez J.C., Romero P.C. Influence of different types of magnetic shields on the thermal behavior and ampacity of underground power cables. *IEEE Transactions on Power Delivery*, Oct. 2011, vol. 26, no. 4, pp. 2659-2667. doi: <https://doi.org/10.1109/tpwrd.2011.2158593>.
10. Hasan G.T., Mutlaq A.H., Ali K.J. The Influence of the Mixed Electric Line Poles on the Distribution of Magnetic Field. *Indonesian Journal of Electrical Engineering and Informatics (IJEI)*, 2022, vol. 10, no. 2, pp. 292-301. doi: <https://doi.org/10.52549/ije.i.v10i2.3572>.
11. Victoria Mary S., Pugazhendhi Sugumaran C. Investigation on magneto-thermal-structural coupled field effect of nano coated 230 kV busbar. *Physica Scripta*, 2020, vol. 95, no. 4, art. no. 045703. doi: <https://doi.org/10.1088/1402-4896/ab6524>.
12. Ippolito L., Siano P. Using multi-objective optimal power flow for reducing magnetic fields from power lines. *Electric Power Systems Research*, 2004, vol. 68, no. 2, pp. 93-101. doi: [https://doi.org/10.1016/S0378-7796\(03\)00151-2](https://doi.org/10.1016/S0378-7796(03)00151-2).
13. Barsali S., Giglioli R., Poli D. Active shielding of overhead line magnetic field: Design and applications. *Electric Power Systems Research*, May 2014, vol. 110, pp. 55-63. doi: <https://doi.org/10.1016/j.epsr.2014.01.005>.
14. Bavastro D., Canova A., Freschi F., Giaccone L., Manca M. Magnetic field mitigation at power frequency: design principles and case studies. *IEEE Transactions on Industry Applications*, May 2015, vol. 51, no. 3, pp. 2009-2016. doi: <https://doi.org/10.1109/tia.2014.2369813>.
15. Beltran H., Fuster V., García M. Magnetic field reduction screening system for a magnetic field source used in industrial applications. *9 Congreso Hispano Luso de Ingeniería Eléctrica (9 CHLIE)*, Marbella (Málaga, Spain), 2005, pp. 84-99.
16. Bravo-Rodríguez J., Del-Pino-López J., Cruz-Romero P. A Survey on Optimization Techniques Applied to Magnetic Field Mitigation in Power Systems. *Energies*, 2019, vol. 12, no. 7, art. no. 1332. doi: <https://doi.org/10.3390/en12071332>.
17. Canova A., del-Pino-López J.C., Giaccone L., Manca M. Active Shielding System for ELF Magnetic Fields. *IEEE Transactions on Magnetics*, March 2015, vol. 51, no. 3, pp. 1-4. doi: <https://doi.org/10.1109/tmag.2014.2354515>.
18. Canova A., Giaccone L. Real-time optimization of active loops for the magnetic field minimization. *International Journal of Applied Electromagnetics and Mechanics*, Feb. 2018, vol. 56, pp. 97-106. doi: <https://doi.org/10.3233/jae-172286>.
19. Canova A., Giaccone L., Cirimele V. Active and passive shield for aerial power lines. *Proc. of the 25th International Conference on Electricity Distribution (CIRED 2019)*, 3-6 June 2019, Madrid, Spain. Paper no. 1096.
20. Canova A., Giaccone L. High-performance magnetic shielding solution for extremely low frequency (ELF) sources. *CIRED - Open Access Proceedings Journal*, Oct. 2017, vol. 2017, no. 1, pp. 686-690. doi: <https://doi.org/10.1049/oap-cired.2017.1029>.
21. Celozzi S. Active compensation and partial shields for the power-frequency magnetic field reduction. *2002 IEEE International Symposium on Electromagnetic Compatibility*, Minneapolis, MN, USA, 2002, vol. 1, pp. 222-226. doi: <https://doi.org/10.1109/isemc.2002.1032478>.
22. Celozzi S., Garzia F. Active shielding for power-frequency magnetic field reduction using genetic algorithms optimization. *IEE Proceedings - Science, Measurement and Technology*, 2004, vol. 151, no. 1, pp. 2-7. doi: <https://doi.org/10.1049/ip-smt:20040002>.
23. Celozzi S., Garzia F. Magnetic field reduction by means of active shielding techniques. *WIT Transactions on Biomedicine and Health*, 2003, vol. 7, pp. 79-89. doi: <https://doi.org/10.2495/ehf030091>.
24. Martynenko G. Analytical Method of the Analysis of Electromagnetic Circuits of Active Magnetic Bearings for Searching Energy and Forces Taking into Account Control Law. *2020 IEEE KhPI Week on Advanced Technology (KhPIWeek)*, 2020, pp. 86-91. doi: <https://doi.org/10.1109/KhPIWeek51551.2020.9250138>.
25. Popov A., Tserne E., Volosyuk V., Zhyla S., Pavlikov V., Ruzhentsev N., Dergachov K., Havrylenko O., Shmatko O., Averyanova Y., Ostroumov I., Kuzmenko N., Sushchenko O., Zaliskyi M., Solomentsev O., Kuznetsov B., Nikitina T. Invariant Polarization Signatures for Recognition of Hydrometeors by Airborne Weather Radars. *Computational Science and Its Applications - ICCSA 2023. Lecture Notes in Computer Science*, 2023, vol. 13956, pp. 201-217. doi: https://doi.org/10.1007/978-3-031-36805-9_14.

26. Sushchenko O., Averyanova Y., Ostroumov I., Kuzmenko N., Zaliskiy M., Solomentsev O., Kuznetsov B., Nikitina T., Havrylenko O., Popov A., Volosyuk V., Shmatko O., Ruzhentsev N., Zhyla S., Pavlikov V., Dergachov K., Tserne E. Algorithms for Design of Robust Stabilization Systems. *Computational Science and Its Applications – ICCSA 2022. ICCSA 2022. Lecture Notes in Computer Science*, 2022, vol. 13375, pp. 198-213. doi: https://doi.org/10.1007/978-3-031-10522-7_15.
27. Ostroverkhov M., Chumack V., Monakhov E., Ponomarev A. Hybrid Excited Synchronous Generator for Microhydropower Unit. *2019 IEEE 6th International Conference on Energy Smart Systems (ESS)*, Kyiv, Ukraine, 2019, pp. 219-222. doi: <https://doi.org/10.1109/ess.2019.8764202>.
28. Ostroverkhov M., Chumack V., Monakhov E. Output Voltage Stabilization Process Simulation in Generator with Hybrid Excitation at Variable Drive Speed. *2019 IEEE 2nd Ukraine Conference on Electrical and Computer Engineering (UKRCON)*, Lviv, Ukraine, 2019, pp. 310-313. doi: <https://doi.org/10.1109/ukrcon.2019.8879781>.
29. Tytiuk V., Chorny O., Baranovskaya M., Serhiienko S., Zachepa I., Tsvirkun L., Kuznetsov V., Tryputen N. Synthesis of a fractional-order PI^aD^b -controller for a closed system of switched reluctance motor control. *Eastern-European Journal of Enterprise Technologies*, 2019, no. 2 (98), pp. 35-42. doi: <https://doi.org/10.15587/1729-4061.2019.160946>.
30. Chorny O., Serhiienko S. A virtual complex with the parametric adjustment to electromechanical system parameters. *Technical Electrodynamics*, 2019, no. 1, pp. 38-41. doi: <https://doi.org/10.15407/teched.2019.01.038>.
31. Shchur I., Kasha L., Bukavyn M. Efficiency Evaluation of Single and Modular Cascade Machines Operation in Electric Vehicle. *2020 IEEE 15th International Conference on Advanced Trends in Radioelectronics, Telecommunications and Computer Engineering (TCSET)*, Lviv-Slavske, Ukraine, 2020, pp. 156-161. doi: <https://doi.org/10.1109/tcset49122.2020.235413>.
32. Shchur I., Turkovskiy V. Comparative Study of Brushless DC Motor Drives with Different Configurations of Modular Multilevel Cascaded Converters. *2020 IEEE 15th International Conference on Advanced Trends in Radioelectronics, Telecommunications and Computer Engineering (TCSET)*, Lviv-Slavske, Ukraine, 2020, pp. 447-451. doi: <https://doi.org/10.1109/tcset49122.2020.235473>.
33. Volosyuk V., Zhyla S., Pavlikov V., Ruzhentsev N., Tserne E., Popov A., Shmatko O., Dergachov K., Havrylenko O., Ostroumov I., Kuzmenko N., Sushchenko O., Averyanova Yu., Zaliskiy M., Solomentsev O., Kuznetsov B., Nikitina T. Optimal Method for Polarization Selection of Stationary Objects Against the Background of the Earth's Surface. *International Journal of Electronics and Telecommunications*, 2022, vol. 68, no. 1, pp. 83-89. doi: <https://doi.org/10.24425/ijet.2022.139852>.
34. Halchenko V., Trembovetska R., Bazilo C., Tychkova N. Computer Simulation of the Process of Profiles Measuring of Objects Electrophysical Parameters by Surface Eddy Current Probes. *Lecture Notes on Data Engineering and Communications Technologies*, 2023, vol. 178, pp. 411-424. doi: https://doi.org/10.1007/978-3-031-35467-0_25.
35. Halchenko V., Bacherikov D., Filimonov S., Filimonova N. Improvement of a Linear Screw Piezo Motor Design for Use in Accurate Liquid Dosing Assembly. *Smart Technologies in Urban Engineering. STUE 2022. Lecture Notes in Networks and Systems*, 2023, vol. 536, pp. 237-247. doi: https://doi.org/10.1007/978-3-031-20141-7_22.
36. Chystiak P., Chorny O., Zhautikov B. Remote control of electromechanical systems based on computer simulators. *Proceedings of the International Conference on Modern Electrical and Energy Systems, MEES 2017* (2017), 2018. – January, pp. 364-367. doi: <https://doi.org/10.1109/MEES.2017.8248934>.
37. Zagimyak M., Bisikalo O., Chorna O., Chorny O. A Model of the Assessment of an Induction Motor Condition and Operation Life, Based on the Measurement of the External Magnetic Field. *2018 IEEE 3rd International Conference on Intelligent Energy and Power Systems (IEPS)*, Kharkiv, 2018, pp. 316-321. doi: <https://doi.org/10.1109/ieps.2018.8559564>.
38. Maksymenko-Sheiko K.V., Sheiko T.I., Lisin D.O., Petrenko N.D. Mathematical and Computer Modeling of the Forms of Multi-Zone Fuel Elements with Plates. *Journal of Mechanical Engineering*, 2022, vol. 25, no. 4, pp. 32-38. doi: <https://doi.org/10.15407/pmach2022.04.032>.
39. Hontarovskiy P.P., Smetankina N.V., Ugrimov S.V., Garmash N.H., Melezhyk I.I. Computational Studies of the Thermal Stress State of Multilayer Glazing with Electric Heating. *Journal of Mechanical Engineering*, 2022, vol. 25, no. 1, pp. 14-21. doi: <https://doi.org/10.15407/pmach2022.02.014>.
40. Kostikov A.O., Zevin L.I., Krol H.H., Vorontsova A.L. The Optimal Correcting the Power Value of a Nuclear Power Plant Power Unit Reactor in the Event of Equipment Failures. *Journal of Mechanical Engineering*, 2022, vol. 25, no. 3, pp. 40-45. doi: <https://doi.org/10.15407/pmach2022.03.040>.
41. Rusanov A.V., Subotin V.H., Khoryev O.M., Bykov Y.A., Korotaiev P.O., Ahibalov Y.S. Effect of 3D Shape of Pump-Turbine Runner Blade on Flow Characteristics in Turbine Mode. *Journal of Mechanical Engineering*, 2022, vol. 25, no. 4, pp. 6-14. doi: <https://doi.org/10.15407/pmach2022.04.006>.
42. Kurenov S., Smetankina N., Pavlikov V., Dvoretzskaya D., Radchenko V. Mathematical Model of the Stress State of the Antenna Radome Joint with the Load-Bearing Edging of the Skin Cutout. *Lecture Notes in Networks and Systems*, 2022, vol. 305, pp. 287-295. doi: https://doi.org/10.1007/978-3-030-83368-8_28.
43. Kurenov S., Smetankina N. Stress-Strain State of a Double Lap Joint of Circular Form. Axisymmetric Model. *Lecture Notes in Networks and Systems*, 2022, vol. 367 LNNS, pp. 36-46. doi: https://doi.org/10.1007/978-3-030-94259-5_4.
44. Smetankina N., Merkulova A., Merkulov D., Misiura S., Misiura I. Modelling Thermal Stresses in Laminated Aircraft Elements of a Complex Form with Account of Heat Sources. *Lecture Notes in Networks and Systems*, 2023, vol. 534 LNNS, pp. 233-246. doi: https://doi.org/10.1007/978-3-031-15944-2_22.
45. Ummels M. *Stochastic Multiplayer Games Theory and Algorithms*. Amsterdam University Press, 2010. 174 p.
46. Ray T., Liew K.M. A Swarm Metaphor for Multiobjective Design Optimization. *Engineering Optimization*, 2002, vol. 34, no. 2, pp. 141-153. doi: <https://doi.org/10.1080/03052150210915>.
47. Xiaohui Hu, Eberhart R.C., Yuhui Shi. Particle swarm with extended memory for multiobjective optimization. *Proceedings of the 2003 IEEE Swarm Intelligence Symposium. SIS'03* (Cat. No.03EX706), Indianapolis, IN, USA, 2003, pp. 193-197. doi: <https://doi.org/10.1109/sis.2003.1202267>.
48. Hashim F.A., Hussain K., Houssein E.H., Mabrouk M.S., Al-Atabany W. Archimedes optimization algorithm: a new metaheuristic algorithm for solving optimization problems. *Applied Intelligence*, 2021, vol. 51, no. 3, pp. 1531-1551. doi: <https://doi.org/10.1007/s10489-020-01893-z>.
49. Baranov M.I., Rozov V.Y., Sokol Y.I. To the 100th anniversary of the National Academy of Sciences of Ukraine – the cradle of domestic science and technology. *Electrical Engineering & Electromechanics*, 2018, no. 5, pp. 3-11. doi: <https://doi.org/10.20998/2074-272X.2018.5.01>.

Received 20.02.2025
Accepted 09.04.2025
Published 02.09.2025

B.I. Kuznetsov¹, Doctor of Technical Science, Professor,
T.B. Nikitina², Doctor of Technical Science, Professor,
I.V. Bovdii¹, PhD, Senior Research Scientist,
K.V. Chunikhin¹, PhD, Senior Research Scientist,
V.V. Kolomiets², PhD, Assistant Professor,
B.B. Kobylanskyi², PhD, Assistant Professor
¹ Anatolii Pidhornyi Institute of Power Machines and Systems of the National Academy of Sciences of Ukraine,
2/10, Komunalnykiv Str., Kharkiv, 61046, Ukraine,
e-mail: kuznetsov.boris.i@gmail.com (Corresponding Author)
² Bakhmut Education Research and Professional Pedagogical Institute V.N. Karazin Kharkiv National University,
9a, Nosakov Str., Bakhmut, Donetsk Region, 84511, Ukraine.

How to cite this article:

Kuznetsov B.I., Nikitina T.B., Bovdii I.V., Chunikhin K.V., Kolomiets V.V., Kobylanskyi B.B. Optimization of combined active-passive electromagnetic shielding system for overhead power lines magnetic field normalization in residential building space. *Electrical Engineering & Electromechanics*, 2025, no. 5, pp. 27-37. doi: <https://doi.org/10.20998/2074-272X.2025.5.04>

F. Mehedi, I. Bouyakoub, A. Yousfi, R. Taleb, Z. Reguieg

Improve of the direct torque control strategy applied to a multi-phase interior permanent magnet synchronous motor using a super twisting sliding mode algorithm

Introduction. Conventional direct torque control (DTC) is a superior control strategy for managing the torque of a five-phase interior permanent magnet synchronous motor (FP-IPMSM). Nevertheless, the DTC's switching frequency results in large flux and torque ripples, which produce acoustic noise and impair control performance. On the other hand, the DTC scheme's performance when using conventional PI controllers results in high flux and torque ripples, which decreases the system's robustness. **Goal.** This work aims to use a modern variable structure control of the DTC scheme based on a super twisting algorithm in order to ensure efficient control of multiphase machine, reduce flux and torque ripples, minimize tracking error, and increase robustness against possible disturbances. **Scientific novelty.** We propose to use super-twisting sliding mode control (STSMC) methods of the DTC based on the space vector modulation (SVM) algorithm of the multiphase motor. **Methodology.** In order to achieve a decoupled control with higher performance and to ensure stability while handling parameter changes and external disturbances, a STSMC algorithm on the DTC technique incorporating the SVM algorithm was implemented in place of the switch table and PI controller. **Results.** The suggested STSMC-DTC based SVM approach outperforms the conventional DTC methods in achieving the finest performance in controlling the FP-IPMSM drive. **Practical value.** The merits of the proposed DTC technique of FP-IPMSM are demonstrated through various tests. The suggested STSMC-DTC approach reduces flux and torque ripples by roughly 50 % and 60 %, respectively, in comparison to the conventional DTC strategy. Furthermore, the proposed technique of FP-IPMSM control method is made to provide robust performance even when machine parameters change. References 24, table 2, figures 8.

Key words: direct torque control, flux and torque ripples, robustness, multi-phase interior permanent magnet synchronous motor, super twisting sliding mode algorithm.

Вступ. Традиційне пряме управління моментом (DTC) є чудовою стратегією управління крутним моментом п'ятифазного синхронного двигуна з внутрішніми постійними магнітами (FP-IPMSM). Однак, частота перемикання при DTC призводить до великих пульсацій потоку та моменту, які створюють акустичний шум та погіршують характеристики керування. З іншого боку, ефективність схеми DTC при використанні традиційних ПІ-регуляторів призводить до великих пульсацій потоку та моменту, що знижує надійність системи. **Мета.** Робота спрямована на використання сучасного управління змінною структурою схеми DTC, заснованої на алгоритмі суперскручування, для забезпечення ефективного управління багатофазною машиною, зменшення пульсацій потоку та моменту, мінімізації помилки стеження та підвищення стійкості до можливих перешкод. **Наукова новизна.** Запропоновано використовувати методи керування ковзним режимом суперскручування (STSMC) з DTC, засновані на алгоритмі просторово-векторної модуляції (SVM) багатофазного двигуна. **Методологія.** Для досягнення розв'язаного управління з більш високою продуктивністю та забезпечення стабільності при обробці змін параметрів та зовнішніх збурень, було реалізовано алгоритм STSMC на основі DTC, що включає алгоритм SVM, замість таблиці перемикання та ПІ-регулятора. **Результати.** Запропонований STSMC-DTC підхід на основі SVM перевершує традиційні DTC методи у досягненні найкращої продуктивності при керуванні приводом FP-IPMSM. **Практична цінність.** Переваги запропонованого DTC методу для FP-IPMSM продемонстровані в ході різних випробувань. Запропонований підхід STSMC-DTC знижує пульсації потоку і крутного моменту приблизно на 50 % і 60 % відповідно в порівнянні з традиційною DTC стратегією. Крім того, запропонований метод керування FP-IPMSM розроблений для забезпечення надійної роботи навіть за зміни параметрів машини. Бібл. 24, табл. 2, рис. 8.

Ключові слова: пряме управління крутним моментом, пульсації потоку та крутного моменту, надійність, багатофазний синхронний двигун з внутрішніми постійними магнітами, алгоритм ковзного режиму суперскручування.

Introduction. Many electrical energy sources are being transformed into mechanical energy through the use of electric motors. The numerous benefits of interior permanent magnet synchronous motors (IPMSM), such as their exceptional efficiency, low operating noise, and high power density, have led to their widespread use in a variety of applications [1–4]. A prolonged flux weakening region is another benefit of IPMSM, along with their strong rotor and reluctance torque, which are essential in high-speed applications [5, 6].

Compared to three-phase systems, multiphase systems offer a number of benefits, such as improved performance, robustness, reduced torque pulsations, high output power rating, and steady speed response [7, 8]. Multiphase machines have attracted interest in a number of application areas where high dependability is required, such as robotics, energy conversion, ship propulsion, pump drives, and multi-machine systems [9, 10].

Several works that make use of the latest technological advancements have addressed the drawbacks of conventional technical approaches. Among them, the following innovative technologies are listed: artificial neural networks (ANNs), adaptive backstepping controller, sliding mode controller (SMC), fuzzy logic, super-twisting sliding mode control (STSMC), high-order sliding mode control, ANFIS algorithm, genetic algorithms and synergetic control.

When compared to the traditional direct torque control (DTC) switching method, the DTC with PI regulator has become more and more popular in polyphase motors due to its higher efficiency.

In the conventional DTC approach uses 2 hysteresis controllers and lookup tables to control rotor flux and torque. Compared to the V/f technique and field oriented control, DTC features a more robust algorithm and a simpler structure [11]. In [12], the ANN with DTC has been introduced to reduce the torque and flux ripples of the five-phase interior permanent magnet synchronous motor (FP-IPMSM). In [13], the authors designed a master-slave virtual vector duty cycle assignment with an enhanced DTC technique of the dual 3-phase PMSM. It has been experimentally confirmed that the suggested technique improves both dynamic and steady-state performance by reducing the phase current total harmonic distortion (THD), significantly reducing the content of the 5th and 7th current harmonics and effectively suppressing torque and flux ripples. In [14], to choose the optimal voltage vector that may greatly reduce the torque ripple, a unique sequential approach combined with a duty ratio optimization technique. The suggested approach can successfully lower the THD and the ripple in both dynamic and steady-state torque, according to experimental data. Due to the parametric sensitivity that a

© F. Mehedi, I. Bouyakoub, A. Yousfi, R. Taleb, Z. Reguieg

In order to provide robust control, a unique method for FP-PMSM is proposed in this section. The developed method, known as super-twisting sliding mode control (STSMC), effectively addresses the primary shortcomings of the standard SMC technique as documented in the literature for uncertain systems. The following is the selection of the sliding surfaces based on (1) and (4):

The suggested second-order SMC is composed of 2 parts and is predicated on the super twisting technique that Levant originally introduced in [15]:

$$\text{with } \begin{cases} \dot{v}_1 = -K_1 \text{sign}(S(\Phi_s)); \\ v_2 = -l_1 |S(\Phi_s)|^\gamma \text{sign}(S(\Phi_s)); \end{cases} \quad (14)$$

$$\text{with } \begin{cases} \dot{w}_1 = -K_2 \text{sign}(S(T_{em})); \\ w_2 = -l_2 |S(T_{em})|^\gamma \text{sign}(S(T_{em})); \end{cases} \quad (16)$$

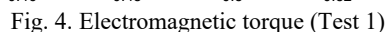
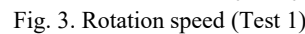
$$\text{with } \begin{cases} \dot{z}_1 = -K_3 \text{sign}(S(\omega_r)); \\ z_2 = -l_3 |S(\omega_r)|^\gamma \text{sign}(S(\omega_r)). \end{cases} \quad (18)$$

$$\begin{cases} k_j > \frac{\lambda_j}{k_{mj}}, & l_j^2 \geq \frac{4\lambda_j}{K_{mj}^2} \frac{K_{mj}(k_j + \lambda_j)}{K_{mj}(k_j - \lambda_j)}; \\ 0 < \gamma \leq 0.5; & j = 1, 2, 3. \end{cases} \quad (19)$$
[illegible]

Results and discussion. In MATLAB/Simulink numerical simulations have been carried out to validate strategies created for a DTC scheme employing the STSMC-based SVM algorithm of the FP-IPMSM. The machine's parameters are as follows: $f = 50$ Hz, $p = 2$, $J_m = 0.004$ kg/m², $\varphi_f = 0.2$ Wb, $L_d = 8.5$ mH, $L_q = 8.5$ mH, $R_s = 0.67$ Ω [24]. The conventional DTC and STSMC-DTC with SVM approaches will be examined and contrasted in 2 different tests – tracking performance and robustness.

Test 1. The reference tracking test is the initial test. The objective is to determine which approach yields superior reference tracking outcomes under the influence of load torque T_r variation. Additionally, in terms of torque ripple value and flux. At initialization, the FP-IPMSM's reference speed is set to 125 rad/s. The rotor speed rises to 50 rad/s at $t = 0.2$ s. A nominal $T_r = 10$ N·m was applied at $t = [0.4, 0.6]$ s, and at $t = 0.8$ s, a consign inversion -50 rad/s was performed.

The results of the rotation speed simulation are shown in Fig. 3. In contrast to the second-order SMC-DTC strategy, which maintains its reference speed within an excellent range, the conventional DTC showed a speed decline from 50 rad/s to 36 rad/s at the instant $t = 0.4$ s while applying T_r . Figure 4 displays the torque T_{em} simulation results. The second-order SMC-DTC strategy minimizes torque oscillations in comparison to the conventional DTC method, where the T_{em} ripple values reached 3 N·m using the proposed technique and 7.5 N·m using the conventional technique (Table 2).



The stator flux was improved using the proposed technique (Fig. 5) with very low ripple (7 mWb) when compared with the conventional DTC method (14 mWb).

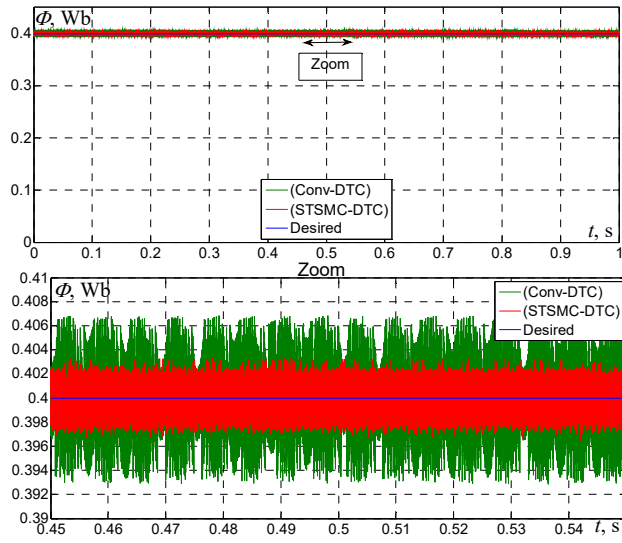


Fig. 5. Stator flux (Test 1)

Table 2

The comparative analysis of the various techniques

Parameter	Conventional DTC	STSMC-DTC
ω_r response time	0.1 s	0.02 s
Torque ripple	6.3–13.8 (7.5 N·m)	8.6–11.6 (3 N·m)
ω_r dropping due to T_r application	36 rad/s	43 rad/s
Flux ripple	0.393–0.407 Wb (0.014 Wb)	0.3965–0.4035 Wb (0.007 Wb)

As can be observed, the second-order SMC-DTC strategy has a better dynamic response for speed, torque and flux when compared to the conventional DTC technique, suggesting that the second-order SMC controller was less sensitive to load disturbance.

Test 2. The robustness test is the second test. The stator resistance R_s and machine's moment of inertia J_m values from the 1st test are multiplied by 2 in this test. The values for the L_q and L_d are reduced by 20 %. Simulation results are presented in Fig. 6–8.

Figure 6 indicates that the conventional DTC speed responses are more impacted by changes in machine's parameters than the STSMC-DTC for the FP-IPMSM. It is also observed that the speed is overshoot at the start as well as when the speed is reduced to 50 rad/s ($t = 0.2$ s), unlike the STSMC-DTC strategy for the FP-IPMSM results where the speed continues to follow the reference without overshoot.

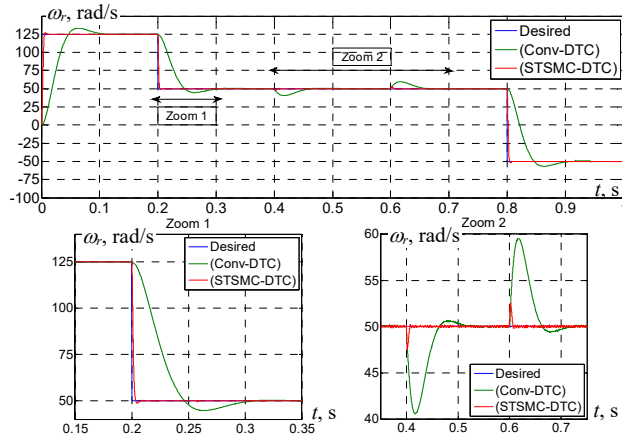


Fig. 6. Rotation speed (Test 2)

The torque T_{em} and stator flux utilizing the conventional DTC, where the torque ripple values reached 11.4 N·m, are clearly impacted by these changes in machine parameters (Fig. 7). Figure 8 shows that the flux ripple values reached 22 mWb for conventional DTC.

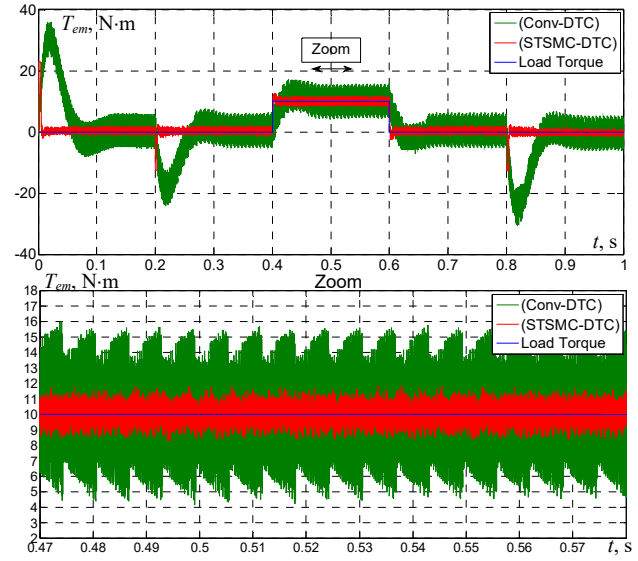


Fig. 7. Electromagnetic torque (Test 2)

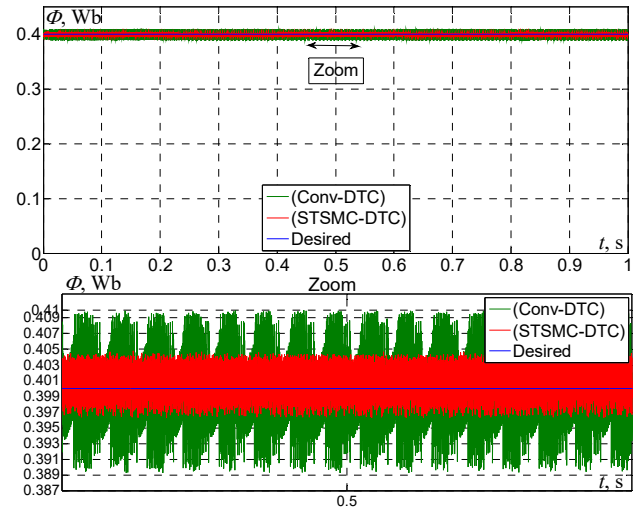


Fig. 8. Stator flux (Test 2)

Conclusions. In this research we proposed a novel method for the DTC scheme applied to the FP-IPMSM drive. We improved the control and the behavior of the FP-IPMSM by controlling the speed, torque, and stator flux using the STSMC technique with SVM approach. A comparison between the conventional DTC and the suggested STSMC-DTC based on SVM is presented where the modification goal was reduce some of the drawbacks of conventional DTC such as flux and torque ripples overshoot, rise time, and decrease in both robustness against changes in machine parameters, stability, and dynamic response.

The following are the main findings:

- A new STSMC-DTC based on SVM technique of the FP-IPMSM was proposed and designed.
- The proposed STSMC-DTC technique is much more robust compared to the conventional DTC technique.
- Minimization of ripples for flux and torque has been shown in two different tests – tracking performance and robustness. The proposed STSMC-DTC-SVM method

lowers torque ripple $\approx 60\%$ and flux ripple $\approx 50\%$ when compared to the conventional DTC method.

The STSMC-DTC-SVM technique will be experimentally implemented and validated in the future work.

Conflict of interest. The authors declare that they have no conflicts of interest.

REFERENCES

- Guo S., Su X., Zhao H. Optimal Design of an Interior Permanent Magnet Synchronous Motor for Electric Vehicle Applications Using a Machine Learning-Based Surrogate Model. *Energies*, 2024, no. 17, pp. 3864. doi: <https://doi.org/10.3390/en17163864>.
- Patel A.N., Doshi P.J., Mahagoakar S.C., Panchal T.H. Optimization of cogging torque in interior permanent magnet synchronous motor using optimum magnet v-angle. *Electrical Engineering & Electromechanics*, 2023, no. 6, pp. 16-20. <https://doi.org/10.20998/2074-272X.2023.6.03>.
- Xu Y., Chen Y., Fu Z., Xu M., Liu H., Cheng L. Design and Analysis of an Interior Permanent Magnet Synchronous Motor for a Traction Drive Using Multiobjective Optimization. *International Transactions on Electrical Energy Systems*, 2024, no. 1, pp. 1-15. doi: <https://doi.org/10.1155/2024/3631384>.
- Duc H.B., Minh D.B., Thanh B.D., Minh T.B., Quoc V.D. Improving Performances of Interior Permanent Magnet Synchronous Motors by Using Different Rotor Angles. *Journal Européen des Systèmes Automatisés*, 2023, vol. 56, no. 1, pp. 115-120. doi: <https://doi.org/10.18280/jesa.560115>.
- Cao L., Zuo Y., Xie S., Hoang C.C., Han B.S., Lee C.H. Comparative study of permanent-magnet Vernier motor and interior permanent-magnet motor for hybrid electric vehicles. *IEEE Transactions on Industry Applications*, 2023, vol. 59, no. 6, pp. 6601-6614. doi: <https://doi.org/10.1109/tia.2023.3292813>.
- Zhao X., Kou B., Huang C., Zhang L. A reverse-salient permanent magnet synchronous motor for electric vehicles considering operating conditions. *IEEE Transactions on Energy Conversion*, 2023, vol. 38, no. 1, pp. 262-272. doi: <https://doi.org/10.1109/tec.2022.3213571>.
- Chaabane H., Khodja D.E., Chakroune S., Hadji D. Model reference adaptive backstepping control of double star induction machine with extended Kalman sensorless control. *Electrical Engineering & Electromechanics*, 2022, no. 4, pp. 3-11. doi: <https://doi.org/10.20998/2074-272X.2022.4.01>.
- Mehedi F., Bouyakoub I., Yousfi A., Reguieg Z. Enhanced Control Technique Based on Fuzzy Logic Algorithms for a Five-phase Induction Motor Fed by a Multilevel Inverter. *International Journal of Engineering, Transactions B: Applications*, 2025, vol. 38, no. 2, pp. 351-361. doi: <https://doi.org/10.5829/ije.2025.38.02b.09>.
- Fan S., Meng D., Ai M. Efficiency analytical of five-phase induction motors with different stator connections for fracturing pump drives. *Energy Reports*, 2022, vol. 8, pp. 405-413. doi: <https://doi.org/10.1016/j.egyr.2021.11.240>.
- Liu Z., Houari A., Machmoum M., Benkhoris M.F., Djeriou A., Tang T. Experimental investigation of a real-time singularity-based fault diagnosis method for five-phase PMSG-based tidal current applications. *ISA Transactions*, 2023, vol. 142, pp. 501-514. doi: <https://doi.org/10.1016/j.isatra.2023.07.038>.
- Saifi R. Implementation of a new flux rotor based on model reference adaptive system for sensorless direct torque control modified for induction motor. *Electrical Engineering & Electromechanics*, 2023, no. 2, pp. 37-42. doi: <https://doi.org/10.20998/2074-272X.2023.2.06>.
- Mehedi F., Benbouhenni H., Nezli L., Boudana D. Feedforward Neural Network-DTC of Multi-phase Permanent Magnet Synchronous Motor Using Five-Phase Neural Space Vector Pulse Width Modulation Strategy. *Journal Européen Des Systèmes Automatisés*, 2021, vol. 54, no. 2, pp. 345-354. doi: <https://doi.org/10.18280/jesa.540217>.
- Geng Q., Qin Z., Jin X., Zhang G., Zhou Z. Direct Torque Control of Dual Three-Phase Permanent Magnet Synchronous Motors Based on Master-Slave Virtual Vectors. *World Electric Vehicle Journal*, 2024, vol. 15, no. 5, art. no. 199. doi: <https://doi.org/10.3390/wevj15050199>.
- Yang G., Yang J., Li S., Wang Y., Hussain H., Deng R., Yan L. A Sequential Direct Torque Control Scheme for Seven-Phase Induction Machines Based on Virtual Voltage Vectors. *IEEE Transactions on Industry Applications*, 2021, vol. 57, no. 4, pp. 3722-3734. doi: <https://doi.org/10.1109/TIA.2021.3068932>.
- Mossa M.A., Echeikh H., Ouanjli N.E., Alhelou H.H., Enhanced second-order sliding mode control technique for a five-phase induction motor. *International Transactions on Electrical Energy Systems*, 2022, vol. 2022, pp. 1-19. doi: <https://doi.org/10.1155/2022/8215525>.
- Song J., Zheng W.X., Niu Y. Self-Triggered Sliding Mode Control for Networked PMSM Speed Regulation System: A PSO-Optimized Super-Twisting Algorithm. *IEEE Transactions on Industrial Electronics*, 2022, vol. 69, no. 1, pp. 763-773. doi: <https://doi.org/10.1109/TIE.2021.3050348>.
- Shao B., Zhu Z.Q., Yan L., Feng J., Guo S., Li Y., Feng L. Torque Ripple Reduction for Direct Torque Control of Dual Three-Phase PMSM Based on Multiple Virtual Voltage Vectors. *IEEE Transactions on Energy Conversion*, 2023, vol. 38, no. 1, pp. 296-309. doi: <https://doi.org/10.1109/TEC.2022.3208784>.
- Parsa L., Toliyat H. Sensorless Direct Torque Control of Five-Phase Interior Permanent-Magnet Motor Drives. *IEEE Transactions on Industry Applications*, 2007, vol. 43, no. 4, pp. 952-959. doi: <https://doi.org/10.1109/TIA.2007.900444>.
- Sakouchi A., Djahbar A., Bounadja E., Benbouhenni H., Iqbal A., Moualdia A., Kechida A. Enhanced control of grid-connected multi-machine wind power generation systems using fuzzy backstepping approaches. *Energy Reports*, 2024, vol. 12, pp. 4208-4231. doi: <https://doi.org/10.1016/j.egyr.2024.09.077>.
- Wang X., Cao B., Mao Z.-H., Grainger B., Yaz E.E. Polyphase Permanent Magnet Synchronous Motors Direct Current Model Predictive Control with Long Prediction Horizons. *IFAC-PapersOnLine*, 2023, vol. 56, no. 2, pp. 2719-2726. doi: <https://doi.org/10.1016/j.ifacol.2023.10.1368>.
- Guezi A., Bendaikha A., Dendouga A. Direct torque control based on second order sliding mode controller for three-level inverter-fed permanent magnet synchronous motor: comparative study. *Electrical Engineering & Electromechanics*, 2022, no. 5, pp. 10-13. doi: <https://doi.org/10.20998/2074-272X.2022.5.02>.
- Liu X., Deng Y., Liu J., Cao H., Xu C., Liu Y. Fixed-time integral terminal sliding mode control with an adaptive RBF neural network for PMSM speed regulation. *Control Engineering Practice*, 2025, vol. 156, art. no. 106236. doi: <https://doi.org/10.1016/j.conengprac.2024.106236>.
- Alyazidi N.M., Bawazir A.F., Al-Dogail A.S. Robust integral sliding mode control for pressure management in multi-phase flow systems. *Results in Engineering*, 2025, vol. 25, art. no. 104024. doi: <https://doi.org/10.1016/j.rineng.2025.104024>.
- Mossa M.A., Echeikh H., Ma'arif A. Dynamic Performance Analysis of a Five-Phase PMSM Drive Using Model Reference Adaptive System and Enhanced Sliding Mode Observer. *Journal of Robotics and Control (JRC)*, 2022, vol. 3, no. 3, pp. 289-308. doi: <https://doi.org/10.18196/jrc.v3i3.14632>.

Received 31.01.2025

Accepted 27.04.2025

Published 02.09.2025

F. Mehedi¹, Associate Professor,
I. Bouyakoub¹, Associate Professor,
A. Yousfi², Associate Professor,
R. Taleb^{1,3}, Professor,
Z. Reguieg¹, PhD Student,

¹ Laboratoire Génie Electrique et Energies Renouvelables (LGEER), Hassiba Benbouali University of Chlef, Algeria, e-mail: f.mehedi@univ-chlef.dz (Corresponding Author); i.bouyakoub@univ-chlef.dz; z.reguieg@univ-chlef.dz

² Laboratory LAGC, Faculty of Science and Technology, Djilali Bounaama University, Khemis Miliana, Algeria, e-mail: a.yousfi@univ-bkm.dz

³ Embedded Systems Research Unit of Chlef, Research Centre for Scientific and Technical Information (CERIST), Ben Aknoun, Algeria, e-mail: r.taleb@univ-chlef.dz

How to cite this article:

Mehedi F., Bouyakoub I., Yousfi A., Taleb R., Reguieg Z. Improve of the direct torque control strategy applied to a multi-phase interior permanent magnet synchronous motor using a super twisting sliding mode algorithm. *Electrical Engineering & Electromechanics*, 2025, no. 5, pp. 38-42. doi: <https://doi.org/10.20998/2074-272X.2025.5.05>

Performance evaluation and analysis by simulation for sliding mode control with speed regulation of permanent magnet synchronous motor drives in electric vehicles

Introduction. This study introduces a sliding mode control (SMC) that utilizes multivariable system command estimation (MSCE-SMC) to create an innovative speed control system for the permanent magnet synchronous motor (PMSM). The motor operates through a 3-phase voltage source inverter when used in an electric vehicle (EV) model, with the goal of achieving fast speed regulation and high performance. **Problem.** The primary challenge is to achieve fast and accurate speed regulation for PMSMs while maintaining high performance, despite varying system parameters and external disturbances. The **goal** is to design a robust and adaptive speed control system for PMSMs using the SMC approach, which ensures precise speed tracking and high-performance regulation. **Scientific novelty.** The integration of MSCE-SMC approach, offering an innovative solution for speed control in PMSMs used in EVs. **Methodology.** SMC approach for the PMSM divides the system into 2 subsystems: electrical and speed. A d-q coordinate frame is used to model the PMSM, and its control strategy is outlined. A detailed model of the PMSM with SMC is presented after an in-depth review of the theoretical concepts and principles of sliding mode control. **Results.** To validate the proposed approach, MATLAB/Simulink is conducted, demonstrating the effectiveness and robustness of the method in PMSM speed regulation. The results confirm that the proposed method provides straightforward and precise control, accurate speed tracking, and high-performance regulation. It also shows adaptability to parameter variations and external disturbances. **Practical value.** The practical value of the proposed method is significant, as it provides a reliable and efficient control system for PMSMs. It offers precise speed control, robust performance under variable conditions, and high adaptability to external disturbances, making it suitable for real-world EV applications. References 22, table 1, figures 18.

Key words: permanent magnet synchronous motor, sliding mode control, electric vehicle, speed regulation.

Вступ. У дослідженні розглядається керування ковзним режимом (SMC), що використовує багатопараметричну оцінку системних команд (MSCE-SMC) для створення інноваційної системи керування швидкістю синхронного двигуна з постійними магнітами (PMSM). Двигун працює через трифазний інвертор напруги при використанні в моделі електромобіля (EV) з метою досягнення швидкого регулювання швидкості та високої продуктивності. **Проблема.** Основне завдання полягає в досягненні швидкого і точного регулювання швидкості для PMSM при збереженні високої продуктивності, незважаючи на параметри системи, що змінюються, і зовнішні збурення. **Метою** є розробка надійної та адаптивної системи керування швидкістю для PMSM з використанням SMC підходу, що забезпечує точне відстеження швидкості та високопродуктивне регулювання. **Наукова новизна.** Інтеграція підходу MSCE-SMC пропонує інноваційне рішення для управління швидкістю PMSM, що використовуються в EV. **Методологія.** SMC підхід для PMSM поділяє систему на 2 підсистеми: електричну та швидкісну. Для моделювання PMSM використовується d-q система координат і описується стратегія його управління. Наведено докладну модель PMSM з SMC після поглибленого аналізу теоретичних концепцій та принципів управління в ковзному режимі. **Результати.** Для перевірки запропонованого підходу проведено аналіз у середовищі MATLAB/Simulink, що показав ефективність та надійність методу регулювання швидкості PMSM. Результати підтверджують, що запропонований метод забезпечує просте і точне керування, коректне відстеження швидкості та високопродуктивне регулювання. Він також демонструє адаптивність до змін параметрів та зовнішніх збурень. **Практична цінність** запропонованого методу значна, оскільки він забезпечує надійну та ефективну систему управління PMSM. Він забезпечує точне управління швидкістю, надійну роботу в змінних умовах, і високу адаптивність до зовнішніх збурень, що робить його придатним для застосування в реальних EV. Бібл. 22, табл. 1, рис. 18.

Ключові слова: синхронний двигун з постійними магнітами, керування ковзним режимом, електромобіль, регулювання швидкості.

Introduction. Electric vehicles (EVs) that use electric motors are used to replace traditional gasoline vehicles that use internal combustion engines in order to reach the level of emissions of fossil fuels [1–4]. permanent magnet synchronous motor (PMSM) in recent years have played an increasingly important role in many industrial applications due to the advances in magnetic materials, recent technological developments in power electronics and control theories [5]. Due to their high torque-power density, high efficiency and low maintenance, PMSM-based drive is also becoming widely used in EVs [6, 7]. There are various nonlinear command methods have been proposed to improve the command performance of PMSM, such as sliding mode control (SMC), adaptive control, predictive control [8, 9], intelligent control, etc. Field-oriented control based conventional PI method is difficult to deal with loud disturbances, variations parameters and cannot adapt to the applications of high-precision control [10]. SMC has attracted many researchers in recent years. High-frequency switching devices and high-performance microprocessors have contributed to the recent increase in interest in this command method [11]. The effectiveness of this solution is attributed to its distinct advantages,

including insensitivity to parameter variations, rapid dynamic response and the ability to reject external disturbances [12].

SMC is a particular mode of operation of systems with variable structure [13]. The theory of these systems was studied and developed in the USSR first by S.V. Emelyanov, then by other collaborators such as V.I. Utkin based on the work of the mathematician A.F. Filippov on differential equations with discontinuous second member. Then the work was taken up elsewhere: in the US by Prof. Slotine, and in Japan by Prof. Young, Prof. Harishama and Prof. Hashimoto. In SMC, the command switches between two different values according to the sign of a switching function (called switching or sliding surface) defined in the state space of the system [14]. This is introduced in order to obtain better stability, and high precision than those generally obtained by classical regulators [15, 16]. Several approaches exist for the choice of the sliding surface. In this work, we are interested in the study of an approach that considers a nonlinear surface [17, 18], the synthesis of which is based on Lyapunov stability theory. The strong robustness,

simplicity and ease of implementation make it an ideal choice for high performance by regularly adjusting the system structure to combat parameter variations and external disturbances [19, 20].

The **goal** of the article is to design a robust and adaptive speed control system for PMSMs using the SMC approach, which ensures precise speed tracking and high-performance regulation. The proposed controller is investigated and analyzed in different control speeds, load conditions, and rotational speed direction.

Model of PMSM. The model of PMSM in d - q frame is represented by equations: electrical, magnetic, and electromagnetic. The stator voltages equations expressed as [21]:

$$V_d = RI_d + \frac{d\varphi_d}{dt} - \omega\varphi_q; \quad (1)$$

$$V_q = RI_q + \frac{d\varphi_q}{dt} + \omega\varphi_d, \quad (2)$$

where $V_d, V_q, \varphi_d, \varphi_q, I_d, I_q$ are the direct and quadrature axis of voltages, fluxes and currents respectively; R is the stator resistance; ω is the mechanical angular speed.

The stator flux equations expressed [21]:

$$\varphi_d = L_d I_d + \varphi_m; \quad (3)$$

$$\varphi_q = L_q I_q, \quad (4)$$

where L_d, L_q are the direct and quadrature stator inductances; φ_m is the constant permanent magnet flux.

The PMSM model equations in d - q axis expressed as:

$$V_d = RI_d + L_d \frac{dI_d}{dt} - \omega L_q I_q; \quad (5)$$

$$V_q = RI_q + L_q \frac{dI_q}{dt} + \omega(L_d I_d + \varphi_m). \quad (6)$$

The expression for electromagnetic torque T_e [21] is:

$$T_e = p((L_d - L_q)I_q I_d + I_q \varphi_m). \quad (7)$$

PMSM is assumed to surface mounted PMSM ($L_d = L_q = L$) the electromagnetic torque becomes:

$$T_e = p I_q \varphi_m, \quad (8)$$

where T_e is the electromagnetic torque; p is the number of pole pairs.

The expression of the mechanical equation [21] is:

$$J \frac{d\omega_m}{dt} + f_v \omega_m = T_e - T_L, \quad (9)$$

where J is the moment of inertia; T_L is the load torque; f_v is the viscous friction coefficient; ω_m is the rotor mechanical speed of the PMSM.

SMC theory. Variable structure systems can be controlled using SMC. Three different parts make up the trajectory (Fig. 1): the convergence mode (CM), the sliding mode (SM) and the permanent mode (PM) [22].

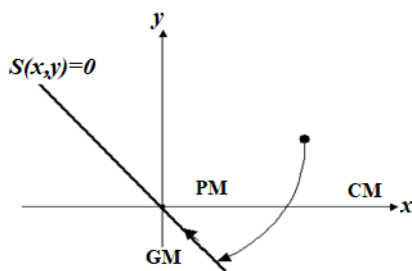


Fig. 1 Different modes trajectory of the SMC

The choice of the surface. The design of SMC was executed in 3 key phases [22]: selection of the surface, conditions necessary for convergence, meaning of the control law. The sliding surfaces choice is shaped by the number and shape of required functions. The control vector u and surface vector have the same dimension defined by:

$$\dot{x} = A(x, t)x + B(x, t)u. \quad (10)$$

The nonlinear form depends on the error in the variable to be regulated, known as x :

$$S(x) = \left(\frac{\partial}{\partial t} + \lambda_x \right)^{r-1} e(x), \quad (11)$$

where $e(x)$ is the difference between the variable to be adjusted and its reference: $e(x) = x^* - x$; λ_x is the positive constant; r is the relative degree and indicates the number of times the surface needs to be differentiated to show control.

The SMC objective is to maintain the surface at zero. The only possible solution for this surface is $e(x) = 0$, which a linear differential equation.

Convergence and existence conditions. Two considerations to ensure convergence mode [22], the discrete switching function (it is proposed and studied by S.V. Emelyanov and V.I. Utkin):

$$\begin{cases} \dot{S}(x) > 0 & \text{if } S(x) < 0; \\ \dot{S}(x) < 0 & \text{if } S(x) > 0. \end{cases} \quad (12)$$

This condition can be formulated in another way:

$$\dot{S}(x)S(x) < 0. \quad (13)$$

The Lyapunov function defines as follows:

$$V(x) = \frac{1}{2} S^2(x). \quad (14)$$

The derivative of this function is:

$$\dot{V}(x) = S(x)\dot{S}(x). \quad (15)$$

Calculation of the control. The SMC structure consists of the exact linearization (u_{eq}) and the other stabilizing (u_n) [22]:

$$u = u_{eq} + u_n. \quad (16)$$

In order to illustrate the previous development, we will consider a system that is described in the state space by (10). The aim is to establish the equivalent expression for the control input u .

The derivative of the surface is:

$$\dot{S}(x) = \frac{\partial S}{\partial t} + \frac{\partial S}{\partial x} \frac{\partial x}{\partial t}. \quad (17)$$

Replacing (10) and (16) in (17), we find:

$$\dot{S}(x) = \frac{\partial S}{\partial x} (A(x, t) + B(x, t)u_{eq}) + \frac{\partial S}{\partial x} B(x, t)u_n. \quad (18)$$

Equivalent command's expression:

$$u_{eq} = - \left(\frac{\partial S}{\partial x} B(x, t) \right)^{-1} \frac{\partial S}{\partial x} A(x, t). \quad (19)$$

For the equivalent control to take a finite value, it is necessary that $\frac{\partial S}{\partial x} B(x, t) \neq 0$.

Substituting the equivalent control with its expression from (18) in convergence mode we obtain:

$$\dot{S}(x, t) = \frac{\partial S}{\partial x} B(x, t)u_n. \quad (20)$$

Attractiveness condition expressed by (13) becomes:

$$S(x,t) \frac{\partial S}{\partial x} B(x,t) u_{eq}. \quad (21)$$

In order to satisfy this condition, the sign of a must be opposite to that of $S(x,t) \frac{\partial S}{\partial x} B(x,t)$.

The simplest form that discrete control (Fig. 2):

$$u_n = K \cdot \text{sign}(S(x,t)), \quad (22)$$

where the sign K must be different from that $\frac{\partial S}{\partial x} B(x,t)$.

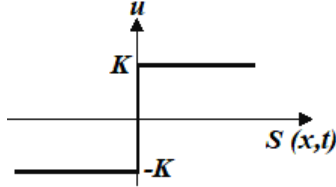


Fig. 2. Representation of discontinuous control

Application the SMC for the speed command of PMSM drive EV. The model of the PMSM, whose state variables are the stator currents and the mechanical speed [21]:

$$\begin{cases} \frac{dI_d}{dt} = -\frac{R}{L_d} I_d + \omega \frac{L_q}{L_d} I_q + \frac{1}{L_d} V_d; \\ \frac{dI_q}{dt} = -\frac{R}{L_q} I_q - \omega \frac{L_d}{L_q} I_d - \frac{\omega}{L_q} \varphi_m + \frac{1}{L_q} V_q; \\ \frac{d\omega_m}{dt} = \frac{1}{J} p \varphi_m I_q - \frac{1}{J} T_L - \frac{f_v}{J} \omega_m. \end{cases} \quad (23)$$

The diagram of the SMC for the PMSM drive in an EV (Fig. 3) includes 3 surfaces.

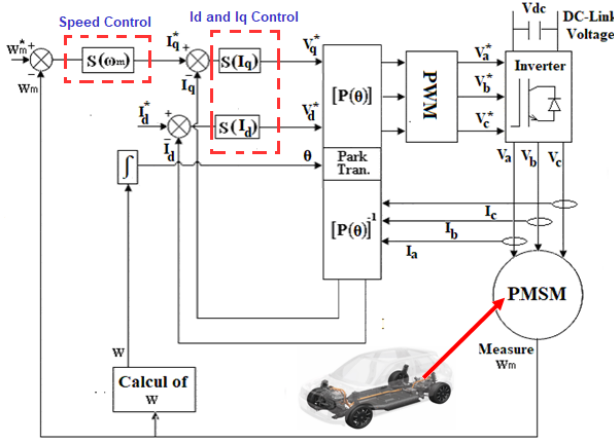


Fig. 3. Diagram of SMC for PMSM drive an EV

Speed control surface ω_m . Speed control surface has the form:

$$S(\omega_m) = \dot{\omega}_m^* - \omega_m. \quad (24)$$

The derivative of the surface is:

$$\dot{S}(\omega_m) = \dot{\omega}_m^* - \dot{\omega}_m. \quad (25)$$

The equation (25) becomes:

$$\dot{S}(\omega_m) = \dot{\omega}_m^* - \left[\frac{1}{J} p \varphi_m I_q - \frac{1}{J} T_L - \frac{f_v}{J} \omega_m \right]. \quad (26)$$

By replacing the current I_q with the control current $I_q = I_{qeq} + I_{qn}$, equation (26) can be written as:

$$\dot{S}(\omega_m) = \dot{\omega}_m^* - \left[\frac{1}{J} p \varphi_m I_{qeq} + \frac{1}{J} p \varphi_m I_{qn} - \frac{1}{J} T_L - \frac{f_v}{J} \omega_m \right]. \quad (27)$$

We have $S(\omega_m) = 0$ and consequently $\dot{S}(\omega_m) = 0$ and $I_{qn} = 0$, the equivalent order I_{qeq} :

$$I_{qeq} = \frac{J}{p \varphi_m} \left[\frac{f_v}{J} \omega_m + \frac{1}{J} T_L \right]. \quad (28)$$

The condition $\dot{S}(\omega_m) S(\omega_m) < 0$ must be checked. Substituting (28) in (27), we find:

$$\dot{S}(\omega_m) = \dot{\omega}_m^* - \frac{1}{J} p \varphi_m I_{qn}. \quad (29)$$

By choosing the discontinuous control form (Fig. 2), we therefore pose:

$$I_{qn} = K \omega \text{sign}(S(\omega_m)). \quad (30)$$

Current quadrature control surface I_q . Current quadrature control surface has the form:

$$S(I_q) = I_q^* - I_q. \quad (31)$$

The derivative of this surface is:

$$\dot{S}(I_q) = \dot{I}_q^* - \dot{I}_q. \quad (32)$$

Taking into account the expression of \dot{I}_q given by the system (23), the equation (32) becomes:

$$\dot{S}(I_q) = \dot{I}_q^* - \left[-\frac{R}{L_q} I_q - \omega \frac{L_d}{L_q} I_d - \frac{\omega}{L_q} \varphi_m + \frac{1}{L_q} V_q \right]. \quad (33)$$

By replacing the voltage V_q with the control voltage $V_q = V_{qeq} + V_{qn}$, we find:

$$\dot{S}(I_q) = \dot{I}_q^* - \left[-\frac{R}{L_q} I_q - \omega \frac{L_d}{L_q} I_d - \frac{\omega}{L_q} \varphi_m + \frac{1}{L_q} V_{qeq} + \frac{1}{L_q} V_{qn} \right]. \quad (34)$$

We have $S(I_q) = 0$ and consequently $\dot{S}(I_q) = 0$ and $V_{qn} = 0$, the equivalent order V_{qeq} :

$$V_{qeq} = R I_q + \omega L_d I_d + \omega \varphi_m. \quad (35)$$

The condition $\dot{S}(I_q) S(I_q) < 0$ must be checked. Substituting (35) in (34), we find:

$$\dot{S}(I_q) = \frac{1}{L_q} V_{qn}. \quad (36)$$

We therefore pose:

$$V_{qn} = K_q \text{sign}(S(I_q)). \quad (37)$$

Current direct control surface I_d . Current direct control surface has the form:

$$S(I_d) = I_d^* - I_d. \quad (38)$$

The derivative of this surface is:

$$\dot{S}(I_d) = \dot{I}_d^* - \dot{I}_d. \quad (39)$$

Taking into account the expression of \dot{I}_d given by the system (23), the equation (39) becomes:

$$\dot{S}(I_d) = \dot{I}_d^* - \left[-\frac{R}{L_d} I_d + \omega \frac{L_q}{L_d} I_q + \frac{1}{L_d} V_d \right]. \quad (40)$$

By replacing the V_d with $V_d = V_{deq} + V_{dn}$, we find:

$$\dot{S}(I_d) = \dot{I}_d^* - \left[-\frac{R}{L_d} I_d + \omega \frac{L_q}{L_d} I_q + \frac{1}{L_d} V_{deq} + \frac{1}{L_d} V_{dn} \right]. \quad (41)$$

We have $S(I_d) = 0$ and consequently $\dot{S}(I_d) = 0$ and $V_{dn} = 0$, from which we derive the equivalent order V_{deq} :

$$V_{deq} = RI_d + \omega L_q I_q. \quad (42)$$

The condition $\dot{S}(I_d)S(I_d) < 0$ must be checked. Substituting (42) in (41), we find:

$$\dot{S}(I_d) = \frac{1}{L_d} V_{dn}. \quad (43)$$

We therefore pose:

$$V_{dn} = K_d \text{sign}(S(I_d)). \quad (44)$$

Simulation results of speed regulation of PMSM-SMC. SMC for PMSM powered voltage source inverter for a model EV has been implemented in MATLAB/Simulink. A constant reference flux ($\varphi_{mref} = 0.12$ Wb) is used to conduct the simulations. In this set of simulation, a load variation is added when the PMSM is under the speed regulation, and the operating speed is 157 rad/s. PMSM is considered in the simulation and parameters as given in Table 1.

Table 1

PMSM parameters	
Parameters	Values
Rated power	1.5 kW
Frequency	50 Hz
Rotor speed	1500 rpm / 157 rad/s
Stator resistance	0.18 Ω
Inductance d axis	2.1 mH
Inductance q axis	4.2 mH
Moment of inertia	0.0066 kg·m ²
Viscous friction coefficient	0.0014 N·s/rad
Constant rotor flux linkage	0.12 Wb
Number of pole pairs	2

Simulation for successive step changes in reference speed under full load conditions (Fig. 4–8). We involve sequential step change in control speed under full load conditions. The PMSM is initially started at 83.5 rad/s step control speed. At $t = 1$ s, a step-up change occurs, increasing the control speed from 83.5 rad/s to 104.5 rad/s. Finally, at $t = 2$ s, another change the command speed from 104.5 rad/s to 157 rad/s.

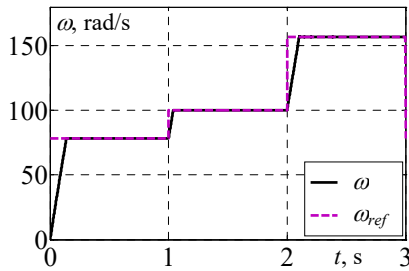


Fig. 4. Reference speed and PMSM speed

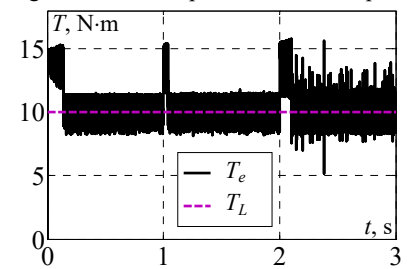


Fig. 5. Electromagnetic torque and load torque

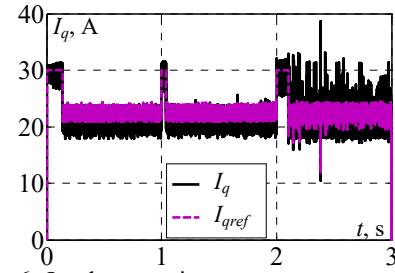


Fig. 6. Quadrature axis component stator current

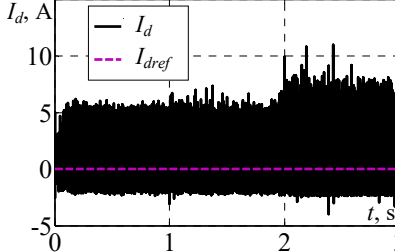


Fig. 7. Direct axis component stator current

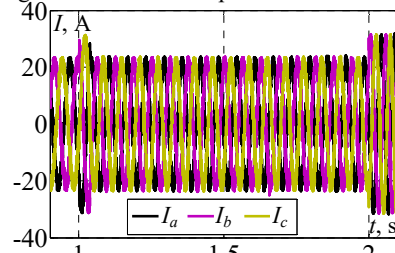


Fig. 8. 3-phase stator currents

Simulation for reference speed fix and step change of load (Fig. 9–13). In this part, the PMSM is under speed control 157 rad/s with a load variation at $t = 1$ s, the load torque changes from 10 N·m to 5 N·m and at $t = 2$ s another change the load torque changes from 5 N·m to 10 N·m.

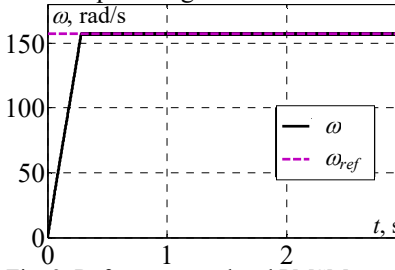


Fig. 9. Reference speed and PMSM speed

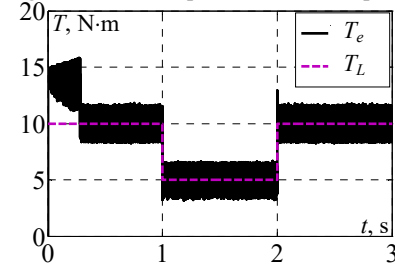


Fig. 10. Electromagnetic torque and load torque

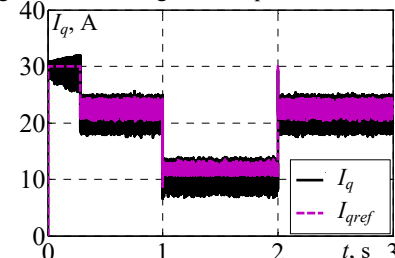


Fig. 11. Quadrature axis component stator current

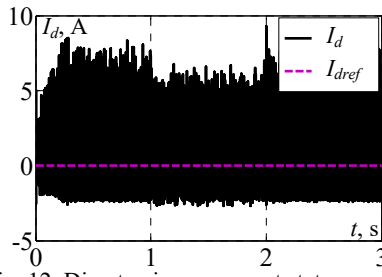


Fig. 12. Direct axis component stator current

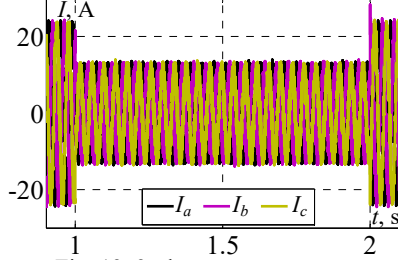


Fig. 13. 3-phase stator currents

Simulation for reference speed and inverse speed and under full load (Fig. 14–18). We apply a full load start of PMSM ($T_L = 10$ N·m) until at $t = 1$ s. The speed reference is equal to the synchronism speed 157 rad/s until $t = 1.5$ s, then the direction of rotation is reversed at a speed -157 rad/s.

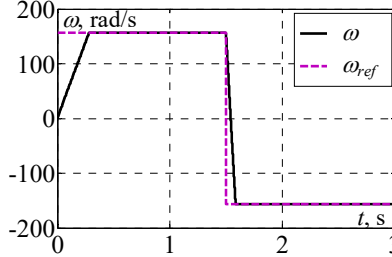


Fig. 14. Reference speed and PMSM speed

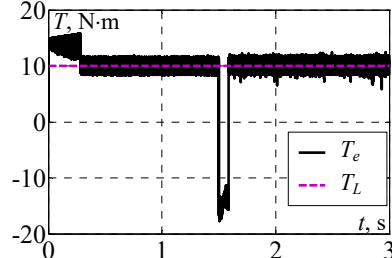


Fig. 15. Electromagnetic torque and load torque

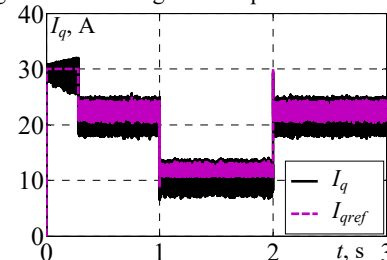


Fig. 16. Quadrature axis component stator current

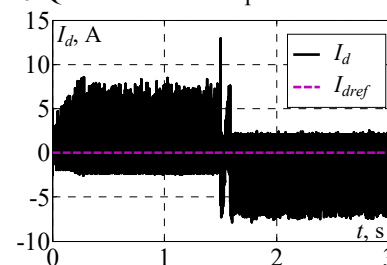


Fig. 17. Direct axis component stator current

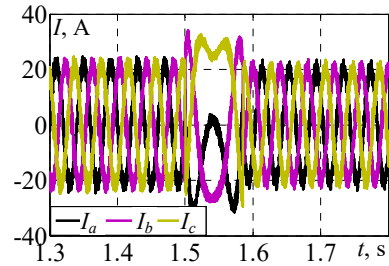


Fig. 18. 3-phase stator currents

Discussions of results. In Fig. 4, 9, 14, the speed of PMSM obtained with SMC the speed appears to be consistent, with the real speed closely mirroring the command speed. The system responds efficiently to changes in command speed and exhibits a smooth rise time from 104.5 rad/s to 157 rad/s. Analyzing the difference between command and real speeds at each stage is crucial to gain insight into the system's performance and potential limitations. In these cases, the rise time indicates how responsive the system is, and shorter rise times generally mean better control dynamics and faster adaptation to command input changes and settling time is satisfying in tree case seamlessly traced the speed reference without exceeding; in Fig. 9 rotation speed equal to rotation speed 157 rad/s seamlessly traced the speed reference without exceeding; in Fig. 14 with a positive speed command of 157 rad/s, speed response with the SMC neatly settled at the reference. Sudden reference speed reversal from 157 rad/s to -157 rad/s leading to change in speed orientation for the 2 models at -157 rad/s, the SMC seamlessly traced the speed reference without exceeding.

The load torque and electromagnetic torque are matched in Fig. 5, 10, 15 by SMC. The electromagnetic torque is kept constant during the speed build-up phase to ensure acceleration. The electromagnetic torque will decrease to 5 N·m once the rotor speed matches the reference speed. This equilibrium is achieved faster in the SMC model due to the absence of speed overshoot. The electromagnetic torque closely tracks the load torque, except during brief intervals when the speed increases (Fig. 5) or reverses (Fig. 15). These deviations are minimal and occur over very short periods.

In Fig. 6, 11, 16, the quadrature component of the stator current are compared with the quadrature component current reference; is in direct proportion to electromagnetic torque T_e .

In Fig. 7, 12, 17, the direct component of the stator current is compared with the direct component current reference is met at zero.

In Fig. 8, 13, 18 the stator 3-phase currents (abc) are shown. When as the PMSM speed rises, the frequency of the current waveform also increases (Fig. 8) and when the load torque decreases from its nominal value (5 N·m) to 3 N·m of the current waveform also decreases (Fig. 15).

Conclusions. This paper describes the creation and execution of speed controllers that use SMC-based technology in a SMC drive structure for a PMSM in an EV drive. The SMC algorithm's speed control loop uses a sliding mode controller based on surface dynamics instead of the traditional PI controller in the outer control

loop. Applied MATLAB/Simulink software was utilized to conduct simulation analyses and evaluations to assess the performance and effectiveness of the SMC for PMSM. The proposed system's dynamic response was tested under different reference speeds, load conditions, and reverse speed scenarios.

The simulation results show that the SMC can perform dynamically quickly and accurately, without any overshoot, minimal steady-state error, and a short rise time, which is superior for PMSM speed control applications. SMC is characterized by its significant torque ripple, which remains a major concern.

Conflict of interest. The authors declare that they have no conflicts of interest.

REFERENCES

1. Liu F., Wang X., Xing Z. Design of a 35 kW Permanent Magnet Synchronous Motor for Electric Vehicle Equipped With Non-Uniform Air Gap Rotor. *IEEE Transactions on Industry Applications*, 2023, vol. 59, no. 1, pp. 1184-1198. doi: <https://doi.org/10.1109/TIA.2022.3206258>.
2. Ibrar A., Ahmad S., Safdar A., Haroon N. Efficiency enhancement strategy implementation in hybrid electric vehicles using sliding mode control. *Electrical Engineering & Electromechanics*, 2023, no. 1, pp. 10-19. doi: <https://doi.org/10.20998/2074-272X.2023.1.02>.
3. Boumegouas M.K.B., Kouzi K. A New Synergetic Scheme Control of Electric Vehicle Propelled by Six-phase Permanent Magnet Synchronous Motor. *Advances in Electrical and Electronic Engineering*, 2022, vol. 20, no. 1, pp. 1-14. doi: <https://doi.org/10.15598/aece.v20i1.4221>.
4. Wang Z., Ching T.W., Huang S., Wang H., Xu T. Challenges Faced by Electric Vehicle Motors and Their Solutions. *IEEE Access*, 2021, vol. 9, pp. 5228-5249. doi: <https://doi.org/10.1109/ACCESS.2020.3045716>.
5. Patel A.N., Doshi P.J., Mahagoakar S.C., Panchal T.H. Optimization of cogging torque in interior permanent magnet synchronous motor using optimum magnet v-angle. *Electrical Engineering & Electromechanics*, 2023, no. 6, pp. 16-20. doi: <https://doi.org/10.20998/2074-272X.2023.6.03>.
6. Mazzi Y., Ben Sassi H., Errahimi F., Es-Sbai N. Speed Control of a PMSM drive system using a nonsingular terminal sliding mode controller. *Statistics, Optimization & Information Computing*, 2024, vol. 13, no. 1, pp. 450-458. doi: <https://doi.org/10.19139/soic-2310-5070-1913>.
7. Djafer L., Taleb R., Mehedi F., Aissa Bokhtache A., Bessaad T., Chabni F., Saidi H. Electric drive vehicle based on sliding mode control technique using a 21-level asymmetrical inverter under different operating conditions. *Electrical Engineering & Electromechanics*, 2025, no. 3, pp. 31-36. doi: <https://doi.org/10.20998/2074-272X.2025.3.05>.
8. Loro J.A.R. Robust Position Control of SM-PMSM Based on a Sliding Mode Current Observer. *International Journal of Electrical and Electronic Engineering & Telecommunications*, 2020, vol. 9, no. 5, pp. 337-341. doi: <https://doi.org/10.18178/ijeetc.9.5.337-341>.
9. Chen Y., Li M., Gao Y., Chen Z. A sliding mode speed and position observer for a surface-mounted PMSM. *ISA Transactions*, 2019, vol. 87, pp. 17-27. doi: <https://doi.org/10.1016/j.isatra.2018.11.011>.
10. Varatharajan A., Pellegrino G., Armando E. Direct Flux Vector Control of Synchronous Motor Drives: A Small-Signal Model for Optimal Reference Generation. *IEEE Transactions on Power Electronics*, 2021, vol. 36, no. 9, pp. 10526-10535. doi: <https://doi.org/10.1109/TPEL.2021.3067694>.
11. Awan H.A.A., Hinkkanen M., Bojoi R., Pellegrino G. Stator-Flux-Oriented Control of Synchronous Motors: A Systematic Design Procedure. *IEEE Transactions on Industry Applications*, 2019, vol. 55, no. 5, pp. 4811-4820. doi: <https://doi.org/10.1109/TIA.2019.2927316>.
12. Lin H., Lee K., Kim S., Ahn H., You K. Speed Regulation for PMSM using a Novel Sliding Mode Controller. *Journal of Multidisciplinary Engineering Science and Technology (JMEST)*, 2021, vol. 8, no. 12, pp. 11842-11845.
13. Wang Q., Wang S., Chen C. Review of sensorless control techniques for PMSM drives. *IEEJ Transactions on Electrical and Electronic Engineering*, 2019, vol. 14, no. 10, pp. 1543-1552. doi: <https://doi.org/10.1002/tee.22974>.
14. Zhang X., Sun L., Zhao K., Sun L. Nonlinear Speed Control for PMSM System Using Sliding-Mode Control and Disturbance Compensation Techniques. *IEEE Transactions on Power Electronics*, 2013, vol. 28, no. 3, pp. 1358-1365. doi: <https://doi.org/10.1109/TPEL.2012.2206610>.
15. Zhang W., Kong J. A novel fast and chattering-free speed control method for PMSM motor drive based on sliding mode control. *International Journal of Dynamics and Control*, 2024, vol. 12, no. 9, pp. 3332-3338. doi: <https://doi.org/10.1007/s40435-024-01419-2>.
16. Kim H., Son J., Lee J. A High-Speed Sliding-Mode Observer for the Sensorless Speed Control of a PMSM. *IEEE Transactions on Industrial Electronics*, 2011, vol. 58, no. 9, pp. 4069-4077. doi: <https://doi.org/10.1109/TIE.2010.2098357>.
17. Chi S., Zhang Z., Xu L. Sliding-Mode Sensorless Control of Direct-Drive PM Synchronous Motors for Washing Machine Applications. *IEEE Transactions on Industry Applications*, 2009, vol. 45, no. 2, pp. 582-590. doi: <https://doi.org/10.1109/TIA.2009.2013545>.
18. Junejo A.K., Xu W., Mu C., Ismail M.M., Liu Y. Adaptive Speed Control of PMSM Drive System Based a New Sliding-Mode Reaching Law. *IEEE Transactions on Power Electronics*, 2020, vol. 35, no. 11, pp. 12110-12121. doi: <https://doi.org/10.1109/TPEL.2020.2986893>.
19. Dandan S., Yugang D., Chengning Z. Sliding Mode Controller for Permanent Magnetic Synchronous Motors. *Energy Procedia*, 2017, vol. 105, pp. 2641-2646. doi: <https://doi.org/10.1016/j.egypro.2017.03.765>.
20. Fallaha C.J., Saad M., Kanaan H.Y., Al-Haddad K. Sliding-Mode Robot Control With Exponential Reaching Law. *IEEE Transactions on Industrial Electronics*, 2011, vol. 58, no. 2, pp. 600-610. doi: <https://doi.org/10.1109/TIE.2010.2045995>.
21. Guezzi A., Bendaikha A., Dendouga A. Direct torque control based on second order sliding mode controller for three-level inverter-fed permanent magnet synchronous motor: comparative study. *Electrical Engineering & Electromechanics*, 2022, no. 5, pp. 10-13. doi: <https://doi.org/10.20998/2074-272X.2022.5.02>.
22. Senani F., Rahab A., Benalla H. Squirrel Cage Induction Motor (SCIM) Rotor Flux Estimation and Observer Using Multivariable Sliding Mode Control (MSMC). *Algerian Journal of Signals and Systems*, 2024, vol. 9, no. 2, pp. 121-127. doi: <https://doi.org/10.51485/ajss.v9i2.219>.

Received 16.02.2025

Accepted 29.04.2025

Published 02.09.2025

F. Senani^{1,2}, PhD in Electrical Engineering, Associate Professor,
A. Rahab^{1,2}, PhD in Electrical Engineering, Associate Professor,
H. Benalla², PhD in Electrical Engineering, Professor,
¹Higher Normal School of Technological Education of Skikda (ENSET Skikda), Technology Department, Algeria,
e-mail: senani.fouzi@gmail.com (Corresponding Author);
rahababderezzak@gmail.com
²Electrotechnical Laboratory of Constantine (LEC),
Department of Electrical Engineering,
Faculty of Science and Technology,
University of Constantine 1, Algeria,
e-mail: benalladz@yahoo.fr

How to cite this article:

Senani F., Rahab A., Benalla H. Performance evaluation and analysis by simulation for sliding mode control with speed regulation of permanent magnet synchronous motor drives in electric vehicles. *Electrical Engineering & Electromechanics*, 2025, no. 5, pp. 43-48. doi: <https://doi.org/10.20998/2074-272X.2025.5.06>

Takagi-Sugeno fuzzy model identification using improved multiswarm particle swarm optimization in solar photovoltaics

Introduction. The particle swarm optimization (PSO) algorithm has proven effective across various domains due to its efficient search space exploration, ease of implementation, and capability to handle high-dimensional problems. However, it is often prone to premature convergence, which limits its performance. **Problem.** This issue becomes critical in identifying Takagi-Sugeno (T-S) fuzzy models, especially in complex systems like solar photovoltaic (PV) applications, where model accuracy is vital for tasks such as maximum power point tracking (MPPT) and shading compensation. **Goal.** This manuscript introduces an improved multiswarm PSO (I-MsPSO), designed to enhance search performance and robustness in identifying T-S fuzzy systems. The method is particularly suited to nonlinear modeling challenges in renewable energy systems. **Methodology.** I-MsPSO divides the swarm into 4 independent subswarms, each operating in a local region with specific inertia weights and acceleration coefficients. Periodic information sharing between subswarms allows the algorithm to converge collectively toward optimal solutions. A new modeling approach, specific Takagi-Sugeno modeling (STaSuM), is introduced, using I-MsPSO to determine both the structure and parameters of T-S fuzzy systems. **Results.** The I-MsPSO's performance was tested on benchmark optimization problems and real-world engineering cases. Results show that STaSuM produces highly accurate and generalizable fuzzy models, outperforming existing techniques. **Scientific novelty** lies in the development of I-MsPSO, which enhances the traditional PSO by using 4 interactive subswarms with customized parameters, and the creation of STaSuM for advanced T-S fuzzy system identification. **Practical value.** I-MsPSO and STaSuM provide a powerful optimization and modeling framework, offering robust and accurate solutions for nonlinear and dynamic environments. Their structure makes them especially valuable for future applications in MPPT control, fault-tolerant modeling, and real-time optimization in PV energy systems. References 39, table 5, figures 8.

Key words: improved multiswarm particle swarm optimization, particle swarm optimization, specific Takagi-Sugeno modeling.

Вступ. Алгоритм оптимізації рою часток (PSO) довів свою ефективність у різних галузях завдяки ефективному дослідженню простору пошуку, простоті реалізації та здатності вирішувати завдання високої розмірності. Однак він часто схильний до передчасної збіжності, що обмежує його продуктивність. Ця **проблема** стає критично важливою при ідентифікації нечітких моделей Такагі-Сугено (T-S), особливо у складних системах, таких як сонячні фотоелектричні системи (PV), де точність моделі є критично важливою для таких завдань, як відстеження точки максимальної потужності (MPPT) та компенсація затінення. **Мета.** У роботі представлений удосконалений багатороевий PSO (I-MsPSO), розроблений для підвищення продуктивності пошуку та надійності при ідентифікації нечітких систем T-S. Цей метод особливо підходить для задач нелінійного моделювання у системах відновлюваної енергії. **Методологія.** I-MsPSO ділить рій на 4 незалежні подрії, кожен з яких працює в локальній області з певними вагами інерції та коефіцієнтами прискорення. Періодичний обмін інформацією між подріями дозволяє алгоритму колективно сходиться до оптимальних рішень. Наведено новий підхід до моделювання, специфічне моделювання Такагі-Сугено (STaSuM), з використанням I-MsPSO для визначення структури та параметрів нечітких систем T-S. **Результати.** Продуктивність I-MsPSO протестована на еталонних задачах оптимізації та реальних інженерних прикладах. Результати показують, що STaSuM створює високоточні та узагальнені нечіткі моделі, що перевершують існуючі методи. **Наукова новизна** полягає в розробці I-MsPSO, який розширює традиційний PSO за рахунок використання 4 інтерактивних подріїв з параметрами, що настраюються, а також у створенні STaSuM для розширеної ідентифікації нечітких систем T-S. **Практична цінність.** I-MsPSO та STaSuM надають потужну платформу оптимізації та моделювання, пропонуючи надійні та точні рішення для нелінійних та динамічних середовищ. Їхня структура робить їх особливо цінними для майбутніх додатків у галузі управління MPPT, відмовостійкого моделювання та оптимізації в реальному часі у PV енергетичних системах. Бібл. 39, табл. 5, рис. 8.

Ключові слова: покращена оптимізація рою часток з кількома роями, оптимізація рою часток, специфічне моделювання Такагі-Сугено.

Introduction. The Takagi-Sugeno (T-S) type fuzzy model, used to model complex systems particularly in the area of fuzzy logic and control systems, was first introduced by Mamdani and Assilian [1]. It was later enhanced by Takagi and Sugeno who developed the T-S type model. In the new approach, fuzzy linguistic rules were replaced by more precise mathematical rules. Historically, a fuzzy model is described by a formalism based on fuzzy rules, providing a prolific framework to study nonlinear dynamic systems and, particularly, to analyze their stability and synthesize laws control (stabilization). From a conceptual point of view, a fuzzy system is identified by determining the structure of the model (the premise parameters) and estimating the consequent parameters [2]. The first step is performed employing identification methods based on coalescence or even fuzzy classification (fuzzy clustering algorithms). Fuzzy coalescence algorithms are also applied to identify nonlinear systems using to the T-S model. In the literature, numerous algorithms derived from the fuzzy c-mean algorithm, such as the Gustafson-Kessel algorithm [3], the fuzzy C-means algorithm [4], the Gath-Geva

algorithm [5], were proposed. After determining the premise parameters of the model, the consequent parameters of the fuzzy rules are estimated. Among the identification techniques proposed in the literature we cite: the graph kernel recursive least-squares algorithms [6], weighted least squares method [7], the orthogonal least squares algorithm [8]. Several works showed that fuzzy coalescence algorithms derived from fuzzy c-means are sensitive to initialization. In fact, random initialization can generally lead to convergence towards a local minimum of the objective function. The problem of synthesizing fuzzy systems was treated by many researchers, as an optimization problem, whose resolution is reduced to the search for the optimal solutions (fuzzy models), in order to satisfy the performance criteria and the predefined constraints. In recent years, researchers have used several algorithms to optimize the structures and parameters of the T-S model. For instance, particle swarm optimization (PSO) has been utilized in many applications [9, 10] given the small number of parameters to adjust, its easy implementation, rapid convergence and

its ability to produce high-quality solutions within a shorter calculation time. The combination of T-S fuzzy systems and PSO algorithms offers a powerful and flexible approach to solve a wide range of optimization problems. By exploiting the strengths of each technique, this approach allows developing more accurate, robust and interpretable models. However, the PSO is easily trapped in a local minimum and it is difficult to guarantee that the fuzzy models obtained will have good performance and the optimized fuzzy model largely depends on the performance of this algorithm.

To deal with these weaknesses, numerous improved versions of PSO and several hybrid methods were suggested [11–13]. In [14], the PSO algorithm was implemented to optimize the 5 parameters of PID controller applying El-Khazali's approach in order to minimize several error functions, satisfying some step response specifications such as the set of time domain and frequency domain constraints. In [15], the population was divided into many small swarms, different grouping strategies were used and the exchange between various small swarms improved the population diversity. Work [16] proposed a dynamic multiple swarms to solve multiobjective problems applying 2 main strategies: the swarm growth strategy and the swarm decay strategy. Besides, in [17] a methodology to automatically extract fuzzy T-S models from data using PSO was developed. In their approach, the parameters and the structures of fuzzy models were encoded in a particle and evolved together to obtain simultaneously the optimal structure and parameters. A new method, where the population was divided into 4 subswarms and heterogeneous search strategies were used to accomplish the optimization task, was applied in [18]. In this method a new strategy was applied under the so-called OptiFel to extract the structure and parameters of the T-S model. In the multiswarm PSO (MsPSO) algorithm used a homogeneous search strategy for all particles and in each subswarm, which reduced the convergence rate. In [19] authors suggested a novel cooperation strategy C-MsPSO based on the distribution of populations into 4 subswarms; each of which used inertia weight parameters and specific acceleration coefficients. This strategy allowed minimizing the risk of trapping the algorithm by the local optima.

In this article, an optimization algorithm, called improved multiswarm particle swarm optimization (I-MsPSO), is introduced to identify fuzzy T-S type models. In I-MsPSO, the population is divided into 4 subswarms; each of which ensures the internal search strategy relying on inertia weight parameters and specific acceleration coefficients. A new parameter search strategy applied by the fuzzy system T-S, called specific Takagi-Sugeno modeling (STaSuM), is also presented with the I-MsPSO algorithm to improve the search performance and ensure that the resulting fuzzy models will be highly efficient. The main contributions of this paper are:

- dividing the population into 4 subcooperative swarms in I-MsPSO algorithm.
- In this algorithm, each subswarm utilizes specific parameters (the subswarm S1 employs sigmoid inertia weights and constant acceleration coefficients, while subswarm S2 uses linear varying inertia weights and constant acceleration coefficients and subswarm S3 employs adaptive inertia weights and the coefficient of the constant accelerations).

- Determining the structure and parameters of the fuzzy models, coded in a particle, in STaSuM.

Preliminaries. Optimization problem. An optimization problem is defined by an objective function, a set of variables, a set of equality (or inequality) constraints and a search space formed by the set of the possible problem solutions where each dimension corresponds to a variable. Depending on the type of the problem to be solved, the best solution consists in finding an extreme value, also called extremum (i.e. the minimum or maximum of this objective function). In fact, an optimization problem corresponds to solving the following problem: min/max (function) under the constraint [20, 21]. It can be mono-objective or multiobjective (several objective functions must be optimized), static or dynamic (the objective function changes over time) and with or without constraints. In the literature many methods, such as Newton's method [22], linear programming methods [23], the simplex method and the gradient method [24] were introduced to obtain the optimal solution of the optimization problem in a reasonable time. They require that the objective function should have a minimum of characteristics such as convexity, continuity or differentiability.

PSO algorithm. PSO is a non-specific heuristic optimization algorithm like evolutionary algorithms, tabu search or ant colonies [25–27]. Its convergence speed also makes it efficiently used in dynamic optimization. Due to its multiple advantages, such as a rapid convergence, ease of implementation and wide search range, PSO has been employed in a variety of research fields and applications. The swarm's particles are initially dispersed randomly over the search space, where each particle has a random displacement position and speed. Thereafter, the algorithm can, at each instance, access its current position; memorize the best solution; communicate with neighboring particles; obtain, from each of them, its best performance; and modify its speed according to better solutions. The displacement of a particle between iteration t and iteration $t+1$ is formulated analytically by the following velocity (1) and position relations (2):

$$v_i(t+1) = wv_i(t) + c_1r_1[x_{pbest} - x_i(t)] + c_2r_2[x_{gbest} - x_i(t)]; \quad (1)$$

$$x_i(t+1) = x_i(t) + v_i(t+1), \quad (2)$$

where x_{pbest} is the best position determined by the i^{th} particle; w is a constant called the inertia weight; c_1, c_2 are the acceleration coefficients while r_1 and r_2 are randomly generated by a uniform distribution in $[0, 1]$; x_{gbest} is the best overall position found by the population.

Thus, to make its next move, each particle applies the following steps:

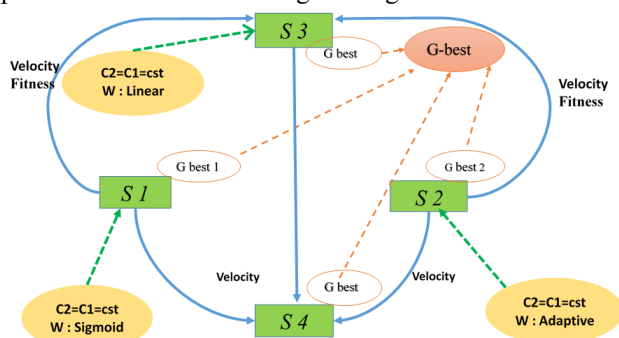
- follow its speed;
- return to its best performance;
- move towards the best performance of its neighbor.

T-S fuzzy model. Although several fuzzy models were introduced in the literature and the most commonly used ones are: Mamdani type model, Takagi-Sugeno-Kong type model and T-S type model. The main difference between these models lies in their consequent part. In fact, a fuzzy model is based on the linguistic partitioning of the values of its variables. The input (premises variables) and output (consequent variables) values are described by fuzzy sets having membership functions. In the fuzzy model of the T-S, the premises of the rules are formulated symbolically and the conclusions

$$R^i : \text{if } x_1 \text{ is } A_1^i, x_2 \text{ is } A_2^i, \dots, x_n \text{ is } A_n^i \text{ then} \quad (2)$$
$$y_i = w_i^T x + b_i, i = 1, 2, \dots, m,$$

The output of the fuzzy model can be calculated by a weighted mean defuzzification, as shown below:

$$y = \sum_{i=1}^m \mu_i y_i / \sum_{i=1}^m \mu_i, \quad (4)$$

$$\mu_i(x) = \prod_{i=1}^n h_i(x), \quad (5)$$
$$h_i(x) = \exp\left(\left(x_i - c_{ij}\right)^2 / \sigma_{ij}\right). \quad (6)$$


I-MsPSO algorithm can be summarized as follows:

Begin.

End.

$$\lim_{t \rightarrow +\infty} x_i(t) = p_i, \quad (7)$$
$$x(t+1) = F \cdot x(t) + R \cdot E, \quad (8)$$
$$x(t) = [x_t^1, x_t^2, x_t^3, x_t^4, x_{t-1}^1, x_{t-1}^2, x_{t-1}^3], \quad (9)$$
$$E=[p^{(1)}, p^{(2)}, p^{(3)}, p^{(4)}, g]^T, \quad (10)$$
$$\begin{cases} \varphi_1 = v_{11} + v_{12} = c_1 r_{11} + c_2 r_{12} \\ \varphi_2 = v_{21} + v_{22} = c_1 r_{21} + c_2 r_{22}, \\ \varphi_3 = v_{31} + v_{32} = c_1 r_{31} + c_2 r_{32} \end{cases} \quad (11)$$
$$x_{t+1}^{(l)} = x_t^{(l)} + v_{t+1}^{(l)} = x_t^{(l)}(1 + w_s - \phi_1) - w_s x_{t-1}^{(l)} + v_{11} p_t^{(l)} + v_{22} g_t, \quad (12)$$

51

$$w_s = \frac{0.9 \cdot \text{numiter} - 0.5i}{\text{numiter}}, \quad (13)$$

where *numiter* is the maximum number of the iterations; *i* is the current iteration.

The equation used to calculate the position of a particle in S2 is:

$$x_{t+1}^{(2)} = x_t^{(2)} + v_{t+1}^{(2)} = x_t^{(2)}(1 + w_a - \varphi_2) - w_a x_{t-1}^{(2)} + v_{11} p_t^{(2)} + v_{22} g_t, \quad (14)$$

where w_a is the adaptive inertia weight:

$$w_a(i) = w_{\max} + (w_{\max} - w_{\min}) \cdot \left(\frac{e^{x(i)} - 1}{e^{x(i)} + 1} \right), \quad (15)$$

where $x_i = (g_{\text{best}} - i) / (g_{\text{best}} + i)$; w_{\min} , w_{\max} are the initial and the final values of inertia weight; *i* is the current iteration.

In the subswarm S3, the equation applied to obtain the position of the particles is:

$$x_{t+1}^{(3)} = x_t^{(3)} + w_L \left[\frac{\gamma}{\gamma_1} v_{t+1}^{(1)} + \frac{\gamma}{\gamma_2} v_{t+1}^{(2)} + v_t^{(3)} \right] + v_{31} [p_t^{(3)} - x_t^{(3)}] + v_{32} [g_t - x_t^{(3)}], \quad (16)$$

where w_L is the linear varying inertia weight represented by the following equation; $\gamma = \gamma_1 + \gamma_2$; γ_1 , γ_2 are the fitness values of the particles in the subswarm S1 and S2. As r_1 and r_2 , r_3 and r_4 are vectors of the random numbers.

$$w_L(i) = \left(\frac{\text{numiter} - 1}{\text{numiter}} \right) (w_{\min} - w_{\max}) + w_{\max}. \quad (17)$$

The equation employed to compute the location of a particle in S4 is:

$$x_{t+1}^{(4)} = \alpha_1 x_t^{(4)} + \alpha_2 p_t^{(4)} + \alpha_3 g_t + v_{t+1}^{(4)}. \quad (18)$$

In this study, 3 impact factors ($\alpha_1 - \alpha_3$) are used to determine the influence of the past information on the current position of the particles within subswarm S4. They are constrained by this expression $\alpha_1 + \alpha_2 + \alpha_3 = 1$. In the performed analysis, the following values were assigned to the impact factors: $\alpha_1 = 1/6$, $\alpha_2 = 1/3$, $\alpha_3 = 1/2$. The bigger α_i ($i = 1, 2, 3$) was the larger the effect of the previous information on the current search would be, and vice versa. The larger effect of the previous information on the current search will be, and vice versa. As shown in (18), the different impact factors regulate the effect of the historical data on the particle's location within S4.

In a convergence analysis, researchers observed that particles within each subswarm converge towards stable positions defined by the limits presented in (19) – (22):

$$\lim_{t \rightarrow +\infty} x^{(1)} = \frac{c_1}{2} p^{(1)} + \frac{c_2}{2} g_{\text{best}}, \quad (19)$$

$$\lim_{t \rightarrow +\infty} x^{(2)} = \frac{c_1}{2} p^{(2)} + \frac{c_2}{2} g_{\text{best}}, \quad (20)$$

$$\lim_{t \rightarrow +\infty} x^{(3)} = w c_1 (p^{(1)} + p^{(2)}) + \frac{c_1}{2} p^{(3)} + g_{\text{best}} (2w c_2 + \frac{c_2}{2}), \quad (21)$$

$$\lim_{t \rightarrow +\infty} x^{(4)} = \frac{(1-w)c_1}{2} (p^{(1)} + p^{(2)}) - \frac{c_1}{2} p^{(3)} + \alpha_2 p^{(4)} + g_{\text{best}} ((1-2w)c_2 - \frac{c_2}{2} + \alpha_3). \quad (22)$$

Methodology of STaSuM based on I-MsPSO.

A new parameter search strategy applied by the fuzzy system T-S, called STaSuM, is also presented with the I-MsPSO algorithm to improve the search performance.

STaSuM framework for T-S fuzzy model identification is presented in this section. The structure and parameters of T-S fuzzy model are all encoded in a particle. The following sections provide the details.

Particle mapping and objective function. In the identification process, the structure and parameters of the fuzzy model were all coded in a particle of the I-MsPSO algorithm, and the mean square error (MSE) value was used to choose the best local position in a swarm and the global optimum in a population. A single nest in the I-MsPSO algorithm is shown in Fig. 3. Each particle is specified as a vector corresponding to a particular fuzzy model and each vector corresponds to a fuzzy rule made up of the premise parameters (structure) and the consequent parameters.

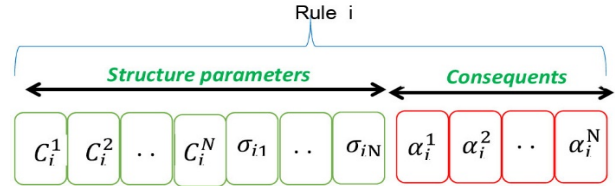


Fig. 3. i^{th} rule encoded in a particle. The code consists of 2 necessary items: structure and consequent parameters

To create an accurate mathematical model, an objective function was applied to measure the difference between the output of the model and that of the actual process. MSE was utilized to measure the difference between the output of the model and the real value. MSE was mathematically formulated as:

$$MSE = \frac{1}{N} \sum_{k=1}^N (y_k - \hat{y}_k)^2, \quad (23)$$

where N is the number of observations; y_k is the actual output; \hat{y}_k is the output estimated by the model.

Implementation of STaSuM. Algorithm 2 describes the implementation of STaSuM. The rules of the T-S fuzzy model were encoded in the particle x^s and the MSE value was utilized to select the best solution in the subswarm. The best overall structure was obtained from the 4 optimal g_{best} in the subswarms $s = 1, 2, 3, 4$.

Algorithm 2. The STaSuM algorithm

1. Initialization.
 - (a) Set the number of iterations and rules s .
 - (b) Specify the size of each subswarm.
 - (c) Initialize the position of particle.
 - (d) Initialize the position of particle.
 - (e) Determine the global best nest g .
2. Set the number of rules as constant.
3. Termination check.
 - (a) If the termination criterion holds stop.
 - (b) Else go to Step 4.
4. For do.
 - (a) Update the position x_k^s according to Equations 12, 14, 16, 18, respectively.
 - (b) Update the velocity v_k^s according to Equation 1.
 - (c) Evaluate the fitness of the i^{th} particle $f(x_k^s)$
 - (d) If the $f(x_k^s)$ is better than $f(p_k^s)$, then $p_k^s = x_k^s$
 End For
 Update $g_{\text{best}} = \arg \{ \min \{ p_{\text{best}} \} \}$.
 End For
 Update $g_{\text{best}} = \arg \{ \min \{ g_{\text{best}} \} \}$.
 Set $t = t + 1$
5. Go to step 3.

Simulation result and discussion. This section is composed of 2 parts. In the initial part, the performance of the I-MsPSO algorithm is evaluated through numerical experiments using benchmark functions and engineering problems. On the other hand, the subsequent part shows the effectiveness of the STaSuM method applied in nonlinear systems.

Convergence analysis of I-MsPSO. To validate the performance and efficiency of the proposed algorithm, 12 benchmark functions from the CEC-2017 test set were selected to test the I-MsPSO algorithm [30]. The upper limit for optimization processes was set at 1000, and each test run a maximum of 30 times. The experimental machine in use is equipped with a 3rd generation i3 processor running at 2.5 GHz with a storage capacity of 128 GB. The utilized programming language is MATLAB. The maximum number of iterations in the numerical experiences was set at 1000 on each of the 12 reference functions for each algorithm. Each experiment was carried out independently of the reference functions. The mean values and standard deviations are presented in Table 1. Figures 4–6 show the average convergence characteristics of each approach on the reference functions. A comparison of the proposed algorithm to common strategies is presented in this section. The performances of different strategies, including adaptive MsPSO (AMsPSO), linear time-varying (L-MsPSO) and standard MsPSO, were analyzed in the experiments carried out on 12 static problems.

Table 1

The results on the 12 benchmark functions of each algorithm

Function	F1	F2
L-MsPSO	$4.97 \cdot 10^{-121} \pm 9.90 \cdot 10^{-121}$	$4.26 \cdot 10^{-60} \pm 1.24 \cdot 10^{-59}$
A-MsPSO	$5.23 \cdot 10^{-153} \pm 5.23 \cdot 10^{-150}$	$2.94 \cdot 10^{-79} \pm 2.40 \cdot 10^{-74}$
MsPSO	$4.01 \cdot 10^{-108} \pm 7.80 \cdot 10^{-108}$	$3.82 \cdot 10^{-54} \pm 6.18 \cdot 10^{-54}$
I-MsPSO	$2.83 \cdot 10^{-186} \pm 2.52 \cdot 10^{-183}$	$7.14 \cdot 10^{-92} \pm 6.12 \cdot 10^{-91}$
Function	F3	F4
L-MsPSO	$2.97 \cdot 10^{-119} \pm 9.22 \cdot 10^{-118}$	$3.02 \cdot 10^{-60} \pm 8.21 \cdot 10^{-60}$
A-MsPSO	$1.60 \cdot 10^{-150} \pm 1.60 \cdot 10^{-149}$	$1.121 \cdot 10^{-76} \pm 1.21 \cdot 10^{-73}$
MsPSO	$9.30 \cdot 10^{-105} \pm 2.92 \cdot 10^{-104}$	$7.37 \cdot 10^{-53} \pm 2.24 \cdot 10^{-52}$
I-MsPSO	$1.03 \cdot 10^{-178} \pm 1.051 \cdot 10^{-178}$	$1.33 \cdot 10^{-94} \pm 1.01 \cdot 10^{-93}$
Function	F5	F6
L-MsPSO	$2.89 \cdot 10^{-01} \pm 2.71 \cdot 10^{-01}$	0
A-MsPSO	$2.89 \cdot 10^{-01} \pm 2.00 \cdot 10^{-01}$	0
MsPSO	$2.89 \cdot 10^{-01} \pm 3.60 \cdot 10^{-02}$	0
I-MsPSO	$2.89 \cdot 10^{-01} \pm 0$	0
Function	F7	F8
L-MsPSO	$1.001 \cdot 10^{-81} \pm 3.966 \cdot 10^{-81}$	$3.995 \cdot 10^{-43} \pm 7.59 \cdot 10^{-43}$
A-MsPSO	$1.401 \cdot 10^{-81} \pm 3.966 \cdot 10^{-81}$	$5.601 \cdot 10^{-43} \pm 8.00 \cdot 10^{-43}$
MsPSO	$1.451 \cdot 10^{-81} \pm 3.966 \cdot 10^{-81}$	$3.005 \cdot 10^{-43} \pm 8.78 \cdot 10^{-43}$
I-MsPSO	$1.321 \cdot 10^{-81} \pm 3.966 \cdot 10^{-81}$	$4.99 \cdot 10^{-43} \pm 8.111 \cdot 10^{-44}$
Function	F9	F10
L-MsPSO	0	$4.665 \cdot 10^{-43} \pm 8.52 \cdot 10^{-43}$
A-MsPSO	0	$4.665 \cdot 10^{-43} \pm 8.52 \cdot 10^{-43}$
MsPSO	0	$4.665 \cdot 10^{-43} \pm 8.52 \cdot 10^{-43}$
I-MsPSO	0	$4.665 \cdot 10^{-43} \pm 8.52 \cdot 10^{-43}$
Function	F11	F12
L-MsPSO	0	$3.65 \cdot 10^{-43} \pm 8.3 \cdot 10^{-44}$
A-MsPSO	0	$4.65 \cdot 10^{-40} \pm 7.52 \cdot 10^{-44}$
MsPSO	0	$4.115 \cdot 10^{-43} \pm 7.51 \cdot 10^{-44}$
I-MsPSO	0	$3.52 \cdot 10^{-43} \pm 8.114 \cdot 10^{-42}$

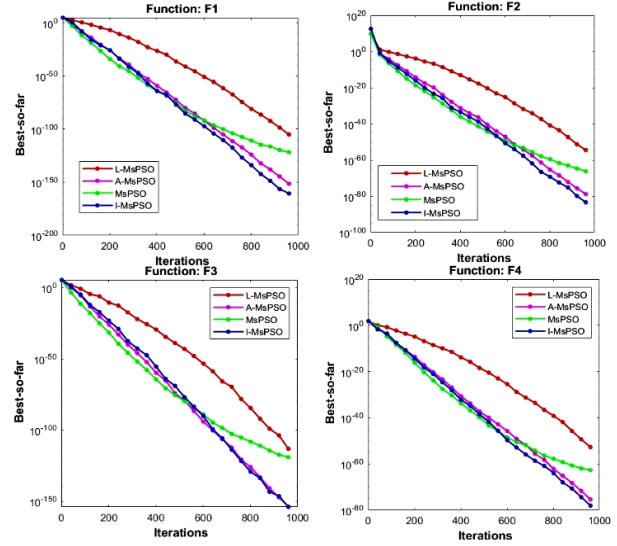


Fig. 4. Convergence characteristics on 4 reference functions (F1–F4) with 30 dimensions

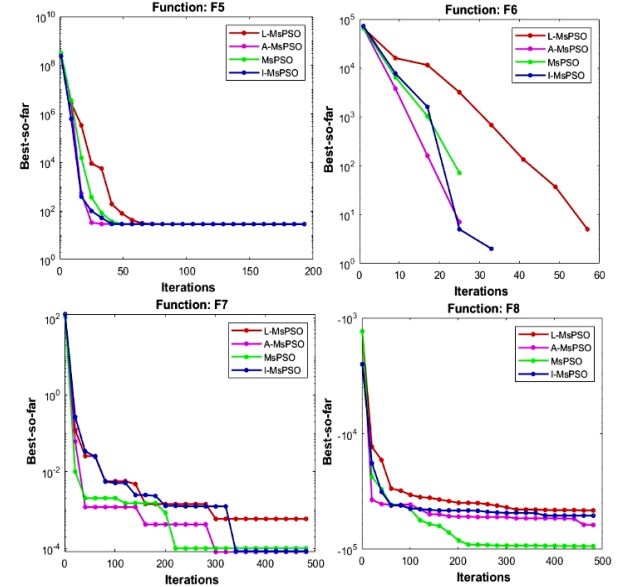


Fig. 5. Convergence characteristics on 4 reference functions (F5–F8) with 30 dimensions

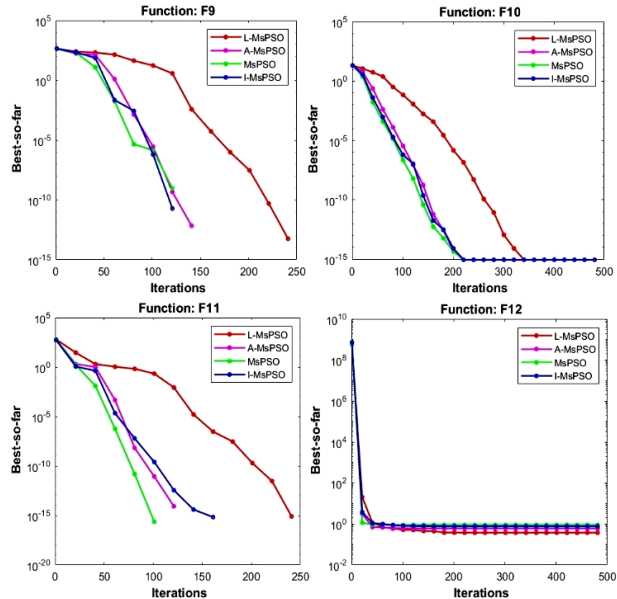


Fig. 6. Convergence characteristics on 4 reference functions (F9–F12)

The mean values and the standard deviation throughout the optimization runs are shown in Table 1. On the other hand, Fig. 4–6 outline the average convergence characteristics to each approach on the reference functions. Figures 4–6 demonstrate that I-MsPSO performs better than the other PSO variants on the benchmark functions. As exposed in Fig. 4–6 I-MsPSO reaches the target optima in the majority of benchmark functions (Table 1). The results obtained by I-MsPSO are superior to those of the other PSO versions on each benchmark function, with the exception of the Function F8 and F11.

Application of I-MsPSO to engineering problems.

This part examines the I-MsPSO's effectiveness by extending its application to solve real-world engineering optimization problems. Specifically, the next section delves into the optimization of the tension/compression spring, while the after section summarizes the findings provided by pressure vessel design. The performance of I-MsPSO is, then, benchmarked against those of the existing algorithms such as PSO [31], genetic algorithm (GA) [32], velocity pausing particle swarm optimization (VPPSO) [33] and grey wolf optimizer (GWO) [34].

Tension/compression spring design (TCSD). TCSD problem is a classic engineering problem whose primary objective consists in minimizing the spring's weight. This optimization task requires finding the lightest possible spring while meeting specific design constraints, including limitations on shear stress, surge frequency and deflection. It ultimately translates into a minimization problem where the weight of the spring is minimized while adhering to all boundary and constraints conditions. The design variables include the wire diameter $d(X_1)$, the mean coil diameter $h(X_2)$, and the number of turns of the spring $P(X_3)$. The following subsection outlines the objective functions and the constraints associated with these three optimization variables. Consider:

$$X = [d, h, P] = [X_1, X_2, X_3]. \quad (24)$$

Minimize:

$$F(x) = X_1^2 X_2 (X_3 + 2). \quad (25)$$

Subject to:

$$g_1(X) = 1 - \frac{X_2^3 X_3}{71785 X_1^4} \leq 0; \quad (26)$$

$$g_2(X) = \frac{4X_2^2 - X_1 X_2}{12566(X_1^3 X_2 - X_1^4)} + \frac{1}{5108 X_1^2} - 1 \leq 0; \quad (27)$$

$$g_3(x) = 1 - \frac{140.45 X_1}{X_2^2 X_3} \leq 0; \quad (28)$$

$$g_4(x) = \frac{X_1 + X_2}{1.5} \leq 0. \quad (29)$$

Variable range: $0.05 \leq X_1 \leq 2$, $0.25 \leq X_2 \leq 1.3$, $2 \leq X_3 \leq 15$.

Table 2 illustrates the statistical results of the TCSD problem. Each algorithm was independently run 50 times, the maximum number of iterations and the population size were set to 1000 and 30, respectively. Overall, the I-MsPSO algorithm ranks first since it explores a solution to make the spring weight smaller for the TCSD problem. VPPSO offer similar solution, ranking second.

Table 2
Optimal solutions of tension/ compression spring design problem optimized by different algorithms

Algorithm	d	H	p	Value
GA	0.0598	0.3521	11.5980	0.032
GWO	0.0513	0.3474	11.8763	0.0127
PSO	0.0500	0.3104	14.998	0.0131
VPPSO	0.0525	0.3756	10.2659	0.0127
I-MsPSO	0.0516	0.356	11.3186	0.01266

Pressure vessel design (PVD). Pressure vessels typically comprise a cylindrical shell and 2 hemispherical heads, fabricated through the welding processes. The design objective is to minimize the overall cost, encompass material acquisition, form operations, and weld expenses. This optimization problem involves 4 design variables: cylinder wall thickness $E_s(X_1)$, the thickness of the spherical cover $E_h(X_2)$, cylinder inner diameter $D(X_3)$, and cylinder length $L(X_4)$. A description of the objective functions and constraints relevant to these 3 optimization variables is presented. Consider:

$$X = [E_s, E_h, D, L] = [X_1, X_2, X_3, X_4]. \quad (30)$$

Minimize:

$$F(x) = 0.6224 X_1 X_3 X_4 + 1.7781 X_2 X_3^2 + 3.1661 X_1^2 X_4 + 19.84 X_1^2 X_3. \quad (31)$$

Subject to:

$$g_1(X) = -X_1 + 0.0193 X_3 \leq 0; \quad (32)$$

$$g_2(X) = -X_2 + 0.00954 X_3 \leq 0; \quad (33)$$

$$g_3(X) = -\pi X_3^2 X_4 - \frac{4}{3} \pi X_3^3 + 1296000 \leq 0; \quad (34)$$

$$g_4(X) = X_4 - 240 \leq 0. \quad (35)$$

Variable range:

$$X_1, X_2 \in \{1 \cdot 0.0625, 2 \cdot 0.0625, \dots, 99 \cdot 0.0625\},$$

$$10 \leq X_3 \text{ and } X_4 \leq 200.$$

Table 3 presents the best solutions of all algorithms. It is evident that I-MsPSO achieved the best result.

Table 3
Optimal solutions of PVD problem optimized by different algorithms

Algorithm	X_1	X_2	X_3	X_4	Optimal cost
GA	0.810	0.436	42.096	176.655	6059.945
GWO	0.812	0.4375	42.098	176.636	6059.719
PSO	0.875	0.4375	45.288	140.743	6096.830
VPPSO	0.8125	0.4375	42.0979	176.646	6059.850
I-MsPSO	0.8125	0.4375	42.0973	176.654	6059.714

Application of STaSuM to Box-Jenkins gas furnace data. Due to its non-linear nature, the Box-Jenkins system [29] has become widely adopted to validate the performance of the recently developed modeling methods. The used dataset contained 296 paired input-output observations $y(t)$, $u(t)$ for a gas furnace process, where t ranged from 1 to 296. At each sampling time t , $u(t)$ is the input gas flow rate and $y(t)$ is the output CO₂ concentration. The simulation was conducted to predict $y(t)$ based on $y(t_1)$, $y(t_2)$, $u(t_1)$, $u(t_2)$. The first 148 input-output data were employed as training data and the final 148 were utilized as testing data in order to validate the efficiency of the suggested method. The population size in the 4 subswarms was set to 6, the number of rules was 3, the number of iterations was 50, the acceleration coefficients were set according to the equations and the

inertia weight was chosen as shown in (13), (15), (17). In prediction case, compared to the A-MsPSO algorithm and other algorithms mentioned in Table 4 the I-MsPSO algorithm had the best performance index of 0.104.

Table 4
Identification results obtained by the different methods on the Box-Jenkins system

Reference	Number of inputs	Number of rules	MSE
[35]	6	—	0.202
[36]	2	3	0.110
[37]	2	4	0.148
[38]	2	2	0.161
[18]	2	3	0.106
I-MsPSO	2	3	0.104

Figure 7 shows the STaSuM model's prediction, the actual outputs and the errors between them for the training set of data. The other 148 data points were used to validate the generalization performance of the obtained fuzzy mode – Fig. 8 reveals the test results. Their respective related MSEs are 0.057 and 0.145.

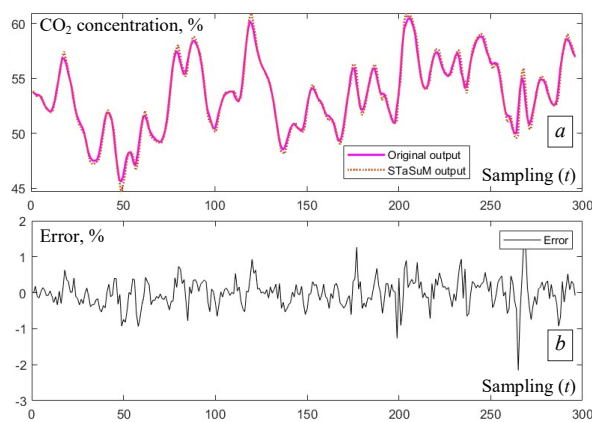


Fig. 7. Modeling with 296 pairs of observations: *a* – the real output and the output of the fuzzy model; *b* – the estimation error

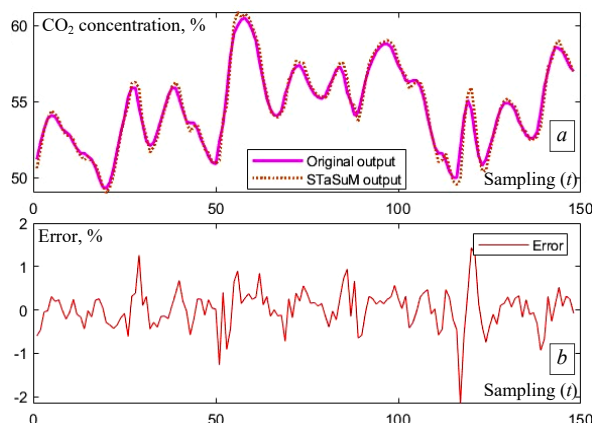


Fig. 8. Testing with 148 pairs of observations: *a* – the real output and the output of the fuzzy model; *b* – the estimation error

Table 5 presents a comparison with various models and demonstrates that our method's generalization ability outperforms that reported in the literature. Therefore, it can be noticed that the real output and the estimated output were within a negligible error. These results were justified by observing the values of the MSE performance index given in Table 5. The latter reveals that the performance indices obtained by the developed model during the identification and validation phase are the best, compared to those provided by other models mentioned in this table, even in the case of reduced number of input variables and minimized number of

rules, which guarantees better quality of approximation. The results show that the proposed model has more powerful generalization ability with a good accuracy in modeling the system of the Box-Jenkins gas furnace dataset.

Table 5
Prediction results provided the different methods on the Box-Jenkins system

Reference	Number of rules	MSE identification	MSE validation
[36]	3	0.059	0.152
[37]	6	0.022	0.236
[39]	3	0.0159	0.126
[18]	3	0.058	0.146
I-MsPSO	3	0.057	0.145

Conclusions. In this paper, improved multiswarm particle swarm optimization (I-MsPSO) algorithm was used to optimize and estimate the parameters of Takagi-Sugeno (T-S) fuzzy systems. In the proposed specific Takagi-Sugeno modeling (STaSuM), the structure and the parameters of T-S fuzzy model were encoded into a nest vector to find the optimal solution simultaneously. The main advantage of STaSuM is that it can keep the inner-correlation between the system structure and the parameters, and more highly-accurate model than the traditional 2-stage identification process method. I-MsPSO divided the population into 4 subswarms; each of which utilized a search strategy independent of the other. The exchange of information between the 4 subswarms allowed collecting useful messages from the subswarms, maintaining particle diversity and improving the search capability. The best personal interactive learning strategy increased the convergence speed. The experimental results on 12 benchmark functions proved that the proposed algorithm had good comprehensive performance in the optimization of unimodal and multimodal functions and kept a good balance between exploration and exploitation. Additionally, the developed method was applied to estimate blur T-S system models using a fuzzy model STaSuM. The obtained finding showed experimental results proved that the suggested method can produce robust, reliable and effective fuzzy T-S models. The obtained finding showed experimental results proved that the suggested method can produce robust, reliable and effective fuzzy T-S models. In our upcoming work, we will: apply I-MsPSO to solve real industry problems; use I-MsPSO in solar PV; analyze the influence of different levels of noise on the accuracy of this algorithm.

Conflict of interest. The authors declare that they have no conflicts of interest.

REFERENCES

1. Mamdani E.H., Assilian S. An experiment in linguistic synthesis with a fuzzy logic controller. *International Journal of Man-Machine Studies*, 1975, vol. 7, no. 1, pp. 1-13. doi: [https://doi.org/10.1016/S0020-7373\(75\)80002-2](https://doi.org/10.1016/S0020-7373(75)80002-2).
2. Alonso Moral J.M., Castiello C., Magdalena L., Mencar C. An Overview of Fuzzy Systems. In: *Explainable Fuzzy Systems. Studies in Computational Intelligence*, 2021, vol. 970, pp. 25-47. doi: https://doi.org/10.1007/978-3-030-71098-9_2.
3. Bas E., Egrioglu E. A fuzzy regression functions approach based on Gustafson-Kessel clustering algorithm. *Information Sciences*, 2022, vol. 592, pp. 206-214. doi: <https://doi.org/10.1016/j.ins.2022.01.057>.
4. Krasnov D., Davis D., Malott K., Chen Y., Shi X., Wong A. Fuzzy C-Means Clustering: A Review of Applications in Breast Cancer Detection. *Entropy*, 2023, vol. 25, no. 7, art. no. 1021. doi: <https://doi.org/10.3390/e25071021>.
5. Wu X., Zhou H., Wu B., Zhang T. A possibilistic fuzzy Gath-Geva clustering algorithm using the exponential distance. *Expert Systems with Applications*, 2021, vol. 184, art. no. 115550. doi: <https://doi.org/10.1016/j.eswa.2021.115550>.

6. Gogineni V.C., Naumova V., Werner S., Huang Y.-F. Graph Kernel Recursive Least-Squares Algorithms. *2021 Asia-Pacific Signal and Information Processing Association Annual Summit and Conference (APSIPA ASC)*, Tokyo, Japan, 2021, pp. 2072-2076.
7. Gholinejad S., Amiri-Simkooei A. Multivariate Weighted Total Least Squares Based on the Standard Least-Squares Theory. *Journal of Surveying Engineering*, 2023, vol. 149, no. 4, art. no. 04023008. doi: <https://doi.org/10.1061/JSUED2.SUENG-1424>.
8. Björck A. *Numerical methods for least squares problems*. 2nd edition. SIAM Publ., 2024. 494 p.
9. Saeed H., Mehmood T., Khan F.A., Shah M.S., Ullah M.F., Ali H. An improved search ability of particle swarm optimization algorithm for tracking maximum power point under shading conditions. *Electrical Engineering & Electromechanics*, 2022, no. 2, pp. 23-28. doi: <https://doi.org/10.20998/2074-272X.2022.2.04>.
10. Labeled M.A., Zellagui M., Benidir M., Sekhane H., Tebbakh N. Optimal hybrid photovoltaic distributed generation and distribution static synchronous compensators planning to minimize active power losses using adaptive acceleration coefficients particle swarm optimization algorithms. *Electrical Engineering & Electromechanics*, 2023, no. 6, pp. 84-90. doi: <https://doi.org/10.20998/2074-272X.2023.6.15>.
11. Jain M., Saihpal V., Singh N., Singh S.B. An Overview of Variants and Advancements of PSO Algorithm. *Applied Sciences*, 2022, vol. 12, no. 17, art. no. 8392. doi: <https://doi.org/10.3390/app12178392>.
12. Gomathi S., Mayurappriyan P.S., BabyPriya B. Performance Improvement of Grid-Tied PV System With Boost and Quadratic Boost Converters Using Innovative Hybridized HPO-PO MPPT. *Electric Power Components and Systems*, 2024, pp. 1-13. doi: <https://doi.org/10.1080/15325008.2024.2318399>.
13. Zanganeh M., Chaji A. A new aspect of the ApEn application to improve the PSO-ANFIS model to forecast Caspian Sea levels. *Regional Studies in Marine Science*, 2024, vol. 69, art. no. 103347. doi: <https://doi.org/10.1016/j.rsma.2023.103347>.
14. Momani S., Batiha I.M. Tuning of the Fractional-order PID Controller for some Real-life Industrial Processes Using Particle Swarm Optimization. *Progress in Fractional Differentiation and Applications*, 2022, vol. 8, no. 3, pp. 377-391. doi: <https://doi.org/10.18576/pfda/080303>.
15. Lin G., Zhao K., Wan Q. Takagi-Sugeno fuzzy model identification using coevolution particle swarm optimization with multi-strategy. *Applied Intelligence*, 2016, vol. 45, no. 1, pp. 187-197. doi: <https://doi.org/10.1007/s10489-015-0752-0>.
16. Yen G.G., Leong W.F. Dynamic Multiple Swarms in Multiobjective Particle Swarm Optimization. *IEEE Transactions on Systems, Man, and Cybernetics - Part A: Systems and Humans*, 2009, vol. 39, no. 4, pp. 890-911. doi: <https://doi.org/10.1109/TSMCA.2009.2013915>.
17. Zhao L., Qian F., Yang Y., Zeng Y., Su H. Automatically extracting T-S fuzzy models using cooperative random learning particle swarm optimization. *Applied Soft Computing*, 2010, vol. 10, no. 3, pp. 938-944. doi: <https://doi.org/10.1016/j.asoc.2009.10.012>.
18. Zdiri S., Chroua J., Zaafouri A. An Expanded Heterogeneous Particle Swarm Optimization Based on Adaptive Inertia Weight. *Mathematical Problems in Engineering*, 2021, vol. 2021, art. no. 4194263. doi: <https://doi.org/10.1155/2021/4194263>.
19. Zdiri S., Chroua J., Zaafouri A. Cooperative multi-swarm particle swarm optimization based on adaptive and time-varying inertia weights. *2021 IEEE 2nd International Conference on Signal, Control and Communication (SCC)*, 2021, pp. 200-207. doi: <https://doi.org/10.1109/SCC53769.2021.9768349>.
20. Tamura K. Evaluation-Number Constrained Optimization Problem and its Solution Strategy. *IEEE Transactions on Electrical and Electronic Engineering*, 2024, vol. 19, no. 4, pp. 490-506. doi: <https://doi.org/10.1002/tee.24000>.
21. Mezhoud N., Ayachi B., Amarouayache M. Multi-objective optimal power flow based gray wolf optimization method. *Electrical Engineering & Electromechanics*, 2022, no. 4, pp. 57-62. doi: <https://doi.org/10.20998/2074-272X.2022.4.08>.
22. Fornæss J.E., Hu M., Truong T.T., Watanabe T. Backtracking New Q-Newton's Method, Newton's Flow, Voronoi's Diagram and Stochastic Root Finding. *Complex Analysis and Operator Theory*, 2024, vol. 18, no. 5, art. no. 112. doi: <https://doi.org/10.1007/s11785-024-01558-6>.
23. Mayer J. *Stochastic Linear Programming Algorithms. A Comparison Based on a Model Management System*. Routledge Publ., 2022. 164 p. doi: <https://doi.org/10.1201/9780203738269>.
24. Braun G., Carderera A., Combettes C.W., Hassani H., Karbasi A., Mokhtari A., Pokutta S. Conditional Gradient Methods. *arXiv preprint*, 2025. doi: <https://doi.org/10.48550/arXiv.2211.14103>.
25. Gad A.G. Particle Swarm Optimization Algorithm and Its Applications: A Systematic Review. *Archives of Computational Methods in Engineering*, 2022, vol. 29, no. 5, pp. 2531-2561. doi: <https://doi.org/10.1007/s11831-021-09694-4>.
26. Labeled M.A., Zellagui M., Benidir M., Sekhane H., Tebbakh N. Optimal hybrid photovoltaic distributed generation and distribution static synchronous compensators planning to minimize active power losses using adaptive acceleration coefficients particle swarm optimization algorithms. *Electrical Engineering & Electromechanics*, 2023, no. 6, pp. 84-90. doi: <https://doi.org/10.20998/2074-272X.2023.6.15>.
27. Anwar N., Hanif A., Ali M.U., Zafar A. Chaotic-based particle swarm optimization algorithm for optimal PID tuning in automatic voltage regulator systems. *Electrical Engineering & Electromechanics*, 2021, no. 1, pp. 50-59. doi: <https://doi.org/10.20998/2074-272X.2021.1.08>.
28. Song R., Huang S., Xiong L., Zhou Y., Li T., Tan P., Sun Z. Takagi-Sugeno Fuzzy Parallel Distributed Compensation Control for Low-Frequency Oscillation Suppression in Wind Energy-Penetrated Power Systems. *Electronics*, 2024, vol. 13, no. 19, art. no. 3795. doi: <https://doi.org/10.3390/electronics13193795>.
29. Hadjidi N., Benbrahim M., Ounnas D., Mouss L.H. Global maximum power point tracking method for photovoltaic systems using Takagi-Sugeno fuzzy models and ANFIS approach. *Electrical Engineering & Electromechanics*, 2025, no. 2, pp. 31-38. doi: <https://doi.org/10.20998/2074-272X.2025.2.05>.
30. Amézquita L., Castillo O., Cortes-Antonio P. A New Variant of the Multiverse Optimizer Using Multiple Chaotic Maps and Fuzzy Logic for Optimization in CEC-2017 Benchmark Suite. *Studies in Computational Intelligence*, 2024, vol. 1149, pp. 267-283. doi: https://doi.org/10.1007/978-3-031-55684-5_18.
31. Kennedy J., Eberhart R. Particle swarm optimization. *Proceedings of ICNN'95 - International Conference on Neural Networks*, 1995, vol. 4, pp. 1942-1948. doi: <https://doi.org/10.1109/ICNN.1995.488968>.
32. Holland J.H. Genetic Algorithms. *Scientific American*, 1992, vol. 267, no. 1, pp. 66-72. doi: <https://doi.org/10.1038/scientificamerican0792-66>.
33. Shami T.M., Mirjalili S., Al-Eryani Y., Daoudi K., Izadi S., Abualigah L. Velocity pausing particle swarm optimization: a novel variant for global optimization. *Neural Computing and Applications*, 2023, vol. 35, no. 12, pp. 9193-9223. doi: <https://doi.org/10.1007/s00521-022-08179-0>.
34. Mirjalili S., Mirjalili S.M., Lewis A. Grey Wolf Optimizer. *Advances in Engineering Software*, 2014, vol. 69, pp. 46-61. doi: <https://doi.org/10.1016/j.advengsoft.2013.12.007>.
35. Jenkins G.M., Box G.E.P. *Time Series Analysis: Forecasting and Control*. Holden-Day Publ., 1976. 575 p.
36. Cheung N.J., Ding X.-M., Shen H.-B. OptiFel: A Convergent Heterogeneous Particle Swarm Optimization Algorithm for Takagi-Sugeno Fuzzy Modeling. *IEEE Transactions on Fuzzy Systems*, 2014, vol. 22, no. 4, pp. 919-933. doi: <https://doi.org/10.1109/TFUZZ.2013.2278972>.
37. Tsekouras G.E. On the use of the weighted fuzzy c-means in fuzzy modeling. *Advances in Engineering Software*, 2005, vol. 36, no. 5, pp. 287-300. doi: <https://doi.org/10.1016/j.advengsoft.2004.12.001>.
38. Bagis A. Fuzzy rule base design using tabu search algorithm for nonlinear system modeling. *ISA Transactions*, 2008, vol. 47, no. 1, pp. 32-44. doi: <https://doi.org/10.1016/j.isatra.2007.09.001>.
39. Li C., Zhou J., Fu B., Kou P., Xiao J. T-S Fuzzy Model Identification With a Gravitational Search-Based Hyperplane Clustering Algorithm. *IEEE Transactions on Fuzzy Systems*, 2012, vol. 20, no. 2, pp. 305-317. doi: <https://doi.org/10.1109/TFUZZ.2011.2173693>.

Received 19.03.2025
Accepted 09.06.2025
Published 02.09.2025

S. Zdiri¹, Doctor of Technical Science,
M. Moulahi¹, Professor,
F. Messaoudi¹, Doctor of Technical Science,
A. Zaafouri¹, Professor,
¹National Higher Engineering School of Tunis (ENSIT),
Laboratory of Engineering of Industrial Systems and Renewable
Energy (LISIER), University of Tunis, Tunisia,
e-mail: zdiri_sami@yahoo.fr (Corresponding Author)

How to cite this article:

Zdiri S., Moulahi M., Messaoudi F., Zaafouri A. Takagi-Sugeno fuzzy model identification using improved multiswarm particle swarm optimization in solar photovoltaics. *Electrical Engineering & Electromechanics*, 2025, no. 5, pp. 49-56. doi: <https://doi.org/10.20998/2074-272X.2025.5.07>

V.Y. Romashko, L.M. Batrak

Regulation characteristics of a step-down pulse regulator in continuous and discontinuous conduction mode

Introduction. Pulse regulators (PRs) are widely used to regulate and stabilize the supply voltage of DC consumers. The main characteristic of any regulator is its regulation characteristic. In the general case, two modes of PR operation are possible: continuous conduction mode and discontinuous conduction mode in the inductance of the PR. **Problem.** When the PR transitions from one operating mode to another, its regulation characteristics change. In the continuous conduction mode, the regulation characteristic is a function of one variable. In the discontinuous conduction mode, the regulation characteristic becomes a function of two variables. Therefore, in such a mode, PR is described by a family of regulation characteristics. The **goal** of the work is to develop a mathematical model that describes the operation of the controller in both continuous and discontinuous conduction modes, as well as to determine the control characteristics that are valid for both of these modes. **Methodology.** In the work, using the example of a step-down type PR, the conditions for the PR transition from one operating mode to another are determined, as well as the dependence of the PR output voltage on the duration of the pause in the inductance current. **Results.** The influence of the parameters of the PR elements on the pause duration is analyzed. A graph of the family of PR control characteristics is constructed, which is valid for both continuous and discontinuous conduction modes. **Scientific novelty.** It is shown that when PR transitions to discontinuous conduction mode, its control characteristics shift towards higher output voltages. This shift is greater, the longer the pause duration in the inductance current. **Practical value.** It is determined that the specified ripple coefficient of the PR output voltage in the discontinuous conduction mode is provided by a smaller value of the LC product of the PR elements, compared to the continuous conduction mode. References 17, tables 2, figures 5.

Key words: discontinuous conduction mode, control characteristics of a pulse regulator, ripple coefficient of the output voltage.

Вступ. Імпульсні регулятори (ІР) широко використовують для регулювання та стабілізації напруги живлення споживачів постійного струму. Основною характеристикою будь-якого регулятора є його регульовальна характеристика. У загальному випадку можливі два режими роботи ІР – режим безперервного струму та режим переривчастого струму в індуктивності ІР. **Проблема.** При переході ІР від одного режиму роботи до іншого, його регульовальні характеристики змінюються. В режимі безперервного струму індуктивності регульовальна характеристика є функцією від однієї змінної. В режимі переривчастого струму регульовальна характеристика стає функцією двох змінних. Тому, в такому режимі, ІР описується сімейством регульовальних характеристик. **Метою** роботи є розробка математичної моделі, яка б описувала роботу ІР у режимах безперервного та переривчастого струму індуктивності, зокрема одержання регульовальних характеристик, які б були дійсними для обох вказаних режимів. **Методика.** В роботі на прикладі ІР понижувального типу визначено умови переходу ІР від одного режиму роботи до іншого, а також залежність вихідної напруги ІР від тривалості паузи у струмі індуктивності. **Результати.** Проаналізовано вплив параметрів елементів ІР на тривалість паузи. Побудовано графік сімейства регульовальних характеристик ІР, який є дійсним, як для режиму безперервного, так і переривчастого струму індуктивності. **Наукова новизна.** Показано, що при переході ІР до режиму переривчастого струму, його регульовальні характеристики зміщуються в сторону більших вихідних напруг. Це зміщення є тим більшим, чим більшою є тривалість паузи у струмі індуктивності. **Практична значимість.** Визначено, що заданий коефіцієнт пульсацій вихідної напруги ІР, у режимі переривчастого струму, забезпечується меншим значенням добутку LC елементів ІР, у порівнянні з режимом безперервного струму. Бібл. 17, табл. 2, рис. 5.

Ключові слова: режим переривчастого струму індуктивності, регульовальні характеристики імпульсного регулятора, коефіцієнт пульсації вихідної напруги.

Introduction. Pulse regulators (PRs) are widely used to regulate and stabilize the supply voltage of DC consumers [1–4]. Due to the widespread use of non-traditional and renewable sources of electrical energy, PRs have been used to match the output resistance of the electrical energy source with the load resistance, in order to extract the maximum possible power from the source [5–9]. The main characteristic of the PR is its regulation characteristic $U_{out} = f(t^*)$ – the dependence of the PR output voltage on the regulated parameter t^* , where $t^* = t_{cl} / T$ – the relative time of the closed state of the key t_{cl} during the period T . In the general case, two modes of operation of the PR are possible [10–13].

- mode of continuous current flow in the inductance;
- mode of intermittent current in the inductance.

At the moment of transition of the PR from one operating mode to another, its regulation characteristics change.

In the continuous current mode in the operating range, the average value of the voltage across the load does not depend on its resistance R . The current flowing through the PR inductance has a relatively small ripple. Since the variable component of this current is closed through the filter capacitor, the capacitance of this capacitor can be relatively small. In the intermittent conduction mode, the shape factor of this current increases. Therefore, the power losses in the PR elements will be greater than in the continuous current mode. The capacitance of the filter capacitor also increases. An important disadvantage of such a mode is that the PR output voltage will depend on the load resistance R . Since in the intermittent conduction mode, the PR regulation characteristic $U_{out} = f(t^*; R)$ is a function of two variables, in this mode the PR is described not by one, but by a family of regulation characteristics. Taking into account

the above disadvantages, PRs in various fields of application operate mainly in the continuous conduction mode. However, in certain cases, for example, to reduce switching losses in the key and valve elements of the PR, its operation in the mode of intermittent inductance current is possible and advisable [14–17].

In the listed works, the continuous and intermittent current modes are considered separately. The regulation characteristic is given only for the continuous current mode. At the same time, the converter can be used simultaneously in two modes. In such cases, it is necessary to have regulation characteristics that would be valid for both of the specified modes. Therefore, it is important to know the features of the PR operation in the intermittent conduction mode, as well as methods for determining the regulation characteristics in such a mode.

The goal of the work is to develop a mathematical model that would describe the operation of the PR in the continuous and intermittent conduction modes, in particular, to obtain regulation characteristics that would be valid for both of the specified modes.

The main part. As is known [16], the continuous current mode in the inductance L will be ensured under the condition

$$\Delta I_L / 2 \leq I_L, \quad (1)$$

where I_L is the constant component of the current through the inductance; $\Delta I_L = I_{L\max} - I_{L\min}$ is the ripple of this current.

In the intermittent current mode, as well as in the limit mode, $I_{L\min} = 0$. Therefore, for these modes $\Delta I_L = I_{L\max} = I_m$. Let us analyze the conditions for the fulfillment of inequality (1) using the example of a common PR circuit of the step-down type. In the analysis, we will assume that the output voltage of the PR is well smoothed, and the losses in its elements are insignificant [14–17].

PR of the step-down type. For PR of the step-down type (Fig. 1) in the mode of continuous current of inductance L , the following conditions are met [16]:

$$U_{out} = U_{in} t^*; I_{out} = I_{in} / t^*, \quad (2)$$

where $t^* = t_{cl} / T$ is the relative time of the closed state of the key S in the period T . These are the regulation characteristics of the PR for the continuous conduction mode.

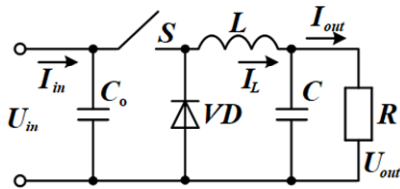


Fig. 1. Step-down type PR

In the steady-state mode of operation of the PR, the change in the inductance current in the stages of the closed and open state of the key S is the same, but has the opposite sign

$$\Delta I_{Lcl} = \Delta I_{Lop} = I_m.$$

Let's determine the value of this change:

$$I_m = \frac{U_{in} - U_{out}}{L} t_{cl} = \frac{U_{out}}{L} t_{op}. \quad (3)$$

Then, the condition for continuous inductance current (1) can be written as follows:

$$\frac{U_{in} - U_{out}}{2L} t_{cl} \leq I_L = I_{out} = \frac{U_{out}}{R}. \quad (4)$$

Divide both sides of the inequality by T :

$$(U_{in} - U_{out}) t^* \leq U_{out} 2 \tau^*,$$

where $\tau^* = L / RT$.

Therefore, the condition for continuity of current in the inductance for the circuit (Fig. 1):

$$\tau^* \geq (1 - t^*) / 2. \quad (5)$$

The larger the parameter t^* , the smaller the inductance L can be, at which the continuous current mode is ensured. To ensure such a mode in the entire control range ($t^* > 0$), the following condition must be met:

$$\tau^* \geq 0.5. \quad (6)$$

If $\tau^* < 0.5$, the mode of intermittent current of inductance L will arise during the PR regulation process. Therefore, $\tau^* = 0.5$ is the critical parameter at which the PR transitions from one operating mode to another:

$$\tau_{cr}^* = L / RT = 0.5. \quad (7)$$

To ensure continuous current mode in the entire control range, the inductance L should be selected from the condition $L \geq 0.5RT$. If the resistance R will change during operation, it is necessary to take its maximum value. Under such a condition, the inductance L is called critical:

$$L_{cr} = 0.5R_{\max}T. \quad (8)$$

Discontinuous conduction mode. Figure 2, *a* shows the inductor current graph in the limit mode, and Fig. 2, *b* – in the discontinuous mode. Since the voltage at the input of the PR is constant and the output voltage is well smoothed, the current in the inductance L at intervals varies linearly and has a triangular shape [14–17].

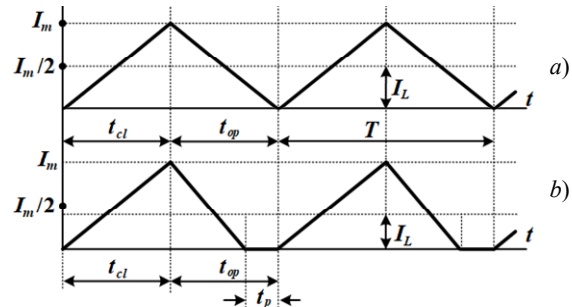


Fig. 2. Inductance current:
a) limit mode; b) intermittent mode

In the steady-state mode of operation of the PR, regardless of the inductance operating mode, the average value of the voltage on it for the period $U_L(T) = 0$. Therefore, the volt-second integrals at the stage of the closed and open state of the key should be the same, but with the opposite sign. According to Fig. 2, *b*, for the intermittent current mode we can write:

$$(U_{in} - U_{out}) t_{cl} = U_{out} (t_{op} - t_p), \quad (9)$$

where t_p is the duration of the pause in the inductance current.

Let's determine the output voltage in the intermittent current mode:

$$U_{in} t_{cl} = U_{out} (t_{cl} + t_{op} - t_p) = U_{out} (T - t_p).$$

Therefore:

$$U_{out} = U_{in} t_{cl} / (T - t_p),$$

or in relative units:

$$U^* = t^* / (1 - t_p^*), \quad (10)$$

where $U^* = U_{out} / U_{in}$; $t_p^* = t_p / T$.

Thus, for a given value of the parameter t^* , the output voltage of the PR will be the greater, the greater the duration of the pause in the inductance current. In the continuous current mode, as well as the limit mode, $t_p = 0$ and the output voltage $U_{out} = U_{in} t^*$, which coincides with (2). Let us determine what the duration t_p depends on.

In the steady-state mode of operation of the PR, its output voltage is:

$$U_{out} = I_{out} R = I_L R.$$

In the limit operation mode (Fig. 2,a), the average value of the inductance current can be determined as:

$$I_L = I_m / 2.$$

According to Fig. 2,b, the average value of the inductance current in intermittent mode:

$$I_L = \frac{I_m}{2} \frac{(T - t_p)}{T} = \frac{I_m}{2} (1 - t_p^*). \quad (11)$$

Similarly to (3), we can write:

$$\frac{I_m}{2} = \frac{U_{out}}{2L} (t_{op} - t_p) = \frac{U_{out} T}{2L} (1 - t^* - t_p^*).$$

Then, according to (11):

$$I_{out} = I_L = \frac{U_{out} T}{2L} (1 - t^* - t_p^*) (1 - t_p^*).$$

Therefore:

$$U_{out} = I_{out} R = \frac{U_{out} T}{2\tau^*} (1 - t^* - t_p^*) (1 - t_p^*).$$

As a result, we obtain the following quadratic equation:

$$t_p^{*2} - t_p^* (2 - t^*) + (1 - t^* - 2\tau^*) = 0. \quad (12)$$

The real root of this equation is the duration of the pause:

$$t_p^* = \frac{(2 - t^*) - \sqrt{t^{*2} + 8\tau^*}}{2}. \quad (13)$$

Table 1 shows the results of calculating the interval duration t_p^* (13) and the PR output voltage (10) for different values of the parameter τ^* .

Table 1

Duration t_p^* calculations

τ^*	t^*	0.1	0.2	0.3	0.4	0.5	0.6	0.7	0.8	0.9	1
$\tau^*=0.5$	$U^*, t_p^*=0$	0.1	0.2	0.3	0.4	0.5	0.6	0.7	0.8	0.9	1
$\tau^*=0.4$	t_p^*	0.06	0	0	0	0	0	0	0	0	0
	U^*	0.106	0.2	0.3	0.4	0.5	0.6	0.7	0.8	0.9	1
$\tau^*=0.3$	t_p^*	0.17	0.12	0.08	0	0	0	0	0	0	0
	U^*	0.12	0.23	0.33	0.4	0.5	0.6	0.7	0.8	0.9	1
$\tau^*=0.2$	t_p^*	0.32	0.26	0.2	0.14	0.07	0	0	0	0	0
	U^*	0.15	0.27	0.38	0.46	0.54	0.6	0.7	0.8	0.9	1
$\tau^*=0.1$	t_p^*	0.5	0.44	0.37	0.31	0.24	0.16	0.08	0	0	0
	U^*	0.2	0.36	0.48	0.58	0.66	0.71	0.76	0.8	0.9	1
$\tau^*=0.05$	t_p^*	0.63	0.57	0.5	0.42	0.34	0.27	0.18	0.09	0	0
	U^*	0.27	0.46	0.6	0.69	0.75	0.82	0.85	0.88	0.9	1

Based on the results of these calculations, in Fig. 3, graphs of the regulation characteristics of the step-down type PR are plotted, which are valid for both the continuous conduction mode and the intermittent mode.

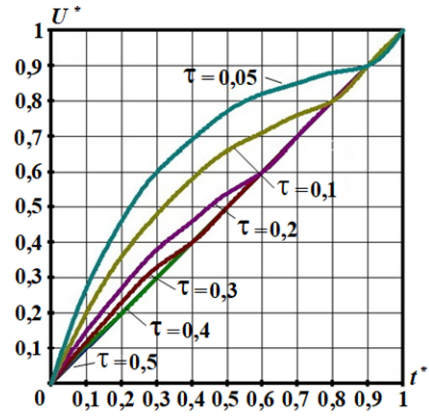


Fig. 3 Regulation characteristics of PR of step-down type

According to these graphs, in the case of $\tau^* < 0.5$ the PR switches to the mode of intermittent current of inductance L . With a decrease in the parameter τ^* , the regulation characteristics will deviate towards higher output voltages compared to the continuous current mode. However, smoothing of the output voltage of PR is provided not only by the inductance L , but also by the capacitance C , or rather by their product LC [16]. Let us determine how the transition of PR to the mode of intermittent current will affect the value of this product.

Let the ripple coefficient of the output voltage of PR be given:

$$K_p = \Delta U_{out} / 2U_{out}, \quad (14)$$

which must be provided on the load R .

Let us consider in more detail one period of the inductance current i_L in intermittent mode (Fig. 4).

Under the influence of the shaded part of this current, the voltage on the capacitance C will increase by the value:

$$\Delta U_C = \Delta q / C, \quad (15)$$

where Δq is the change in charge on a capacitor.

This current has the shape of a triangle with height $(I_m - I_L)$ and duration t_x . The average value of this current, which is proportional to the area of the triangle, will determine the change in charge on the capacitor:

$$\Delta q = \frac{(I_m - I_L)t_x}{2} = \frac{(I_m - I_L)T t_x^*}{2}. \quad (16)$$

Taking into account (11):

$$I_m - I_L = I_m - \frac{I_m}{2} (1 - t_p^*) = \frac{I_m}{2} (1 + t_p^*). \quad (17)$$

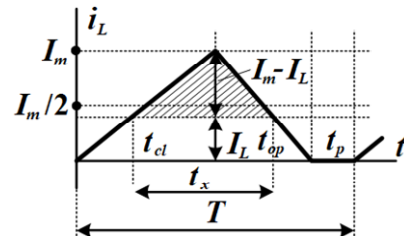


Fig. 4. Inductance current in intermittent mode

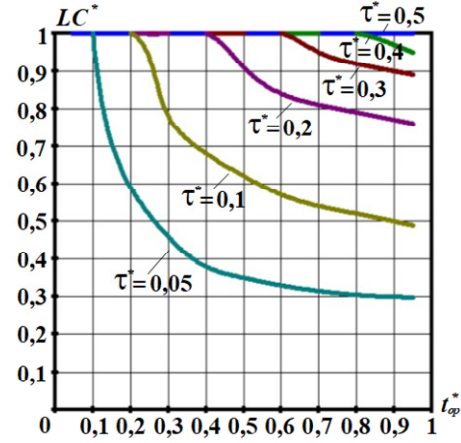
Using the properties of similar triangles, we can write:

$$\frac{I_m}{I_m - I_L} = \frac{T - t_p}{t_x} = \frac{1 - t_p^*}{t_x^*}. \quad (18)$$

Table 2

Calculation results of $(LC)^*$

τ^*	t_{op}^*	0.9	0.8	0.7	0.6	0.5	0.4	0.3	0.2	0.1
$\tau^*=0.5$	$(LC)^*_{t_p^*=0}$	1	1	1	1	1	1	1	1	1
	t_p^*	0.06	0	0	0	0	0	0	0	0
$\tau^*=0.4$	$(LC)^*$	0.97	1	1	1	1	1	1	1	1
	t_p^*	0.17	0.12	0.08	0	0	0	0	0	0
$\tau^*=0.3$	$(LC)^*$	0.92	0.93	0.95	1	1	1	1	1	1
	t_p^*	0.32	0.26	0.2	0.14	0.07	0	0	0	0
$\tau^*=0.2$	$(LC)^*$	0.77	0.79	0.82	0.84	0.91	1	1	1	1
	t_p^*	0.5	0.44	0.37	0.31	0.24	0.16	0.08	0	0
$\tau^*=0.1$	$(LC)^*$	0.5	0.52	0.54	0.57	0.62	0.68	0.78	1	1
	t_p^*	0.63	0.574	0.5	0.42	0.34	0.27	0.18	0.09	0
$\tau^*=0.05$	$(LC)^*$	0.3	0.305	0.321	0.34	0.35	0.38	0.46	0.59	1

Fig. 5 Dependence $(LC)^* = f(t_{op}^*)$ for different values τ^*

Analysis of the obtained graphs shows:

- in the intermittent conduction mode, the specified ripple coefficient of the PR output voltage K_p is provided by a smaller value of the product LC of its elements;
- with a decrease in the parameter $\tau^* = L/RT$, the required value of the product decreases;
- with an increase in the duration of the interval t_{op}^* , the required product LC decreases. In the extreme case ($t_{op}^* \rightarrow 1$)

$$(LC)^* \rightarrow (1 - t_p^{*2})^2. \quad (28)$$

In the continuous current mode, by changing the inductance L to kL , we can reduce the capacitance C by C/k . The intermittent current mode occurs when the inductance $L < L_c$ decreases. However, in this case, the necessary increase in the capacitance C will be less than in the continuous current mode. For example, in the case of $\tau^* = 0.05$, $L < L_c$ by a factor of 10. At the same time, according to the graphs (Fig. 5), to ensure the same K_p , in the case of $t_{op}^* > 0.4$, the capacitance will have to be increased only by a factor of 3.5. This can be explained by the fact that in the discontinuous mode, at a given input voltage, the output voltage increases, which, according to (14), reduces K_p . Therefore, the given ripple coefficient can be obtained using a smaller value of the product LC .

Conclusions.

1. A mathematical model is proposed that describes the behavior of the PR in the continuous and intermittent conduction modes, which made it possible to unify the description of both modes within a single theoretical basis.

Therefore, taking into account (17):

$$t_x^* = \frac{(I_m - I_L) \cdot (1 - t_p^*)}{I_m} = \frac{I_m(1 + t_p^*) \cdot (1 - t_p^*)}{2I_m} = \frac{1 - t_p^{*2}}{2}. \quad (19)$$

Then, according to (16):

$$\Delta q = \frac{I_m(1 + t_p^*) \cdot T \cdot (1 - t_p^{*2})}{2 \cdot 2 \cdot 2} = \frac{I_m T (1 + t_p^*) \cdot (1 - t_p^{*2})}{8}. \quad (20)$$

Taking into account (9) and (15), we finally obtain:

$$\Delta U_{out} = \Delta U_C = \frac{\Delta q}{C} = \frac{U_{out} T^2}{8LC} (t_{op}^* - t_p^*) (1 + t_p^*) (1 - t_p^{*2}). \quad (21)$$

Then, according to (14), we obtain the formula for determining the ripple coefficient of the output voltage of PR of the step-down type, which is valid for the modes of continuous and intermittent current of inductance L :

$$K_p = \frac{\Delta U_{out}}{2U_{out}} = \frac{T^2}{16LC} (t_{op}^* - t_p^*) (1 + t_p^*) (1 - t_p^{*2}). \quad (22)$$

In particular, for the continuous conduction mode ($t_p = 0$), we obtain the well-known formula [16]:

$$K_p = \frac{T^2}{16LC} t_{op}^*. \quad (23)$$

Thus, in the continuous current mode, in particular in the limit mode, for a given value of the LC product, the ripple coefficient of the output voltage will depend on the duration of the open state of the key t_{op}^* and, in the worst case ($t_{op}^* \rightarrow 1$), reaches the maximum value:

$$K_{p \max} = \frac{T^2}{16LC}. \quad (24)$$

Suppose that the task is to provide a given value of the ripple coefficient of the PR output voltage K_p . In the continuous current mode, to provide a given K_p , the product LC :

$$(LC)_{CCM} = \frac{T^2}{16K_p} t_{op}^*, \quad (25)$$

and the given K_p can be obtained by increasing the inductance and decreasing the capacitance, and vice versa.

In the intermittent current mode, the required product LC :

$$(LC)_{DCM} = \frac{T^2}{16K_p} (t_{op}^* - t_p^*) (1 + t_p^*) (1 - t_p^{*2}), \quad (26)$$

will depend not only on the duration of the open state of the key t_{op}^* , but also on the duration of the pause t_p^* . To analyze this dependence, we define the relation:

$$(LC)^* = \frac{(LC)_{DCM}}{(LC)_{CCM}} = \frac{(t_{op}^* - t_p^*) (1 + t_p^*) (1 - t_p^{*2})}{t_{op}^*}. \quad (27)$$

Taking into account the results presented in Table 1, Table 2 shows the results of the calculations of the relation $(LC)^*$. Figure 5 shows the graphs of the dependence $(LC)^* = f(t_{op}^*)$ for different values of the parameter τ^* , on which the duration of the pause t_p^* depends at a given t_{op}^* .

2. A family of regulation characteristics is determined that are valid for both modes of operation of the PR and show that when the PR transitions to the mode of intermittent conduction current, its regulation characteristics are shifted towards higher output voltages. This shift is greater, the longer the duration of the pause in the inductance current.

3. It is shown that to ensure a given ripple coefficient of the PR output voltage, in the intermittent current mode, a smaller value of the LC product of the PR elements is required than in the continuous current mode, which makes it possible to reduce the size and cost of the PR element base.

Conflict of interest. The authors declare no conflict of interest.

REFERENCES

1. Valarmathy A.S., Prabhakar M. High gain interleaved boost-derived DC-DC converters – A review on structural variations, gain extension mechanisms and applications. *E-Prime - Advances in Electrical Engineering, Electronics and Energy*, 2024, vol. 8, art. no. 100618. doi: <https://doi.org/10.1016/j.prime.2024.100618>.
2. Romashko V.Y., Batrak L.M., Abakumova O.O. Features of the work of pulse regulators in the maximum power transmission mode, with the presence of an accumulator at their output. *Electrical Engineering & Electromechanics*, 2023, no. 6, pp. 63-66. doi: <https://doi.org/10.20998/2074-272X.2023.6.11>
3. Sarowar G., Ahmed I., Rahman S., Al Mamun A., Salim K.M. Investigation of a power factor correction converter utilizing SEPIC topology with input current switching. *Results in Engineering*, 2024, vol. 22, art. no. 102271. doi: <https://doi.org/10.1016/j.rineng.2024.102271>.
4. Pallekonda A.K., Ch R.K. High gain interleaved PFC converter for torque ripple minimization in industrial PMBLDC motor based drives. *Results in Engineering*, 2024, vol. 23, art. no. 102413. doi: <https://doi.org/10.1016/j.rineng.2024.102413>.
5. Bushra E., Zeb K., Ahmad I., Khalid M. A comprehensive review on recent trends and future prospects of PWM techniques for harmonic suppression in renewable energies based power converters. *Results in Engineering*, 2024, vol. 22, art. no. 102213. doi: <https://doi.org/10.1016/j.rineng.2024.102213>.
6. Pirashanthiyah L., Edirisinghe H.N., De Silva W.M.P., Bolonne S.R.A., Logeeshan V., Wanigasekara C. Design and Analysis of a Three-Phase Interleaved DC-DC Boost Converter with an Energy Storage System for a PV System. *Energies*, 2024, vol. 17, no. 1, art. no. 250. doi: <https://doi.org/10.3390/en17010250>.
7. Oliver J.S., David P.W., Balachandran P.K., Mihet-Popa L. Analysis of Grid-Interactive PV-Fed BLDC Pump Using Optimized MPPT in DC-DC Converters. *Sustainability*, 2022, vol. 14, no. 12, art. no. 7205. doi: <https://doi.org/10.3390/su14127205>.
8. Srividya S., Praveena A., TatiReddy Ravi, SathishKumar K. Single Switch DC-DC Boost Converter with MPPT Control for Fuel Cell Electric Vehicle Applications. *2023 Innovations in Power and Advanced Computing Technologies (i-PACT)*, 2023, pp. 1-6. doi: <https://doi.org/10.1109/i-PACT58649.2023.10434573>.
9. Romashko V.Y., Batrak L.M., Abakumova O.O. Step-up/step-down regulators in maximum power transmission mode. *Electrical Engineering & Electromechanics*, 2022, no. 2, pp. 18-22. doi: <https://doi.org/10.20998/2074-272X.2022.2.03>.
10. Huang L. Reduced-order discrete modeling method and nonlinear analysis of a discontinuous conduction mode buck converter with a constant power load. *Energy Reports*, 2023, vol. 9, pp. 1021-1036. doi: <https://doi.org/10.1016/j.egy.2023.04.133>.
11. Serra F.M., Esteban F.D., Montoya O.D. Control of DC-DC boost converter in discontinuous conduction mode feeding a constant power load. *Results in Engineering*, 2024, vol. 23, art. no. 102732. doi: <https://doi.org/10.1016/j.rineng.2024.102732>.
12. Veeramraju K.J., Eisen J., Rovey J.L., Kimball J.W. A New Discontinuous Conduction Mode in a Transformer Coupled High Gain DC-DC Converter. *2022 IEEE Applied Power Electronics Conference and Exposition (APEC)*, 2022, pp. 237-244. doi: <https://doi.org/10.1109/APEC43599.2022.9773417>.
13. Madrid E., Murillo-Yarce D., Restrepo C., Muñoz J., Giral R. Modelling of SEPIC, Ćuk and Zeta Converters in Discontinuous Conduction Mode and Performance Evaluation. *Sensors*, 2021, vol. 21, no. 22, art. no. 7434. doi: <https://doi.org/10.3390/s21227434>.
14. Parada Salado J.G., Herrera Ramírez C.A., Soriano Sánchez A.G., Rodríguez Licea M.A. Nonlinear Stabilization Controller for the Boost Converter with a Constant Power Load in Both Continuous and Discontinuous Conduction Modes. *Micromachines*, 2021, vol. 12, no. 5, art. no. 522. doi: <https://doi.org/10.3390/mi12050522>.
15. González I., Sánchez-Squella A., Langarica-Cordoba D., Yanine-Misleh F., Ramirez V. A PI + Sliding-Mode Controller Based on the Discontinuous Conduction Mode for an Unidirectional Buck-Boost Converter with Electric Vehicle Applications. *Energies*, 2021, vol. 14, no. 20, art. no. 6785. doi: <https://doi.org/10.3390/en14206785>.
16. Goncharov Y.P., Budonny O.V., Morozov V.G., Panasenkov M.V., Romashko V.Y., Rudenko V.S. *Peretovoyuvalna technicala. Navchalnyi posibnyk. Chastyna 2* [Power conversion equipment. Text book. Part 2]. Kharkiv, Folio Publ., 2000. 360 p. (Ukr).
17. Serra F.M., Magaldi G.L., Martin Fernandez L.L., Larregay G.O., De Angelo C.H. IDA-PBC controller of a DC-DC boost converter for continuous and discontinuous conduction mode. *IEEE Latin America Transactions*, 2018, vol. 16, no. 1, pp. 52-58. doi: <https://doi.org/10.1109/TLA.2018.8291454>.

Received 28.04.2025

Accepted 03.06.2025

Published 02.09.2025

V.Y. Romashko¹, Doctor of Technical Science, Professor,
L.M. Batrak¹, PhD, Associate Professor,
¹National Technical University of Ukraine
«Igor Sikorsky Kyiv Polytechnic Institute»,
37, Prospect Beresteiskiy, Kyiv, 03056, Ukraine,
e-mail: batrakln5@gmail.com (Corresponding Author)

How to cite this article:

Romashko V.Y., Batrak L.M. Regulation characteristics of a step-down pulse regulator in continuous and discontinuous conduction mode. *Electrical Engineering & Electromechanics*, 2025, no. 5, pp. 57-61. doi: <https://doi.org/10.20998/2074-272X.2025.5.08>

M.I. Boiko, A.V. Makogon

Disinfectant treatment of liquids with high specific electrical conductivity by high-voltage nanosecond pulses with a subnanosecond front

Purpose. The purpose of the work is to determine, using computer modelling, energy-efficient modes of disinfecting treatment of water-containing liquids with high specific electrical conductivity using high voltage nanosecond pulses with a subnanosecond front including pulsed discharges in gas bubbles. **Methods.** We considered methods of obtaining high-voltage nanosecond pulses with sub-nanosecond fronts. To achieve this goal, we used computer simulation using Micro-Cap 12. We also used analytical and empirical formulas for calculating the electric field strength, inductive and resistive phases of energy switching from a capacitive source to resistive-inductive loads. We have applied the method of comparing calculated and experimental results. **Results.** Energy-efficient modes of disinfecting treatment of water-containing liquids with high specific electrical conductivity using nanosecond discharges with a subnanosecond front in gas bubbles are such modes when the active resistance of the treated liquid is 10–40 Ω . In this case, the lumped inductance of the discharge circuit during liquid treatment does not exceed 2 nH, the capacitance of the layer of the treated liquid is 3.6–14 pF with an amplitude of pulses from a high-voltage low-resistance source of at least 30 kV and a pulse frequency of 1500–2000 pulses per second. With an increase in the active resistance of the liquid within the specified limits, the amplitude of the voltage on the layer of the treated liquid increases under other unchanged conditions, including with an unchanged amplitude of the voltage from the source. The voltage amplitude on the layer of the treated liquid with such an increase can exceed the voltage amplitude from the source by 1.6 times, and exceed the voltage on the reactor as a whole (the series connection of the bulk streamer and the water layer). This happens due to the presence of a lumped inductance in the discharge circuit, in which energy is stored during discharge. **Scientific novelty.** We have shown the possibility of using nanosecond discharges with sub-nanosecond fronts in gas bubbles for energy-efficient disinfection of liquids, including those with high specific electrical conductivity. In this case, a plasma electrode – a volumetric streamer – acts as a high-voltage electrode in the disinfection of liquids. **Practical value.** The obtained of the computer modelling results confirm the possibility of industrial application of nanosecond discharges with a sub-nanosecond front for disinfection and purification of water-containing liquids with high specific electrical conductivity. References 23, figures 13.

Key words: water disinfection with high-voltage pulses, discharge unit, high-voltage streamer plasma electrode, nanosecond discharge in gas bubbles in water, long electric line, sub-nanosecond rise time of high voltage.

Мета. Метою роботи є визначення за допомогою комп'ютерного моделювання енергоефективних режимів дезінфікуючої обробки водовмісних рідин з високою питомою електропровідністю з використанням високовольтих наносекундних імпульсів із субнаносекундним фронтом, включаючи імпульсні розряди в газових бульбашках. **Методи.** Розглянуто методи отримання високовольтих наносекундних імпульсів із субнаносекундними фронтами. Для досягнення цієї мети було використано комп'ютерне моделювання за допомогою Micro-Cap 12. Також було використано аналітичні та емпіричні формули для розрахунку напруженості електричного поля, індуктивної та резистивної фаз перемикання енергії від ємнісного джерела до резистивно-індуктивних навантажень. Застосовано метод порівняння розрахункових та експериментальних результатів. **Результати.** Енергоефективними режимами дезінфікуючої обробки водовмісних рідин з високою питомою електропровідністю за допомогою наносекундних розрядів із субнаносекундним фронтом у газових бульбашках є такі режими, коли активний опір оброблюваної рідини становить 10–40 Ом, зосереджена індуктивність розрядного кола під час обробки рідини не перевищує 2 нГн, ємність шару оброблюваної рідини становить 3,6–14 пФ з амплітудою імпульсів від високовольтного низькоомного джерела не менше 30 кВ та частотою імпульсів 1500–2000 імпульсів за секунду. Зі збільшенням активного опору рідини в заданих межах амплітуда напруги на шарі оброблюваної рідини зростає за інших незмінних умов, у тому числі за незмінної амплітуди напруги від джерела. Амплітуда напруги на шарі оброблюваної рідини при такому збільшенні може перевищувати амплітуду напруги від джерела в 1,6 рази, а також перевищувати напругу на реакторі в цілому (послідовне з'єднання об'ємного стримера та шару води) через наявність зосередженої індуктивності в колі розряду, в якій накопичується енергія під час розряду. **Наукова новизна.** Показано можливість використання наносекундних розрядів із субнаносекундними фронтами в газових бульбашках для енергоефективної дезінфекції рідин, у тому числі з високою питомою електропровідністю. У цьому випадку плазмовий електрод – об'ємний стример – виступає в ролі високовольтного електрода при дезінфекції рідин. **Практична значимість.** Отримані результати комп'ютерного моделювання підтверджують можливість промислового застосування наносекундних розрядів із субнаносекундним фронтом для дезінфекції та очищення водовмісних рідин з високою питомою електропровідністю. Бібл. 23, рис. 13.

Ключові слова: знезараження води високовольтними імпульсами, розрядний блок, високовольтний стримерний плазмовий електрод, наносекундний розряд у газових бульбах у воді, довга електрична лінія, субнаносекундний час наростання високої напруги.

Introduction. Liquids with high specific electrical conductivity, which exceeds the electrical conductivity of river and tap water, are, for example, seawater, milk. Is it possible to disinfect such liquids using discharges in gas bubbles inside such liquids?

Discharges are permissible in water, unlike in food products, because discharges in food products cause undesirable changes that impair their organoleptic properties. It follows that water can be disinfected and purified using a wider range of factors. This range includes such powerful factors as high-energy electrons and microparticles with high electrochemical potential: OH⁻ radicals, hydrogen peroxide H₂O₂, ozone O₃, as well as broadband radiation from discharges. However, these factors can be used jointly and effectively only when

discharges are carried out inside a volume of water in a gaseous environment, for example, in gas bubbles. This action is fundamentally different from the action that is widely used in the world today, which is provided by ozone technologies. In ozone technologies is used only one active factor from electrical discharges (barrier discharges are most often used) – ozone, which is also not the most effective active factor that can be obtained and usefully used for disinfection and purification of water from discharges.

The most effective can be considered nanosecond discharges, when in a gas volume (for example, in gas bubbles) inside the water, a volumetric streamer is created in a fraction of a nanosecond, which glows and covers the entire gas discharge gap along its length. This is ensuring

© M.I. Boiko, A.V. Makogon

the presence of a strong electric field in the water itself, contact over the maximum area on the plasma interface surface of the volumetric streamer with water and the transition of active microparticles (electrons, ions, atomic oxygen O, radicals OH[•], hydrogen peroxide H₂O₂, ozone O₃, etc. in the paradigm of de Broglie's theory of matter waves) into the water for its disinfection and purification. It is method minimizes specific energy consumption and the cost of disinfecting water treatment.

The interest in using high-voltage pulses as short as possible for disinfection of water and liquid food products is to reduce the specific energy costs for disinfection and to increase the efficiency of such treatment by increasing the amplitude of the electric field strength in the treated liquid while reducing the duration of the operating high-voltage pulses. For example, magnetic-semiconductor high-voltage generators with nanosecond stream interrupters are known [1, 2]. At present, researches have achieved sub-nanosecond fronts of high-voltage voltage and current pulses with durations from one to several nanoseconds (in the load). They are using both closing and opening switches [3–5]. It is for such pulses that it is possible to obtain a volumetric streamer plasma in the discharge gap without transitioning to a contracted (cord) discharge.

Purpose. The purpose of the work is to determine, using computer modelling, energy-efficient modes of disinfecting treatment of water-containing liquids with high specific electrical conductivity using nanosecond discharges with a subnanosecond front in gas bubbles. More energy-efficient modes are the ones that provide a higher disinfection degree than traditional technologies of high-voltage ozonation of water and air environments, with the same specific energy for disinfection. The efficiency of a high-voltage pulse modes significantly exceeds 70 %, because the installation is based on a Tesla transformer, the efficiency of which exceeds 80 %. The proposed flow-through mode of water disinfection provides specific energy consumption of less than 0.7 kWh/m³.

Electrical diagram and calculating the parameters of a high-voltage pulsed installation discharge circuit, where volumetric nanosecond streamer discharges with a sub-nanosecond front in gas bubbles are possible. The electrical circuit of the experimental installation for water disinfection using discharges in gas bubbles is given in [6]. Figure 1 shows the electrical circuit, with the help of which in this work, the computer simulation in Micro-Cap 12 of the process of processing liquids with high specific electrical conductivity by pulsed electrical discharges in gas bubbles inside the liquid was carried out.

The main high-voltage storage capacity in the diagram (Fig. 1) is designated C2. The circuit for simulation was chosen to emphasize the importance of the main high-voltage discharge circuit, namely, C2-SW1-L2-TD (long line with input capacitance C4 and output capacitance C3)-SW3-parallel connection L1 and R1-parallel connection R7 and C1-C2. The letters SW denote switches that operate instantly. Elements of the electric circuit: SW3-parallel connection L1 and R1-parallel connection R7 and C1 simulate the reactor – a series connection of the gas discharge gap (with a transient active resistance R1) with the plasma after switching (with the inductance of the plasma volume L1) and the liquid layer with the active resistance R7 and the capacitance C1.

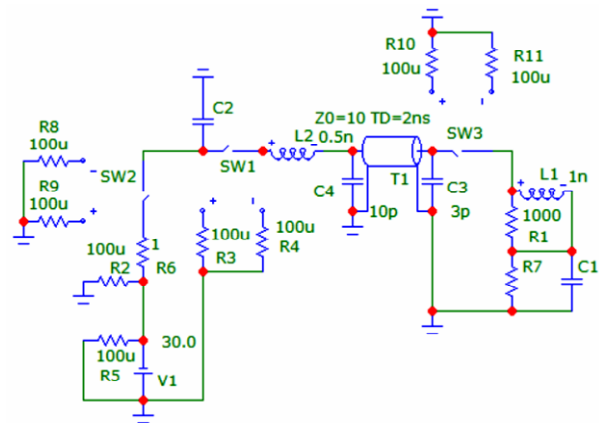


Fig. 1. The electrical circuit diagram used for the computer simulation in this work

The capacitance C2 in our calculations we took equal to C2=150 pF, which corresponds to the value of C2 used in our experiments, or C2=1000 pF. The active resistance of the water layer R7 we took equal to R7=10 Ω or R7=40 Ω. In this case, the capacitance C1 of the water layer was taken equal to C1=14 pF or C1=3.6 pF, respectively.

Since the bandwidth of the Rigol DS1102E digital oscilloscope, which we used to measure voltage and current pulses, is 100 MHz, the oscillograms may not transmit the high-frequency component of real pulses. Therefore, computational studies of the capabilities of the electrical circuit of our installation are required. According to [7], we assumed the specific electrical conductivity γ when calculating the resistance $R7 \equiv R_w$ of the liquid layer (see Fig. 1) equal to $\gamma=5 (\Omega \cdot m)^{-1}$, which approximately corresponds to the specific electrical conductivity of sea water. In the calculations, we did not take into account electrode effects, which can cause a nonlinear dependence of the electrical conductivity [8] of the «water–metal electrodes» system on the applied voltage, because their contribution is minimal when the high-voltage pulses have a voltage amplitude of approximately 30 kV and a duration of less than 50 ns.

If, during a discharge in a gas bubble, we assume the thickness of the water layer for the flow of a pulsed current through the water layer to be $l=5 \cdot 10^{-3}$ m, and the cross-sectional area S of the current flow through the water $S=0.25 \cdot 10^{-4}$ m², then the active resistance of the water layer will be: $R_w = l/(\gamma S) = 5 \cdot 10^{-3} / (5 \cdot 0.25 \cdot 10^{-4}) = 40 \Omega$. The capacitance $C_w = \epsilon_0 \cdot \epsilon \cdot S/l = 8.85 \cdot 10^{-12} \cdot 81 \cdot 0.25 \cdot 10^{-4} / (5 \cdot 10^{-3}) = 3.58 \cdot 10^{-12}$ F, where ϵ_0 is the dielectric constant (absolute dielectric permeability of vacuum); ϵ is the relative dielectric permeability of the medium. At $R_w=10 \Omega$ of a volume of water with the same specific electrical conductivity $\gamma=5 (\Omega \cdot m)^{-1}$, its capacitance will be:

$C_w = \epsilon_0 \cdot \epsilon \cdot S/l = 8.85 \cdot 10^{-12} \cdot 81 \cdot 0.25 \cdot 10^{-4} / (5 \cdot 10^{-3}) \approx 14 \cdot 10^{-12}$ F. We have assumed that the relative dielectric constant of water is a real constant, which is equal to 81.

The time constant τ_w of the discharge of the capacitance C_w of the water volume to the internal resistance R_w of this volume is determined as:

$$\tau_w = R_w \cdot C_w = [l/(\gamma S)] \cdot \epsilon_0 \cdot \epsilon \cdot S/l = \epsilon_0 \cdot \epsilon / \gamma.$$

From this formula it follows that this time constant is determined by the ratio of the dielectric constant (permeability) of water to its specific electrical conductivity and is the smaller, the greater the specific electrical conductivity of water. At $\gamma = 5 (\Omega \cdot m)^{-1}$ $\tau = 8.85 \cdot 10^{-12} \cdot 81 / 5 \approx 1.43 \cdot 10^{-10}$ s. This means that after the

instant disconnection of the external source of high-voltage pulses, the capacitance of this volume of water will be discharged to the active resistance of this volume with a time constant $\tau_w \approx 1.43 \cdot 10^{-10}$ s.

With a capacitance C of the high-voltage pulse source $C=150$ pF, the time constant τ of its discharge into a resistive load with a resistance $R=10 \Omega$ will be $\tau=R \cdot C=10 \cdot 150 \cdot 10^{-12}=1.5 \cdot 10^{-9}$ s. It follows from this that the duration of the front (rise time) of the voltage on the load $R=10 \Omega$ must be less than 1 ns so that the real maximum voltage on the load is not significantly less than the maximum (possible) voltage on it, to which it can be charged by a pre-charged capacitive source of high-voltage pulses with a capacitance C . If the duration of the front of the pulses on the load is determined mainly by the inductive component, namely $t_f=2.2 \cdot L/R$, then with $L=2$ nH and $R=10 \Omega$ $t_f=2.2 \cdot L/R=2.2 \cdot 2 \cdot 10^{-9}/10=4.4 \cdot 10^{-10}$ s = 0.44 ns. Thus, the lumped inductance of the discharge circuit with a load $R=10 \Omega$ should not exceed $L=2$ nH.

We use the formula for the inductances of short conductors to determine approximately the inductance of the volumetric discharge channel in a gas bubble [9]:

$$L = \frac{\mu_0 l}{2\pi} \left(\ln \frac{2l}{r_c} - \frac{3}{4} + \frac{128 \cdot r_c / 45\pi}{l} - \frac{r_c^2}{4l^2} \right), \quad (1)$$

where l is the length of the discharge channel, and r_c is its radius. At $l=5 \cdot 10^{-3}$ m, $r_c=2.5 \cdot 10^{-3}$ m $L=2 \cdot 10^{-7} \cdot 5 \cdot 10^{-3} (\ln 4 - 3/4 + 0.4527 - 0.0625) \approx 10^{-9} \cdot (1.386 - 0.75 + 0.4527 - 0.0625) \approx 1.03 \cdot 10^{-9}$ H. In Fig. 1, the inductance of the volumetric discharge channel (volume streamer) is denoted by $L1$.

To estimate the resistive phase τ_R of the commutation, we use the empirical formula of J.C. Martin [10, 11]:

$$\tau_R = 88R \frac{1}{3} E_0^{-4/3} (\rho/\rho_0)^{1/2}. \quad (2)$$

The dimension of the time constant τ_R of the resistive switching phase (exponential voltage drop) is [ns], for the electric field strength E_0 along the discharge channel near it is 10 kV/cm. The dimension for R – the generator impedance (in our case, this is the active resistance of the water layer in the discharge circuit) is [Ω]; ρ/ρ_0 – the ratio of the density of a gas in a gap to the density of the same gas under normal conditions; in our case $\rho/\rho_0=1$.

The field strength E_0 at the sharp edge of the end of the high-voltage rod electrode in the gap between the

high-voltage rod electrode and the grounded electrode with zero potential opposing it is determined using the evaluation formula [12]:

$$E_0 = \frac{U_0}{r} \left(\ln \frac{2d}{r} \right)^{-1}, \quad (3)$$

where $U_0=U_c=V$ is high-voltage potential of the rod electrode.

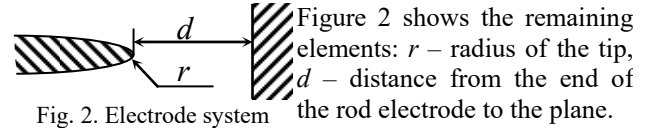


Fig. 2. Electrode system

At $U_0=50$ kV, $r=0.1$ mm, $d=10$ mm according to (3) we obtain:

$$E_0 = (50/0.1) / \ln(2 \cdot 10/0.1) \approx 500/5.3 \approx 94 \text{ kV/mm.}$$

$$\text{At } d=5 \text{ mm } E_0 \approx 500/4.6 \approx 109 \text{ kV/mm.}$$

At $R=10 \Omega$, $E_0=94$ (10 kV/cm)=940 kV/cm, $(\rho/\rho_0)^{1/2}=1$ we get the following result:

$$\tau_R = 88 \cdot 10^{-1/3} \cdot 94^{-4/3} = 88 \cdot 0.464 \cdot 0.00237 \approx 0.1 \text{ ns.}$$

$$\text{At } E_0 \approx 109 \text{ kV/mm:}$$

$$\tau_R = 88 \cdot 10^{-1/3} \cdot 109^{-4/3} = 88 \cdot 0.464 \cdot 0.002 \approx 0.08 \text{ ns.}$$

In Fig. 1, the active resistance of the water layer in the discharge circuit is designated $R7$.

A typical picture of pulsed discharges in a gas bubble inside water and a sketch of the design of a reactor (unit) for disinfecting water in a stream using nanosecond discharges with a subnanosecond front in gas bubbles. Figure 3 shows a typical integral picture (photo) with many pulsed discharges in a gas bubble inside water. We received this photo while conducting our experiments. The image in Fig. 3 can be spectrally analysed, for example, using the methods described in [13].

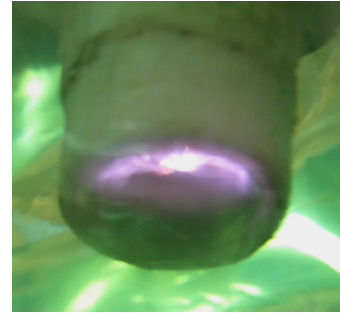


Fig. 3. A typical photo with many pulsed discharges in a gas bubble inside water

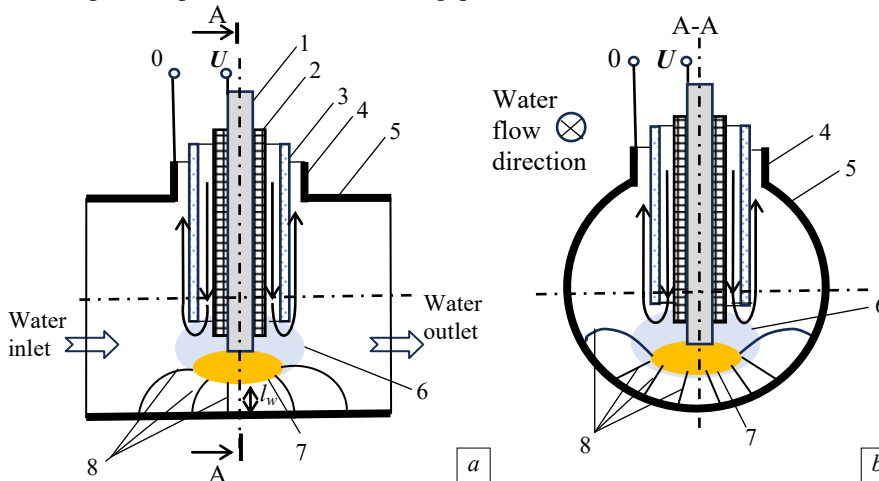


Fig. 4. a – axial longitudinal section of the pipe-reactor with running water; b – cross-section A-A of the pipe-reactor with running water

Figure 4 shows a reactor (unit) design variant for disinfection treatment of water in a stream using nanosecond discharges with a subnanosecond front in gas bubbles in real dimensions. We have used the following notations here. The arrows (\rightarrow) indicate the direction of gas movement in the reactor; 1 – high-voltage rod electrode under U potential; 2 – the insulation of high-voltage electrode 1; 3 – insulating cylinder to ensure gas movement in water, creation of bubbles in the reactor with flowing water; 4 – metal pipe with zero potential for introducing high-voltage pulses and gas into the

reactor through it; 5 – metal reactor pipe with flowing water and gas bubbles in it (water), to which (pipe) pipe 4 is short-circuited; 6 – gas bubble; 7 – volume inside the gas bubble, which is filled with plasma of a pulse discharge in gas (volume streamer or near high-voltage electrode plasma). It (plasma) borders on the water being disinfected. 8 – conventionally depicted electric field lines in water in the zone of the most effective disinfection treatment in the presence of a discharge in a gas bubble. l_w – the minimal distance in water between the plasma high-voltage electrode and the inner surface of the metal reactor pipe (tube). When breakdown pulse voltage in the gas bubble equals 50 kV $l_w \approx 2-5$ mm.

Results and discussion. In [14], based on experimental data, the possibility of the existence of a primary volumetric ionization zone during switching of high-voltage dischargers is shown. In [15], the existence of volumetric streamers is shown by calculation. In [16], the possibility of the operation of a high-voltage trigatron in the subnanosecond time range is shown by calculation.

Figure 5 shows the result of our computer modelling of the electric field distribution in the discharge gap (in the reactor) with a gas bubble and a layer of treated water at the time $t = 1.5$ ns after the start of the nanosecond discharge in the gas bubble. It follows from this figure that inside the volumetric streamer between the rod metal high-voltage electrode (in Fig. 5 it is represented by a white figure) and the surface of the water layer the electric field strength does not exceed 25 kV/cm. At the same time, in the water layer near the interface with the plasma of the bulk streamer, the electric field strength reaches 100 kV/cm.

Calculations [15] and experiments [17] have shown that when the duration of the discharge pulse front in a gas bubble is approximately 1–2 ns, a plasma volume (volume streamer) is created in the discharge gap, which covers the entire length of the gap to the water interface. In the process of creating volume streamers runaway electrons play an important role, and in the case of creating negative streamers, the emission of electrons from a high-voltage cathode [18, 19]. The potential of the high-voltage metal electrode, because of the appearance of a plasma formation (a streamer) in the discharge gap, moves by the streamer towards the interface between the gas bubble and water. Inside the streamer, the electric field strength is significantly lower than in water near the water-gas bubble interface. That is, a strong electric field penetrates the water, creating a volume in the water with a strength of more than 40 kV/cm. Thus, in the water layer between the plasma volume high-voltage electrode and the grounded metal electrode, a volume zone of a strong electric field

with an intensity of 40 kV/cm to 120 kV/cm is created. In addition, broadband radiation, including ultraviolet and even shorter wavelength radiation, as well as active microparticles, including OH^- radicals, enters the water from the volume streamer, or a volume nanosecond discharge [20]. This set of factors of the combination of high-voltage pulse actions provides a significant reduction in specific energy consumption for disinfecting water treatment compared to traditional ozonation.

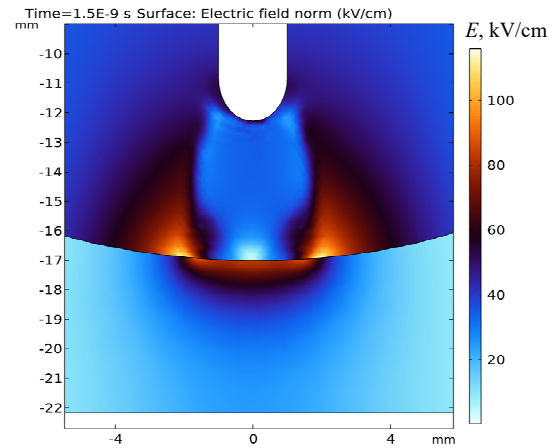


Fig. 5. Distribution of electric field intensity inside reactor

Due to the short length of the discharge pulses (less than 10 ns), they may not change the organoleptic properties of food products, which opens up the possibility of using such short high-voltage discharge pulses for disinfecting food products.

Figure 6 shows the result of calculating of the pulse voltage $V1$ on the reactor (serial connection of the plasma discharge channel in the gas bubble and the water layer) and the pulse voltage $V2$ on the water layer through which the current flows. In this case a capacitance $C2=150$ pF, an active resistance of the water layer $R_w=10$ Ω and a capacitance of the water layer $C_w \approx 14 \cdot 10^{-12}$ F.

With a volumetric discharge channel (volume streamer) in a gas bubble with a channel diameter of approximately 5 mm and a length of 5 mm, it is possible to achieve a channel inductance of 1 nH [9]. Then, it is possible to obtain voltage pulses with an amplitude of up to 28 kV. It is possible if the amplitude of the pulse voltage from the pulse generator is 30 kV, in a reactor with a volumetric discharge channel in an air bubble 5 mm long and a water layer 5 mm thick, which is connected in series with the discharge volumetric streamer. Then the amplitude of the voltage pulses will be 25.2 kV in the water layer (see Fig. 6).

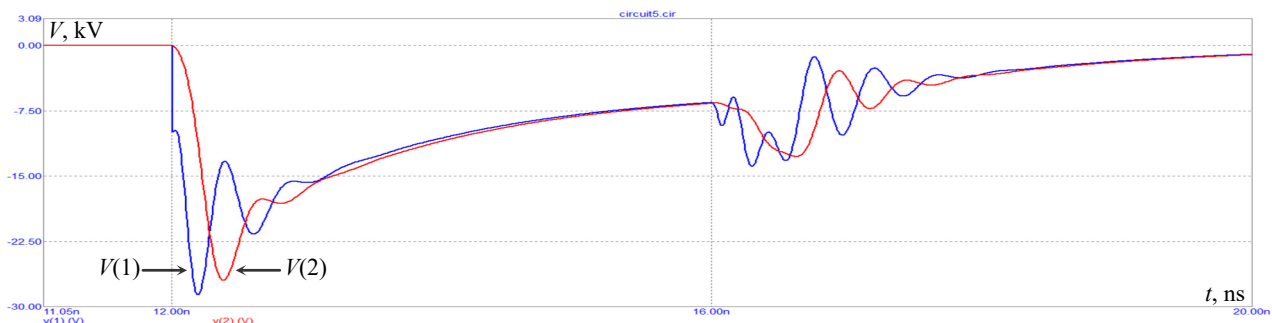


Fig. 6. The result of the calculation (according to the scheme in Fig. 1) of the pulse voltage $V(1)$ on the reactor voltage and $V(2)$ on the water layer at $C2=150$ pF, $C1=14$ pF, $R_w=10$ Ω . The long TD line is taken into account

The wave impedance of the long line should be made small (approximately $10\ \Omega$), because with an increase in the wave impedance of the long line, the amplitude of the pulse voltage on the water layer decreases. As can be seen from Fig. 6, the calculated pulse duration on the load – a reactor with a discharge in a gas bubble and a water layer – is in the considered case approximately 1.5 ns at half-wavelength, and the pulse front duration on the water layer is ≈ 0.4 ns.

Figure 7 presents the result of calculating the pulse voltage $V(1)$ on the reactor (serial connection of the

plasma discharge channel in the gas bubble and the water layer) and the pulse voltage $V(2)$ on the water layer. This is in the case when the circuit on Fig. 1 does not have a long TD line, and the high-voltage outputs (terminals) of the capacitors $C3$ and $C4$ are short-circuited, $R7=10\ \Omega$, $C1=14\ \text{pF}$, $C2=150\ \text{pF}$. Compared to the option when the presence of a long TD line is taken into account (Fig. 6), the time dependence of $V(1)$ and $V(2)$ has a more oscillatory nature, and the amplitude of $V(2)$ and $V(2)$ is a little more.

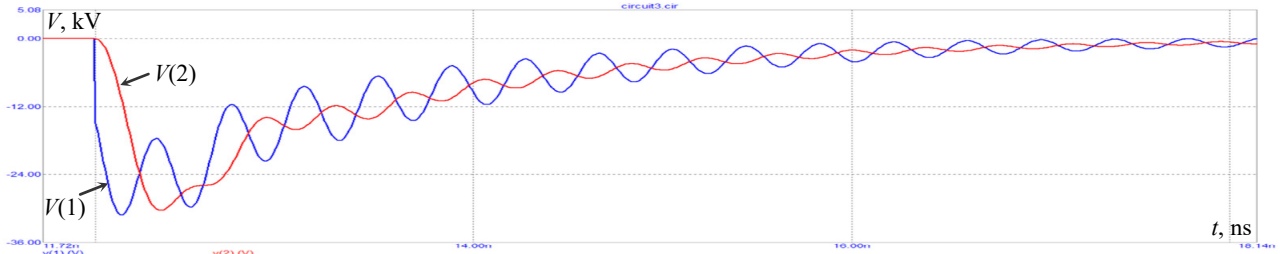


Fig. 7. The result of the calculation (according to the scheme in Fig. 1) of the pulse voltage $V(1)$ on the reactor voltage and voltage $V(2)$ on the water layer at $C2=150\ \text{pF}$, $C1=14\ \text{pF}$, $R_w=10\ \Omega$. The long TD line is not taken into account

Creating a technologically advanced installation for the disinfection treatment of liquids with high specific electrical conductivity up to $\gamma=5\ (\Omega\cdot\text{m})^{-1}$ using discharges in gas bubbles is a complex scientific and technical problem, but one that can be solved right now.

Figure 8 shows the result of calculating the pulse voltage $V(1)$ on the reactor (serial connection of the plasma discharge channel in the gas bubble and the water layer) and the pulse voltage $V(2)$ on the water layer

through which the current flows. In this case the active resistance of the water layer $R_w=40\ \Omega$ and the capacitance of the water layer $C_w\approx 3.6\cdot 10^{-12}\ \text{F}$ according to the scheme in Fig. 1. It can be seen that in this case the amplitude of the voltage $V(2)$ on the water layer exceeds the voltage from the pulse source by approximately 1.5 times, and the amplitude of the voltage $V(1)$ on the reactor as a whole exceeds the voltage from the pulse source by approximately 1.3 times.

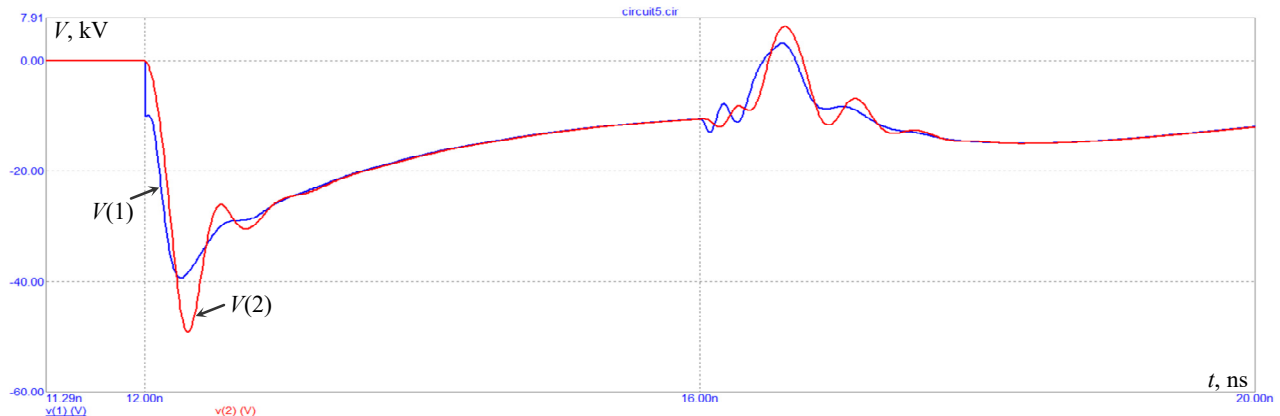


Fig. 8. The result of the calculation (according to the scheme in Fig. 1) of the pulse voltage $V(1)$ on the reactor voltage and $V(2)$ on the water layer at $C2=150\ \text{pF}$, $C1=C_w\approx 3.6\ \text{pF}$, $R_w=40\ \Omega$. The long TD line is taken into account

Figure 9 shows the result of calculating the pulse voltage $V(1)$ on the reactor (serial connection of the plasma discharge channel in the gas bubble and the water layer) and the pulse voltage $V(2)$ on the water layer. This is in the case when the circuit on Fig. 1 does not have a long line TD , and the high-voltage terminals of the capacitors $C3$ and $C4$ are short-circuited together, $R7=40\ \Omega$, $C1=3.6\ \text{pF}$. Compared to the option when the presence of a long line TD is taken into account (Fig. 8), the time dependence of $V(1)$ and $V(2)$ has a more oscillatory nature, the amplitudes of $V(1)$ and $V(2)$ are almost the same (as in Fig. 8), there is no reflection from the ends of the long line.

Figure 10 shows the result of calculating the pulse voltage $V(1)$ on the reactor (serial connection of the plasma discharge channel in the gas bubble and the water layer) and the pulse voltage $V(2)$ on the water layer. This is at $C2=1000\ \text{pF}$, $C1=3.6\ \text{pF}$, $R7=40\ \Omega$.

Figure 11 shows the initial part of the same pulse. These figures show the results taking into account the presence of a long line in the circuit in Fig. 1.

It follows from Fig. 10, 11 that the amplitude of $V(2)$ on the water layer is slightly larger than at $C2=150\ \text{pF}$ (other conditions being equal).

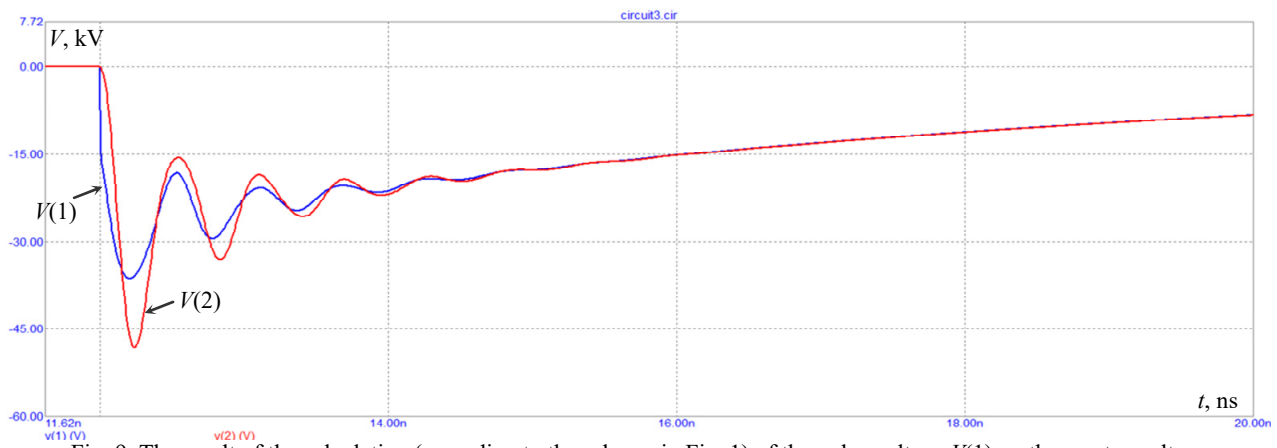


Fig. 9. The result of the calculation (according to the scheme in Fig. 1) of the pulse voltage $V(1)$ on the reactor voltage and $V(2)$ on the water layer at $C_2=150$ pF, $C_1=C_w\approx 3.6$ pF, $R_w=40$ Ω . The long TD line is not taken into account

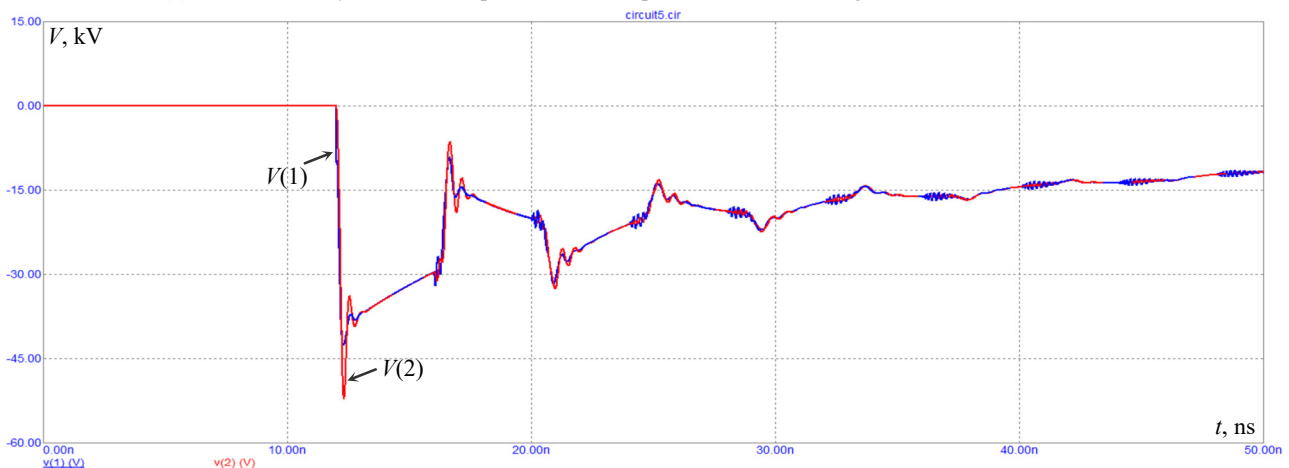


Fig. 10. The result of the calculation (according to the scheme in Fig. 1) of the pulse voltage $V(1)$ on the reactor voltage and $V(2)$ on the water layer at $C_2=1000$ pF, $C_1=C_w\approx 3.6$ pF, $R_w=40$ Ω . The long TD line is taken into account

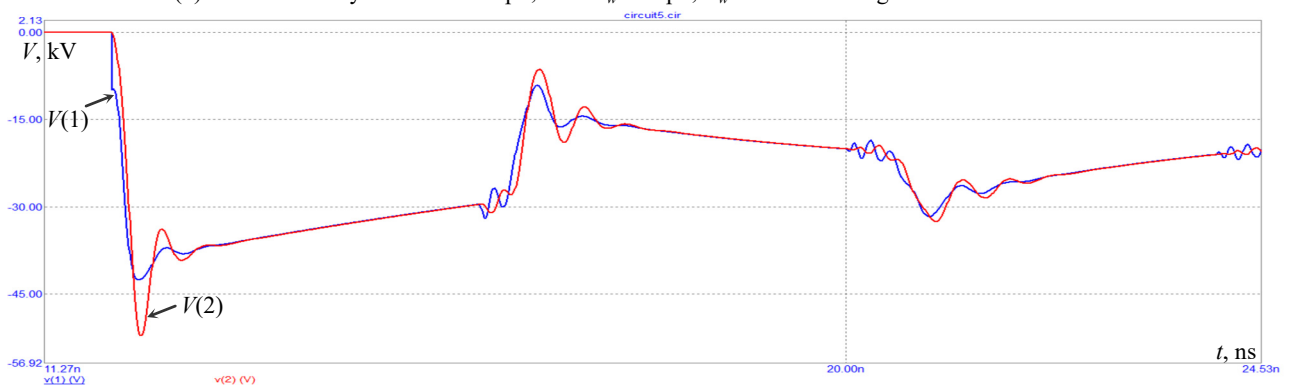


Fig. 11. The initial part of the pulses from Fig. 10

Figure 12 shows the result of the calculation (according to the scheme in Fig. 1) of the pulse voltage $V(1)$ on the reactor (serial connection of the plasma discharge channel in the gas bubble and the water layer). It shows also the pulse voltage $V(2)$ on the water layer at $C_2=1000$ pF, $C_1=14$ pF, $R_7=10$ Ω , and Fig. 13 shows the initial part of the same pulse.

The emergence of a volume streamer in the discharge gap of the reactor and, as a consequence, subnanosecond volume avalanche-streamer switching are possible only at voltage rise rates in the discharge gap on the gas bubble of the order of 10^{14} V/s (3×10^{13} – 10^{14} V/s) [16, 21]. To achieve such a rise rate at a breakdown voltage of 50 kV, the time required for the voltage rise on the gas bubble to breakdown is of the order of $5 \cdot 10^4 \text{ V} / (3 \cdot 10^{13} \text{ V/s}) \approx (5 \cdot 10^{-10} \text{ s} - 1.7 \cdot 10^{-9} \text{ s})$. This is a

very short, but already achieved switching time of high-voltage switches [17, 21, 22].

The question of the possibility of using short discharge pulses in gas bubbles, when the high-voltage electrode in contact with the processed liquid is plasma (in the form of a volumetric streamer), for the processing of liquid and flowing food products remains open. Appropriate experimental studies are needed. It is not clear whether any chemical and biochemical reactions take place during processing with nanosecond pulses. It is necessary to find out, if such reactions take place, what exactly the reactions are processing during such, and what the final products of such reactions are. Will the organoleptic properties of liquid food products change during such processing with nanosecond pulses with subnanosecond fronts?

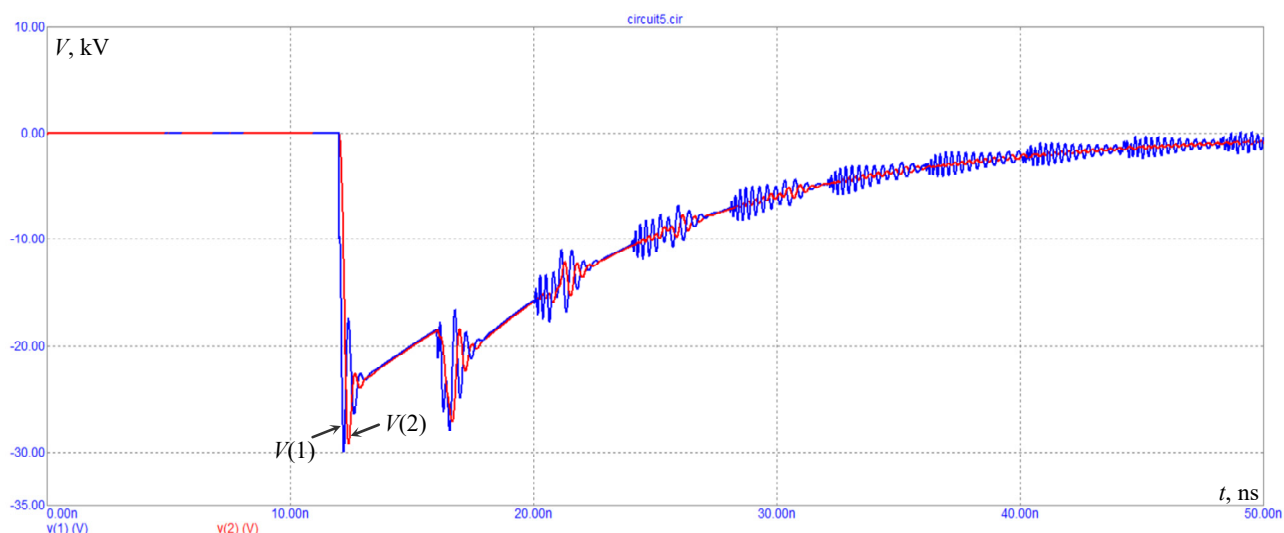


Fig. 12. The result of the calculation (according to the scheme in Fig. 1) of the pulse voltage $V(1)$ on the reactor voltage and $V(2)$ on the water layer at $C_2=1000$ pF, $C_1=14$ pF, $R_7=10$ Ω . The long TD line is taken into account

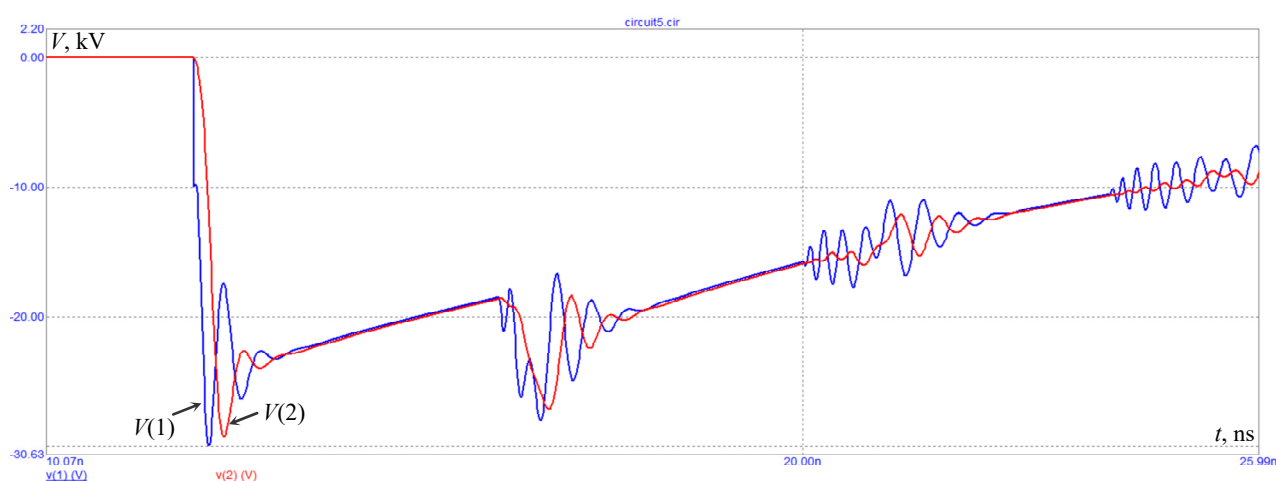


Fig. 13. The initial part of the pulses from Fig. 12

From the analysis of the above calculated results, previously obtained experimental results and results of other authors (including the results presented in [23]), we can conclude that the energy-efficient modes of disinfecting treatment of water-containing liquids with high specific electrical conductivity using nanosecond discharges with a subnanosecond front in gas bubbles are the following modes. Namely, these are modes when the active resistance of the treated liquid in one reactor in one discharge circuit is 10–40 Ω , the lumped inductance of the discharge circuit during liquid treatment does not exceed 2 nH. Add, such modes use the capacitance of the treated liquid layer is 3.6–14 pF with an amplitude of pulses from a high-voltage low-resistance source of at least 30 kV, and a frequency of passing pulses is 1500–2000 pulses per second. When the active resistance of the liquid increases within the specified limits, the voltage amplitude on the layer of the processed liquid increases under other constant conditions, including at a constant voltage amplitude from the source. The voltage amplitude on the layer of the processed liquid with such an increase can exceed the voltage amplitude from the source by 1.6 times. It also exceeds the voltage at the whole reactor (the series connection of the volumetric streamer and the water layer) because of the presence of concentrated inductance

in the discharge circuit, where (in the inductance) energy is stored during discharge.

Conclusions.

1. The possibility of obtaining nanosecond high-voltage pulses (with volumetric streamers in gas bubbles inside water) with subnanosecond fronts in reactors for the disinfection treatment of liquids with high specific electrical conductivity up to 5 S/m=5 ($\Omega\cdot\text{m}$)⁻¹ has been shown. Such pulses can provide a higher disinfection degree at lower specific energy consumption than longer pulses, because of the lower energy in each pulse and the higher amplitude of the electric field strength in the treated liquid. Experiments that we have already conducted have shown that nanosecond pulses provide a higher disinfection degree at lower specific energy consumption than microsecond pulses [6]. Therefore, further reduction of pulse duration and duration of their fronts is promising. In addition, such short pulses with a subnanosecond front ensure the presence of volumetric plasma formations – volumetric streamers, as an extension of a metal high-voltage electrode. These plasma formations provide an additional disinfection effect on the liquid being treated by supplying it with active microparticles and broadband radiation, including ultraviolet and even shorter-wave radiation.

2. Experimental results obtained by various researchers, including the authors of this material, confirm the possibility of obtaining volumetric pulse discharges in gas environments (mediums) at atmospheric pressure.

3. An example of a sketch of the design of a liquid processing unit in the flow mode is given, when as a result of a pulse discharge in a gas bubble, a volumetric streamer (volumetric plasma electrode) is created. This plasma electrode is an extension of a high-voltage metal electrode and creates a volumetric zone of the most effective decontamination treatment in the treated liquid with an electric field strength that can reach 100 kV/cm and more.

4. Using computer modelling, energy-efficient modes of decontamination treatment of water-containing liquids with high specific electrical conductivity using nanosecond discharges with a subnanosecond front in gas bubbles are determined. These are such modes when the active resistance of the liquid being processed is 10–40 Ω , the lumped inductance of the discharge circuit during liquid processing does not exceed 2 nH. At the same time, the capacitance of the layer of the liquid being processed is 3.6–14 pF with amplitude of pulses from a high-voltage low-resistance source of at least 30 kV and a pulse frequency of 1500–2000 pulses per second.

Conflict of interest. The authors declare that they have no conflicts of interest.

REFERENCES

1. Volkov I.V., Zozulyov V.I., Sholoh D.A. *Magnetic semiconductor pulse devices of conversion technology*. Kyiv, Naukova Dumka Publ., 2016. 230 p. (Rus).
2. Khrysto O.I. Energy characteristics for nanosecond current interrupter of semiconductor-magnetic pulse generator's terminal stage. *Electrical Engineering & Electromechanics*, 2023, no. 3, pp. 59-65. doi: <https://doi.org/10.20998/2074-272X.2023.3.09>.
3. Rai V.N., Shukla M. A high-voltage pulser circuit with subnanosecond rise time. *Review of Scientific Instruments*, 1994, vol. 65, no. 6, pp. 2134-2136. doi: <https://doi.org/10.1063/1.1144710>.
4. Matsukubo D., Minamitani Y. Development of a high frequency cluster burst pulse generator based on a SOS diode using transmission line resonant for bioelectrics applications. *2013 19th IEEE Pulsed Power Conference (PPC)*, 2013, pp. 1-5. doi: <https://doi.org/10.1109/PPC.2013.6627494>.
5. Takahashi K., Yagi I., Takaki K., Satta N. Development of Pulsed Discharge Inside Bubble in Water. *IEEE Transactions on Plasma Science*, 2011, vol. 39, no. 11, pp. 2654-2655. doi: <https://doi.org/10.1109/TPS.2011.2164095>.
6. Boyko N.I., Makogon A.V. The micro- and nanosecond discharges in gas bubbles for water disinfection and purification. *Electrical Engineering & Electromechanics*, 2019, no. 3, pp. 50-54. doi: <https://doi.org/10.20998/2074-272X.2019.3.08>.
7. Sauerheber R., Heinz B. Temperature effects on conductivity of seawater and physiologic saline, mechanism and significance. *Chemical Sciences Journal*, 2016, vol. 6, no. 4, art. no. 1000109. doi: <https://doi.org/10.4172/2150-3494.1000109>.
8. Shydlovska N., Zakharchenko S., Cherkaskyi O. The influence of electric field parameters and temperature of hydrosols of metals' plasma-erosive particles on their resistance and permittivity. *Computational Problems of Electrical Engineering*, 2014, vol. 4, no. 2, pp. 77-84.
9. Kalantarov P.L., Tseitlin L.A. *Calculation of inductances. Reference book. 3rd ed.* Leningrad, Energoatomizdat Publ., 1986. 488 p. (Rus).
10. Martin J.C. *Multichannel Gaps*. Aldermaston, Berks, 1970. 42 p.
11. Kovalchuk B.M., Kremnev V.V., Potaltsyn Yu.F. *High-current nanosecond switches*. Novosibirsk, Nauka Publ., 1979. 176 p. (Rus).
12. Rusin Yu.S. *The calculation of electromagnetic systems*. Leningrad, Energiya Publ., 1968. 132 p. (Rus).
13. Shydlovska N.A., Zakharchenko S.M., Zakharchenko M.F., Kulida M.A., Zakusilo S.A. Spectral and optic-metric methods of monitoring parameters of plasma channels caused by discharge currents between metals granules in working liquids. *Electrical Engineering & Electromechanics*, 2024, no. 6, pp. 72-83. doi: <https://doi.org/10.20998/2074-272X.2024.6.10>.
14. Boyko N.I., Evdoshenko L.S., Zarochentsev A.I., Ivanov V.M., Artyukh V.G. 400-kV trigatrons for high-power low-inductance pulse generators. *Instruments and Experimental Techniques*, 2008, vol. 51, no. 1, pp. 70-77. doi: <https://doi.org/10.1134/S0020441208010077>.
15. Nijdam S., Teunissen J., Ebert U. The physics of streamer discharge phenomena. *Plasma Sources Science and Technology*, 2020, vol. 29, no. 10, art. no. 103001. doi: <https://doi.org/10.1088/1361-6595/abaa05>.
16. Boiko M.I. Sub-nanosecond switching of high-voltage trigatrons. *Technical Electrodynamics*, 2024, no. 3, pp. 83-88. doi: <https://doi.org/10.15407/techne2024.03.083>.
17. Heeren T., Camp J.T., Kolb J.F., Schoenbach K.H., Katsuki S., Akiyama H. 250 kV sub-nanosecond generator with adjustable pulse-width. *IEEE Transactions on Dielectrics and Electrical Insulation*, 2007, vol. 14, no. 4, pp. 884-888. doi: <https://doi.org/10.1109/TDEL.2007.4286520>.
18. Chanrion O., Bonaventura Z., Çinar D., Bourdon A., Neubert T. Runaway electrons from a 'beam-bulk' model of streamer: application to TGFs. *Environmental Research Letters*, 2014, vol. 9, no. 5, art. no. 055003. doi: <https://doi.org/10.1088/1748-9326/9/5/055003>.
19. Wong T., Timoshkin I., MacGregor S., Wilson M., Given M. A computational study on the effects of fast-rising voltage on ionization fronts initiated in sub-mm air and CO₂ gaps. *Scientific Reports*, 2024, vol. 14, no. 1, art. no. 1185. doi: <https://doi.org/10.1038/s41598-024-51727-y>.
20. He Y., Uehara S., Takana H., Nishiyama H. Experimental and theoretical study on chemical reactions and species diffusion by a nano-pulse discharged bubble for water treatment. *The European Physical Journal D*, 2018, vol. 72, no. 1, art. no. 11. doi: <https://doi.org/10.1140/epjd/e2017-80240-5>.
21. Mesiats G.A. *Pulsed power and electronics*. Moscow, Nauka Publ., 2004. 704 p. (Rus).
22. Zhang X., Lu W., Chen Z., Yang Z., Liu T. Optimizing design of sub-nanosecond gas switch with adjustable gap. *Qiangguang Yu Lizishu/High Power Laser and Particle Beams*, 2009, vol. 21, no. 9, pp. 1380-1384.
23. Gucker Sarah M.N. *Plasma Discharges in Gas Bubbles in Liquid Water: Breakdown Mechanisms and Resultant Chemistry*. PhD Dissertation, University of Michigan, 2015. 243 p. Available at: <https://hdl.handle.net/2027.42/116739>.

Received 14.03.2025

Accepted 01.05.2025

Published 02.09.2025

How to cite this article:

Boiko M.I., Makogon A.V. Disinfectant treatment of liquids with high specific electrical conductivity by high-voltage nanosecond pulses with a subnanosecond front. *Electrical Engineering & Electromechanics*, 2025, no. 5, pp. 62-69. doi: <https://doi.org/10.20998/2074-272X.2025.5.09>

Analysis of energy characteristics of a transistor pulse generator in the process of electric spark dispersion of current-conductive granular media

Introduction. Studies of electrophysical and technological aspects of electric discharge in reaction chambers with granular metal loading to obtain its highly dispersed states have been conducted for many decades, however, the power sources of electric spark dispersion installations today remain mainly classical in terms of the method of generating current pulses on the electric spark load. The main **problem** of using powerful current pulse generators and reaction chambers with a plane-parallel electrode system is to imitate the principle of the thermo-explosive mechanism of developing an electrical breakdown of dense intergranular gaps, which leads to deterioration of the dispersion of the eroded material, and the use of smaller energy ranges (<1 J) in such installations is complicated by the electrophysical limitations of the existence of plasma channels and the loss of energy efficiency of the electric spark treatment process. **Goal.** Research on the energy efficiency of the electric spark dispersion process of heterogeneous conductive granular media in a reaction chamber with a cylindrical electrode system, provided that it is powered by a transistor pulse generator. **Results.** Specific energy consumption in the process of electric spark dispersion of aluminum and titanium granules was determined, which correlate with the average power consumption indicators of processing depending on their bulk volume within a certain configuration of the electrode system. **Scientific novelty.** The flow of current through ohmic contacts until the formation of the main discharge in the intergranular volumes of the reaction chamber causes a voltage drop across the inductance of the discharge circuit, which accordingly reduces the amplitude of the applied voltage to the interelectrode gap, due to which the maximum of the average power consumption characteristic of the transistor pulse generator, which occurs before the beginning of the saturation section of the effective frequency curve of the discharge pulses, corresponds to the most consistent mode of energy input into the electric spark load. The **practical value** of the considered model of the electric discharge installation proves the feasibility of its use for the tasks of electric spark treatment of conductive granular media. References 21, tables 2, figures 7.

Key words: energy characteristics, electric spark dispersion, transistor pulse generator, cylindrical electrode system, layer of metal granules, ohmic contact current.

Вступ. Дослідження електрофізичних і технологічних аспектів електричного розряду в реакційних камерах з гранульованим металевим завантаженням для одержання його високодисперсних станів ведуться вже на протязі багатьох десятиліть, проте джерела живлення установок електроіскрового диспергування на сьогодні залишаються переважно класичними щодо способу генерації імпульсів струму в електроіскрове навантаження. Основною **проблемою** використання формувачів потужних імпульсів струму та реакційних камер з плоско-паралельною системою електродів є наслідування принципу термовибухового механізму розвинення електричного пробою щільних міжгранульних проміжків, що призводить до псування дисперсності еродованого матеріалу, а використання менших діапазонів енергій (<1 Дж) у таких установках ускладнюється через електрофізичні обмеження існування плазмових каналів та втрату енергоефективності процесу електроіскрової обробки. **Мета.** Дослідження енергоефективності процесу електроіскрового диспергування гетерогенних струмопровідних гранульованих середовищ у реакційній камері з циліндричною системою електродів за умови її живлення від транзисторного генератора імпульсів. **Результати.** Проведено порівняльний аналіз поведінки характеристик середньої споживаної потужності транзисторного генератора імпульсів в залежності від насипного об'єму завантаження та діаметру зовнішнього електрода реакційної камери для металевих гранул з різною величиною їх міжконтактного активного опору до утворення у середовищі ланцюжків наскрізної провідності. Визначені питомі енергозатрати у процесі електроіскрового диспергування алюмінієвих та титанових гранул, що корелюють з показниками середньої споживаної потужності обробки в залежності від їх насипного об'єму у межах певної конфігурації електродної системи. **Наукова новизна.** Присутність струму крізь контактний опір до формування основного розряду у міжгранульних об'ємах реакційної камери викликає падіння напруги на індуктивності розрядного контуру, що відповідно зменшує амплітуду прикладеної напруги до міжелектродного проміжку, через що максимум характеристики середньої споживаної потужності транзисторного генератора імпульсів, який виникає до початку ділянки насичення кривої ефективної частоти розрядних імпульсів відповідає найбільш погодженому режиму введення енергії в електроіскрове навантаження. **Практична значимість** отриманих результатів розглянутої моделі електророзрядної установки доказує доцільність її використання для задач електроіскрової обробки струмопровідних гранульованих середовищ. Бібл. 21, табл. 2, рис. 7.

Ключові слова: енергетичні характеристики, електроіскрове диспергування, транзисторний генератор імпульсів, циліндрична система електродів, шар металевих гранул, струм омичних контактів.

Problem definition. One of the widely used methods for obtaining powders, both pure metals and compounds based on them, is the method of electric spark dispersion (ESD) of metal granules [1–3] immersed in a liquid with relatively low electrical conductivity. As is known, the peculiarity of the electric spark dispersion method is the presence of two most probable ways of developing a spark discharge between adjacent surfaces of contacting granules [4]: thermal breakdown in the area of contact microprotrusions caused by the flow of high

current density and electrical breakdown due to the presence of surface oxide films or cavitation bubbles. Therefore, one or another breakdown mechanism will occur depending on the surface purity of the metal and the ability of the contacting surfaces of the granules to form conductive bridges between them. But regardless of the mechanism by which the spark discharge is formed, the process of forming erosion particles can mainly occur due to the heat of melting or evaporation of local zones of

metal interacting with non-equilibrium plasma of high-energy electrons. The balance between the melting and evaporation energy will depend on the rate of energy input into the formed channel, its degree of ionization, temperature and electrical resistance. The regulation of this process is complicated by the fact that the volt-ampere characteristic of the spark discharge has a decreasing character and leads to an avalanche-like increase in current, which requires the use of parametric methods of controlling the process of energy transfer to the load. That is, a positive current feedback is formed between the power source and the load, which can lead to critical heating of the contact zones, their welding or, conversely, boiling and splashing out a significant amount of a large fraction of metal particles into the surrounding liquid. Most often, these phenomena occur due to the presence in the medium of a large number of dense contact zones between the surfaces of the granules, which have a low active resistance and counteract favorable conditions for the development of the electric spark treatment reaction. For their destruction in laboratory practice, accumulated high energies and long-term discharge currents are usually used. At the same time, in the work [5] it is reported that the energy in a more prolonged part of the pulse is mainly spent on heating the medium or electrochemical reactions in it due to the enhancement of recombination processes and extinction of plasma channels.

In the direction of improving the efficiency of energy transfer to the electric spark load (ESL), many approaches have been developed that use nonlinear, parametric or nonlinear-probabilistic models of its dynamic resistance [5–7]. Also, spectrometric methods of analyzing plasma channels have been recently practiced, which, due to the power and color of radiation, provide information about their number and energy distribution between them, on which the size of the particles and the efficiency of their production depend [8, 9]. On the other hand, for the synthesis of erosion particles with a controlled size and a reduced range of their dispersion, the plasma in a volume filled with many layers of metal granules (VMLMG) must be «colder», and this is possible by limiting the amplitude and duration of the discharge current pulses.

Analysis of recent research and publications.

Today, laboratory installations for initiating the ESD process of heterogeneous conductive granular media use both high-voltage single-power pulse generators and semiconductor pulse generators of micro- and submicrosecond duration [10, 11]. The advantage of high-voltage electric spark treatment [12, 13] is the high speed of leading edges formation and the possibility of using a wide range of energies ($0.1\text{--}10^3$ J), as well as long interelectrode gaps (IEGs) of the reaction chamber. But the main disadvantage of such systems is the low frequency of reproduction of the ESD process due to the use of gas-filled switches or air dischargers. A more promising direction of high-voltage pulse technology in the direction of increasing the efficiency of ESD is the use of inductive energy storage in combination with drift diodes [14], which allows stabilizing the current in the load with a rapidly decreasing volt-ampere characteristic.

In contrast to these systems, thyristor or transistor converters are characterized by a high pulse frequency (0.1–10 kHz) and an energy range from a fraction to hundreds of joules. For example, dual-circuit charge-discharge circuits of thyristor generators [15] have proven themselves as a reliable solution for forming sufficiently long kiloampere pulses of aperiodic nature on a low-impedance load with a high rate of growth of their leading edge, provided that the inductance (1 μH) of the discharge circuit of the capacitive energy storage device (100 μF) is minimized. However, the main disadvantage of these converters is the limitation of the accuracy of current duration regulation, and the use of recharging circuits or circuits that shunt the load only increases additional energy consumption and reduces the efficiency of such devices. In addition, a stochastic increase in the equivalent resistance of the VMLMG can lead to emergency modes of operation of thyristor switches. In the case of a prolonged current pulse through the load, the discharge thyristor can remain in a conductive state until the next charging cycle arrives, which causes a through current to flow from the power source to the load. It should also be noted that the energy efficiency of such devices is significantly reduced when using a working capacitor capacitance of less than 20 μF and forming pulses with a duration of less than 15 μs . From the point of view of material dispersion, the main problem of introducing powerful pulses into the environment is the appearance of an undesirable microfraction (10–100 μm), which is formed mainly due to the droplet mechanism of condensation of metal particles.

Transistor converters for ESD tasks have not gained sufficient popularity to date, because they have much smaller limiting parameters for the current amplitude and rate of its growth than thyristor ones, however, their main advantage is the possibility of regulating the current duration under the condition of their rigid switching or dynamic adjustment to the period of circuit oscillations. For example, in work [16], a generator of quasi-rectangular current pulses with duration of 0.5 to 5 μs was used to obtain iron nanoparticles based on a sequential pulse-width-step down converter. As the authors of the work note, before the start of the experiment, the surface of the metal granules was thoroughly cleaned of unwanted oxide films. It can be assumed that under these conditions the mechanism of electric erosion formation mostly followed the path of thermal breakdown of the conductive bridges formed. Considering that the maximum current amplitude in the experiment was only 48 A, therefore, in the case of a large number of formed contacts along the length of the chamber and a short pulse duration, such a current strength may be insufficient to effectively initiate the thermal breakdown mechanism and form spark channels, and accordingly, the energy introduced into the medium will more likely go to thermal dissipation. As for the rational choice of the geometric parameters of the reaction chamber, the shape of the electrode system and the bulk height of the VMLMG from the position of their influence on the energy indicators of the ESD, many publications [15, 17] provide only an empirical assessment, referring to the range of stabilization of processing in the absence of idle and short-circuit modes.

Separation of previously unsolved part of the problems. In general, the considered problems of ESD of metallic materials can be divided into two ways - the use of longer pulses with high energy (1 J – 1 kJ) or shorter pulses with energy up to a fraction of a joule. The main problem with the introduction of a significant amount of energy into local zones is the damage of erosion particles due to their agglomeration. First, local overheating of contact microp protrusions causes thermal breakdown and initiates a blast wave, which in itself is an uncontrolled process. Second, the plasma formation reaction is stochastic in nature, and the number of plasma channels and the energy ratio between them in the VMLMG are randomly distributed, so there is a probability of introducing a significant amount of energy only into a separate local plasma formation zone, instead of its uniform distribution throughout the volume of the medium. On the other hand, when using low energies, plasma channels last less time, have a smaller diameter and, accordingly, a heating zone and allow for, so to speak, «point spraying» of the material surface, which accordingly improves the dispersion distribution and orderliness of the structure formation of erosion particles. But the main problem in this energy range is that short-pulse generators operate mainly by the mechanism of electrical gap breakdown and are extremely sensitive to the formation of conductive bridges in the medium, because for their destruction it is necessary to introduce much more energy to implement the thermal breakdown mechanism. Given the stochastic nature of the change in the ESL resistance, the amount of energy introduced into the plasma channels from pulse to pulse can vary significantly and depend on many factors such as the conditions of preliminary ionization of the contact gaps, the field strength between them, the roughness of the surfaces, the current density between the microp protrusions, etc. At the same time, to assess the efficiency of the ESD process, it is sufficient to rely on the average value of the energy introduced into the plasma channels for a certain period of time, which directly affects the total mass of eroded metal, which is removed from the contact local zones between the granules as a result of the supply of heat of melting or evaporation. Thus, the search for conditions for increasing the useful power from the pulse generator, which goes to heating the local zones and the formation of eroded metal particles in the direction of improving the energy efficiency of the ESD of a heterogeneous conductive granular medium remains an urgent task.

The goal of the work is to study the energy efficiency of the process of electric spark dispersion of heterogeneous conductive granular media in a reaction chamber with a cylindrical system of electrodes, provided that it is powered by a transistor pulse generator.

Features of the proposed ESD system. Unlike existing ESD reactors, which have a rectangular shape and the same flat shape of the electrodes in the form of plates, located at an average distance of 40–50 mm, in this work it is proposed to carry out processing in a reaction chamber with a cylindrical electrode system. The distance

between the electrodes was set to be somewhat reduced within 20–35 mm to increase the energy input into the contact zones between the surfaces of the granules. The angular symmetry of the radial electric field strength of the cylindrical electrode system, in contrast to the flat system, where the field strength is highest at the edges of the electrodes, allows the use of smaller technological gaps provided that the plasma channels are evenly distributed over the volume of the reaction chamber. The design of the reaction chamber also includes a mechanical stirrer, which is a disk with vertically fixed rods at a certain distance relative to its axis of rotation, the edges of which are immersed in the VMLMG and practically lean against the bottom of the chamber. The disk with rods is mounted on the shaft of the gear mechanism and is driven by a stepper motor. In turn, the rods touch the adjacent granules with their edges and force them to move, giving them translational and rotational movements.

As a power source for the reaction chamber, a dual-circuit transistor pulse generator (TPG) circuit is used (Fig. 1), which contains the charging C_0 - VT_0 - VD_0 - L_0 - C_1 and the discharging C_1 - VT_1 - VD_2 - L_1 - R circuits. This converter is similar in structure to dual-circuit thyristor devices [6, 18], which use the recharging circuits of the working capacitor, but with the following feature of the circuit solution that the function of the current limiter of this circuit is performed by the charging choke L_0 . High-speed diodes in series with the transistors prevent reverse integrated diodes from being blocked and limit electrical oscillations in each circuit to one half-cycle of current. The rectified voltage at the input of the converter is set from 400 to 500 V and is controlled by a laboratory autotransformer. Due to the resonant charging of the working capacitor C_1 , the voltage on it can rise to 800 V.

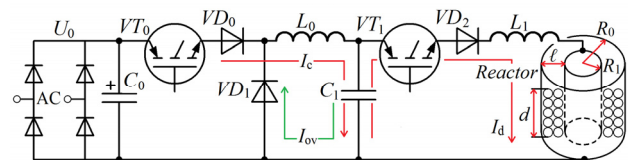


Fig. 1. Schematic diagram of a TPG with a load in the form of a reaction chamber with a cylindrical electrode system

Unlike the existing generally accepted practice of powering ESD reaction chambers using capacitors with a nominal value of at least 25 μ F and an energy of 2 J and more, in the experiments performed, the range of energies operated by the generator did not exceed 1/3 J. The parameters of the discharge circuit were chosen such that its characteristic resistance was 4 Ω .

An important function of the reverse diode VD_1 , which is placed in parallel with the working capacitor C_1 , is to prevent an uncontrolled increase in voltage on it due to its resonant charge under non-zero initial conditions caused by the mismatch of the discharge circuit due to the stochastic nature of the equivalent resistance of the ESL. Despite the fact that the charging voltage on C_1 in the ESD process in a certain energy range of generator oscillations may have a modulation component, such a solution allows the generator to operate reliably from the idle mode to the short-circuit mode. For example, a

characteristic feature of the short-circuit mode is the stationarity of its oscillations, during which the charge of the capacitor C_1 occurs under the condition of a constant positive residual voltage on it. The appearance of a negative residual voltage on C_1 indicates that the equivalent load resistance is lower than the characteristic resistance of the discharge circuit. Such a situation can occur both during the formation of conductive bridges and plasma channels. However, every time a negative voltage appears on C_1 , diode VD_1 turns on, which causes the excitation of reverse oscillation and returns the voltage on C_1 to the polarity of the input DC source. Figure 2 shows the charge, discharge and recharge cycles of C_1 .

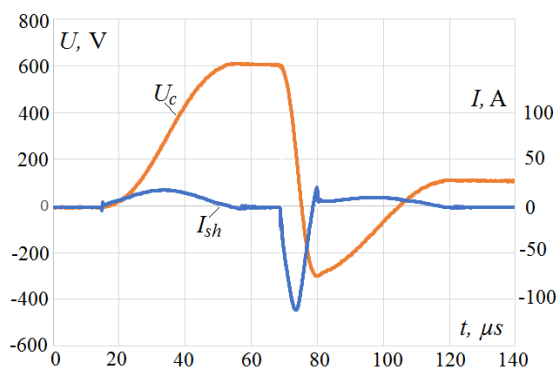


Fig. 2. Synchronous oscillograms of current and voltage of the working capacitor C_1 in the ESD process

Using a digital control system, the switching time intervals of each transistor can be set arbitrarily. However, unlike VT_1 , the switching of the VT_2 lock-up can be carried out only if the discharge current reaches the zero point. The reverse fast diode VD_1 also plays a secondary function, similar to the circuit of a single-stroke step-down voltage converter, closing the residual magnetizing current of the charging choke L_0 .

In the ESD process, plasma channels are formed chaotically, because of this, the energy invested in each pulse will be different, as indicated by the residual voltage on C_1 (Fig. 3), which has a step-like character. But this mode of generator oscillations is more pronounced only in a certain section of the energy curve, where the energy transfer processes in the ESL have a branched character.

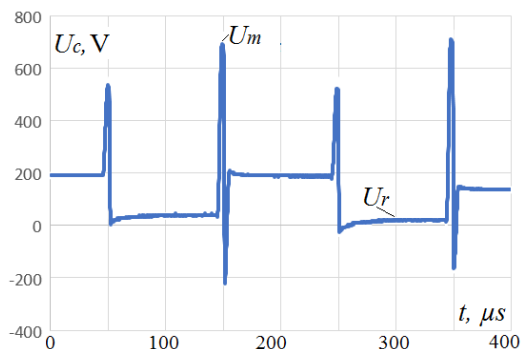


Fig. 3. Step-shaped voltage of the working capacitor C_1 in the ESD process

To measure the active instantaneous power and consumed energy in the installation, a household energy

meter (model TM55) is used, which is connected between the generator input and the primary AC network. It has been experimentally established that for metal granules that are prone to the formation of conductive chains, such as Ti , Cu , Fe , as a result of the conditionally short-circuit mode, the generator power is approximately 2 times less (30 W) than for the mode when the electric spark treatment reaction is initiated with a minimum monolayer height of metal granules. In this case, the dynamics of voltage and current on the capacitor C_1 have a high stationary stability of the steady-state oscillation mode of the generator. Since the electrical resistance of the conductive bridges is much lower than the characteristic resistance of the discharge circuit, only a fraction of the energy of C_1 will be dissipated in the VMLMG and on the active elements of the circuit. In addition, the steady-state voltage on C_1 between energy conversion cycles will be close to the voltage of the power source. Otherwise, if Al granules, which are prone to the formation of oxide films on their surfaces, are loaded into the reaction chamber, the generator may experience a mode close to idle. In this oscillation mode, the voltage curve on C_1 will also be stationary, but will differ in the presence of only an added amplitude of pulsations and even lower power consumption. In addition, a small part of the accumulated energy C_1 will be dissipated in the environment due to losses in electrolysis and electrochemical reactions in the liquid.

However, it has been observed that the system shift from a conditionally quiescent state (idle or short circuit mode) towards the ignition of the plasma formation reaction and the initiation of the ESD process is possible due to the preliminary mechanical displacement of each metal particle of the VMLMG. That is, the forced destruction of conductive bridges or oxide films on the contact surfaces between the granules creates conditions for the preliminary ionization of the medium and the formation of plasma channels. For this purpose, the chamber design, as noted above, involves a mechanism of forced agitation and activation of the medium. To avoid the situation of blocking the movement of the mechanical stirrer due to the mutual adhesion of the granules to each other, their shape was chosen to be close to quasi-spherical. In addition, it was also observed that for granules that have a smooth surface and form more dense contacts with each other, it is difficult to finally reach the ignition limit of the self-pickup reaction of the EISD mechanism even by moving them. However, due to the continuous mixing of the medium from the mechanical stirrer and the support of the ESD reaction by the transistor pulse generator, the smooth surface of the metal granules (Ti , Cu , Fe) is gradually covered with erosion holes and becomes rougher with the formation of a larger number of microp protrusions. This allows, after some time of forced mixing of the medium, to initiate the self-catch reaction of «continuous» plasma formation of electric spark treatment, after which further mixing of the granules already has an indirect effect and can be suspended. During the studies on the example of Al granules, it was also noticed that the TPG power even

increased with an increase in the rotation frequency of the rod mechanism. It should be noted that for the majority of the group of granules, additional disturbance was appropriate only at the stage of activation of their surfaces, because it caused some instability and intermittent ignition of the plasma channels. The implementation of such an additional processing method is also noted in the literature, but when using other mechanisms of medium disturbance. In particular, in [19] it is noted that the spatial oscillatory movement of granules relative to their static position as a result of the action of an additional source of mechanical disturbances (vibration, ultrasound) forcibly affects the length of plasma channels, restrains their development, limits the energy supplied to them, and enhances their migration along the surface of granules, which generally increases the dispersion of erosion particles and the energy efficiency of processing. But, on the other hand, the use of an additional mechanism and excessive agitation of the medium can significantly worsen the overall energy efficiency of electric spark processing.

Experiment setting. To achieve the goal, it is necessary to solve the following tasks:

- measurement of the power consumption of the electric discharge installation from the power supply network depending on the design parameters of the reaction chamber and the features of the VMLMG at other fixed parameters of the TPG (maximum charging voltage and energy of the working capacitor, frequency and pulse duration);
- assessment of the relationship between the power indicators of the electrical installation and the specific energy consumption of the ESD process of metal granules with different values of their intercontact active resistance (*Al*, *Ti*) in terms of kWh/kg;
- analysis of the electrophysical processes of EID to determine the effective modes of energy transfer from the TPG to the nonlinear ESL.

For clarity of the presentation of the experimental methodology, the input and output data operated by the electrophysical model of the TPG – ESL were determined.

Fixed parameters of the TPG and the reaction chamber: voltage on the input electrolytic capacitor C_0 – 420 V; maximum charging voltage and capacity of the working capacitor C_1 – 750 V and 1 μ F; inductance of the discharge circuit L_0 – 14.6 μ H; generator conversion frequency – 1 kHz; maximum current pulse duration – 12 μ s; working fluid – water with a specific electrical conductivity of 30–50 μ S/cm; diameter of the inner electrode 30 mm; duration of the ESD process – 10 min.

Adjustable installation parameters: technological gap between the cylindrical electrodes of the reaction chamber; mass of the granulated material before the start of dispersion – m_i , g; height and number of elementary layers of the VMLMG – h_i , mm, N_{sh} ; diameter of the outer electrode; average diameter of the granule (quasi-spherical approximation).

Initial parameters of the technological process after processing: average power of the consumed energy of the electric discharge installation from the power supply network – P , W; residual mass of the granulated material after processing – m_{ex} , g; mass of dispersed material – Δm , g; specific electricity consumption for dispersion of granular material – Q , kWh/kg.

The concentration of metal granules (*Al*, *Ti*) was calculated using a measuring cup with a working volume of 50 ml, a height of 125 mm and a diameter of 22 mm. Then, after recalculating the number of granules in the bulk volume, their average N_a concentration per 1 cm^3 was determined, and after weighing, their bulk density. The average diameter of the granules was obtained in the approximation of their quasi-spherical shape and under the condition of their cubic model of location in space ($d_{Al} = 2.4$ mm, $d_{Ti} = 3.5$ mm). To calculate the bulk number of layers in the axial direction along the length of the reaction chamber with a cylindrical electrode system, the formula was used:

$$N_d = \frac{\sqrt[3]{N_a} \cdot V_t}{\pi \cdot (R_0^2 - R_1^2)}, \quad (1)$$

where R_0 , R_1 are the outer and inner radii of the electrodes; V_t is the bulk volume of metal granules; $\sqrt[3]{N_a}$ is the number of granules per unit length in an arbitrary direction. The value $V_t / \pi \cdot (R_0^2 - R_1^2)$ is the height of the VMLMG in the axial direction along the length of the reaction chamber.

Measurement of the average TPG power in the process of electric spark treatment depending on the volume of each material was carried out in the range of their weights from 50 to 300 g with an analysis step of every 20 g and a processing duration of no more than 30 s, in such a way as to have the least impact on the previous initial state of the VMLMG in the ESD process.

Based on the obtained family of dependences of the average converter power on the bulk volume of granules and the diameter of the external electrode – $d_0=72$ mm, $d_1=82$ mm, $d_2=98$ mm (Fig. 4, a, b), both for aluminum and titanium loading, it can be stated that a common feature of all curves is the presence of distinct power maxima, which appear at approximately the same height of the VMLMG (for a certain number of layers) for each case of the geometry of the metal granular loading. In the range of the left section of the VMLMG experimental dependences also have a similar gradual growth pattern, close to linear. At the same time, with an increase in the diameter of the external electrode, the angular slope of each curve of the family decreases, and their maxima increase which is especially noticeable for titanium backfill. In addition, a distinctive feature is the electrophysical features of the behavior of titanium granules in the rear part of their dependences, where the power drops sharply. This is explained by the fact that the pulse energy at which the study was carried out (0.25 J) is no longer enough in this section of the VMLMG (to the right of the maximum) for continuous maintenance of the plasma formation reaction and a stable process of electric spark treatment.

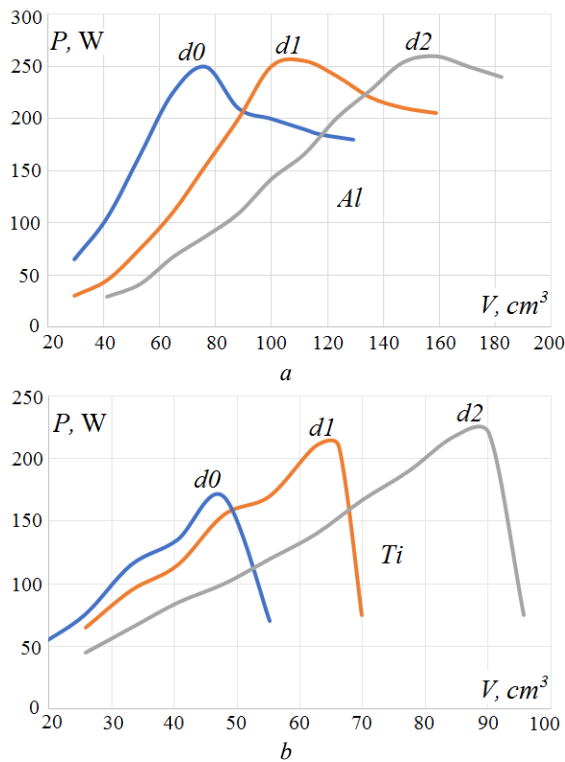


Fig. 4. Curves of dependence of generator power on the VMLMG of the reaction chamber for three values of the diameter of the external electrode:
a – Al granules; b – Ti granules

If the generator circuit enters a short-circuit mode or is close to it, then the discharge completely dies out in the reaction chamber or the plasma formation reaction occurs only near the central electrode-anode, and the power of the process still remains low (30–50 W). The maxima of the curves for aluminum backfill have a less pronounced growth pattern with increasing diameter of the external electrode, and their rear parts gradually decrease depending on the VMLMG. It should also be noted that all power maxima P_{\max} , both for aluminum and for titanium, arise at approximately the same height of the bulk volume of granules, or according to the number of their layers (1). Therefore, for Al: $h_{Al} = 22$ mm, $N_l = 8$ layers, for Ti: $h_{Ti} = 13.5$ mm, $N_l = 5$ layers. At the same time, the value of the power maximum tends to increase with increasing length of the IEG, on which a certain number of granules are placed depending on their diameter. For the average number of granules in the radial direction along the length of the IEG ($R_0 - R_1$) of the reaction chamber, respectively, for the above-mentioned model of their packing, we have the expression:

$$N_l = \sqrt[3]{N_a} \cdot (R_0 - R_1). \quad (2)$$

Therefore, guided by the above, it can be assumed that the average power consumption of the TPG in the process of ESD of metal granules is a unique function that depends to a certain extent on both the initial voltage on the IEG, the pulse energy and the frequency of their passage, and on the parameters of the packing of the VMLMG in the reaction chamber – the number of elementary layers in the bulk volume of metal granules and the number of granules in one of their layers. In addition, the surface tendency of titanium granules to

form conductive bridges in the environment is manifested in a rapid decrease in the TPG power due to the onset of the short-circuit mode.

The next stage of the work is to determine the specific electricity consumption in terms of obtaining 1 kg of powder raw material. In this case, the accumulated value of the average power for a longer ESD period was already measured. For Al granules, the treatment was carried out with a 72 mm diameter of the external electrode and fixed system parameters, as indicated above. Experimental and calculated data on the ESD of Al and Ti granules are given in Table 1, 2 respectively. The electrical parameters of the ESD of titanium granules were chosen to be the same as for aluminum granules, but with the exception of the increased diameter of the external electrode of 82 mm.

Table 1

m_i , g	m_{ex} , g	Δm , g	V_{is} , cm ³	h_i , mm	N_l	P , W	Q , kWh/kg
50	48,68	1,35	29,4	8,5	3,2	65	8,02
70	67,52	2,48	41,2	11,8	4,5	105	7,1
90	85,12	4,88	52,9	15,2	5,8	165	5,6
110	103,22	6,78	64,7	18,6	7,1	225	5,4
130	121,62	8,38	76,4	22	8,4	250	5
150	143,25	6,75	88,2	25,4	9,8	210	5,13
170	163,85	6,15	100	28,7	11	190	5,2

Table 2

m_i , g	m_{ex} , g	Δm , g	V_{is} , cm ³	h_i , mm	N_l	P , W	Q , kWh/kg
70	69,32	0,68	25,7	5,5	2	65	15,9
90	88,78	1,22	33,1	7,1	2,7	95	13
110	108,14	1,86	40,5	8,7	3,4	130	11,8
130	127,6	2,4	47,8	10,3	4	155	10,7
150	147	3	55,2	11,9	4,6	170	9,5
170	166,15	3,85	62,5	13,5	5,2	210	9
190	175,5	4,5	66,2	14,3	5,5	230	8,5

Thus, the obtained specific energy consumption indicators in the Al-Ti ESD process also correlate with the corresponding indicators of their average power. For Al, a lower dispersion energy consumption value was achieved than for Ti – 5 kWh/kg, but under the condition of a 20 W advantage. The obtained Q value correlates with the indicator given in [20] – 5.45 kWh/kg. However, this Q value was achieved at a very low productivity of electric spark treatment and power of the power source – during 3 h of treatment, the total mass of Al granules and electrodes decreased by only 1.8 g. The lowest value of the Q indicator for Ti – 8.5 kWh/kg was achieved only when the input voltage of the generator was increased to 450 V, which allowed stabilizing the plasma formation process, and despite the tendency in Fig. 4,b to increase the processing power. Taking into account the determined mass of the eroded material obtained during its processing time and the frequency of the generator pulses, it is possible to calculate the fraction of particles formed per one discharge pulse – $m_0 = \Delta m / (T \cdot f) = \Delta m / 6 \cdot 10^5$. Accordingly, we have: $m_{0,Al} = 13.9$ μg, $m_{0,Ti} = 7.5$ μg. Next, based on the thermodynamic equations [21] and the corresponding thermophysical coefficients for Al-Ti, the energy costs that go to melting E_m and evaporation E_v of this particle of eroded material are determined. Therefore,

for *Al*: $E_m=13.5$ mJ, $E_v=189$ mJ; *Ti*: $E_m=9$ mJ, $E_v=84$ mJ. The average pulse energy for *Al* is 250 mJ, for *Ti* – 210 mJ. If we assume that all eroded particles completely pass the evaporation stage, then the efficiency of the ESD in relation to the energy E_v will be: *Al* – $\eta = 76$ %, *Ti* – $\eta = 40$ %. At the same time, the energy E_v for *Ti* in terms of the same mass of material is 17 % lower than for *Al*. If we refer to Fig. 4,b, the generator power tends to increase, but does not reach its saturation threshold due to the cessation of the plasma formation reaction. For example, with an external electrode diameter of 98 mm, the generator power drops after 90 cm³ of the volume filled with metal granules. For this geometry of the VMLMG, energy consumption can be reduced to the level of 8.3 kWh/kg. Therefore, this indicator once again confirms the reality that with an increase in the number of contacts between granules along the length of the IEG and with an increase in the number of layers along the height of the reaction chamber, there is a gradual increase in the generator power and a decrease in the specific energy consumption of the ESD until its saturation threshold is reached.

An important aspect of the study is still the explanation of the behavior of the obtained experimental dependences of the average power on each section of the VMLMG. Therefore, to solve this issue, measurements of the current-voltage characteristics were carried out both on the electrodes of the chamber and on the TPG elements. The conversion of electrical oscillations to the level of amplitudes of signals safe for oscillography was performed using a mixed-type voltage divider with a transfer ratio of 1:46.5 and a coaxial current shunt with an active resistance of 1.55 mΩ. Both signals are fed via coaxial lines to the inputs of a dual-channel storage oscilloscope SDS1022. The digitized data were stored in text format and transferred to Excel for mathematical calculations. The number of sampling points provided by the oscilloscope on each channel is 104 with an interval of 10 ns and an amplitude value in millivolts. The digitization results were converted taking into account the vertical shift and the transmission coefficient for each signal. After processing many synchronous pairs of oscillographic data, it was found that the efficiency of ignition of plasma channels increases with each added layer of metal granules of the reaction chamber. At the initial levels of the bulk volume, many ineffective discharges are observed and only a small part of it is taken from the energy of the working capacitor. In this interval, the effective frequency of discharge pulses (EFDP) is less than the frequency of the generator pulses. According to the step-like voltage diagram on C_1 , it is possible to separate ineffective discharges from their total number for a certain period of time, and from the voltage drops from the charging to the residual at each switching cycle of the power switches, the average energy and conversion power can be calculated. To maintain the accuracy of signal digitization, the maximum width of the window for storing data on a time sweep of 1 ms/div. was 20 ms. In order to more accurately approximate the average power values, 5 voltage diagrams were processed with a total time of 100 ms. Therefore, according to the

presented algorithm, the average effective discharge energy (AEDE) can be calculated as:

$$E_a = \frac{\sum_{i=0}^{N_{sp}} E_i}{N_{sp}} = \frac{C}{2} \cdot \frac{\sum_{i=0}^{N_{sp}} (U_c^2 - U_r^2)_i}{N_{sp}}, \quad E_i \geq E_{th}, \quad (3)$$

where U_c , U_r are the charging and residual voltages on C_1 ; C is the capacitance of capacitor C_1 , N_{sp} is the number of effective discharges for the measurement time interval; E_i is the energy of effective discharge; E_{th} is the minimum threshold energy of discharge current.

The measurements were carried out with preservation of the same geometry of electrodes as in the previous experiment. A distinctive feature of the obtained curve of dependence of EFDP for *Al* granules (Fig. 5,a) is the presence of a section of its saturation (75–100 cm³), where the frequency of effective discharges coincides with the frequency of conversion of the generator 1 kHz. The average energy of effective discharges in this section of volumes after reaching its maximum (0.22 J) as well as the average power gradually decreases. In the case of *Ti* granules, the EFDP curve (Fig. 5,b) corresponds to the generator frequency only when it enters the short-circuit mode, and the maximum AEDE value is reached at the level of 60 cm³ of the VMLMG.

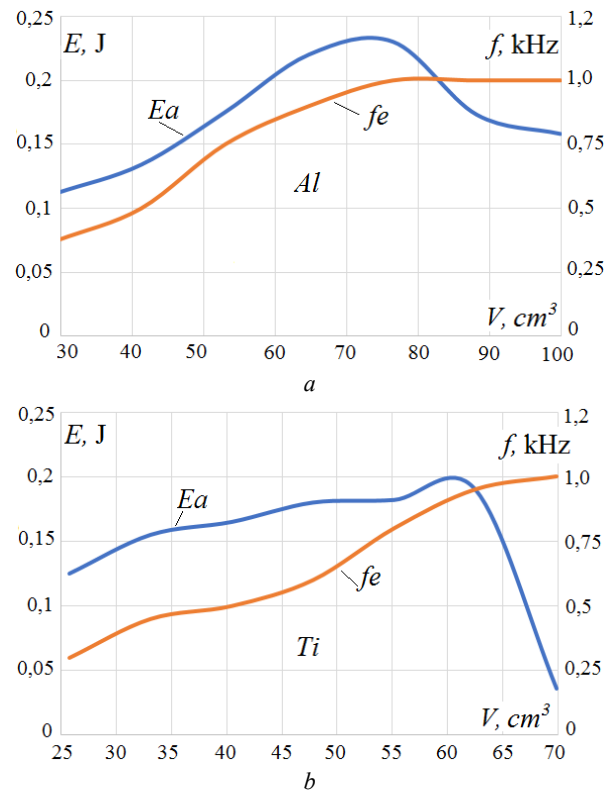


Fig. 5. Curves of the average energy and effective frequency of discharge pulses on the VMLMG of the reaction chamber: a – aluminum granules; b – titanium granules

Stationary electrical oscillations in the TPG in the saturation region of the VMLMG curve for *Al*, in contrast to *Ti*, are characterized by greater stability and a smaller value of reverse oscillations. Therefore, provided that the frequency of discharge pulses and their amplitude are stable, it is possible to take the current-voltage characteristics at several points of the EFDP saturation

region and calculate the instantaneous power and dynamics of the resistance on the load.

The equivalent value of the resistance R_{eq} of the VMLMG during the pulse duration is usually calculated by the formula [6], but the approximation to the integral expressions is performed using the trapezoidal approximation method:

$$R_{eq} = \frac{\sum_{k=0}^n (u_k \cdot i_k + u_{k+1} \cdot i_{k+1})}{\sum_{k=0}^n (i_k^2 + i_{k+1}^2)}, \quad (4)$$

where u_k , i_k are the instantaneous values of current and voltage in the discharge circuit at the k -th integration step.

The instantaneous power characteristics, which are allocated to the ESL, are calculated based on the obtained pairs of synchronous current and voltage oscillograms at 3 points of the saturation area of the effective discharge frequency (Fig. 6).

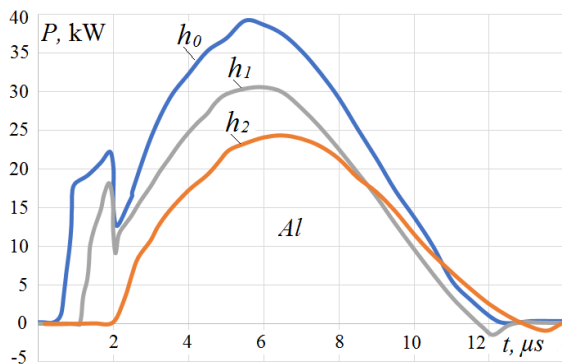


Fig. 6. Instantaneous power characteristics for 3 height levels of aluminum VMLMG

Synchronization of all characteristics was carried out on the first rapidly falling front of the voltage pulse on the IEG, which corresponds to the moment of the final electrical breakdown of the medium and the beginning of the development of the spark discharge with the subsequent transfer of the main part of the energy from the capacitive energy storage to the load. As can be seen from the characteristics for the filling levels $h_0 = 22$ mm, $h_1 = 25$ mm, their main feature is the presence of a significant power surge until the moment of development of the plasma channel. The power jump is mainly associated with the flow of current in ohmic contacts in local zones between the granules, the development of ionization avalanches and polarization of the working fluid in the intergranular volumes. It should be noted that the final voltage value, which is set on the IEG after the transistor key is completely unlocked, will be primarily determined by the current in the ohmic contacts of the load and the reactive parameters of the discharge circuit. The flow of current through the ohmic contacts causes a voltage drop across the choke L_1 , which accordingly reduces the maximum amplitude of the applied voltage to the IEG, the value of which in turn affects the consistency of the energy input into the ESL. As found out based on the analysis of many synchronous pairs of volt-ampere data, the voltage on the IEG is maintained for some time and remains practically constant, while a voltage «plateau» is formed before the start of the development of

the plasma discharge. In turn, the intensity of electron avalanche propagation and the further development of plasma channels will depend on the value of the ohmic contact current, which heats the contacting surfaces of the granules.

The increase in the ohmic contact current from the layer height is explained by the increase in the surface area of contact of the granules with the electrodes of the reaction chamber. But at some point, at the height of the VMLMG $h_2 = 29$ mm, the ohmic contact current becomes quite significant and merges with the spark discharge current, at the same time the voltage «plateau» – the ionization voltage shelf completely disappears, which worsens the development of plasma channels. Therefore, it is advantageous to perform the ionization process hold, when the voltage plateau on the IEG lasts for some time, on average several microseconds, which is important for increasing the number of plasma channels and the efficiency of their growth. The ohmic contact current in this sense heats the contacting layers of granules and stimulates thermionic emission from their surfaces, which in turn affects the ionization current, which is the trigger – the primary source for the formation of plasma channels. On the other hand, a sufficient potential difference between the heated surfaces of the granules will create conditions for the effective propagation of electron avalanches and the formation of plasma channels.

For the considered family of instantaneous power curves for the duration of the discharges (12 μs), the energy dissipated in the ESL is calculated. Again, if the power integral over time is approximated by the trapezoidal method, then we can obtain the expression:

$$E_a = 0.5 \cdot \sum_{k=0}^n (U_k \cdot i_k + U_{k+1} \cdot i_{k+1}) \cdot \Delta t, \quad (5)$$

where Δt is the integration time step, $\Delta t = 10$ ns.

From which we have that the energy for the curve h_0 is 240 mJ, h_1 – 190 mJ, h_2 – 160 mJ. These results also correlate with the values obtained by (3) for the generator power curve in Fig. 4,a.

Regarding the dynamics of the load resistance over time (Fig. 7), each curve has its own initial resistance value. However, a distinctive feature of the curve h_2 is the presence of a zero resistance value and its instantaneous jump in a short period of time from the zero mark to the initial value R_0 .

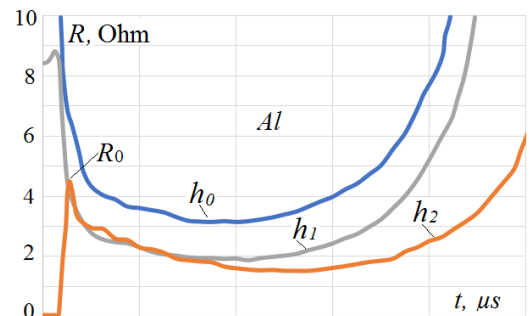


Fig. 7. Dynamics of the resistance of the electric spark load

At a layer height of at least 30 mm, the presence of the displacement current of the intergranular volumes of the working fluid becomes significantly noticeable, which

causes the appearance of a reactive component in the dynamics of the load resistance. Further, using (4) for all 3 curves h_0 – h_2 , we have the following values of the equivalent load resistance: $h_0 = 3.95 \, \Omega$, $h_1 = 2.41 \, \Omega$, $h_2 = 1.84 \, \Omega$. If the characteristic resistance of the C_1 - VT_1 - VD_2 - L_1 circuit is $4 \, \Omega$, then it can definitely be stated that the main reason for the decrease in the AEDB with the increase in the VMLMG in the EFDP saturation region is the decrease in its equivalent resistance. Because of this, the transient process in this circuit becomes more oscillatory and branched [7].

At the same time, the R_{eq} values correlate with the initial resistance values at the time of IEG breakdown, which also tend to decrease – $R_0(h_0)=25 \, \Omega$, $R_0(h_1)=8.5 \, \Omega$, $R_0(h_2)=4.5 \, \Omega$. The obtained relationship between the height of the VMLMG and the initial resistance of the ESL can also be an addition to the parametric model of the electric spark load [4], where the dependence of this resistance on the initial applied voltage to the IEG is established.

Another interesting circumstance is that the presence of ohmic contact current when switching the discharge circuit with a thyristor key is difficult to notice due to its inertial features – the process of heating the intergranular gaps and the formation of plasma channels merge in time. In addition, the low value of the circuit inductance only contributes to the rapid development of the plasma discharge and, in principle, makes it impossible to recognize this phenomenon. In [17], only approximate intervals of existence of each current are given, because the volt-ampere characteristics on the IEG are similar to a smooth curve of the pulse power at the point of a noticeable drop in the contact resistance of the ESL, which is shown in Fig. 6 (curve h_2). In this sense, the advantage of the transistor switch is the possibility of quickly applying voltage to the IEG and immediately separating several stages of the spark discharge development in the volume of the metal loading of the reaction chamber.

Conclusions.

1. The proposed model of an electric discharge installation – TPG with a maximum pulse voltage of up to 800 V and energy of up to 0.3 J in combination with a reaction chamber with a cylindrical system of electrodes confirms its effectiveness for ESD tasks of heterogeneous conductive granular media with different degrees of activity of intercontact resistance.

2. It was established that the average power consumption of the TPG when operating on the ESL under the condition of a fixed input supply voltage and pulse frequency is dependent on the geometric dimensions of the metal loading in the reaction chamber – the number of its layers and the number of granules along the length of the IEG in one layer. In addition, the nature of the TPG power after reaching its maximum in the saturation region of the effective frequency of the discharge pulses is influenced by the electrophysical features of the behavior of the intercontact resistance of the granules and their tendency to form chains of through-conduction in the medium.

3. The specific energy consumption Q in the ESD process of aluminum granules (5 kWh/kg) turned out to be lower than for titanium granules (8.3 kWh/kg), at the same time, the obtained power curve for the titanium load is characterized by the absence of its saturation area due to the onset of the short-circuit mode in the TPG. In the case of increasing the outer diameter of the reaction chamber and, accordingly, the inter-contact gaps along the length of the IEG, provided that there is a certain number of layers of the VMLMG, the maximum power also increases, which accordingly correlates with the Q indicator in the direction of its decrease.

4. It was found that the effective frequency of ESD discharge pulses depends on the ohmic contact current, the direct flow of which before the start of the main discharge causes heating of the contact surfaces of the granules, which affects the ionization processes of the development of electron avalanches and the formation of plasma channels.

5. It was established that the main reason for the decrease in average power with increasing bulk volume of metal granules in the saturation region of the curve of the effective frequency of discharge pulses is the decrease in both its initial and equivalent resistance, which is caused by an increase in the surface area of contact of the granules with the electrodes of the reaction chamber, therefore the transient process in the discharge circuit becomes more branched.

Conflict of interest. The author declares no conflict of interest.

REFERENCES

1. Monastyrsky G. Nanoparticles formation mechanisms through the spark erosion of alloys in cryogenic liquids. *Nanoscale Research Letters*, 2015, vol. 10, no. 1, art. no. 503. doi: <https://doi.org/10.1186/s11671-015-1212-9>.
2. Jin C.H., Si P.Z., Xiao X.F., Feng H., Wu Q., Ge H.L., Zhong M. Structure and magnetic properties of Cr/Cr₂O₃/CrO₂ microspheres prepared by spark erosion and oxidation under high pressure of oxygen. *Materials Letters*, 2013, vol. 92, pp. 213-215. doi: <https://doi.org/10.1016/j.matlet.2012.10.126>.
3. Vinnychenko D.V., Nazarova N.S., Adamchuk Y.O., Vinnychenko I.L., Vyshnevskiy O.A. Synthesis of Tungsten Carbides Submicron Powders by High-Frequency Electrospark Treatment Method. *Springer Proceedings in Physics*, 2024, vol. 312 SPPHY, pp. 385-395. doi: https://doi.org/10.1007/978-3-031-67527-0_27.
4. Shydlovska N.A., Zakharchenko S.M., Cherkaskiy O.P. Physical prerequisites of construction of mathematical models of electric resistance of plasma-erosive loads. *Technical Electrodynamics*, 2017, no. 2, pp. 5-12. (Ukr). doi: <https://doi.org/10.15407/techned2017.02.005>.
5. Shydlovska N.A., Zakharchenko S.M. Discrete nonlinear-probabilistic model of the equivalent electrical resistance of a layer of metal granules. *Technical Electrodynamics*, 2021, no. 2, pp. 3-12. (Ukr). doi: <https://doi.org/10.15407/techned2021.02.003>.
6. Shcherba A.A., Suprunovska N.I. Cyclic transients in the circuits of electric discharge installations taking into account the influence of magnitude and rate of discharge currents rise on resistance of electric spark load. *Technical Electrodynamics*, 2018, no. 2, pp. 3-10. (Ukr). doi: <https://doi.org/10.15407/techned2018.02.003>.
7. Shcherba A.A., Suprunovska N.I., Ivashchenko D.S. Modeling of nonlinear resistance of electro-spark load for synthesis of discharge circuit of capacitor by time parameters. *Technical Electrodynamics*, 2014, no. 3, pp. 12-18. (Ukr).

8. Shydlovska N.A., Zakharchenko S.M., Zakharchenko M.F., Kulida M.A., Zakusilo S.A., Yakovenko R.A. Distribution of volumes of plasma channels components between metal granules in working liquids. *Electrical Engineering & Electromechanics*, 2025, no. 1, pp. 73-85. doi: <https://doi.org/10.20998/2074-272X.2025.1.10>.
9. Shydlovska N.A., Zakharchenko S.M., Zakharchenko M.F., Kulida M.A., Zakusilo S.A. Spectral and optic-metric methods of monitoring parameters of plasma channels caused by discharge currents between metals granules in working liquids. *Electrical Engineering & Electromechanics*, 2024, no. 6, pp. 72-83. doi: <https://doi.org/10.20998/2074-272X.2024.6.10>.
10. Petrov O., Petrichenko S., Yushchishina A., Mitryasova O., Pohrebennyk V. Electrospray Method in Galvanic Wastewater Treatment for Heavy Metal Removal. *Applied Sciences*, 2020, vol. 10, no. 15, art. no. 5148. doi: <https://doi.org/10.3390/app10155148>.
11. Khrysto O.I. Current-voltage characteristics of single-stage semiconductor magnetic pulse generators with a distinctive structure of the conversion link in the input circuit. *Electrical Engineering & Electromechanics*, 2023, no. 6, pp. 41-47. doi: <https://doi.org/10.20998/2074-272X.2023.6.07>.
12. Syzonenko O.M., Tashev P., Torpakov A.S., Lypian Ye.V., Prystash M.S., Kandeve M., Dyakova V. Influence of the High-Voltage Discharge Treatment of Powders on the Properties of Metal Matrix Composites of the Ti-TiC System. *Materials Science*, 2022, vol. 58, pp. 165-174. doi: <https://doi.org/10.1007/s11003-022-00645-3>.
13. Khrysto O. Energy transfer processes in high-voltage circuits based on magnetic pulse compression. *Acta Electrotechnica et Informatica*, 2020, vol. 20, no. 3, pp. 3-10. doi: <https://doi.org/10.15546/aeci-2020-0013>.
14. Khrysto O.I. Energy characteristics for nanosecond current interrupter of semiconductor-magnetic pulse generator's terminal stage. *Electrical Engineering & Electromechanics*, 2023, no. 3, pp. 59-65. doi: <https://doi.org/10.20998/2074-272X.2023.3.09>.
15. Petrichenko S., Malyushevskaya A., Ivanov A., Mitryasova O., Salamon I. Improving the Efficiency of Water Purification from Heavy Metals using the Electric Spark Method. *Journal of Ecological Engineering*, 2024, vol. 25, no. 8, pp. 1-9. doi: <https://doi.org/10.12911/22998993/189230>.
16. Zakharchenko S.N., Kondratenko I.P., Perekos A.E., Zalutsky V.P., Kozyrsky V.V., Lopatko K.G. Influence of discharge pulses duration in a layer of iron granules on the size and structurally-phase conditions of its electroerosion particles. *Eastern-European Journal of Enterprise Technologies*, 2012, vol. 6, no. 5 (60), pp. 66-72. (Rus).
17. Zakharchenko S.N. Modelling of dependence of electrical resistance of granulated current-carrying mediums from a pulse current proceeding in them. *Technical Electrodynamics*, 2012, no. 5, pp. 17-27. (Ukr).
18. Shcherba A.A., Suprunovska N.I., Shcherba M.A. Features of the formation of multi-channel pulse currents and fast-migrating electric sparks in the layer of current-conducting granules of electric-discharge installations. *Tekhnichna Elektrodynamika*, 2022, no. 2, pp. 3-11. doi: <https://doi.org/10.15407/techned2022.02.003>.
19. Liu Y., Zhu K., Li X., Lin F., Li Y. Analysis of multi-scale Ni particles generated by ultrasonic aided electrical discharge erosion in pure water. *Advanced Powder Technology*, 2018, vol. 29, no. 4, pp. 863-873. doi: <https://doi.org/10.1016/j.appt.2018.01.003>.
20. Zakharchenko S.M., Shydlovska N.A., Perekos A.O., Zakharchenko M.F. Power Efficiency of Electrophysical Methods of Dispersion and Electrochemical Dissolution of Several Metals. *Metallofizika i Noveishie Tekhnologii*, 2021, vol. 43, no. 4, pp. 465-487. (Ukr). <https://doi.org/10.15407/mfint.43.04.0465>.
21. Gulbinowicz Z., Goroch O., Skoczylas P. Mathematical Modeling of Material Erosion During the Electrical Discharge. *Advances in Science and Technology Research Journal*, 2020, vol. 14, no. 2, pp. 27-33. doi: <https://doi.org/10.12913/22998624/114959>.

Received 24.03.2025

Accepted 01.06.2025

Published 02.09.2025

O.I. Khrysto¹, PhD, Senior Researcher,

¹ Institute of Pulse Processes and Technologies of NAS of Ukraine,

43-A, Bogoyavlenskij Avenue, Mykolayiv, 54018, Ukraine,

e-mail: alexander.khristo@gmail.com

How to cite this article:

Khrysto O.I. Analysis of energy characteristics of a transistor pulse generator in the process of electric spark dispersion of current-conductive granular media. *Electrical Engineering & Electromechanics*, 2025, no. 5, pp. 70-79. doi: <https://doi.org/10.20998/2074-272X.2025.5.10>

S.Yu. Shevchenko, D.O. Danylchenko, R.O. Hanus, S.I. Dryvetskyi, S.K. Berezka, O.M. Grechko

Features of designing high-voltage overhead power lines in an underground collector

Problem. Protection of high-voltage (HV) overhead power lines (OPL) from external atmospheric and military influences and reduction of their hazardous electromagnetic radiation is possible if they are made in a compact form and placed in an underground collector. But to ensure high capacity and reliable operation of such compact HV OPL, it is necessary to improve the existing designs of their current-carrying elements. The **goal** of the work is to determine promising design parameters of busbars of compact high-voltage overhead power lines laid in an underground collector. The **methodology** for calculating permissible long-term currents of HV OPL laid in an underground collector is based on the analytical model proposed by the authors for describing the processes of mass and heat transfer in the air of an underground collector. **Scientific novelty.** For the first time, the possibility of efficient use of HV OPL in an underground collector conditions is substantiated and the conditions for their reliable transmission of electric energy with increased capacity are determined. This is achieved through the use of rectangular flat vertical conductive busbars with an increased surface area and providing better convective heat exchange compared to traditional round wire, as well as by determining the rated current for such overhead lines at a reduced ambient temperature (15 °C), which is typical for operating conditions in underground collectors (25 °C) adopted for overhead lines located outdoors. **Practical value.** The use of the proposed HV OPL laid in an underground collector should ensure reliable transmission of electrical energy, sufficient throughput and increased protection from external factors while reducing the electromagnetic impact on the environment (due to a significant reduction in the interphase distance from 3–4 m to 0.3–0.6 m for 110 kV HV OPL), and has advantages over SF₆-insulated cable lines and cable lines characterized by an increased insulation cost). References 36, table 1, figures 6.

Key words: compact high-voltage overhead power line, underground collector, busbar conductor, thermal modeling.

Проблема. Захист високовольтних повітряних ліній електропередавання (ПЛ) від зовнішніх атмосферних та військових впливів, та зменшення їх небезпечного електромагнітного випромінювання можливо при їх виконанні у компактному вигляді і розміщенні у підземному колекторі. Але для забезпечення високої пропускної спроможності та надійної роботи таких компактних повітряних ПЛ необхідно удосконалення існуючих конструкцій їх струмопровідних елементів. **Метою** роботи є визначення перспективних конструктивних параметрів струмопроводів компактних високовольтних повітряних ліній електропередавання, які прокладені у підземному колекторі (ПЛПК). **Методика** розрахунку допустимих тривалих струмів ПЛПК заснована на запропонованій авторами аналітичній моделі опису процесів масотеплоперенесення в повітрі підземного колектору. **Наукова новизна.** Вперше обґрунтовано можливість ефективного використання ПЛ в умовах підземного колектору та визначено умови надійної передачі ними електроенергії з підвищеною пропускною спроможністю. Це досягнуто завдяки застосуванню прямокутних плоских вертикальних струмопровідних шин, які мають збільшену площу поверхні та забезпечують крайній конвекційний теплообмін порівняно з традиційним круглим проводом, а також за рахунок визначення допустимого тривалого струму для таких ПЛ при зменшеній температурі зовнішнього середовища (15 °C), що характерна для умов експлуатації в підземних колекторах і суттєво нижча за стандартну температуру (25 °C), прийняту для ПЛ, розміщених на відкритому повітрі. **Практична значимість.** Використання запропонованої ПЛПК має забезпечити надійне передавання електричної енергії, достатню пропускну спроможність і підвищену захищеність від зовнішніх факторів при зменшенні електромагнітного впливу на оточуюче середовище (за рахунок істотного зменшення міжфазної відстані з 3–4 м до 0,3–0,6 м для ПЛ 110 кВ), і має переваги над відомими підземними електромережами (лініями електропередавання з елазовою ізоляцією та кабельними лініями, що характеризуються підвищеною вартістю ізоляції). Бібл. 36, табл. 1, рис. 6.

Ключові слова: компактна високовольтна повітряна лінія електропередавання, підземний колектор, струмопровід із плоских шин, моделювання теплового режиму.

Introduction. Ensuring reliable power supply to consumers is the main task of the electric power industry. To achieve this, it is necessary to improve the technical and economic indicators of high-voltage (HV) power grids. Two main types of power grids are most often used to supply consumers with electricity: HV overhead power lines (OPLs) and HV underground cable lines (CLs). However, during the operation of OPLs and CLs, problems arise with ensuring their reliable functioning. This is due to the influence of natural atmospheric factors (ice, solar radiation, strong winds and rain, etc.), as well as the high vulnerability of these lines in the event of fighting using modern artillery and missile weapons.

In addition, the problem of improving the power supply of modern megacities with dense construction

requires an urgent solution. The increase in load in cities leads to the need to find new methods for organizing their power supply.

One of the effective methods of increasing the reliability of power supply in cities and the protection of power grids from negative external man-made, natural and military influences is the placement of power grids in underground reinforced concrete tunnels (collectors), which is quite widespread in the world. Thus, in [1–11] examples of the development of pilot projects for the construction of underground power grids of different voltage classes with insulation from air, cross-linked polyethylene and SF₆ are given.

In [1, 2] the issues of choosing insulation for underground lines and substations of various designs are

considered, examples of their calculations are given. Work [3] is devoted to the analysis of the impact on the environment of OPLs and underground CLs. It is shown that underground lines have a significantly smaller number of external influence parameters and have a much smaller impact on the environment.

The works [12–14] are devoted to the comparison of the parameters of OPLs and underground CLs made of cross-linked polyethylene. It has been shown that CLs are more protected from external factors and have a compact design that reduces the electromagnetic impact on the environment and does not require the alienation of large land plots. However, with the same capacity, CLs are 2–10 times more expensive than overhead lines due to the high cost of HV insulation made of cross-linked polyethylene [13, 14]. It should also be noted that the repair work of OPLs and CLs can differ in cost by 5–10 times.

The works [4, 5] contain materials on the construction of a 500 kV underground line in California, made with a direct current cable. This decision is due to the impossibility of using AC CL in the required length. The choice of an underground line is due to the community's resistance to the construction of a ground OPL.

The works [6, 7] provide data on the implementation of a project to build a completely underground 220 kV substation in the Chinese city of Wuhan. Currently, no detailed information about this project is provided in open sources, but the fact that it is located in a shopping mall imposes additional requirements on its design.

The work [8] is devoted to the development in 2013 by the LLC Kharkiv Design Development Institute «Teploelektroproekt-Soyuz» of a project for an underground 220 kV substation with SF₆ insulation.

The works [9, 10] show the possibility of building underground power networks, identify the advantages of such networks, but do not provide data on their design features.

The work [11] is devoted to the analysis of the use of SF₆ insulation in power networks. The advantages and disadvantages of using SF₆ as an insulating medium are given. Gas insulated transmission lines (GILs) are considered. Direct burial of the GIL system into the ground combines advantages of underground laying of cables with high throughput of ground OPLs of the corresponding power. It is shown that GILs have high reliability, high throughput, and low magnetic field levels. Such lines are similar in design to the so-called complete current conductors and have insulators inside the structure that limit the radius of rotation and the value of the permissible short-circuit currents. In addition, the GIL housings must be made hermetic, which significantly complicates their design. It is also worth noting the high cost and complexity of maintaining such a line compared to the OPL of the analog power.

In the works [15–18] it is shown that the magnitude of the magnetic field harmful to humans and the environment, created by OPLs and CLs, is proportional

to the interphase distance of their current conductors. Therefore, the value of their magnetic field is significantly (by an order of magnitude) reduced in the compact design of electrical networks, which are characterized by an interphase distance of less than 1 m.

The main parameter that significantly affects the characteristics of electrical networks is the design of their phase power lines, including their material and geometry. Currently, the choice of current conductors of OPLs and CLs is regulated by regulatory documents [19]. It should be noted that their recommendations are more for different voltage classes. Thus, to determine the cross-section and number of wires in a phase for OPLs with a nominal voltage of up to 20 kV, it is necessary to exclude electrical calculations, and those parameters for a line with a higher voltage are performed without any technical or economic calculations in [19] in the form of Table 2.5.16. This necessitates the search for other approaches to the selection of material and design of current conductors in comparison with the traditional approach [20–23], and especially, given that the specified sources do not consider the issue of selecting the parameters of the current conductor for power networks located in underground collectors.

In the works [24–26], examples of the use and selection of so-called high-temperature wires are given. In the works [27, 28], information is provided and the advantages of wires with a composite core are highlighted, which can increase the mechanical characteristics and increase the length of OPL's spans. The works [29, 30] describe the advantages of using wires made of aluminum alloys and provide examples of their use for OPLs.

It should be noted that the above advantages of the latest wire brands cannot be decisive for the choice of the design of current conductors of OPLs in an underground collector. It is necessary to take into account that the determination of the design of current conductors for OPLs located in an underground collector will be quite close to the choice of the design of phases of closed switchgear with air insulation in accordance with [19–23]. These sources provide tables with the values of wire and bus cross-sections and their maximum permissible continuous currents. However, it is not indicated under what conditions they operate.

The works considered above, which are devoted to the creation of compact underground electrical networks of various types and their structural elements, do not contain specific technical parameters of the completed or proposed projects.

According to the authors of the article, the greatest interest for practical use is HV compact OPLs with air insulation laid in an underground collector (OPLs in UC). But OPLs in UC in comparison with ground OPLs, underground CLs and underground GILs have not been studied enough to date. The rational design parameters of their current conductors, which at limited cost allow to realize increased throughput with increased protection from external factors and reduce electromagnetic impact on the environment, remain still not defined.

The goal of the work is to determine the promising design parameters of current conductors of compact high-voltage overhead power lines, which are laid in an underground collector.

The above analysis shows that OPLs in UC can be considered as a promising means of transmitting electrical energy under the conditions of ensuring their competitive technical and economic characteristics. Thus, OPL in UC has quite significant advantages over OPL, and primarily because in the underground collector there are no negative natural factors that affect OPLs, which are located in the open air. Therefore, OPLs in UC can be considered as an alternative to CLs and GILs, which have a more complex design of current conductor insulation and high cost.

Thus, the requirements for the structural elements of OPLs in UC will be very different from the known requirements for the structural elements of OPLs. This fact confirms the need to conduct research to determine the rational design of OPLs in UC elements, and primarily the design of their phase current conductor.

Determination of the design of the phase current conductor of the OPL in UC. One of the main design parameters of both the OPLs and the OPLs in UC is the cross-section of the current conductor. Based on the unambiguous recommendations of regulatory documents regarding the phase cross-section of the OPL with nominal voltage of 110 kV, a phase cross-section of 240 mm² was adopted, recommended in [19] for AC type wires. For phase current conductors of the OPLs in UC of busbars, the cross-section can be chosen the same as for the AC type wire. However, if we calculate the permissible continuous current of the 110 kV OPL wire based on its maximum natural power of 30 MW, we will obtain a current value in the phase of about 272 A. With an increase in power by 25 % (standard practice for using 110 kV lines), the current will increase to approximately 340 A. For such current values, it is possible to determine the cross-sections of AC wires of 95 mm² and 150 mm², respectively, from [19]. The choice of such wire cross-sections will lead to an increase in active power losses, but will reduce capital investment in the line. Therefore, to determine the rational wire cross-section, it is necessary to conduct a technical and economic comparison of the phase design, taking into account all the factors affecting it.

However, the conditions for using phase wires for OPLs in the open air and current conductors of the OPLs in UC, as noted above, are quite different. Regulatory documents recommend selecting phase wires based on the permissible continuous current. To determine it, it is necessary to calculate the heat transfer coefficient, which significantly depends on the design features of the phase current conductors and the air temperature in the underground collector.

Based on the current values (0.3–2 kA) that must be provided for the OPLs in UC, their creation does not require the use of special complex current conductor designs in the form of boxes, pipes, I-beams or several rectangular-section buses [19–23]. Therefore, the authors

propose to consider using either a conventional AC type wire for OPLs or a rectangular busbar as a phase current conductor for OPLs in UC. This necessitates the performance of thermal calculations of rectangular busbars, which are widely used for low and medium voltages. This necessity is due to the fact that the nomenclature of busbars [19–23] does not meet the conditions of their use for power transmission lines. For OPLs in UC, completely different busbar sizes may be rational, which meet the requirements [19] for the cross-section of phase current conductors for different classes of rated voltage.

When determining the heat transfer coefficient and permissible long-term current of phase current conductors of the OPLs in UC, it is also necessary to take into account the specific conditions of their operation. The main difference from the OPLs is that for OPLs in UC, it is not necessary to take into account the strength and direction of the wind, as well as solar radiation, which affect the thermal mode at a given long-term permissible temperature of the current conductor of 70 °C [19–23].

The cooling efficiency of current conductors of the OPL in UC is estimated by their heat transfer coefficient [31], which determines the intensity of heat transfer from a solid surface to the air in the environment. For its calculation under conditions of laminarity and natural convection, the following relationship can be used [32]:

$$Nu = C (Gr \cdot Pr)^n, \quad (1)$$

where Nu is the Nusselt criterion; Gr is the Grashof criterion; Pr is the Prandtl criterion; the coefficients C and n depend on the free motion mode and the surface washing conditions.

The Nusselt criterion Nu [33] characterizes the intensity of heat transfer in the boundary layer between the gas and the surface of the body flown around it:

$$Nu = \alpha \cdot l / \lambda_p, \quad (2)$$

where l is the characteristic size, m; λ_p is the thermal conductivity of the gas, W/(m·K).

The Prandtl criterion Pr [33] determines the physical properties of the gas:

$$Pr = \mu \cdot C_p / \lambda_p = \nu_p / a, \quad (3)$$

where μ is the dynamic viscosity coefficient, N·s/m²; ν_p is the kinematic viscosity coefficient of the gas at a given temperature of the medium t_p , m²/s; a is the coefficient of temperature stability of the gas at a given temperature, m²/s; C_p is the isobaric mass heat capacity of the gas, kJ/(kg·K).

The Grashof criterion Gr characterizes the ratio of the lifting forces that arise in the gas during heating and the viscous forces [33]:

$$Gr = \frac{\beta \cdot g \cdot d^3 \cdot \Delta t}{\nu_p^2}, \quad (4)$$

where β is the coefficient of volumetric expansion of the gas, 1/K; g is the acceleration due to gravity, m/s²;

Δt is the temperature difference between the surface (wall) of size d and the gas between which heat is exchanged, °C or K.

Let us use the relationships (1–4) to calculate the permissible long-term current of the current conductor of the OPLs in UC made of a round wire of type AC.

Calculation of the permissible continuous current of the OPL in UC made of round wire. The geometry of the current conductor of the OPL in UC made of round wire is shown in Fig. 1.

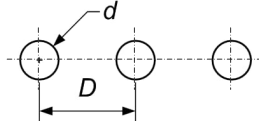


Fig. 1. To determining the heat transfer coefficient of a round wire of the OPL in UC

For the calculation, the recommended [19] design of a 110 kV phase with one AC type wire with cross section of 240 mm², which is used for overhead lines, was selected.

The calculation was performed under the following conditions.

The 110 kV OPL in UC is located in a reinforced concrete collector with minimum internal size of 3×4 m, which is located underground at a depth of at least 4 m. In this case, the calculated air temperature in the collector according to [34] will be 14–16 °C. Therefore, we will perform the calculation for the air temperature $t_p = 15$ °C, and also for comparison for the temperature $t_p = 25$ °C, which according to [19–23] is calculated for ground OPLs.

Long-term permissible temperature of the current conductor $t_{st} = 70$ °C, thermal conductivity $\lambda = 0.0287$ W/m·K; kinematic viscosity coefficient $\nu_p = 17.46 \cdot 10^{-6}$ m²/s; Prandtl criterion for air $Pr = 0.698$; volumetric expansion coefficient of air $\beta = 0.00343$ 1/K.

The following phase wire parameters were used in the calculation: diameter of the AC wire 240/32 $d = 21.4$ mm; radiation coefficient of a completely black body $G_0 = 5.67 \cdot 10^{-8}$ W/m²; blackness coefficient of the body $E_b = 0.4$; active resistance of the wire $r_0 = 0.1182$ mΩ/m.

Taking into account the fact that the AC type wire is made of a bundle of wires of smaller diameter, the equivalent wire diameter increased by a factor of 1.33 was used [35]. The presence of collector walls was not taken into account in the calculation.

The Grashof criterion Gr was calculated according to (4). Taking into account the value of the Prandtl criterion for air, the Nusselt criterion is defined as [33]:

$$Nu = 0.5 (Gr \cdot Pr)^{0.25}. \quad (5)$$

The heat transfer coefficient from the wire is calculated using the formula:

$$\alpha = Nu \cdot \lambda / d. \quad (6)$$

The heat flux from the wire due to convection from 1 m² is equal to:

$$q = \alpha_2 (t_{st} - t_p). \quad (7)$$

Heat release from the wire due to convection from 1 m² of the surface of the wire AC 240/32 [33] is equal to:

$$Q_C = \alpha_1 (t_{st} - t_p) F, \quad (8)$$

where F is the surface area of the wire.

Heat release from 1 m² of the surface of the AC240/32 wire due to radiation is [33]:

$$Q_R = \varepsilon_0 C_0 \left((t_{st}/100)^4 - (t_p/100)^4 \right) \cdot F. \quad (9)$$

The total heat release in the channel is equal to:

$$Q_p = Q_C + Q_R. \quad (10)$$

The heat release from the flow of current I is:

$$Q_e = I^2 R, \quad (11)$$

where R is the electrical resistance of the conductor.

The permissible value of the current flowing in the conductor under the condition $Q_e = Q$ is equal to:

$$I = (Q_p / R)^{0.5}. \quad (12)$$

The results of calculating the permissible continuous current for the AC 240/32 wire, which is made in accordance with (5–12) by (1–4), are presented in Fig. 3 and allow us to compare it with the tabular one given in [19]. The calculation error was 2.6 % (tabular value 505 A, calculated value 518.13 A). This confirms the correctness of the developed calculation method and the possibility of its use for determining the permissible continuous currents of current conductors placed in an underground collector. At the same time, the operating conditions of current conductors in the collector are practically the same as the conditions of their operation in the room.

Calculation of the permissible continuous current of the current conductors of the OPL in UC of busbar.

It is proposed to perform the phase current conductor of the OPL in UC in the form of one busbar of rectangular cross-section. This design of the phase current conductor was chosen taking into account the simplicity of its installation and operation. When analyzing the busbar cross-section, we take it equal to the wire cross-section for AC 240 110 kV OPL, which is recommended in [19]. It should be noted that with an equal cross-section with an AC type wire, busbar, unlike AC, may have a different design.

For the calculation, variants of the busbar with the geometry corresponding to the following dimensions h/d ratio (Fig. 2) were selected: 240/1, 120/2, 80/3, 60/4, 48/5, 24/10, 20/12, 12/20, 12/24, 5/48, 4/60, 3/80, 2/120, 1/240.

The calculation of the permissible continuous current of the busbar is based on the relationships (1–4), which are also used for round wire. The geometry of the current conductor with the busbar is shown in Fig. 2.

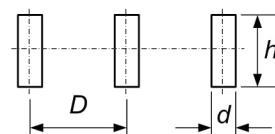


Fig. 2. To determining the heat transfer coefficient of a current conductor of the OPL in UC of busbars

In busbars, the heat release process is different because of presence of clearly expressed busbar vertical and horizontal surfaces for which, in presence of natural convection, heat transfer conditions are another. This difference is taken into account by different coefficients in (1).

Relation for the determination of the Nusselt criterion for the busbar horizontal part is [32]:

$$Nu = 1,18 \cdot (Gr \cdot Pr)^{0,125}. \quad (13)$$

For the vertical part of the busbar [32]:

$$Nu = 0,75 \cdot (Gr \cdot Pr)^{0,25}. \quad (14)$$

Calculation of the heat transfer coefficient due to natural convection is carried out in accordance with (6). The calculation conditions are similar to those specified above for the round wire of AC type.

Let us calculate the Prandtl and Grashof similarity criteria necessary to determine the Nusselt criterion by (3) and (4), respectively. The Nusselt criterion is determined for horizontal and vertical busbar surfaces.

The heat transfer coefficient of the busbar from the horizontal surface is:

$$\alpha_1 = Nu \cdot \lambda / d, \quad (15)$$

where d is the thickness of the rectangular busbar.

The heat transfer coefficient from the vertical surface is:

$$\alpha_2 = Nu \cdot \lambda / h, \quad (16)$$

where h is the height of the rectangular busbar.

The area of the busbar horizontal surface (Fig. 2) is:

$$F_1 = 2 \cdot d \cdot L, \quad (17)$$

where L is the length of the rectangular busbar.

The area of the busbar vertical surface (Fig. 2) is:

$$F_2 = 2 \cdot h \cdot L. \quad (18)$$

The heat flow due to convection from the horizontal busbar surface is:

$$q_{C1} = \alpha_1 \cdot (t_{st} - t_p). \quad (19)$$

Heat release due to convection from the busbar horizontal surface is:

$$Q_{C1} = q_{C1} \cdot F_1. \quad (20)$$

The heat flow due to convection from the vertical busbar surface is:

$$q_{C2} = \alpha_2 \cdot (t_{st} - t_p). \quad (21)$$

Heat release due to convection from the busbar vertical surface is:

$$Q_{C2} = q_{C2} \cdot F_2. \quad (22)$$

Heat release due to convection is determined as:

$$Q_C = Q_{C1} + Q_{C2}. \quad (23)$$

The heat release from busbars due to radiation is determined by (9), and total one by (10).

The permissible continuous current for busbars is determined in accordance with (12). The results of its calculation in accordance with (12–23) are presented in Fig. 3.

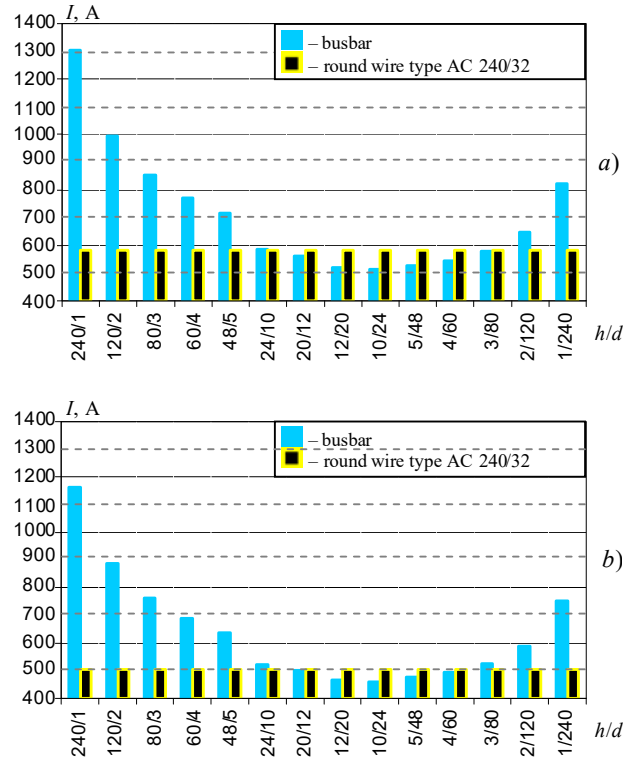


Fig. 3. Results of calculation of permissible continuous current of the OPL in UC with different design of the phase current conductor with cross-section of 240 mm² and different air temperatures: a) at $t_p = 15$ °C; b) at $t_p = 25$ °C

Analysis of the results of calculation of permissible continuous currents and choice of design of the phase current conductor of the OPL in UC. The analysis of the results obtained shows that busbars of the OPL in UC in comparison with round wire of the same cross-section have greater values of permissible continuous currents.

In Fig. 3, the abscissa axis shows the ratio h/d for different geometries of the busbars considered. Therefore, at an air temperature of 15 °C in the collector, the limiting values of currents for the OPLs in UC with busbars compared to temperature of 25 °C can be increased. Thus, for the OPLs in UC 110 kV with busbars 240/1, the permissible continuous current will increase by 12 % (from 1164 A to 1302 A), which will allow increasing the power of the power grid by 15 MW. At the same time, when performing the OPL in UC from the AC 240/32 wire, a change in air temperature from 25 °C to 15 °C leads to an increase in the permissible continuous current by only 9 %.

The results of calculations of permissible continuous currents for busbars with different h/d ratios allow us to determine the most rational designs of phase conductors of OPLs in UC with busbars. Such designs should be taken into account in the feasibility study when implementing a specific OPL in UC project, taking into account other technical parameters such as the line route, the presence of man-made influences, the presence of a rated voltage network, the impact on the environment, the costs of operation and repair, the required throughput, mechanical strength, reactive and active resistance, etc.

Determining rational designs of OPLs in UC with busbars will allow us to reduce the number of options for a more detailed technical and economic analysis.

OPLs in UC with busbars have greater permissible continuous currents which is connected with increase in the current conductor heat transfer surface P (Fig. 4).

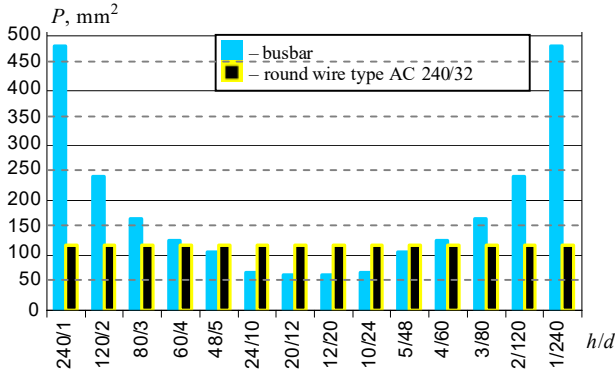


Fig. 4. Heat transfer surface area P of different designs of current conductors of the OPL in UC with cross-section of 240 mm^2

Analyzing the results shown in Fig. 3, 4, we can conclude that there are designs of busbars that have a smaller surface area or perimeter than the AC wire (with the same length) and have higher permissible continuous currents. With equal lengths of the compared conductors, their area is proportional to the perimeter of the conductor. At the same time, the perimeters of current conductors with busbars differ significantly from the perimeter of the AC 240/32 type wire. This confirms that the permissible continuous currents for OPLs in UC with busbars will be greater than the current for a round wire. This is also confirmed by Fig. 5, which shows the ratio k between the perimeters of different designs of busbars and a round wire and the ratio k for permissible continuous currents of busbars and a round wire.

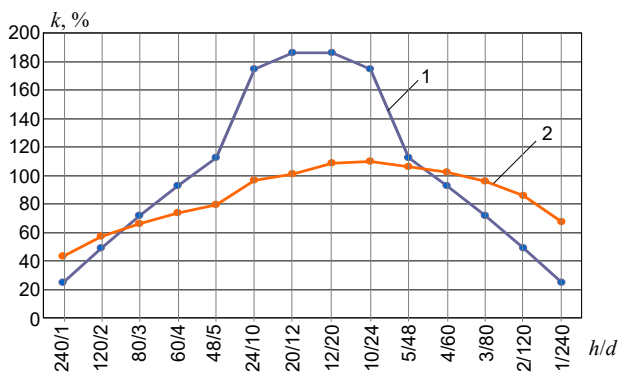


Fig. 5. Ratio k between wire parameters:
1 – ratio of the area of heat transfer surface for the wire type AC 240/32 for different busbar designs with cross-section of 240 mm^2 ;
2 – ratio of permissible continuous currents for the wire type AC 240/32 or different busbar designs

As shown above, the cooling efficiency of the current conductors of the OPLs in UC and the intensity of natural convection are determined by their heat transfer coefficient α according to (1–4, 6, 15, 16). At given air

temperatures in the collector and the limiting temperature of the current conductor, α significantly depends on its geometry, which determines the surface area, as well as on the spatial orientation of the conductor, which is illustrated in Fig. 3.

Thus, the greatest cooling efficiency and the greatest values of permissible continuous currents are provided by current conductors with busbars (Fig. 2) with the maximum ratio of its height h to its width d . Theoretically, such structures include busbars with an side ratio h/d of 240/1, 120/2, 80/3, 48/5 with a vertical busbar installation (at $h > d$) in accordance with Fig. 2. However, taking into account ensuring the necessary mechanical strength of the busbars, when designing an OPLs in UC it is advisable to limit oneself to a vertical current conductor with thickness of at least 2 mm.

In case of horizontal installation of busbars ($h < d$) the cooling efficiency and values of permissible continuous currents decrease (Fig. 3) due to worsening natural convection.

Determination of the interphase distance and the length of the spans for OPLs in UC with busbars.

The geometric dimensions of OPLs in UC with busbars are determined by their minimum interphase distance D (Fig. 2), which depends on the insulating properties of air. For closed switchgear 110 kV, the smallest interphase distance between their buses according to [36] is 250–450 mm, which can also be accepted for OPLs in UC.

Another important issue is the determination of the minimum length of the spans of the OPLs in UC with busbars at the accepted interphase distance, which depends on the electrodynamic forces that arise when a short-circuit shock current flows through the current conductors of the OPL in UC. In such an emergency mode, phase current conductors should not approach the adjacent phase at a distance at which insulation breakdown is possible.

To study this issue, calculations of the minimum allowable value of the span between supports of the OPL in UC when using busbars were performed. The analysis assumed that the busbar can be represented as a beam supported by several supports. Under this assumption, the allowable breaking force σ of the aluminum busbar can be defined as [35]

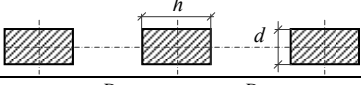
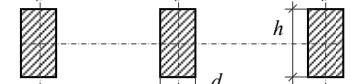
$$\sigma = \sqrt{3} \cdot 10^{-8} \cdot \frac{i_y^2 \cdot l^2}{W \cdot D}, \quad (24)$$

where i_y is the short-circuit current, kA; l is the span length; D is the interphase distance, m; W is the moment of resistance of the busbar relative to the axis perpendicular to the force action, m^3 .

The minimum span length of the OPL in UC is determined from the following relationship, obtained according to (24) and Table 1, limiting the allowable force σ for the aluminum busbar to a value of 40 MPa:

$$l = \left((\sigma \cdot W \cdot D) / (\sqrt{3} \cdot 10^{-8} \cdot i_y^2) \right)^{0.5}. \quad (25)$$

Table 1
Determination of moment of inertia and moment of resistance of the busbars of the OPL in UC

Busbar location	Moment of inertia	Moment of resistance
	$d \cdot h^3 / 12$	$d \cdot h^2 / 6$
	$h \cdot d^3 / 12$	$h \cdot d^2 / 6$

The results of calculating the length of spans for different designs of OPLi in UC with busbars under the action of different short-circuit shock currents, which are performed in accordance with [35] for the minimum possible under the conditions of air insulation breakdown the interphase distance of 300 mm for the PL in UC 110 kV [36] are presented in Fig. 6.

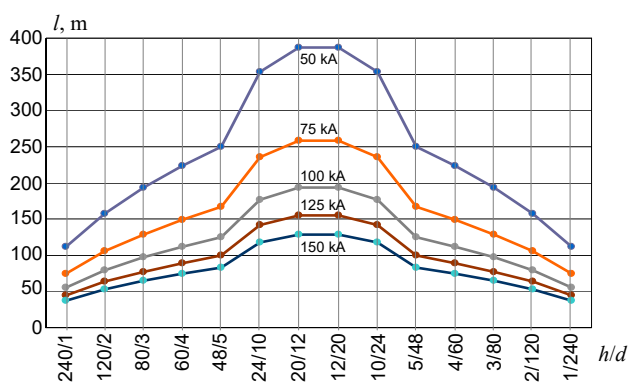


Fig. 6. Results of calculation of the length of the spans l of the OPL in UC depending on the design of the busbars with cross section of 240 mm² (h/d) at different currents

Analysis of the obtained results (Fig. 6) shows that the permissible span length of the OPL in UC with busbars depends quite significantly on its design parameters. The values of the span lengths obtained during the calculations indicate the possibility of constructing OPLs in UC with busbars for almost all busbar structures considered in the work. This indicates that the OPLs in UC with busbars, even for the smallest span values (50 m), will be cheaper than a conventional OPL due to the absence of traditional supports, which in our case are replaced by cheaper garlands of insulators, or support insulators. Therefore, the OPLs in UC, even when its spans are reduced to the minimum value (50 m), are competitive in comparison with OPLs.

Thus, OPLs in UC proposed by authors, in comparison with ground OPLs, as well as with underground OPLs of the same power, allow for reliable transmission of electricity with high throughput, the increase of which compared with ground OPLs 110 kV is from 3 % to 230 % (depending on the design of the busbars) with the same cross-sections of their current conductors. At the same time, the proposed OPLs in UC provide high protection from negative external atmospheric and military factors while reducing the electromagnetic impact on the environment.

At voltages of 20–110 kV, the proposed OPLs in UC are competitive with underground lines with SF₆ insulation, since with similar technical characteristics they have a simplified design of current conductors, which requires lower capital and operating costs.

Conclusions.

1. The technical and economic advantages of using OPLs in UC when placed in an underground collector are substantiated based on a comparative analysis of the characteristics of OPLs, CLs, and lines with SF₆ insulation.

2. A method for calculating permissible continuous currents of OPLs in UC is proposed, which is based on the analytical model developed by the authors for describing mass and heat transfer processes in the air of an underground collector and allows justifying the rational design of phase current conductors made of busbars.

3. It is shown that the implementation of the current conductors of the OPLs in UC from vertical busbars with side ratio of 240/1, 120/2, 80/3, 48/5, which are characterized by an increased surface area and increased natural convection heat transfer compared to a round wire of the same cross-section, as well as taking into account the decrease in air temperature in the underground tunnel to 15 °C compared to the external environment (25 °C), allows to significantly increase the throughput of the OPLs in UC compared to OPLs.

4. Based on the analysis of thermal, electromagnetic, electrodynamic processes in the OPLs in UC and literature sources, the possibility of significantly reducing the interphase distance for OPLs in UC compared to OPLs (for 110 kV OPLs from 3–4 m to 0.3–0.6 m) is substantiated, which allows to design the OPLs in UC in a compact design with a reduced level of electromagnetic fields.

5. For the first time, the technical and economic advantages of using the OPLs in UC in comparison with ground OPLs, as well as underground OPLs and underground CLs with SF₆ insulation are substantiated, and conditions are determined to ensure reliable transmission of electricity by the OPLs in UC with high throughput, the increase of which is from 3 % to 230 % (depending on the design of the busbars) compared to 110 kV OPLs in the open air with the same cross-sections of their conductors.

6. The proposed OPLs in UC are competitive with underground lines with SF₆ insulation for voltage of 20–110 kV, since with similar technical characteristics they have a simplified design of current conductors, which requires lower capital and operating costs.

7. The design and construction of the proposed OPLs in UC will ensure reliable transmission of electrical energy, sufficient throughput capacity and increased protection from negative external atmospheric and military factors while reducing the electromagnetic impact on the environment.

8. Further research is planned to focus on developing scientific foundations for regulatory documents on the design of OPLs in UC, which are currently absent in Ukraine.

Conflict of interest. The authors declare no conflict of interest.

REFERENCES

1. Faria J.H.S., Santos I.N., Rosentino A.J.P., Antunes A.H.P., Silva F.M., de Paula H. Design of an Underground, Hermetic, Pressurized, Isolated and Automated Medium Voltage Substation. *IEEE Open Journal of Industry Applications*, 2020, vol. 1, pp. 205-215. doi: <https://doi.org/10.1109/OJIA.2020.3034764>.
2. Shevchenko S., Danylchenko D., Hanus R., Radohuz S., Tomashevskiy R., Makhonin M., Potryvai A. Methods of Calculating Moisture Discharge Characteristics of Insulators. *Problems of the Regional Energetics*, 2025, no. 1(65), pp. 146-157. doi: <https://doi.org/10.52254/1857-0070.2025.1-65.11>.
3. CIGRE Joint Working Group 21/22.01. Comparison of high voltage overhead lines and underground cables - Report and Guidelines. CIGRE, 1996. 68 p.
4. Chino Hills Underground Project Update. 2015. 26 p. Available at: <https://www.chinohills.org/DocumentCenter/View/11427> (Accessed: 26 March 2025).
5. GridLAB. Transmission in California. 2023. 42 p. Available at: <https://gridlab.org/wp-content/uploads/2023/03/Transmission-in-California.pdf> (Accessed: 26 March 2025).
6. 华中第一个全地下变电站首台变压器吊装. Available at: http://m.cnhubei.com/content/2022-02/12/content_14493225.html (Accessed: 26 March 2025). (Chinese).
7. Prahladao S. Wuhan's First Fully Underground 220-kilovolt Substation Supports World-class Power Grid. Available at: <https://www.arcweb.com/blog/wuhans-first-fully-underground-220-kilovolt-substation-supports-world-class-power-grid> (Accessed: 26 March 2025).
8. LLC Kharkiv Design Development Institute «Teploelektroproekt-Soyuz». Unique Underground 220 kV «Smirnov» SS Construction. Available at: <https://tep-soyuz.com.ua/en/projects/raspredelenie-elektroenergii/stroitelstvo-unikalnoj-podzemnoj-ps-220-kv-smirnov> (Accessed: 26 March 2025).
9. Danylchenko D., Meshkov T. Study of the Possibility of Placing the Transformer Underground in Compliance with the Thermal Regime. *2024 IEEE 5th KhPI Week on Advanced Technology (KhPIWeek)*, 2024, pp. 1-5. doi: <https://doi.org/10.1109/KhPIWeek61434.2024.10878057>.
10. Shevchenko S., Danylchenko D., Dryvetskiy S., Potryvai A., Hanus R. Justification of the need to build underground substations and power lines. *Bulletin of the National Technical University «KhPI». Series: Energy: Reliability and Energy Efficiency*, 2023, no. 2(7), pp. 91-98. doi: <https://doi.org/10.20998/2224-0349.2023.02.14>.
11. Grechko O., Kulyk O. Current State and Future Prospects of Using SF6 Gas as an Insulation in the Electric Power Industry. *2024 IEEE 5th KhPI Week on Advanced Technology (KhPIWeek)*, Kharkiv, Ukraine, 2024, pp. 1-6. doi: <https://doi.org/10.1109/KhPIWeek61434.2024.10877987>.
12. Newton E. Overhead vs. Underground Power: Why Do We Use Both Locations? Energy Central, 2022. Available at: <https://www.energycentral.com/energy-management/post/overhead-vs-underground-power-why-do-we-use-both-locations-ch64fqBV7Og1Daf> (Accessed: 26 March 2025).
13. Fenrick S.A., Getachew L. Cost and reliability comparisons of underground and overhead power lines. *Utilities Policy*, 2012, vol. 20, no. 1, pp. 31-37. doi: <https://doi.org/10.1016/j.jup.2011.10.002>.
14. MacDonald M. *A Comparison of Electricity Transmission Technologies: Costs and Characteristics*. An Independent Report by Mott MacDonald in Conjunction with the IET. 2025, 335 p. Available at: https://www.theiet.org/media/axwkktkb/100110238_001-rev-j-electricity-transmission-costs-and-characteristics_final-full.pdf (Accessed: 26 March 2025).
15. SOU-N EE 20.179:2008. Calculation of electric and magnetic fields of power lines. Methodology (with changes) (in the edition of the order of the Minenergvygillya dated July 1, 2016, no. 423). Kyiv, Minenergvygillya Ukraine Publ., 2016. 37 p. (Ukr).
16. Rozov V.Y., Pelevin D.Y., Kundius K.D. Simulation of the magnetic field in residential buildings with built-in substations based on a two-phase multi-dipole model of a three-phase current conductor. *Electrical Engineering & Electromechanics*, 2023, no. 5, pp. 87-93. doi: <https://doi.org/10.20998/2074-272X.2023.5.13>.
17. Rozov V., Grinchenko V., Tkachenko O., Yerisov A. Analytical Calculation of Magnetic Field Shielding Factor for Cable Line with Two-Point Bonded Shields. *2018 IEEE 17th International Conference on Mathematical Methods in Electromagnetic Theory (MMET)*, 2018, pp. 358-361. doi: <https://doi.org/10.1109/MMET.2018.8460425>.
18. Rozov V.Y., Reutskiy S.Y., Pelevin D.Y., Yakovenko V.N. The research of magnetic field of high-voltage ac transmissions lines. *Technical Electrodynamics*, 2012, no. 1, pp. 3-9. (Rus).
19. *Electrical installation regulations*. Kharkiv, Fort Publ., 2017. 760 p. (Ukr).
20. Reut M.A., Rokotyan S.S. *Handbook of Power Transmission Line Design*. Moscow, Energiya Publ., 1980. 296 p. (Rus).
21. Rokotyan S.S., Shapiro I.M. *Handbook of Electrical Power Systems Design*. Moscow, Energoatomizdat Publ., 1985. 352 p. (Rus).
22. Grigsby L.L. *Power systems*. CRC Press, 2007. 452 p.
23. Pardalos P.M., Rebennack S., Pereira M.V.F., Iliadis N.A. *Handbook of power systems I*. Springer, 2010. 494 p.
24. Reddy B.S., Mitra G. Investigations on High Temperature Low Sag (HTLS) Conductors. *IEEE Transactions on Power Delivery*, 2020, vol. 35, no. 4, pp. 1716-1724. doi: <https://doi.org/10.1109/TPWRD.2019.2950992>.
25. Nuchprayoon S., Chaichana A. Performance Comparison of Using ACSR and HTLS Conductors for Current Upgrading of 230-kV Overhead Transmission Lines. *2018 IEEE International Conference on Environment and Electrical Engineering and 2018 IEEE Industrial and Commercial Power Systems Europe (IEEEIC / I&CPS Europe)*, 2018, pp. 1-5. doi: <https://doi.org/10.1109/IEEEIC.2018.8493888>.
26. Alawar A., Bosze E.J., Nutt S.R. A Composite Core Conductor for Low Sag at High Temperatures. *IEEE Transactions on Power Delivery*, 2005, vol. 20, no. 3, pp. 2193-2199. doi: <https://doi.org/10.1109/TPWRD.2005.848736>.
27. Hadzimuratovic S., Fickert L. Impact of gradually replacing old transmission lines with advanced composite conductors. *2018 IEEE PES Innovative Smart Grid Technologies Conference Europe (ISGT-Europe)*, 2018, pp. 1-5. doi: <https://doi.org/10.1109/ISGTEurope.2018.8571614>.
28. Dong X., Wang Q., Zhou Z., Li R., Liao Y., He J., Gong B., Zheng D., Chen W., Fan L., Zhu Y. Technical and Economic Analysis of Aluminum Conductor with Multi-stranded Composite Core and Its Application. *2019 IEEE Innovative Smart Grid Technologies - Asia (ISGT Asia)*, 2019, pp. 2634-2638. doi: <https://doi.org/10.1109/ISGT-Asia.2019.8880908>.
29. Lew J. Aluminum-Calcium Composite Conductors: The Future of America's Power Grid. *2020 IEEE MIT Undergraduate Research Technology Conference (URTC)*,

- 2020, pp. 1-4. doi: <https://doi.org/10.1109/URTC51696.2020.9668908>.
30. Tian L., Russell A., Riedemann T., Mueller S., Anderson I. A deformation-processed Al-matrix/Ca-nanofilamentary composite with low density, high strength, and high conductivity. *Materials Science and Engineering: A*, 2017, vol. 690, pp. 348-354. doi: <https://doi.org/10.1016/j.msea.2017.03.010>.
31. Alvarez Gómez F., Garcia de María J.M., Garcia Puertas D. Numerical study of the thermal behaviour of bare overhead conductors in electrical power lines. *Recent Researches in Communications, Electrical & Computer Engineering*, 2011, no. 1, pp. 149-153. Available at: <http://www.wseas.us/e-library/conferences/2011/Meloneras/ACELAE/ACELAE-25.pdf> (Accessed: 26 March 2025).
32. Mikheyev M.A., Mikheyeva I.M. *Basics of Heat Transfer*. Moscow, Energiya Publ., 1977. 344 p. (Rus).
33. Wang H. *Basic Heat Transfer Formulas and Data for Engineers*. Moscow, Atomizdat Publ., 1979. 216 p. (Rus).
34. Soil temperature at 2 m depth. Available at: <https://renouvelable-habitat.fr/en/soil-temperature-at-2m-depth> (Accessed: 26 March 2025).

How to cite this article:

Shevchenko S.Yu., Danylchenko D.O., Hanus R.O., Dryvetskyi S.I., Berezka S.K., Grechko O.M. Features of designing high-voltage overhead power lines in an underground collector. *Electrical Engineering & Electromechanics*, 2025, no. 5, pp. 80-88. doi: <https://doi.org/10.20998/2074-272X.2025.5.11>

35. Lezhniuk P.D., Lahutin V.M., Teptia V.V. *Design of electrical parts of power plants*. Vinnytsia, VNTU Publ., 2009. 194 p. (Ukr).
36. *SOU 45.2-00100227-24:2010* Protection of wires and cables of overhead power lines from wind vibrations (vibrations, galloping, sub-oscillations). Methodological guidelines.

Received 12.03.2025

Accepted 04.05.2025

Published 02.09.2025

S.Yu. Shevchenko¹, Doctor of Technical Science, Professor,
D.O. Danylchenko¹, PhD, Associate Professor,
R.O. Hanus¹, PhD Student,
S.I. Dryvetskyi¹, PhD, Associate Professor,
S.K. Berezka¹, PhD,
O.M. Grechko¹, PhD, Associate Professor,
¹ National Technical University «Kharkiv Polytechnic Institute»,
2, Kyrpychova Str., Kharkiv, 61002, Ukraine,
e-mail: dmytro.danylchenko@khpi.edu.ua (Corresponding Author)

Матеріали приймаються за адресою:

Кафедра "Електричні апарати", НТУ "ХПІ", вул. Кирпичева, 2, м. Харків, 61002, Україна

Електронні варіанти матеріалів по e-mail: a.m.grechko@gmail.com

Довідки за телефонами: +38 067 359 46 96 Гречко Олександр Михайлович

Передплатний індекс: 01216